

Modeling Effects of Extracellular
Stimulation on Retinal Bipolar Cells

Dissertation

zur Erlangung des Grades eines
Doktors der Naturwissenschaften

der Mathematisch-Naturwissenschaftlichen Fakultät
und
der Medizinischen Fakultät
der Eberhard-Karls-Universität Tübingen

vorgelegt

von

Heval Benav
aus Dohuk, Irak

September – 2012

Tag der mündlichen Prüfung: 20.12.2012

Dekan der Math.-Nat. Fakultät: Prof. Dr. W. Rosenstiel

Dekan der Medizinischen Fakultät: Prof. Dr. I. B. Autenrieth

1. Berichterstatter: Prof. Dr. Eberhart Zrenner

2. Berichterstatter: Prof. Dr. Dr. Dr. Frank Rattay

Prüfungskommission:
Prof. Dr. Thomas Euler
Prof. Dr. Frank Schäffel
Prof. Dr. Dr. Dr. Frank Rattay
Prof. Dr. Eberhart Zrenner

SUMMARY

Neuroprosthetic retinal implants have been developed to restore vision in profoundly blind patients suffering from degenerative retinal diseases such as Retinitis Pigmentosa. The Tübingen subretinal implant project is currently conducting a multi-center clinical study with promising results. However, several issues remain unsolved and decrease the quality of visual percepts elicited by the subretinal implant. One of the reasons may be the simultaneous stimulation of opposing retinal ON and OFF pathways.

The present thesis describes the development of a realistic computational model of retinal bipolar cells and the biophysical events leading to activation of the retinal network during extracellular electrical stimulation. Retinal bipolar cells are the focus of this model, since they initiate ON and OFF pathways and are the primary target for stimulation with subretinal implants. The electric potential induced by the electrodes of the implant was calculated using a Finite Element Method. Monopolar and dipolar electrode configurations were implemented. Published imagery of retinal bipolar cells was used to create realistic morphological models. Passive and active membrane models were used for calculation of transmembrane voltage and ionic currents. While the passive model assumed constant conductances, the active model included several systems of differential equations for calculation of voltage-dependent ion channel gating mechanisms and intracellular calcium concentration. Two different active models have been created for ON and OFF cone bipolar cells. The inventory of ion channels used in the models was based on a literature review including all voltage-gated ion channels that have been found in retinal cone bipolar cells of the rat. For each ion channel type, an existent model was adapted or a new model was created, based on data from published electrophysiological recordings.

Several simulations were conducted with monopolar and dipolar configurations, single and multiple electrodes, the passive and the active model, monophasic and biphasic pulses as well as repetitive stimuli. Intracellular calcium concentration changes in the synaptic axon terminals were used as the main indicator for neuronal activation. A series of simulations with different combinations of biphasic pulses revealed that ON cone bipolar cells may respond preferentially to biphasic pulses with a short strong cathodic phase and a long weaker anodic phase when compared to OFF cone bipolar cells. It should be noted, that these results are based on several assumptions that have been made during the development of the computational model. However, preliminary electrophysiological recordings using this specific stimulus paradigm suggested that a certain differential effect on ON and OFF cone bipolar cells may in fact exist and that further experiments should be conducted for a better understanding of this phenomenon.

TABLE OF CONTENTS

1	INTRODUCTION	1
1.1	ARTIFICIAL VISION	1
1.1.1	THE TÜBINGEN SUBRETINAL IMPLANT	3
1.2	THE RETINA	5
1.2.1	ANATOMY	5
1.2.2	NEUROPHYSIOLOGY	7
1.3	RETINAL DEGENERATIONS	9
1.3.1	SIGNIFICANCE OF BIPOLAR CELLS FOR SUBRETINAL PROSTHESES	11
1.4	MODELING APPROACH	12
1.4.1	RESOURCES	12
1.4.2	LIMITATIONS	13
1.4.3	SIMULATION ENVIRONMENTS	13
1.4.4	MODEL ANIMAL	14
1.5	AIM OF THIS STUDY	14
2	THE PASSIVE MODEL	16
2.1	INTRODUCTION / MOTIVATION	16
2.2	MODELING AND METHODS	17
2.2.1	CALCULATION OF THE ELECTRIC FIELD	17
2.2.2	THE SIMULATED SPATIAL VOLUME	19
2.2.3	ELECTRODE SHAPE AND PROPERTIES	21
2.2.4	CALCULATION OF THE NEURONAL RESPONSE	23
2.2.5	IMPLEMENTATION	27
2.3	SIMULATIONS AND RESULTS	28
2.3.1	SINGLE ELECTRODE SIMULATIONS	28
2.3.2	MULTI-ELECTRODE SIMULATIONS	39
2.4	DISCUSSION	42
3	THE ACTIVE MODEL	44
3.1	INTRODUCTION	44

3.2	LITERATURE REVIEW	44
3.2.1	EXPLANATION OF COMMON METHODS	45
3.2.2	FIRST EVIDENCE OF VOLTAGE-GATED Na^+ CURRENTS IN MAMMALIAN CONE BIPOLAR CELLS	48
3.2.3	KINETICS OF K^+ CURRENTS IN RAT RETINAL BIPOLAR CELLS	49
3.2.4	DETECTION OF DIFFERENTIALLY EXPRESSED HCN CHANNELS IN RAT RETINAL BIPOLAR CELLS	52
3.2.5	AN INVENTORY OF RETINAL CONE BIPOLAR CELL ION CHANNELS IN THE RAT	54
3.2.6	LOCALIZATION OF HCN CHANNELS IN THE RAT RETINA	58
3.2.7	TWO TYPES OF CONE BIPOLAR CELLS EXPRESS VOLTAGE-GATED Na^+ CHANNELS IN THE RAT RETINA	59
3.2.8	T-TYPE Ca^{++} CHANNELS IN RAT RETINAL BIPOLAR CELLS	63
3.2.9	LITERATURE SUMMARY	65
3.2.10	CONCLUSIONS FOR THE ACTIVE BIPOLAR CELL MODEL	70
3.3	ION CHANNEL MODELING	74
3.3.1	HODGKIN HUXLEY MODEL	75
3.3.2	SODIUM CHANNELS - I_{Na}	80
3.3.3	POTASSIUM CHANNELS - I_{Kv}	81
3.3.4	HYPERPOLARIZATION-ACTIVATED CHANNELS – $I_{\text{HCN1}}, I_{\text{HCN2}}, I_{\text{HCN4}}, I_{\text{Kir}}$	83
3.3.5	Ca^{++} CONCENTRATION, Ca^{++} CHANNELS AND Ca^{++} -ACTIVATED CHANNELS – $I_{\text{Ca,T}}, I_{\text{Ca,L}}, I_{\text{K(CA)}}$	89
3.4	SIMULATIONS AND RESULTS	95
3.4.1	ON CONE BIPOLAR CELL	97
3.4.2	OFF CONE BIPOLAR CELL	112
3.4.3	SELECTIVE STIMULATION OF ON AND OFF BIPOLAR CELLS	129
3.5	DISCUSSION	132
4	CONCLUSIONS	138
5	REFERENCES	141
6	APPENDIX	150
6.1	ACKNOWLEDGEMENTS	150
6.2	SWC FILES	150
6.3	PUBLICATION ON THE TÜBINGEN SUBRETINAL IMPLANT	153
6.4	CURRICULUM VITAE	163

1 Introduction

This work has been conducted in the scope of the Tübingen subretinal implant project. The overall goal of this project is the restoration of vision in blind patients using a subretinal multiphotodiode array (MPDA). This thesis aims at a deeper understanding of the processes that occur in retinal neurons, especially in retinal bipolar cells, during extracellular electrical stimulation. Possibilities of more optimal stimulation procedures are investigated here using computational modeling methods with a special focus on differential activation of ON and OFF pathways in the retina.

1.1 Artificial Vision

A continuously growing number of people are affected by blindness. According to a report released by the World Health Organization (WHO) 37 million people worldwide were blind in 2007, not including impaired vision due to refractive errors or other low vision patients (WHO 2007). This number had increased to 45 million by the year 2006 constituting a 21% increase. The leading causes for blindness in Germany in decreasing order are age-related macular degeneration (AMD), glaucoma and diabetic retinopathy (Resnikoff et al. 2004). Considering the growing percentages of elderly people in technologically developed nations, the prevalence of blindness is expected to further increase, especially in regard to AMD. Additional to the decreased quality of life blindness can cause for patients, the existence of blindness also generates excessive costs for the economy (WHO 2007).

Different approaches are being undertaken worldwide in an attempt to restore vision by electrical stimulation of neuronal tissue. Due to the heterogeneity of the causes for blindness, most approaches only are relevant to one or a few types of blindness. The advent of new fabrication techniques for micro- and nanotechnology facilitated the production of multielectrode arrays in silicon-based chips, which can stimulate parts of the visual system. Current technologies include electrical stimulation of the retina (Rizzo III et al. 1996, Zrenner et al. 1999, Humayun 2001, Hornig et al. 2005, Fujikado et al. 2007, Zhou et al. 2008, Dommel et al. 2009, Mathieson et al. 2012), the optic nerve (Veraart et al. 2003, Li et al. 2008), the thalamus (Pezaris and Reid 2007) and the visual cortex (Fernández et al. 2005, Normann et al. 2009). For all types of visual prostheses, it is commonly assumed that the patient must have had previously functioning vision before becoming blind. The reason is that cortical processing of the visual information sent from the eye to the brain is not hard-wired into cortical neurons, but has to be learned during early childhood. Neuronal plasticity of the networks involved in learning vision, however, is assumed to decrease with increasing age

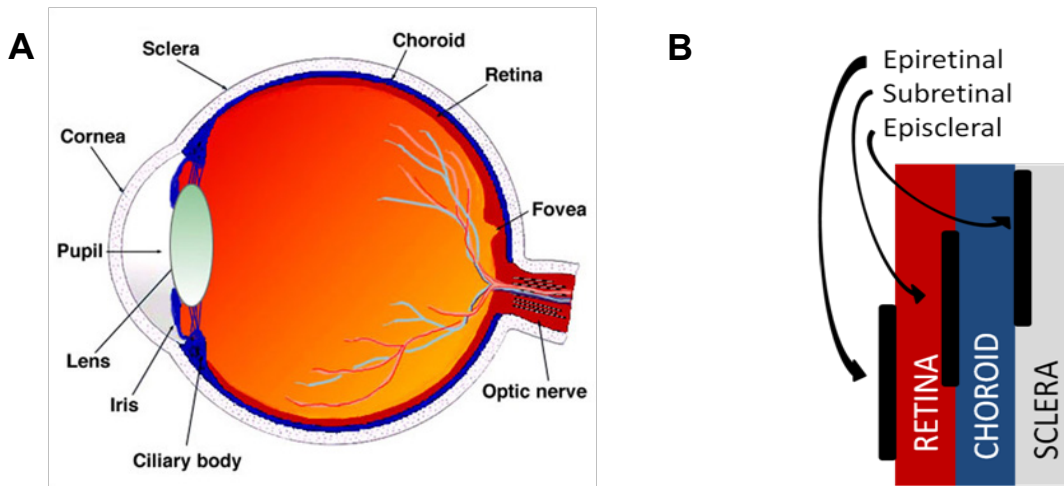


Figure 1.1

Sagittal section through the human eye (A). Image adapted from (Kolb et al. 2005). Schematic depiction of the different positions of epiretinal, subretinal and episcleral implants (B) Subretinal implants occupy the area of degenerated rods and cones and are located close to the retinal bipolar cells. Epiretinal implants are attached to the inner limiting membrane located close to the ganglion cell layer. Episcleral implants stimulate the retina through the choroid.

(Nieto-Sampedro and Nieto-Díaz 2005). The brain of an adult who was born blind is therefore thought to be physically unable to initiate this learning process.

Optic nerve implants are a possible treatment for patients who had to undergo enucleation (removal of an eye), mostly due to cancer including retinoblastoma or choroidal melanoma. If the optic nerve is damaged, for example due to glaucoma or Leber's hereditary optic neuropathy (LHON), cortical stimulation may be feasible. Due to the parallel processing scheme of neural systems as well as convergence and divergence in neural processing the complexity of the stimulation pattern required by neuroprosthetic devices increases in higher order locations of the nervous systems, making stimulation at the retinal level most straightforward in respect to stimulus complexity. Retinal implants are an additional option, if patients suffer from diseases leading to the loss of photoreceptors such as AMD or retinitis pigmentosa (RP). The reason will be discussed in more detail in Section 1.3. The focus of this thesis will be on retinal implants.

Figure 1.1 A shows a sagittal section through the human eye. Several different approaches exist with the target to stimulate the retina in order to evoke visual perceptions. In the subretinal approach (Figure 1.1 B) an electrode array is positioned in the subretinal space between the retina and the choroid (See also section 1.1.1). Other retinal implant techniques include episcleral implants with an electrode array located between the sclera and the choroid (Fujikado et al. 2007) or epiretinal implants (Humayun 2001) where an electrode array is attached to the inner limiting membrane (ILM) using retinal tacks, close the ganglion cell layer (GCL, Figure 1.1 B, Figure 1.3 C and Figure 1.4).

Additional to the different location relative to the retina, the techniques can also differ with regard to the need for a separate camera. No camera is needed when an MPDA is used which is sensitive to visible light, as it is the case in the Tübingen subretinal implant. Another subretinal technique employs an MPDA which is sensitive to infrared light, carrying not only the visual information but also the energy required to activate the electrodes (Mathieson et al. 2012). In that case the image is recorded by an external camera built in to video goggles. All presently developed epiretinal implants also utilize head mounted external cameras. When the image is recorded using head mounted cameras one advantage is the possibility of computational image pre-processing before it is sent to the stimulating electrodes. However, with a head-mounted camera eye movements of the patient do not move the scene which the person is seeing, instead the entire head has to be moved. Feasible eye-tracking techniques do not yet exist for blind people, since the calibration of such systems requires feedback from the subject. A subretinal MPDA sensitive to visible light has the advantage that the image recording unit (photodiode) is moved simultaneously with the patient's eye. The images seen by the patient therefore move accordingly.

1.1.1 The Tübingen Subretinal Implant

The Tübingen subretinal implant project involves a consortium of groups and was initiated in 1995 (Zrenner et al. 1999). On the basis of data from *in-vitro* measurements (Stett et al. 2000) and animal experiments (Eckhorn et al. 2006), a subretinal microphotodiode-array (MPDA, Figure 1.2 A) was developed. It contains approximately 1500 units (Figure 1.2 G), each consisting of a light-sensitive photodiode, a difference-amplifier and a stimulating electrode which generates voltage-controlled pulses. Each electrode is 50 μm x 50 μm in size, the center-to-center distance of two electrodes is 70 μm . The version of the implant shown in (Figure 1.2 A) also has an additional direct-stimulation (DS) array consisting of 16 stimulating units with 4 electrodes each (Figure 1.2 C). The DS array acts independently of external light stimulation and can be controlled via a computer in order to present specific stimuli as depicted in Figure 1.2 D, E, and F. The entire implant is shown in Figure 1.2 B. It is implanted into the subretinal space of the patient's eye (Figure 1.3 B, C) using a transchoroidal implantation procedure (Sachs et al. 2009). During the implantation procedure, the vitreous body of the eye is replaced with silicone oil (vitrectomy) (Besch et al. 2008). The extraocular part of the implant (Figure 1.3 E) is implanted subdermally (Figure 1.3 A) and exits the patient's skin in a location behind the ear. The patient carries a controller for adjustment of sensitivity and gain parameters as well as power supply (Figure 1.3 D). As shown in Figure 1.3 C, the subretinal location of the MPDA implies that the stimulating electrodes are located close to the retinal bipolar cells (BC) in a perpendicular position. Light entering the patient's eye through the lens is incident on the MPDA at the retinotopically appropriate location, since the implant is moved by eye movements. Each

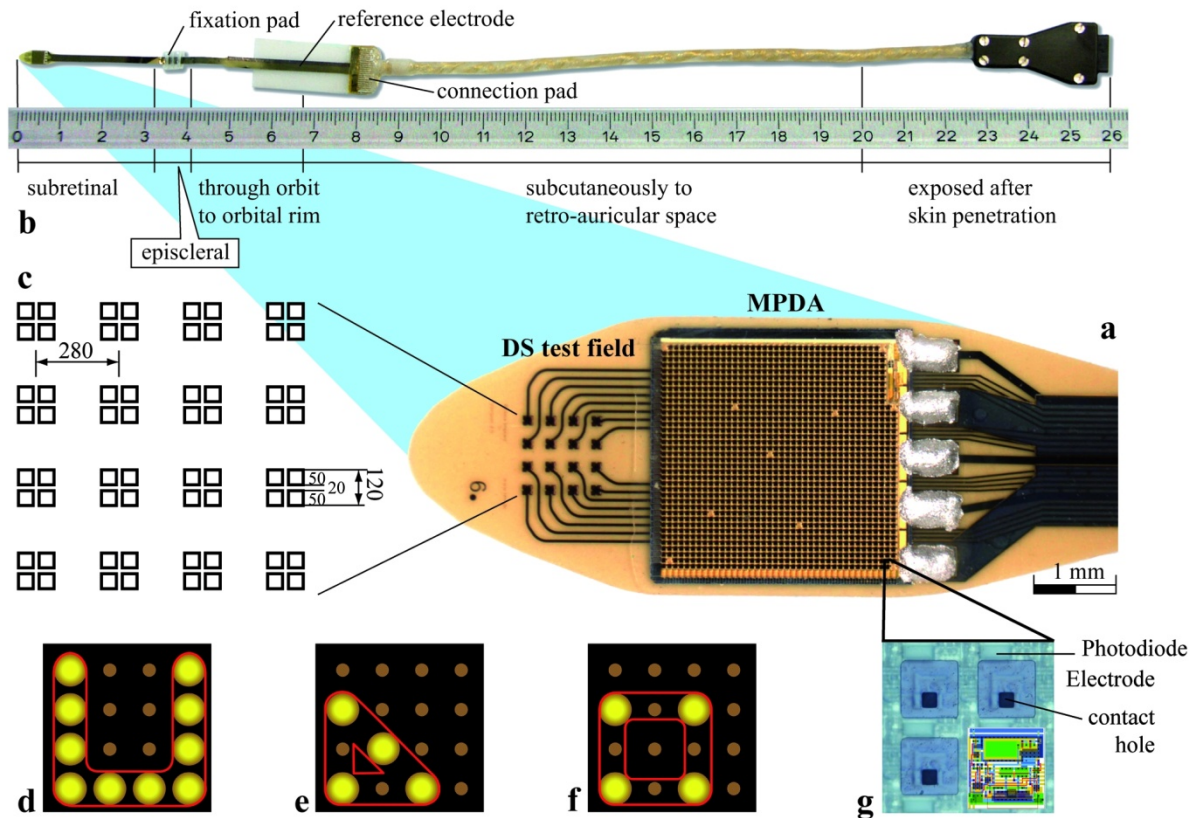


Figure 1.2

Overview of the technology of the Tübingen subretinal implant. The light-sensitive microphotodiode-array (MPDA) (A) contains 1500 units with a spacing of $70\ \mu\text{m}$. An additional direct stimulation (DS) array with 16 units each consisting of 4 electrodes (C) can be activated through the computer to create patterns as shown in D, E and F. Each of the MPDA units (G) consists of a photodiode, a difference amplifier and a stimulating electrode ($50\ \mu\text{m} \times 50\ \mu\text{m}$). Figure from (Zrenner et al. 2010).

photodiode causes one electrode to generate a voltage pulse with an amplitude proportional to the intensity of incident light. The electric fields generated by these voltage pulses therefore activate the retinal network through extracellular stimulation of bipolar cells.

During the clinical pilot study (Zrenner et al. 2010) it was shown that light perception is possible with the Tübingen subretinal implant. Some patients were able to discern contrast levels of 15% and could identify objects like forks and knives on dark background. The maximal visual acuity (VA) which could be achieved using spatial discrimination tasks was 20/1000, which is the threshold for legal blindness in Germany. Patients were able to read large letters on dark background, to move freely in a room and to identify unknown objects. Following the clinical pilot study, a multicenter study was initiated in which patients received a new generation of the implant in several ophthalmological centers worldwide (Zrenner et al. 2011). Patients had the ability to detect movement directions up to $7^\circ/\text{s}$ angular speed and demonstrated improved eye-hand coordination after they received the implant. A recent publication (Zrenner et al. 2010) with further details can be found in the appendix, section 6.3.

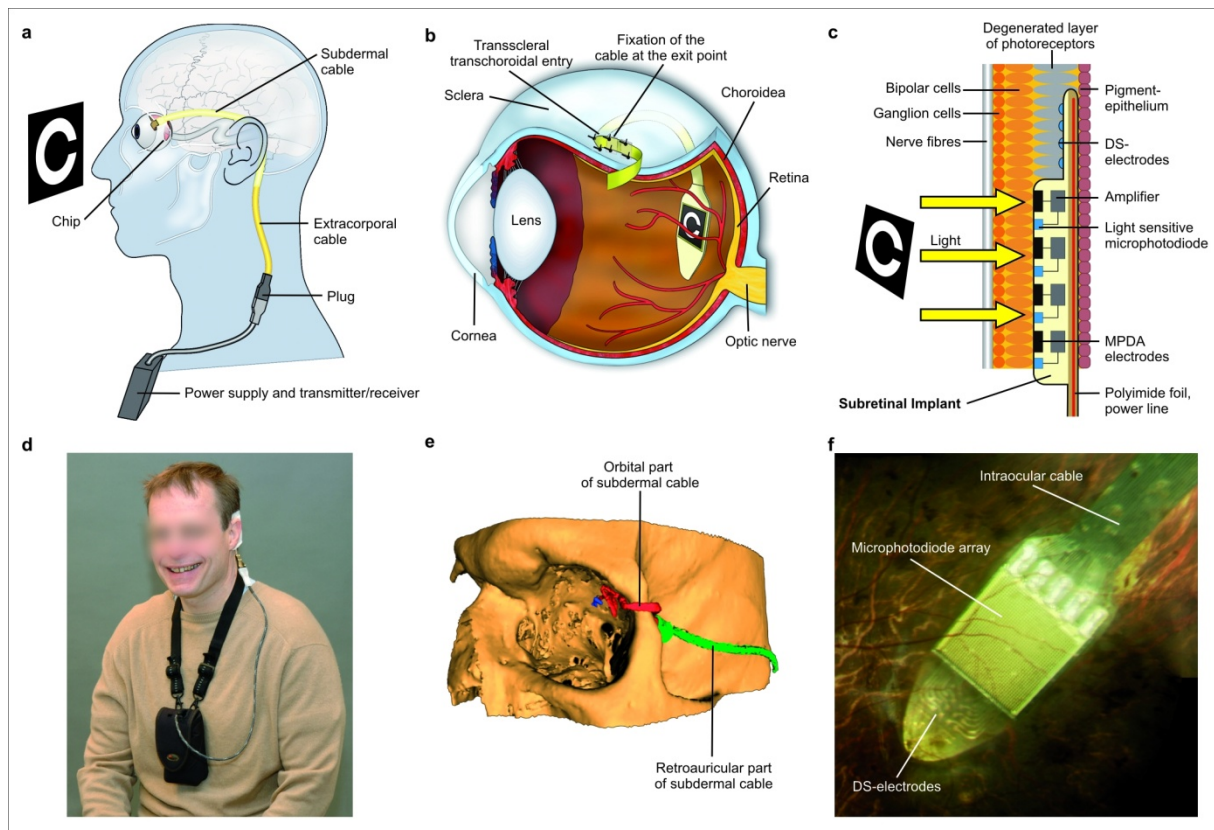


Figure 1.3

Location of the Tübingen subretinal implant. The cable for power supply leaves the orbita subdermally and exits the skin behind the patients ear (A). Subretinal position of the implant in the eye (B). Location of the electrodes relative to the retinal layers (C). Patient with the control and power supply unit (D). CT scan of the subdermal cable (E). Image of the implanted chip taken with an ophthalmoscope (F). Figure from (Zrenner et al. 2010).

1.2 The Retina

1.2.1 Anatomy

Visual perception starts in the eye. After crossing the optical apparatus of the lens, light initiates the phototransduction chain in the light sensitive layer of the retina - the photoreceptor (PR) layer containing rods and cones (Figure 1.4). Through a second messenger signaling pathway the stimulation is translated into electrical signals by hyperpolarization of the transmembrane voltage (V_m) in PRs and is sent to second order retinal neurons through chemical synapses. After passing all other retinal layers and the associated signal processing, retinal ganglion cells (RGC) relay the perceptually relevant visual information through the optic chiasm and the thalamic lateral geniculate nucleus (LGN) to the primary visual cortex and higher order visual processing areas in the brain. Only the retinal visual processing stages are relevant to this thesis and will be addressed here. Higher order visual processing and actual perception of vision are beyond the scope of this thesis.

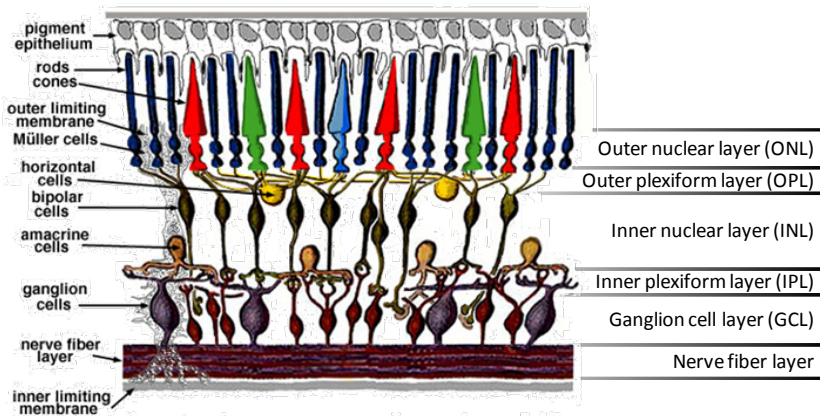


Figure 1.4

A schematic diagram of the retinal layers and neuron classes in vertebrates. Photons enter from below, pass the translucent retina and are absorbed by rhodopsin and cone opsin complexes in the rods and cones, respectively. The neuronal signal is then sent through all layers and exits the retina in the nerve fibers of ganglion cells. Image adapted from (Kolb et al. 2005)

Retinal neurons have been divided into the following 6 classes:

- Rods (photoreceptor cells, PR)
- Cones (photoreceptor cells, PR)
- Horizontal cells (HC)
- Bipolar cells (BC)
- Amacrine cells (AC)
- Ganglion cells (GC)

Each of these classes can be divided into more specialized cell types. In primates for example, three different types of cones exist which are sensitive to short, middle or long wavelength spectra of visible light (S, M and L cones) and therefore responsible for the first step in color perception. The human retina contains about 120 million rods and 6 million cones (Osterberg 1935). Their information is converged through the retinal network to more than 1 million GCs (Polyak 1941, Balazsi et al. 1984). The most diverse class are ACs as 29 different types have been identified (MacNeil and Masland 1998). The thickness of the retina can vary, especially after retinal degenerations. It is thought to have an average thickness of 200 μm - 300 μm (Boycott et al. 1969, Garcia-Martin et al. 2012).

Bipolar cells usually connect either to rods or to cones (Ramon y Cajal 1893). Only one type of BC connects to rods exclusively (Boycott et al. 1969), the rod bipolar cell (RBC or RB). Most of the literature on BCs has been collected from the rat as a model animal. An exploratory investigation on the diversity of retinal BCs (Euler and Wässle 1995) identified nine different cone bipolar cell (CBC) types in the rat (Figure 1.5) additional to one RBC. Later studies have identified the presence of additional CBC types in the rat. Based on different ion channel equipment and axon terminal stratification, type 6 CBCs have been divided into type 6a and type 6b (Ivanova and Müller 2006) and later similar aspects lead to the differentiation of type 5a and type 5b CBCs (Fyk-Kolodziej and Pourcho 2007). One additional bipolar cell of the rat receives mixed input from rods and cones (Marc and Liu 2000).

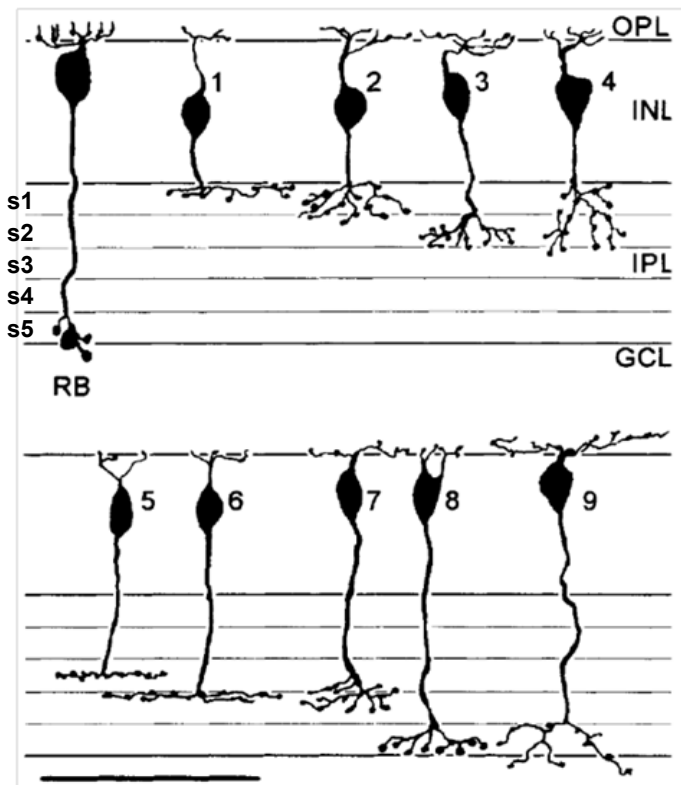


Figure 1.5

Morphological classification of bipolar cells in the rat retina. The cells were filled with Lucifer Yellow and neurobiotin. Additional to the rod bipolar cell (RBC or RB), nine different cone bipolar cell types were identified and arranged according to their stratification level in the IPL. The IPL is further divided into 5 strata of equal width (s1-s5), marked with thin lines. The scale bar equals 50 μm . Figure modified from Euler and Wässle 1995.

1.2.2 Neurophysiology

Unlike most neurons which generate action potentials after their transmembrane potential has been depolarized above a certain threshold voltage, receptor cells have so-called receptor potentials which increase or decrease gradually in correlation to the intensity of the stimulating signal. In the case of PRs, the receptor potential hyperpolarizes after incidence of light has been registered, leading to more negative values for membrane voltage (V_m) in PRs when light is switched on (Figure 1.6). This “ON” signal thus correlates with hyperpolarization (more negative potential) of V_m on the level of PRs. In the absence of a light stimulus, the receptor potential of a PR is depolarized (more positive values). Changes in V_m reach the axon terminal of PRs and cause voltage-dependent changes in intracellular Ca^{++} concentration. The intracellular Ca^{++} concentration controls the rate of synaptic neurotransmitter (glutamate) release into the synaptic cleft and therefore the degree at which the V_m of second order retinal neurons changes. Higher depolarization leads to larger increases of intracellular Ca^{++} concentration.

It was previously believed that all retinal neurons except GCs and one type of AC (Werblin and Dowling 1969, Masland 2001) had such graded potentials. GCs transmit information through their axons to the LGN and fast, reliable transportation of neuronal signals over such distances is facilitated by active amplification in the form of action potentials. The wide-field AC also has processes that can span more than one mm in the retina (Taylor 1996). Most other

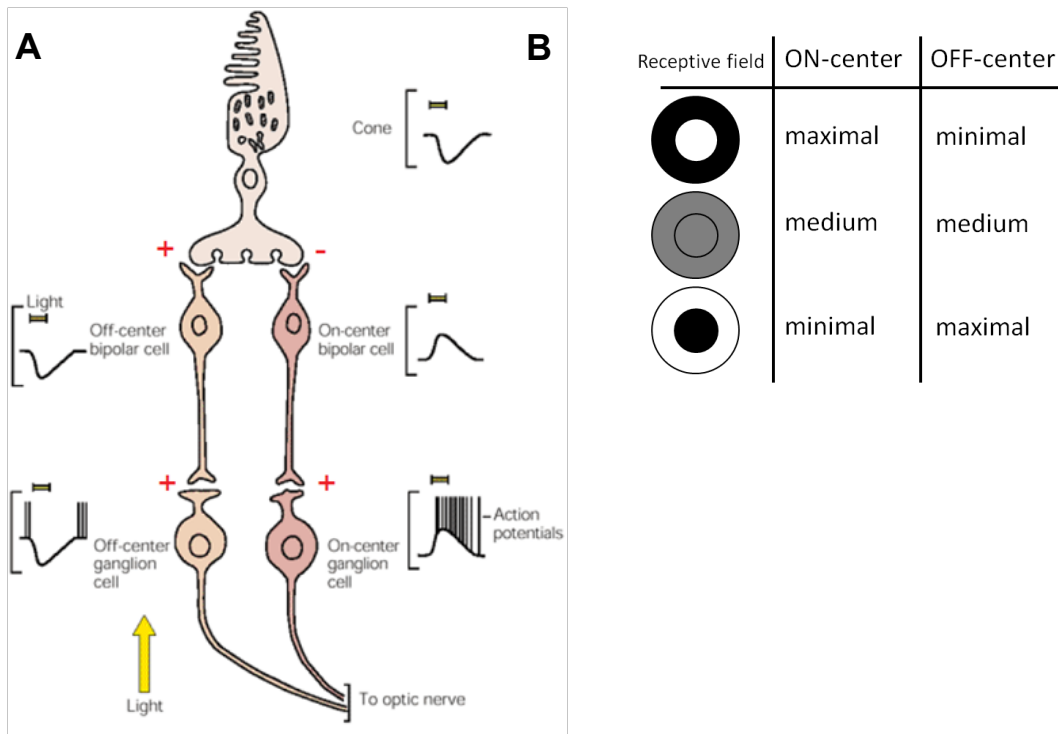


Figure 1.6

Schematic diagram of the parallel pathways for ON and OFF signals in the retina and associated membrane potentials (A). Light hyperpolarizes cones. A sign-conserving (+) synaptic connection causes OFF-type bipolar cells to hyperpolarize when light is "on", while a sign-inverting (-) synapse from cones to ON-type BC results in a depolarized membrane potential at the same time. Synapses between BC and GC are sign-conserving (+). GCs encode the visual information with action potentials. Image adapted from (Tessier-Lavigne 2000). Preferred receptive field stimulation for ON-center and OFF-center cells (B). A bright center and dark periphery raises the maximal response in ON-center cells and affects OFF-center cells only minimally, vice versa for dark center and bright periphery. Both ON- and OFF-center have intermediate responses to an evenly illuminated receptive field.

retinal neurons however, have processes that are usually less than 100 μm in length and such distances can be overcome without action potentials. Nevertheless, it has been shown that certain BCs are able to generate Ca^{++} based action potentials (Protti et al. 2000) and that these spikes appear to be modulated by light (Dreosti et al. 2011). The concrete function of these spikes in BCs is not fully known.

An early study has shown that vertebrate BCs are most sensitive if stimulated by PRs directly under the BC and not stimulated by PRs in the vicinity (ON-center) or vice versa (OFF-center) (Kaneko 1973). This center-surround antagonism is initiated in the first synaptic stage of the retina between PRs and BCs (Figure 1.6). While PRs always hyperpolarize during light stimulation, the synaptic connection between cones and CBCs differs depending on the type of CBC. The neurotransmitter released by PRs as a result of depolarization is glutamate. A hyperpolarization of the cone membrane potential leads to decreased amounts of glutamate in the synaptic cleft between cones and CBCs. Dendrites of ON-center or ON-type CBCs express a specific metabotropic glutamate receptor, mGluR6, which initiates

the closure of a cyclic guanosine monophosphate (cGMP)-gated cation selective channel when glutamate binds to the receptor. Therefore, ON-type CBCs depolarize when less glutamate is present in the synapse, making this synaptic connection sign-inverting (Figure 1.6). Dendrites of OFF-center or OFF-type CBCs have ionotropic glutamate receptors which are cation selective ion channels that open their gates when glutamate binds to them. This constitutes a sign-conserving synaptic connection and leads to a hyperpolarization of the OFF-type CBC transmembrane potential when light reaches PRs (Figure 1.6).

Another key difference between ON-type and OFF-type CBCs is that their axon terminals stratify in different areas of the IPL. CBC types 1-4 (all OFF-type) stratify in stratum (s) 1 and/or s2, also called the OFF-layer. CBC types 5-9 however (all ON-type), stratify in s3, s4 and/or s5, also called the ON-layer of the IPL (Figure 1.5). Further differences between ON- and OFF-type CBCs lay in their complement of ion channels and will be addressed in more detail in chapter 3. The ON/OFF antagonism is not restricted to BCs, since ON-center BCs feed their information at the next retinal level to ON-center GCs and OFF-center BCs to OFF-center GCs. The optic nerve, consisting of GC axons, therefore has separate axons for the ON and OFF signals. The function of ON and OFF pathways is the detection of signals that stand out by being brighter or darker than the background, respectively (Kuffler 1953). Evenly illuminated areas are less “interesting” to biological life than areas with a high contrast profile. A BC that is maximally sensitive to a contrast-rich stimulus thus initiates the first stage in the process of detection of borders and objects.

Additional to the ON/OFF pathways, other parallel pathways in the retina are the parvocellular and magnocellular pathway. Cells of the parvocellular pathway have smaller dendritic fields and therefore smaller receptive fields. GCs in the parvocellular pathway have low temporal resolution but higher spatial resolution. Cells of the magnocellular pathway have broader dendritic fields as well as larger receptive fields, three to ten times larger than those of the parvocellular pathway (Dacey and Petersen 1992). GCs in the magnocellular pathway have higher temporal resolution and lower spatial resolution. Axons from parvo- and magnocellular pathways project to different layers of the LGN.

1.3 Retinal Degenerations

As mentioned in Section 1.1, retinal implants can restore vision only in patients with AMD or RP since these diseases affect only PRs directly. AMD is the leading cause for blindness in many industrially developed countries and affects only persons above 50 years (Bird et al. 1995). Patients first lose the cones leading to macular scotoma and a loss of central vision (Figure 1.7 B). In later stages, peripheral vision also can be affected. The clinical pilot study in Tübingen excludes patients with

AMD from the selection of subjects. Reasons are the late onset of AMD with 50 years and the rather slow progression after the loss of central vision. Theoretically, the technique should be feasible for treatment of AMD. In a later stage of development the potential benefits for AMD patients may outweigh the risk of surgery.

Retinitis pigmentosa (RP) is the most frequent hereditary cause for blindness (Zrenner et al. 1992). Typically in adolescence, the initial symptom of RP is impaired night-vision. Groups of rods degenerate (Figure 1.7 C) due to certain gene defects. The degeneration progresses to all rods, resulting in tunnel-vision (Figure 1.7 D). In later stages, RP can also lead to loss of central vision due to subsequent degeneration of cones, leading to complete blindness. The genetic causes of RP are highly heterogeneous as more than 100 gene defects have been linked to the disease so far (Hartong et al. 2006) accounting for only 60% of the patients. Currently, no cure is available. This is partly due to the high variability of phenotypes which results from the large number of different causes for RP. However, attempts at restoration of vision for RP patients are being undertaken with different approaches, including electronic retinal prostheses (Zrenner 2002) and gene therapy (MacLaren 2009).

In both diseases only photoreceptors are affected by degeneration directly and all other retinal layers can remain functional. There have been reports that 80% of the inner nuclear layer (INL) neurons and 30% of GCs were found to be preserved in post-mortem retinal explants of patients with advanced RP (Santos et al. 1997).

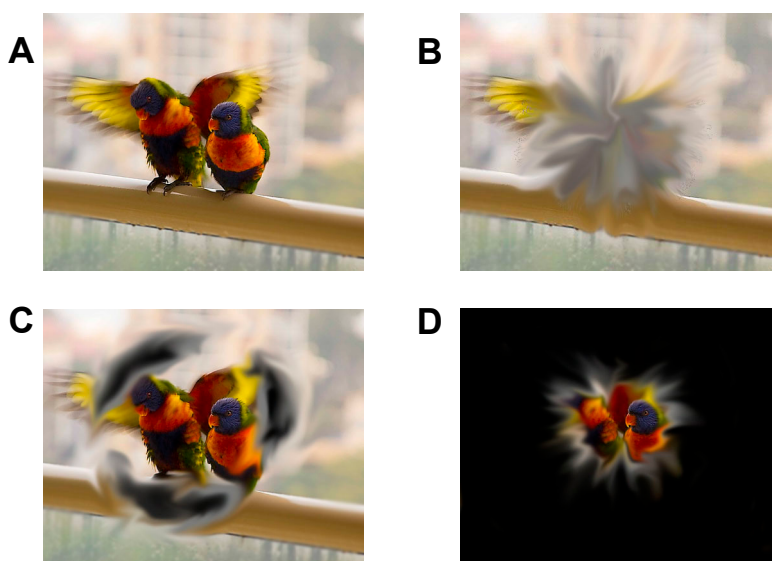


Figure 1.7

Schematic illustration of visual field losses during retinal degenerations. Original scene (A) as it might be seen during AMD (B), early stage RP (C) or late stage RP (D). Complete loss of vision can also occur.

1.3.1 Significance of Bipolar Cells for Subretinal Prostheses

During the implantation procedure, the Tübingen subretinal implant is moved to the area previously occupied by PRs, bringing the microphotodiodes and electrodes into the subretinal space just under BC and HC dendrites (Figure 1.8). The implant assumes the previous role of PRs by converting light into a retinotopically ordered electrical stimulation pattern for the remaining retinal neurons. Electric impulses sent out by electrodes from this location stimulate the same set of cells that was previously stimulated by the lost PRs in that location. This stimulation then progresses by neuronal communication through the retinal interneurons and is conducted to the brain through GC axons.

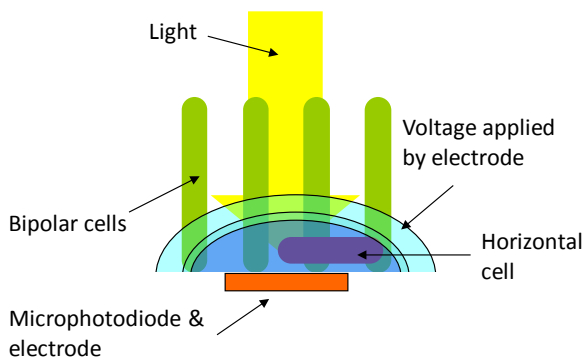


Figure 1.8

Schematic diagram of the MPDA position relative to bipolar cells and horizontal cells. Incoming light initiates retinotopic activation of the electrodes ($50 \times 50 \mu\text{m}$) which generate an extracellular voltage. Bipolar cells are located perpendicularly to the electrode while horizontal cells are in a parallel orientation.

As shown in Figure 1.8, the position of BCs is perpendicular to the stimulating electrodes which are $50 \mu\text{m} \times 50 \mu\text{m}$ in size. Therefore, the electric potential applied by the electrodes gradually decreases along the longitudinal axis of BCs. HCs are also located proximal to the electrodes, however, their longitudinal axis is parallel to that of the electrodes, leading to smaller external voltage gradient along the HC. Since it is the gradient of externally applied voltage that leads to electrical stimulation of the cell (McNeal 1976), BPs are the main target of direct stimulation with the Tübingen subretinal implant. Therefore, retinal BCs are the central focus of this thesis and the computational model developed here.

Some studies on the degenerated retina in model animals have shown that potentially extensive retinal remodeling is possible in the non-functioning retina (Marc et al. 2003). Groups of extending neuronal processes called microneuroma were observed, possibly “seeking” sources of stimulation. Furthermore, after the complete degeneration of rods and cones a glial seal may position itself in the subretinal space and increase the distance between the INL and a subretinal implant. However, not enough data is present in the human in order to be able to conclude general rules. This is especially true in the case of RP which is a strongly polygenetic disease and has many different forms and stages. Furthermore, electrical stimulation of retinal neurons itself can potentially have regenerative effects on the degenerated retina (Ciavatta et al. 2009, Naycheva et al. 2010).

1.4 Modeling Approach

Physiological experiments are indispensable for the development of a neuroprosthetic device like the Tübingen subretinal implant. However, even an experimental neuroscientist must use models. The design of an experiment and the proposal of a hypothesis are based on an informal model of the experimental subject. With growing knowledge and increasing complexity of the modeled system, the need for formalization of this model emerges. When the amount of considered dynamic processes exceeds a certain number and hundreds or even thousands of parameters have to be estimated and/or evaluated, formalization of the model becomes necessary. For example, in order to find all genes in the human genome consisting of more than 3×10^9 base pairs, the creation of gene-identification and gene-detection models using methods from bioinformatics was the only way to identify and locate all 23.000 protein coding genes (Venter et al. 2001).

A large set of tools for modeling has been developed and is available to researchers in neuroscience, such as integrate-and-fire models (Izhikevich 2001), Markov-Chains (Clay and DeFelice 1983), Monte-Carlo models (Stiles and Bartol 2001), Hodgkin-Huxley (HH) based models (Hodgkin and Huxley 1952), thermodynamic models (Keizer 1987), Bayesian models (West and Harrison 1997), multi-compartment-models, artificial neural networks (ANN), combinations of these, and many other mathematical and physical models. Together in combination with the increasing computational power which is at the disposal of researchers, this has led to raising popularity and practical fields for mathematical and biophysical modeling in neuroscience.

A computational model allows the formalized fusion of theoretical, experimental and also clinical knowledge in an objective way. In order to formulate a model the parameters usually have to be estimated from generalization and/or fitting of experimental results. The interplay of biophysical rules, parameters deducted from experiments and quickly reproducible calculations can help in understanding the system of interest. In turn, a model can influence experimental procedures. Running a model with a set of parameters that had not been previously investigated, this specific combination can lead to results that point out a certain novel correlation. Such an insight can give rise to new experimental paradigms.

1.4.1 Resources

The revolution in availability of data promoted by the internet has added to the speed at which theoretical models can be used and further developed. Numerous databases in the internet collect and maintain not only information from many experiments (such as gene sequences), but some of them are large collections of computational models that have been developed in the course of

scientific studies. The developers of Neuron (Hines and Carnevale 1997), a tool for conductance based simulation of neuronal responses, have also created ModelDB (<http://senselab.med.yale.edu/ModelDB>) (Hines et al. 2004), a website collecting various models of neuronal stimulation and information on ion channels. The Neuromorpho website (<http://neuromorpho.org/neuroMorpho>) (Ascoli et al. 2007) is an online database of morphological 3D models of various neurons, submitted by researchers who have identified and traced those cells. Simulation Platform (<http://sim.neuroinf.jp>), a cloud-based simulation environment (Yamazaki et al. 2011) with an associated database for models has been published by members of the RIKEN institute in Japan. The Blue brain project of EPFL Lausanne (Markram 2006) is a combined effort to model whole parts of the brain, which also has accumulated information on neuronal ion channels on their website (Channelpedia, <http://channelpedia.epfl.ch>). Information from all of these projects and websites was used during the creation of the model in this thesis.

1.4.2 Limitations

During the development of a model, it is crucial that all parameters included in the model have a plausible basis. Usually, simplifying assumptions have to be made in order to reduce the often enormous amount of complexity. These simplifications need to be made with the appropriate caution, and the awareness that omission of significant facts or parameters would bias or falsify the outcome substantially. In some cases, an explorative model can be used to compare more complex assumptions with more simplified ones. If tests yields that the consequences of simplification are reasonable, such simplifications should be employed in the final model.

1.4.3 Simulation Environments

The model developed in the course of this thesis consists of two parts. In order to calculate the membrane potential V_m of bipolar cells during electrical stimulation, the extracellular voltage V_e which is generated by the electrodes on the subretinal implant has to be known.

The first step of the simulation therefore is carried out using a Finite Element Method (FEM) simulation. If the appropriate parameters for the volume of interest and the electrodes are fed into this model, it delivers a quantitative approximation for the amplitude of V_e across the volume. Further details are elaborated in section 2.2.1. The numerical solution of FEM problems can be done in an efficient way using dedicated software such as Comsol Multiphysics. After all necessary model specifications have been made the software outputs the amplitude of V_e for the coordinates of interest.

These V_e values are the input to the multi-compartment model of a retinal bipolar cell. Naturally, the neuronal model requires a number of other parameters; however, V_e determines the intensity of extracellular electrical stimulation. The procedures of this model are described in detail in chapter 2 and chapter 3. Initially, this model had been implemented in NEURON (Hines and Carnevale 1997). While it is a powerful tool for neuroscientists, NEURON has the disadvantage that all neuronal compartments must be cylinders. While this simplification may be applicable for processes of neurons such as dendrites and the axon, the author intended to simulate the soma of a neuron as a sphere. The geometrical shape of a sphere is significantly closer to the actual shape of a neuronal soma than that of a cylinder, even if the cylinder can have different radii at either end. Therefore, the multi-compartment neuron model was then implemented in Matlab by Mathworks. Matlab is a matrix based development environment and allows the formulation of arbitrary geometrical shapes. Any discrete equation, such as an ordinary differential equation (ODE), can be applied to the shapes. Matlab also has an interface to Comsol Multiphysics and models can be imported from or exported to the FEM environment.

1.4.4 Model Animal

The Tübingen subretinal implant is used in a clinical study with human subjects. Therefore, optimally all physiological data used for the parameters of a computational model should have been based on human data, as well. However, the availability of physiological and electrophysiological parameters for retinal bipolar cells of the human is greatly limited due to the rare opportunity for researchers to make *in-vitro* experiments with human retinal tissue. The retina of primates in general has many similarities, therefore the next best choice should be data from primates. Such data is, unfortunately, still too limited for the purpose of creating a rather complete model. For these reasons, all physiological data used here were based on rats. Retinal functions and morphologies have numerous similarities across all mammals (Wässle and Boycott 1991, Schiller 1995, Wässle 2004). The amount of electrophysiological data from rats was sufficient to create an at least partly complete model. Furthermore, verification of hypotheses based on simulations is also more feasible, due to the good availability of rats for experimental purposes.

1.5 Aim of this Study

The overall subject of this study was to deepen our understanding of the processes occurring during extracellular electrical stimulation of retinal bipolar cells with the Tübingen subretinal microphotodiodes array using computational modeling methods. In particular, dynamics of the transmembrane potential V_m were simulated. In order to achieve this goal, the present electrode

configuration, passive electrotonic properties of bipolar cells and the morphologies of bipolar cells were included into the model. Having developed such a model, an additional goal of this thesis was to determine, whether it is possible to find electrical stimulation paradigms that would allow differential stimulation of ON and OFF bipolar cells using extracellular electrodes. For the pursuit of this goal, all differences known to be present between ON and OFF bipolar cells were included in the model. Additional to their morphologies, their main difference lies in their complement of ion channels.

The motivation for this objective arises from the clinical results seen in the Tübingen subretinal implant project (Zrenner et al. 2010) . The implant provides approximately 1500 electrodes for subretinal stimulation. However, perceptions with this resolution could not be elicited yet, and the borders of perceived objects can appear blurred to the patients. Several reasons may lead to this loss of resolution and contrast in perception. One factor may be crosstalk between electric fields generated by the electrodes. A series of experiments preceding the clinical study (Stett et al. 2000) and computational models (Benav et al. 2008) have shown that such crosstalk should not impair the visual perceptions of patients to the extent which has been observed. Another working point is the probable simultaneous stimulation of ON and OFF BCs during homogeneous extracellular stimulation from the subretinal space. Activation of both ON and OFF pathways of the retina is a likely candidate for impairment of the achievable resolution that could be conveyed by the implant. If a certain stimulation pattern can be found which does not lead to simultaneous activation of both ON and OFF pathways but instead allows the selective stimulation of either pathway. Such a stimulation paradigm could cause lowered perceptual threshold and increased perceived contrast leading to enhanced properties of the images seen by patients carrying the Tübingen subretinal implant.

2 The Passive Model

2.1 Introduction / Motivation

The ability to predict efficacy of different electrode configurations, electrode materials as well as electrical stimulation paradigms and strategies can be an important and very advantageous tool for the engineering process of a device interfacing to neural tissue, such as the Tübingen subretinal implant. The effects of a neuroprosthetic on neural target tissue depend greatly on the morphological and biophysical properties of the respective neurons. However, knowledge on the exact morphological conditions of retinal cells in the degenerated retina is sparse, even more so in the human, since the availability of experimental tissue is greatly limited. Most of the relevant literature on morphological changes during the years of retinal degeneration processes has been published by the Marc Lab at the University of Utah (Marc et al. 2003). Large parts of the published material on mathematical modeling of electrical retinal stimulation are restricted to morphologically rather simple neuronal models (Gerhardt et al. 2010, Kameneva et al. 2010). The reasons are simplicity of computation and easier control over a smaller number of parameters. While drastic changes certainly occur in the retinal tissue of retinitis pigmentosa (RP) patients, clinical trials in Tübingen and elsewhere (see section 1.1) have shown that visual impressions can be generated in RP patients, even more than 15 years after patients are regarded legally blind, and with resolutions allowing patients to discriminate up to 0.4 cycles per degree (cpd). These encouraging results have motivated more detailed investigations on possibilities for differential excitation of ON and OFF retinal bipolar cone cells (CBC). Mammalian ON and OFF CBCs differ in their inventory of ion channels (Pan and Hu 2000, Hu and Pan 2002, Ma et al. 2003, Ma et al. 2005, Ivanova and Müller 2006, Fyk-Kolodziej and Pourcho 2007, Cui and Pan 2008, Hu et al. 2009) and in their morphology (Euler and Wässle 1995). Both these properties require close observation during the creation of a computational model. However, it is necessary to evaluate the influences of different CBC properties successively. The evaluation of differences in the ion channel inventory can only be done reliably if influences of morphological parameters are identified beforehand (Major 2001), qualitatively and quantitatively.

The following chapter describes in detail the development of a passive neuronal model, beginning with simple, schematic morphologies, and then advancing to complex realistic morphologies of traced bipolar cells from the available literature. The main difference between linear, passive neuron models and active models is the lack of voltage-dependent (active) ion channels creating nonlinear responses. Transmembrane voltage (V_m) gradients cannot be actively amplified by energy consuming

biophysical processes like gating processes and ion pumps. They therefore depend mainly on membrane resistance (R_m) and capacitance (C_m). While retinal bipolar cells have active ion channels (Ivanova and Müller 2006), the insights delivered by the passive model create an understanding of underlying morphological and passive influences on the cellular response and thus facilitate the evaluation of results delivered by a more accurate active model.

2.2 Modeling and Methods

The calculation of changes in neuronal V_m is realized in two separate and methodologically different steps. These changes of V_m are induced by changes in the current flow and resulting intracellular and transmembrane potential gradients, which in turn are influenced by the extracellular potential (V_e) (Rattay 1999, Rattay et al. 2003). In order to be able to calculate the change of V_m (ΔV_m), a quantification of V_e , the potential generated by an extracellular electrode, is a necessary first step. This chapter describes how V_e and V_m can be quantitatively calculated, and which prerequisites are required for this calculation.

2.2.1 Calculation of the Electric Field

The electric fields that stimulate the retinal cells are generated by an array of microelectrodes. In the case of the Tübingen subretinal implant, 1500 Titanium-Nitride (TiN, a ceramic alloy) electrodes ($50 \times 50 \mu\text{m}^2$), deliver the stimulating charge into the retinal tissue. In this case the retina and its surrounding tissues were the volume conductor, which amongst other compounds contained the stimulating electrodes, cell bodies, axons and dendrites. The number of inhomogeneities as well as the specific electrode configurations can vary between different volume conductor models. The presence of single cells, including the target cell or cells for which V_m was calculated was neglected in this model. The electrical characteristics of a current flowing through a homogeneous medium are linear, and unaffected by the presence of very small objects such as cells (Coburn 1989).

Exact analytical solutions are only available for point current sources or flat disc electrodes located in an infinite homogeneous medium. If the electrode is modeled as an ideal point source, the generated extracellular potential V_e at a distance r from the electrode can be calculated using

$$V_e(r) = \frac{\rho_e I_{el}}{4r\pi}, \text{ and } V_e = 0 \text{ for } r \rightarrow \infty \quad (2.1)$$

where I_{el} denotes the amplitude of the electrode current and ρ_e the resistivity of the extracellular space.

Assuming a flat disc electrode in a semi-infinite medium the extracellular potential can be calculated by

$$V_e(r, z) = \frac{2V_0}{\pi} \sin^{-1} \left(\frac{2a}{\sqrt{(r-a)^2+z^2} + \sqrt{(r+a)^2+z^2}} \right) \quad (2.2)$$

where r and z denote the radial and axial distance to the center of the disc using a cylindrical coordinate system. V_0 and r are the potential and the radius of the disc, respectively.

However, to have a more realistic approximation to actual electrode form used in the Tübingen subretinal implant and different volume layers with different electric properties, it was desirable to calculate more spatially detailed models. Therefore, an inhomogeneous and finite volume was assumed. In this study, such computations of the extracellular potential V_e were conducted using finite element simulations. The Finite Element Method (FEM) is a procedure in which discretized simulated volume is into finite elements by dividing it into a mesh of tetrahedrons (Figure 2.1) with different size to optimally sample the desired spatial locations. The differential equation in question can then be solved numerically, by providing the necessary parameters and boundary conditions.

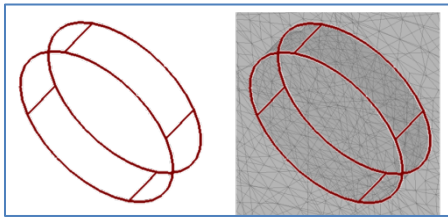


Figure 2.1

Example for discretization of the simulated volume into a mesh of tetrahedrons. Both panels show a monopolar electrode on top of a surface.

In the electrostatics of conducting materials, the relation between the scalar electrostatic potential V and the electric field density \vec{E} is given by $\vec{E} = -\nabla V$ (where ∇ is the Nabla operator, a vector containing partial differentials). Consideration of the Maxwell equation $\nabla \cdot \vec{D} = \rho$, and the relationship $\vec{D} = \epsilon_0 \epsilon_r \vec{E} + \vec{P}$, where \vec{P} is the polarization vector, leads to the partial differential equation (PDE):

$$-\nabla \cdot (\epsilon_0 \epsilon_r \vec{E} + \vec{P}) = -\nabla \cdot (\epsilon \nabla V - \vec{P}) = \rho \quad (2.3)$$

which is a derivation of Poisson's equation with permittivity ϵ and space charge density ρ . ϵ_r denotes the relative permittivity. The relative permittivity is a material property which describes the relation between the electric field \vec{E} , and the electric displacement \vec{D} , in a material. ϵ_0 is the permittivity of vacuum (8.854×10^{-12} F/m). For electromagnetic calculations, permittivity is given in units of Siemens per meter (S/m), or conductivity. The conductivity and resistivity values used for simulations in this study are given in Table 2.1. For the resistivity of the retina, $57 \Omega cm$ were chosen, similar to the resistivity of saline solution (Geddes and Baker 1967, Doslak et al. 1980). Higher values for the retinal resistivity of $110 \Omega cm$ (Coleman and Miller 1989) or more also have been measured. However, a

different value would affect the modeling results only quantitatively with limited effects, since the layers below and above the retina acted as insulators. Additionally, the retina of RP patients can have water inclusions or edema (Fetkenhour et al. 1977) moving the actual resistivity closer to that of saline solution. While the electrodes on the Tübingen implant are made from TiN, the conductivity value for copper was used here, since these values were more already available in the FEM suite and because the temporal dynamic of charge development on the surface of the electrodes were not of significant meaning to this study. For both the electrode carrier (chip) and the silicone oil tamponade which replaces the vitreous body of the implanted eye, very small values were chosen for conductivity in order to create the required barriers for current flow. The actual conductivity of silicone oil is lower (Borofsky and Partridge 1963), but the contact to human tissue may increase the conductivity of this material once it is inserted into the human eye.

Layer	Resistivity (Ωcm)	Conductivity (S/m)
Chip	10^6	$1 \cdot 10^{-5}$
Retina	57	1.7544
Silicone	10^6	$1 \cdot 10^{-5}$
Electrodes	$1.6672 \cdot 10^{-6}$	$5.998 \cdot 10^7$

Table 2.1

Resistivity and conductivity values used for the material properties in the FEM simulation.

2.2.2 The Simulated Spatial Volume

Using the FEM technique, it is possible to simulated arbitrary volumes and solve for the extracellular potential at any position. In a modeling study by S. Resatz (Resatz 2005) the simulated volume included the entire eye, considering aqueous humor, vitreous body, retina, sclera, lens and cornea, as well as some neighboring structures outside the eye. Comparison of this extensive volume and a simpler model covering only a $2 \times 2 \times 0.5$ mm patch of tissue surrounding the electrodes revealed that the difference was smaller than the error made with the assumptions of the model and the numerical evaluations. The more complex model, however, was considerably more demanding in terms of computation power and time. Generally, the medium in all following simulations of the current study consists of three layers. In an initial example these layers occupy 2×2 mm in the x and the y dimension. Figure 2.2 shows the volume and the three layers.

2.2.2.1 Chip (electrode carrier)

This layer represented the retinal implant chip, which carried the electrode array. The thickness (extent in the z dimension) in this example was $100 \mu m$. Attached to the surface of this layer were

the electrodes. In the example in Figure 2.4, one monopolar disc electrode with radius 50 μm and height 10 μm was used.

2.2.2.2 Retina

A 300 μm thick layer represented the retina, corresponding to thicknesses of 200 μm - 300 μm or more measured in patients suffering from retinal degenerations such as Retinitis Pigmentosa (Garcia-Martin et al. 2012). However, the retina in this model was treated as a homogeneous piece of tissue and did not consist of several million cells of different shape and size. Due to the small distances which the current in this model had to overcome, and the excessive complexity of a realistic retina, it appeared acceptable to neglect the presence of single cells in this medium. In contrast to the silicone layer and the chip layer, the retinal layer was conductive to current from the electrodes.

2.2.2.3 Silicone (replacement for the vitreous body in chip patients)

A 300 μm thick layer with very low conductivity in the model represented the silicone which had been injected into the eyes of the chip patients after vitrectomy (Besch et al. 2008), a surgical removal of the vitreous body. Essentially, it acted as an insulator.

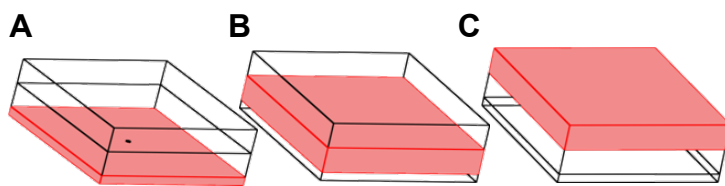


Figure 2.2

Volume covered by the FEM simulation. Chip (A), retina (B) and silicone (C). Width and height of all layers was 2x2 mm. The thicknesses were: chip: 100 μm , retina: 300 μm , silicone: 300 μm . The small structure on the chip layer is the stimulating electrode.

2.2.2.4 Boundary Conditions

The current source in all simulations was the stimulating electrode located centrally on or in the chip layer. As pointed out in Table 2.1, the chip layer and the silicone layer acted as an insulator. Therefore, the current from electrodes travelled flowed from the electrodes through the retinal layer. Consequently, boundary conditions had to be set for the outer boundaries of the retinal layer (Figure 2.3). These boundary conditions depended on the electrode configuration, see section 2.2.3, and could either be set to 0 V or to a freely floating potential.

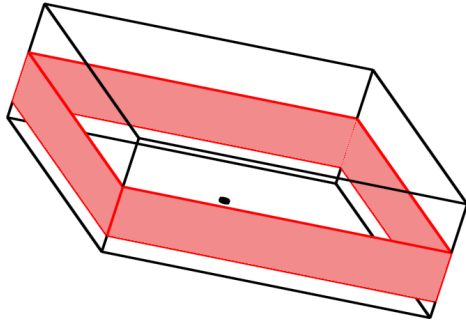


Figure 2.3

Boundaries of the retinal layer (red) were set to act as a counter electrode for current return in the monopolar configuration. In the dipolar configuration it had a free floating potential.

2.2.3 Electrode Shape and Properties

Using COMSOL Multiphysics, a simulation environment for FEM simulations, it is possible to create arbitrary electrode geometries and configurations. For testing purposes, two distinct electrode types were implemented. The first type (electrode configuration 1) was characterized by a distant current return location. One such electrode consisted of one single part, a cylinder (Figure 2.4 A, magnification), which was attached to the chip layer surface (Figure 2.4 B) or embedded into this layer. This three-dimensional structure was represented in COMSOL by six surfaces, four bended ribbons and two disks, as shown in Figure 2.4 A. In configuration 1, the extracellular potential V_e decayed between the surface of the electrode (e.g. 1 V) and the outer boundary of the retina layer, where the potential is set to 0 V. In Figure 2.4 B a cross section through the electrode and its adjacent layers is shown. Arrows represent the total current density vector field, which indicates the net flux direction of the current. All arrows are directed away from the electrode cylinder body, and towards the outer boundaries of the retinal layer in the model geometry. Electrode configuration 1 was used in the majority of simulations in this thesis, the major reason being that this configuration was close to the electrode geometries used in the Tübingen subretinal implant. In order to consolidate the similarities, the diameter used in the model was equal to the diameter of the chip-electrodes used in the clinical studies to date (50 μm). Furthermore, configuration 1 was implemented such that rectangular arrays of electrodes could be generated, in accordance with the fact that the subretinal implant is a multi-photodiode-array (MPDA). The overlay of neighboring electric fields could lead to effects such as crosstalk, which could be investigated using simulated multi-electrode-arrays. The boundary condition for the retinal layer (Figure 2.3) was 0 V for this configuration.

A second electrode configuration, configuration 2, was created in order to investigate a possible setup with a local current return in close proximity to the current source. In Figure 2.5 this configuration is depicted. Figure 2.5 A shows the outer boundaries of the applied electrode design.

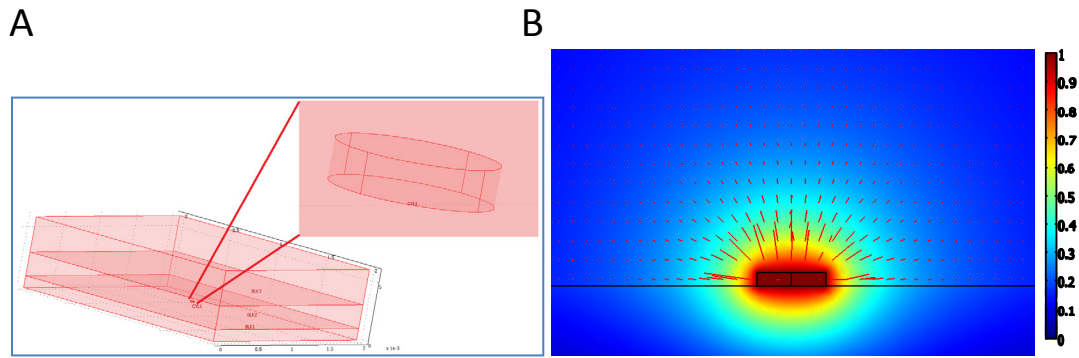


Figure 2.4 Configuration 1, monopolar

Geometrical shape of a monopolar electrode (A). Cross section through this electrode (B), the arrows represent the current density vector field. The colors represent the intensity of the extracellular potential (+1 V at the electrode surface).

Additional to the central cylinder used also in configuration 1, each electrode was surrounded by a second ring structure which had a surface equal or greater than that of the central disk. The decay of the potential occurs mainly on paths between the central cylinder, e.g. +1 V, and the outer ring structure which could be set to e.g. -1 V. The total current density vector field shown in the cross-section in Figure 2.5 B illustrates how the current mainly is directed from the central cylinder towards the outer ring structure. In this configuration, retinal boundary (Figure 2.3) was set to be a free floating potential.

The effects and differences between unipolar (configuration 1) and dipolar (configuration 2) electrode configurations in the scope of subretinal implants have been described previously (Gerhardt 2009, Gerhardt et al. 2010). One major consequence of the different current flow direction was the penetration depth (reach) of the current, and the resulting contrasts in the potential gradient of the electric field.

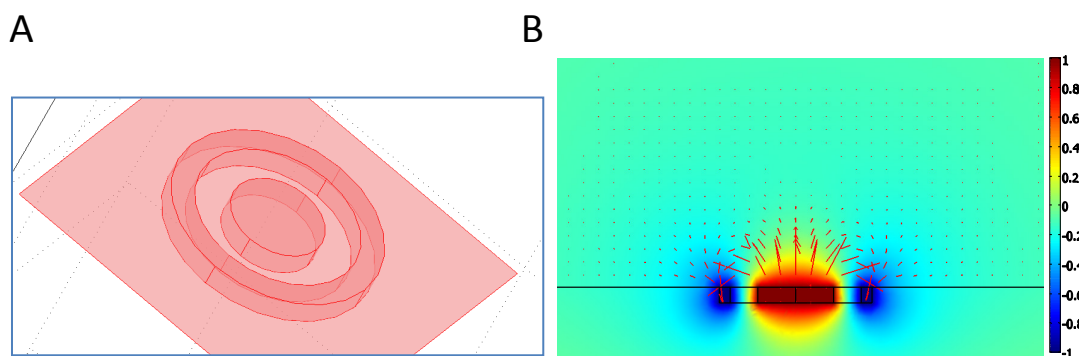


Figure 2.5 Configuration 2, dipolar

Geometrical shape of a dipolar electrode (A). Cross section through this electrode (B), the arrows represent the current density vector field. The colors represent the intensity of the extracellular potential (+1 V at the surface of the central cylinder, -1 V at outer ring surface).

Dipolar stimulation can also be achieved using electrode configuration 1, if more than one electrode is used. In a rectangular array of disk electrodes, it is possible to set the voltages applied to each electrode surface according to a checkerboard pattern (e.g. white: +1 V, black: -1 V). This creates a potential gradient of 2 V between current source and current sink, and can therefore be compared to monopolar stimulation with 2 V at the source and 0 V at the sink. Section 2.3.2.2 in this chapter addresses this setup in detail.

2.2.4 Calculation of the Neuronal Response

2.2.4.1 Electrical Network Model

A neuronal cell membrane is a lipid bilayer consisting mainly of amphipathic phospholipids. The phospholipids have no covalent lateral connections to each other, and therefore different membrane proteins mostly can float around in or on the membrane. Cell membranes are so called two-dimensional liquids. The lipid part of the membrane has a very low electric conductance per unit area and can be considered an insulator. However, the membrane itself can take up charge and therefore is a capacitor. Some membrane proteins are transmembrane proteins which can act as ion channels. Certain ion channels are constitutively open and create a constant conductance to selected ions or ionic species such as cations or anions (Hille 2001). Other ion channels have gating mechanisms and open up their gates only if they are exposed to a supra-threshold transmembrane voltage gradient (voltage-dependent) or if they have bound with Ca^{++} (calcium-dependent). These channels are capable of transient conductance changes in different time scale. Each small patch of membrane thus is electrically equivalent to a variable resistor operating in series with a battery, in parallel to a capacitor, creating an electric connection between the extracellular and intracellular space. That part of the membrane conductance and capacitance which effectively stays constant during changes in intra- and extracellular voltage can be approximated by a fixed resistor and capacitor, respectively.

Commonly, electrical network only taking into account the presence of ion channels with constant resistances are called linear or passive models. If a model also includes voltage-dependent or Ca^{++} -dependent ion channels with transient conductance properties, it is called an active model. Active models will be described in detail in Chapter 3.

2.2.4.2 Multi-Compartment-Model

The neuron model was implemented consisting of several segments with different electrical and morphological properties. These properties were characteristic for specific cellular areas, for example the dendrites of a retinal bipolar cell had other electrical attributes than the soma, or axon. For more accurate modeling, these areas were further divided into smaller segments, such that one segment

had a homogeneous radius, and ion channel equipment. Due to the large number of ion channels in the neuronal membrane, the assumed density of one type of ion channel was proportional to a homogeneous conductivity value for an entire compartment. One such segment constituted one compartment in the model and could be represented using one resistor-capacitor (RC) circuit. A multi-compartment model is a parallel series of such RC circuits (Figure 2.6). All compartments of the neuron were represented by cylinders, except for the soma, which was modeled as a sphere in the model developed for this work. One compartment was a non-branching segment of a neuron with constant radius across its length.

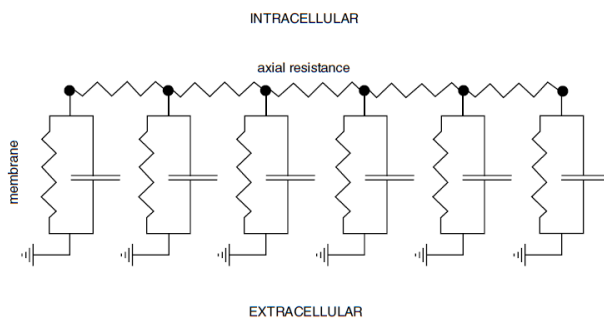


Figure 2.6
Parallel resistor capacitor electrical network represented by a multi-compartment model. Figure from (Major 2001).

A realistic multi-compartment model requires knowledge on the three-dimensional morphology of a neuron. This morphology can be identified using cellular tracing techniques. Cells can be tagged with fluorescent markers before they are imaged with a two-photon microscope. The disadvantage in this technique is the relatively low resolution of the resulting images. Additionally the cells tend to appear too large if they are not exactly in the focal layer of the imaging apparatus. Another imaging possibility is the use of an electron microscope. This technique delivers images of higher quality, however the substrate can be damaged in the course of the microscopy and thus generate erroneous images. In both cases a stack of images in different layers is obtained, which can be used to computationally reconstruct the three dimensional morphology of the neuron. This morphological data can be stored in several ways – in this study the “SWC” file format was used (See section 2.3.1.2 for an explanation of swc-files). Each compartment of a cell stored in the swc-format is assigned a “type” which determines the biophysical properties of that compartment.

2.2.4.3 Formulation of the Neuron Model

In the multi-compartment model every compartment had an individual shape as well as geometric and electric parameters. During computation a single point in the center of the cylinder or sphere electrically represented the compartment. In the previous sections, it was elaborated that all currents to and from the n -th compartment consist of these following components: capacitive

current ($I_{C,n}$), ionic currents across the membrane ($I_{ion,n}$) and ohmic currents to neighboring compartments ($I_{R,n}$).

Application of Kirchoff's law of charge conservation leads to:

$$I_{C,n} + I_{ion,n} + I_{R,n} = 0 \quad (2.4)$$

In more detail, this can also be written as (Rattay 1999):

$$\frac{d(V_{i,n}-V_{e,n})}{dt} C_n + I_{ion,n} + \frac{V_{i,n}-V_{i,n-1}}{R_n/2+R_{n-1}/2} + \frac{V_{i,n}-V_{i,n+1}}{R_n/2+R_{n+1}/2} + \dots = 0 \quad (2.5)$$

where V_i is the intracellular and V_e the extracellular potential, C denotes the capacity of the cell membrane, I_{ion} is the ionic current, which was computed from an appropriate membrane model (see equation 2.7 for the passive model and section 3.3 for the active model) and $R_n/2$ represents the internal resistance between the center and the border of the compartment. The letter n indicates the compartment number; $n-1$ and $n+1$ are arbitrarily chosen numbers of the neighbor compartments. The dots in equation 2.5 represent terms similar to the previous ones which have to be added in the case of more than two neighbor compartments, e.g., at the soma or in other branching regions. In the case of just one neighbor element equation 2.5 has only three summands.

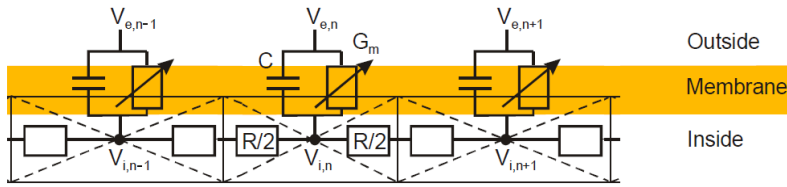


Figure 2.7

Parallel RC network diagram including the extracellular voltage V_e into the multi-compartment model. Figure modified from (Rattay 1999).

Use of the reduced membrane voltage $V_n = V_{i,n} - V_{e,n} - V_r$ with V_r being the resting potential of the membrane yields $V_n(t=0) = 0$ (Hodgkin and Huxley 1952) and the following system of differential equations (Rattay 1999):

$$\frac{dV_n}{dt} = \left[-I_{ion,n} + \frac{V_{n-1}-V_n}{R_{n-1}/2+R_n/2} + \frac{V_{n+1}-V_n}{R_{n+1}/2+R_n/2} + \dots + \frac{V_{e,n-1}-V_{e,n}}{R_{n-1}/2+R_n/2} + \frac{V_{e,n+1}-V_{e,n}}{R_{n+1}/2+R_n/2} \right] \frac{1}{C_n} \quad (2.6)$$

The system described by equation 2.6 allowed calculating the influence an extracellular potential generated by an electrode had on V_n of each neuronal compartment. The dimension of this system was determined by the number of compartments.

Division of total ionic currents I_{ion} by the membrane surface A_n of a specific compartment (given in cm^2) allowed conversion of currents to current densities i_{ion} . Analogously:

$$C_n = A_n c$$

The surface and the resistance of cylindrical compartments with Δx were calculated by (Resatz 2005):

$$A_n = d_n \Delta x_n \pi \text{ and } \frac{R_n}{2} = \frac{2\rho_i \Delta x_n}{d_n^2 \pi}$$

ρ_i is the intracellular resistivity and d is the diameter.

For the spherical soma (Resatz 2005):

$$A_{soma} = 4\pi r_{soma}^2 - \sum_j 2r_{soma} \pi h_j, \text{ with } h_j = r_{soma} - z_j \text{ and } z_j = \sqrt{r_{soma}^2 - (d_j/2)^2} \text{ and}$$

$$\frac{R_{soma,j}}{2} = \frac{\rho_i}{2\pi r} \ln \left(\frac{r_{soma} + z_j}{r_{soma} - z_j} \right)$$

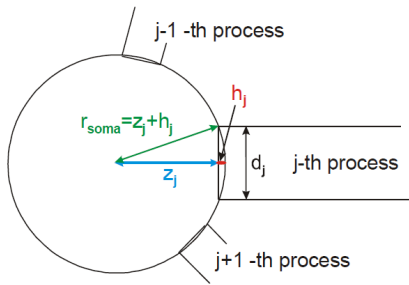


Figure 2.8

Calculation of the spherical soma membrane surface A_{soma} . For each neighboring process, the appropriate area was subtracted from the surface of the entire sphere. Figure from (Resatz and Rattay 2004)

Most of the electric parameters are based on whole-cell recording data which include the value for membrane capacitance ($1.1 \mu F/cm^2$) and intracellular resistivity of $130 \Omega cm$ (Oltedal et al. 2009). These values were assumed to be uniform throughout the entire cell and were used in all simulations for all compartments. The other parameters are specified in the context of the description of each specific simulation. The extracellular resistance could be neglected for this model (Rattay 1987), since it had been shown that only minor changes in the range of few mV occur even if an action potential passes a neighboring neuron (Plonsey 1974).

In the passive membrane model, the ionic current density i_{ion} is the product of a constant specific passive conductivity and difference of the passive (leak) equilibrium potential and transmembrane potential:

$$i_{ion} = g_L (E_L - V_m) \tag{2.7}$$

Where $g_L = 0.041668 \frac{mS}{cm^2}$ and $E_L = -41 mV$

2.2.5 Implementation

The entire model simulation program was written in the Matlab programming language (see also section 1.4.3). The formulation of the FEM problem and the appropriate geometry were generated in Matlab, however, the solution of the problem was conducted by Comsol Multiphysics through the interface from Matlab to Comsol. The flow-chart of function calls and information flow is presented in Figure 2.9. This flow-chart was used for the passive and the active model (chapter 3). The Matlab-file “runBP.m” was at the start of the simulation. It defined whether a single simulation should be performed or multiple simulations with one or more changing parameters. The file “setBP.m” set all parameters which were needed to complete the simulation, such as the size of the FEM geometry, electrode shape and configuration, the file which stored the neuronal morphology, the conductances for ion channels and leak current, the subcellular locations of those ion channels, the initial parameters for channel gating variables and Ca^{++} concentration, stimulus parameters and some plot parameters. The ON and OFF bipolar cells had two separate “setBP.m” files. Then, “simNeuron.m” was called, which constituted the central instance for the simulation. Initially, it called “comsol2matlab.m”, which through “monopolar.m” or “dipolar.m” prepared the FEM geometry based on the parameters from “setBP.m” and passed them to Comsol through the Matlab-Comsol interface. After solution of the FEM problem these data were returned to “simNeuron.m”, which then prepared all variables for the solution of the ordinary differential equations (ODE) formulated in “activeODE.m”. The file “activeODE.m” contained all differential equation systems of the entire model, including the solution of membrane voltage, ion channel gating parameters and Ca^{++} concentration. The ODE was solved by the Matlab ODE-solver ode15s, an implementation of numerical differentiation formulas (NDF) also using backward differentiation formulas (BDF) (Shampine and Reichelt 1997, Shampine et al. 1999). While a separation of each ODE system into one single file would be easier to read for the programmer, the combination of all systems into one file greatly enhanced the temporal requirements for the simulation. The file “activeODE.m” returned only those parameters to “simNeuron.m” which were a direct result of an differential equation, such as the membrane voltage. The currents passing through each of the ion channels were indirect results and calculated based on the direct results. Therefore, the current time-courses were not returned to “simNeuron.m” as this would have increased the complexity of the ODE-variables and the temporal demands of the computation. All information was therefore returned by “simNeuron.m” to “setBP.m” which then called “calcCurrent.m”. This file parsed the contents of “activeODE.m” and calculated all currents that had been used during the calculation. This did not require an ODE, since the membrane voltage was known as this step. Based on these results, all plots were then created. The source-code of the model is available from the author upon request.

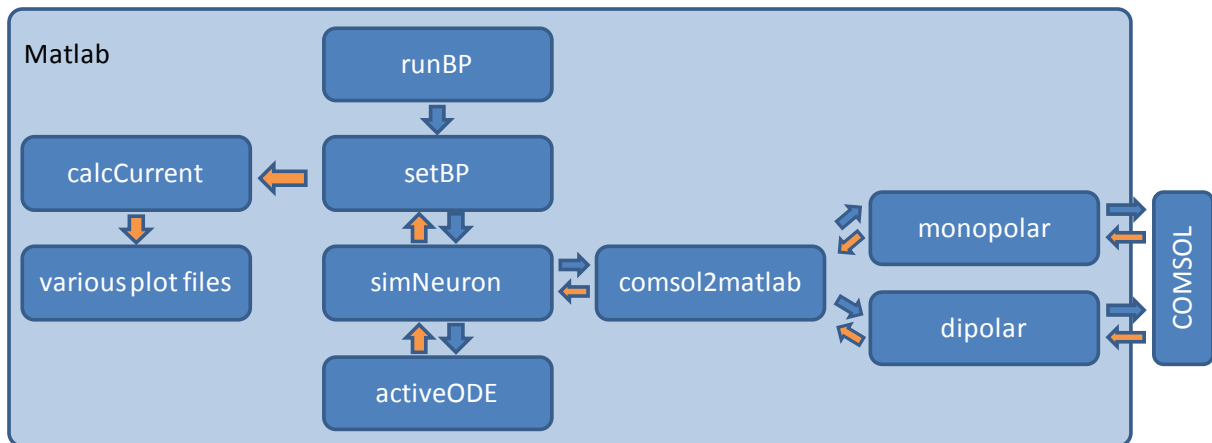


Figure 2.9

Flow-chart diagram of the implemented model. Each box in the bright blue frame represents a Matlab m-file. Comsol conducted the solution of the FEM problem. Blue arrows represent normal function calls. Orange arrows show the flow of information after a calculation has been completed.

2.3 Simulations and Results

2.3.1 Single Electrode Simulations

2.3.1.1 Simple Stick Model

For evaluation purposes, the neuronal model developed here was first computed without a morphology resembling actual retinal neurons. A stick model was chosen due to the basic, non-branching form which is easily expandable from only few compartments to several hundred compartments. The stick model shown in Figure 2.10 has 10 compartments, discernible by the different colors representing the externally applied Voltage V_e which has been calculated in the FEM procedure with COMSOL for each compartment, on the basis of a pulse with amplitude 1 V (see Figure 2.11 bottom). The total length of this stick-model cell was kept constant at 100 μm , while the length of each compartment was adapted if the number of compartments was increased. The 10 compartment stick-model thus had compartments with 10 μm length. The radius of the compartments was 3 μm . Figure 2.10 does not display the entire volume which had been used for the FEM simulation, only the vicinity of the cell is shown. The stick model was positioned centrally in the 2mm x 2 mm x 0.6 mm volume, perpendicular to the surface of the disk electrode. The center of the compartment closest to the electrode had a distance of 40 μm to the surface of this electrode (see also Figure 2.18).

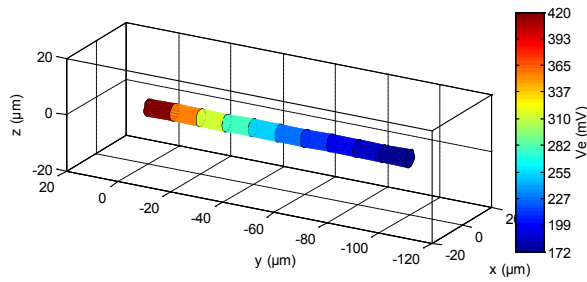


Figure 2.10

Simple stick model used for evaluation of the multi-compartment model. The colors represent V_e at each compartment.

Transmembrane Potential V_m

The main computational result of the passive neuronal model was the transmembrane voltage V_m . Figure 2.11 shows the time courses of V_m for the 10-compartment stick model shown in Figure 2.10. The entire simulation covered a duration of 1 ms. After a 0.1 ms delay the rectangular anodic stimulus was activated for a duration of 0.5 ms, then a 0.4 ms period allowed V_m to return to its resting state. The amplitude applied in this simulation was 1 V. The entire Matlab model was implemented in a way such that a cell must have a soma; therefore, in this case the compartment closest to the electrode was called the somatic compartment. All other compartments were called axonal compartment. Nonetheless, in this initial simulation, somatic and axonal compartment had identical membrane properties. For all compartments the specific transmembrane resistance was set to $24 \text{ k}\Omega\text{cm}^2$, the intracellular axial resistivity had a value of $130 \text{ }\Omega\text{cm}$. The resting potential V_r was set to -60 mV , and the membrane capacitance C_m to $1.1 \text{ }\mu\text{F}/\text{cm}^2$. These values were taken from (Oltedal et al. 2009) who conducted electrophysiological measurements on rat rod bipolar cells and fitted the corresponding parameters to obtain these values.

For each of the 10 compartments, the model returned a time course of V_m along the 1 ms simulation time. After onset of the stimulus all time courses show changes in V_m . A general ramification of anodic stimulation in this setup was that compartments close to the stimulating electrode experienced a negative change in V_m (hyperpolarization), while those compartments further away from the electrode underwent a change towards a more positive potential (depolarization). However, the traces of some compartments that ultimately were depolarized could initially be hyperpolarized, before the overall effect of the stimulation and the influence of neighboring compartments drove them to the positive level. For example, this was the case in Figure 2.11 in the V_m trace which is closest to the resting potential -60 mV .

The V_m traces shown in Figure 2.11 did not assume their maximal displacement instantaneously. Instead the initial rise or decay had a certain slope, which mainly depended on the membrane capacitance as well as the target potential. Similarly, the slope with which the potential returned back to the resting value also depends on C_m .

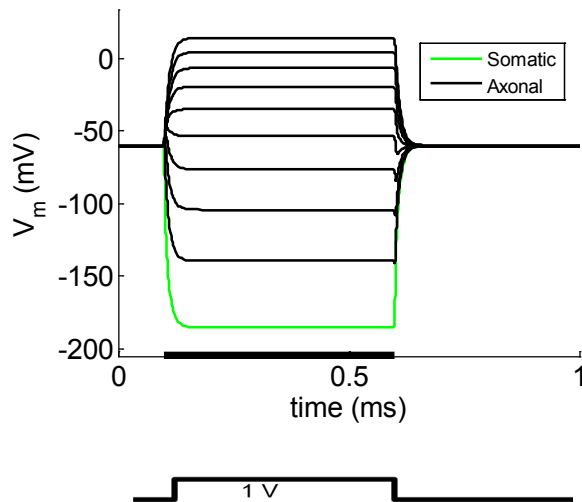


Figure 2.11

Time courses for the transmembrane potential V_m returned by the passive model for a stick-like morphology with 10 compartments. The 1 V stimulus is presented below. Each line represents one compartment. The first compartment which was closest to the extracellular electrode was generally considered to be somatic. However, all compartments had identical properties.

Convergence Analysis

The calculation of the transmembrane potential V_m was based on a discretization of the cable equation. Mathematically, discretization is a procedure in which a continuous model or function that is defined for a real, continuous function domain, is transferred into discrete, separate steps. Therefore, a discretization behaves similarly to an approximation, and the accuracy of the continuous function is the upper limit for its correctness, where the error resulting from the approximation is the smallest. The magnitude of the error depends on the number of discrete steps which are calculated for the model. The computational error decreases with an increasing number of discretization steps, due to a denser “sampling” of the underlying function.

In this simulation, the stick-model initially had five compartments with 20 μm length each. The number of compartments was gradually increased (from 5 compartments to 100 compartments in steps of 5 and from 100 to 600 in steps of 10 compartments). V_m of the stick-model model with 600 compartments was used as a basis to calculate the error. It was assumed that the 600 compartment model delivered the most accurate results, since an asymptotic behavior could be observed with increasing compartment numbers (Figure 2.12). Any discrepancy to the result with 600 compartments was assumed to be an error made resulting from discretization. This simulation yielded to the insight, that a stick-model with 70 or more compartments with a length of 1.42 μm or less) delivered results that differed only 1% or less from the 600 compartment stick-model, see Figure 2.12.

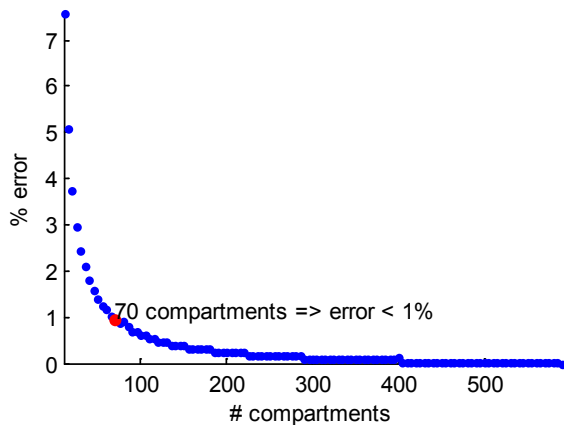


Figure 2.12

Result of the convergence analysis. The number of compartments in a 100 μm stick model was increased from 5 to 600. Error was calculated as discrepancy from the 600 compartment model.

Computation Time Analysis

An analysis of the computation time for the passive stick-model showed that this computation time increased approximately linearly as a function of the number of compartments, Figure 2.13. The measurement of computation time had certain random influences, as it depended on the current state of the processor which might have been influenced by possible simultaneous background computations of the Windows operating system. Across all simulations from 5 to 200 compartments, an average computation time per compartment of 5.7 ms was achieved (Intel Core 2 Duo CPU, operating at 2.53 GHz).

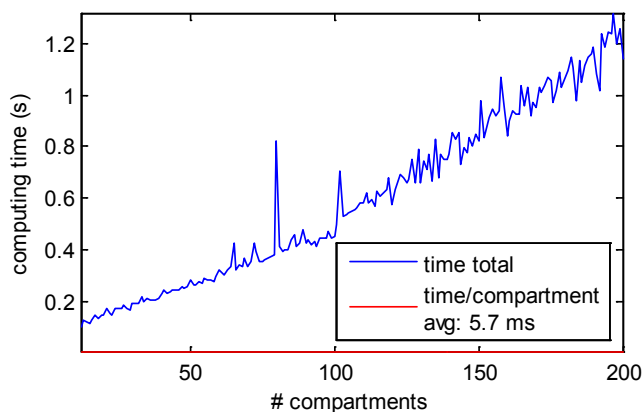


Figure 2.13

Analysis of computational time requirements of the multi-compartment stick-model. The randomness bias on the results was probably caused by additional background processes of the operating system.

2.3.1.2 Simplified Bipolar Cell Morphology

Subsequently, a morphological model was created with the intent to achieve a closer resemblance to retinal bipolar cells (BC). Using the cell-builder tool included in the NEURON software (Hines and Carnevale 1997), a simple cell with certain key morphological features of BCs was created, BP1, see Figure 2.14.

A

```
# SWC FILE BP1
# ID TYPE X Y Z R Par
# t x y z r p
1 1 0 0 0 4 -1 # SOMA
2 1 0 -8 0 4 1 # SOMA
3 2 0 -28 3 0.5 2 # AXON FIRST
4 2 -1 -40 -1 0.5 3 # AXON
5 2 0 -48 2 0.5 4 # AXON
6 2 -3 -64 0 0.5 5 # AXON
7 2 -3 -78 -2 0.5 6 # AXON LAST
8 3 -1 8 -2 1 1 # DEND SOMATIC
9 3 0 16 1 1 8 # DEND LAST
10 3 -4 18 0 1 9 # DEND POSTSYN LEFT
11 3 4 18 2 1 9 # DEND POSTSYN RIGHT
12 3 0 22 -1 1 9 # DEND POSTSYN MID
13 2 -7 -85 -4 0.5 7 # AXON SYN LEFT
14 4 -10 -88 -5 2 13 # SYN LEFT
15 2 -3 -86 0 0.5 7 # AXON SYN MID
16 4 -3 -91 0 2 15 # SYN MID
17 2 -20 -80 -3 0.5 7 # AXON SYN RIGHT
18 4 -25 -80 -4 2 17 # SYN RIGHT
```

B

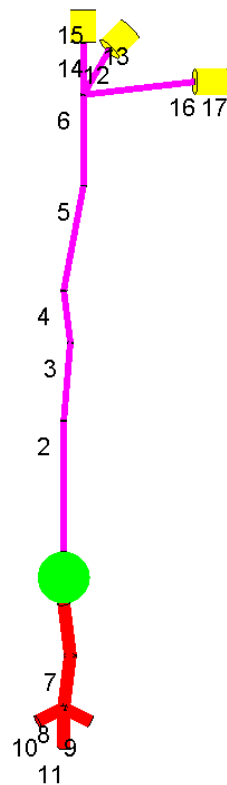


Figure 2.14

A: SWC file structure in which morphological data required to construct the morphology of the cell BP1 was stored.

Each line defines one compartment by specification of its ID (first column), type (second column), its end-point in a three-dimensional coordinate system (third to fifth column, in μm), radius (sixth column, in μm) and the ID of its parent compartment (last column). The hash symbol marks comments. The spherical soma is the only compartments defined in two lines (1 and 2).

B: Two-dimensional projection of BP1. The morphology contains key features of the morphology of retinal bipolar cells. Color coding refers to compartment types as defined in the second column of the SWC-File (green: somatic (1), purple: axonal (2), red: dendritic (3), yellow: synaptic (4)). The numbers identify the compartments.

The total length of BP1 in the y dimension (perpendicular to the surface of the electrode) is 113 μm . This is slightly above lengths measured for ON-Bipolar Cell in rodents (Ghosh et al. 2004). It has the general morphology of a bipolar cell, which by definition requires two principal processes from the soma. In this specific model, four biophysical types of compartments were assigned a different radius: soma (4 μm), axon (0.5 μm), dendrite (1 μm) and synapse (at the axon terminal, 2 μm). The cell was placed centrally above the center of the stimulating electrode. The somatic compartment of the BP1 had a distance of 45 μm to the surface of the electrode (Figure 2.18). The biophysical properties of this passive neuron were set according to parameters published by (Olstedal et al. 2009). All regions (soma, axon, dendrite and synapse) in the passive model were assigned identical biophysical parameters, as shown in Table 2.2.

Specific membrane resistance (R_m)	24 $k\Omega\text{cm}^2$
Axial, cytoplasmatic resistivity (ρ_a)	130 Ωcm
Equilibrium potential (V_{rest})	-41 mV
Membrane capacitance (C_m)	1.1 $\mu\text{F}/\text{cm}^2$

Table 2.2

Biophysical parameters for the passive, linear model.

In the first simulation run with morphology of BP1, the dependence of V_m on the timing of the stimulus was investigated. The rectangular cathodic pulse was applied for a duration of 0.5 ms or 2 ms after an initial delay of 0.1 ms allowing the system to be in a steady state (this is more important in the active model). The entire duration of the simulation was 2 ms (for 0.5 ms stimulation) or 4 ms (for 1.5 ms stimulation), allowing V_m to return to its initial value V_r . Using a delay of 0.1 ms, stimulus duration of 2 ms simulation time of 4 ms, the voltage time courses displayed in Figure 2.16 A were obtained with an electrode Voltage of $V_e = 1$ V. The stimulus duration was chosen such that the time allowed V_m to saturate, as it can be seen by the asymptotic behavior of the time-courses. Figure 2.16 B shows results from a stimulus of 0.5 ms, which is the time typically used for monophasic pulses in the Tübingen subretinal implant. The maximal positive deflection of V_m from resting state potential $V_r = -41$ mV is achieved in the synaptic compartment 15, which was the compartment with the largest distance to the stimulating electrode. The compartment closest to the electrode experienced the maximal negative displacement of V_m , see also Figure 2.15. This was the case for all anodic stimulations and the opposite was true for cathodic stimuli.

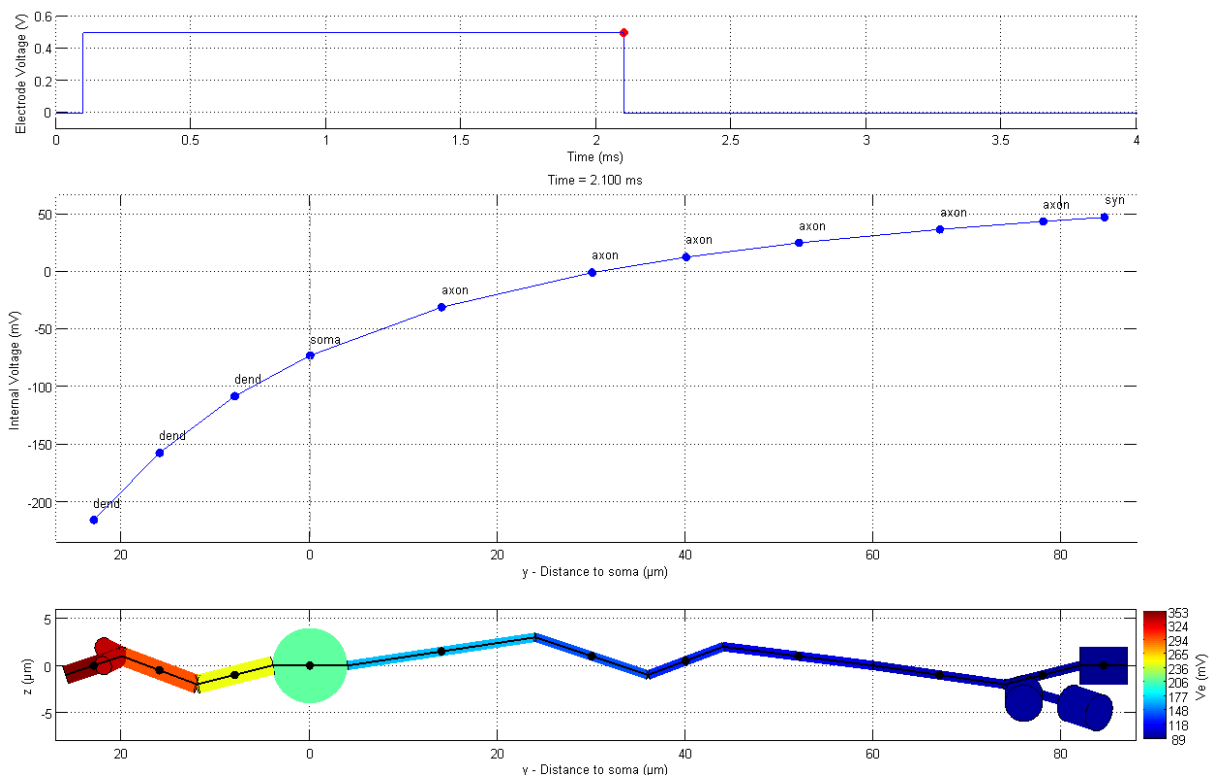


Figure 2.15

Transmembrane voltage of all compartments at the time of maximal displacement, before deactivation of the stimulus (red dot in the top graph). Figure in the middle graph shows the V_m values at a given time following the longest path through the neuron (bottom graph, colors code extracellular potential V_e , stimulus amplitude was 0.5 V).

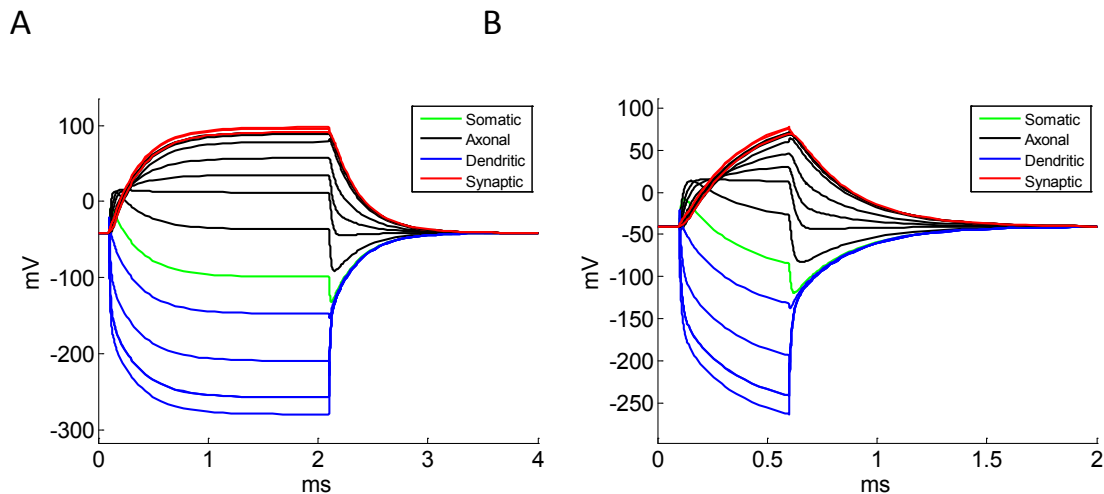


Figure 2.16

Simulated time courses V_m in the BP1 model cell during a 1 V extracellular stimulation. A: delay = 0.1 ms, stimulus duration = 2 ms; B: delay = 0.1 ms, duration = 0.5 ms. Each curve represents V_m of one compartment in BP1. The compartments are grouped into four regions (soma, axon, dendrite and synapse)

Both simulations (with durations of 0.5 ms and 2 ms) show that initially axonal V_m is subject to a faster change, after about 0.2 ms however, synaptic V_m surpasses axonal V_m and continues to rise towards a saturation value, which in for the first set of temporal parameters is around is 97.59 mV. In the second simulation, 77.4 mV was the maximum.

The amount of time required for V_m to rise to its maximal value depended on the membrane capacitance C_m , since the capacitive properties of the lipid bilayer in the neuronal membrane prevent a sudden, step-like surge to the saturation value. The membrane depolarization achieved in the synaptic compartments were of special importance, because these are the compartments which contact the next layer in retinal signal processing, retinal ganglion cells (RGC).

The morphology used in BP1 was schematic and simplified in several assumptions. Figure 2.17 demonstrates the model predictions during a 2 V anodic pulse based on BP1 (A) and a similar cellular morphology (B), where the radius of synaptic compartments was reduced from 2 μm to a smaller value of 0.6 μm . An increased maximal membrane depolarization resulted from this alteration. This increase affected all synaptic compartments, as well as the axonal compartments located close to the synaptic compartments. Based on the resting potential of -41 mV, synaptic depolarization was 23% stronger in the cell with thinner synaptic compartments (+272 mV vs. +220 mV).

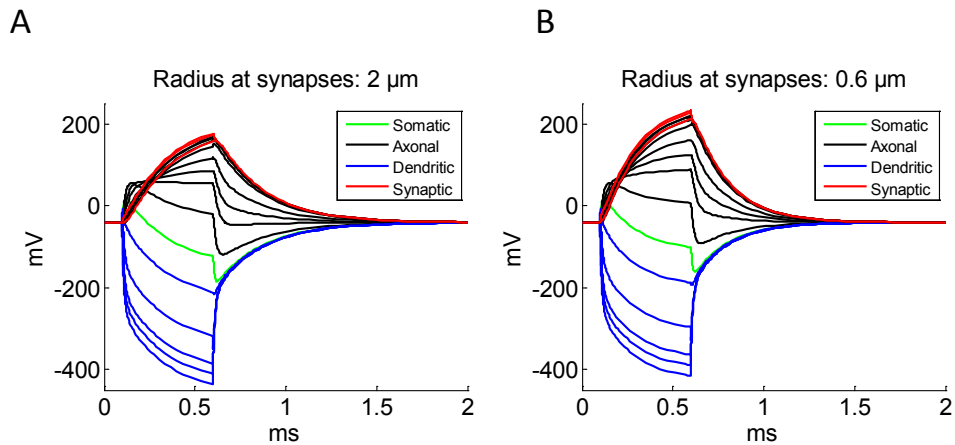


Figure 2.17

Simulated time courses V_m in the BP1 model (A) cell during 0.5 ms 2 V extracellular stimulation. Identical stimulation parameters with the same cell (B), but the radius of synaptic compartments was reduced from 2 μm to 0.6 μm . An increase of synaptic and some axonal V_m time-courses was calculated.

2.3.1.3 Cellular Position

The electrodes on the Tübingen subretinal implant are located on the array with an inter-electrode spacing of 70 μm (Zrenner et al. 2009). Multi-electrode array (MEA) – experiments with explanted chicken retina showed that at this spacing the electrodes would be able to convey the contrast profile of an image from the chip to the retinal neurons with acceptable accuracy (Stett et al. 2007). Considering that bipolar cell density is higher than one per 70 μm (Wässle et al. 2009), the question arises, how the electrical stimulation of cells not located centrally above the electrode differs in latency when compared to the activation profile of cells located optimally above the electrode.

Three simulations were conducted with one monopolar disc electrode as presented in configuration 1. While the distance of the soma to the plane of the electrode surface was kept at 45 μm across these three simulations (z-Dimension), the cell was shifted laterally using a shift of 0 μm , 20 μm and 35 μm . With an inter-electrode distance of 70 μm a 35 μm step corresponds to the area in the center of two neighboring electrodes, and is the largest step required for this observation, Figure 2.18.

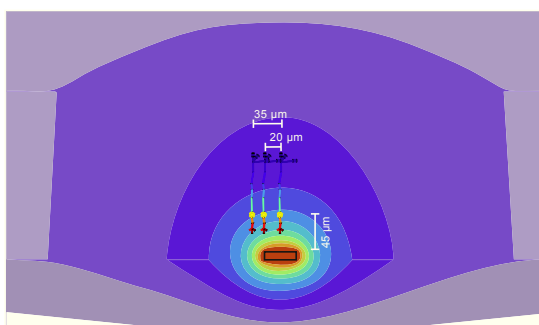


Figure 2.18

Position of the BP1 model cell above the center of the stimulating electrode (radius 50 μm) and with two vertical shifts of 20 μm and 35 μm . Colors represent the extracellular Voltage V_e . Colors of cell compartments are normalized to the maximal V_e .

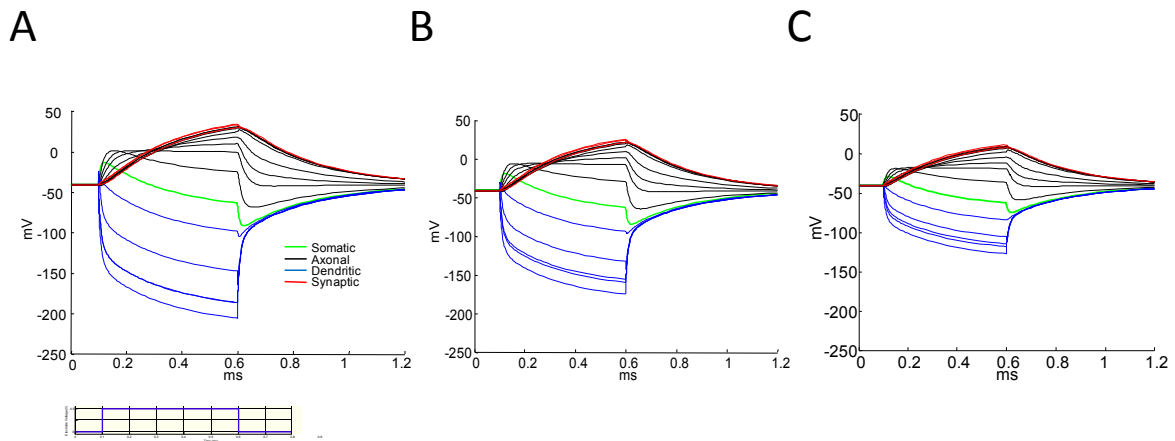


Figure 2.19

Traces of V_m at 3 different, laterally shifted positions. Cells are shifted from a position centrally above the electrode for A: $0 \mu\text{m}$, B: $20 \mu\text{m}$, C: $35 \mu\text{m}$. Cells were stimulated with a 0.5 V , 0.5 ms rectangular pulse. The lower panel of A depicts the stimulus timing.

At a stimulation amplitude of 0.5 V , the cell located above the center of the electrode (Figure 2.19 A) reached a maximal synaptic $V_m = 34.2 \text{ mV}$. The values were decreased in the synaptic compartments #13, #15 and #17 by 27%, 25% and 29%, respectively, in the run with a shift of $20 \mu\text{m}$, any by 70%, 67% and 75% with a $35 \mu\text{m}$ shift.

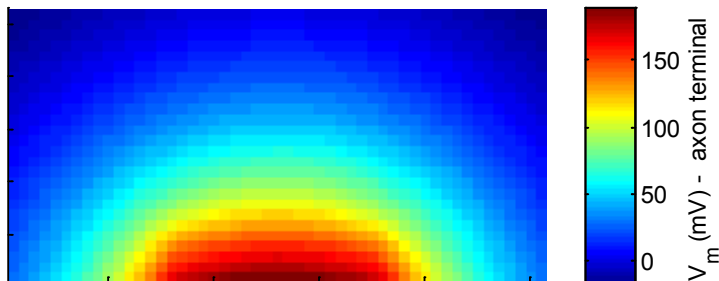


Figure 2.20

Result of 1356 simulations at different cellular positions. Starting from the first bottom row in the center, each pixel represents the maximal synaptic V_m value, at a cellular location shifted by $2 \mu\text{m}$ from its neighboring pixel.

Figure 2.20 shows the result of 1356 simulations with different shifts for the cellular position. The central pixel in the bottom row is the maximal synaptic V_m at a position $45 \mu\text{m}$ centrally above the electrode. One pixel to the left represents a shift of the cell to the left by $2 \mu\text{m}$, the pixel in the row above represents a shift $2 \mu\text{m}$ further up from the electrode.

2.3.1.4 Realistic Bipolar Cell Morphology

Several databases in the internet provide sources for morphological models of neurons, such as neuromorpho.org and others. Several thousand morphologies are submitted by different labs and made available for research. A large number of RGC morphologies are available for download. However, no data has been submitted for BP cells until today.

A Matlab program has been written, in which a semi-automated procedure allows to create a 3D morphological model of neuron on the basis of a 2D image of the neuron. The user clicks on the intended starting and end points of all compartments. The program then creates a preliminary swc file on the basis of the selected points. Information on depth of the cell (z-dimension) is not available in the image, and therefore is generated using a confined, normally distributed random variable. In the case of a bifurcation, the user has to define the parent compartment. Finally, a compartment type is assigned to each of the compartments, as well as a radius which is mostly uniform within one compartment type. All radii used in this thesis were uniform along one compartment. Possible irregularities in compartment thickness can be adjusted by the user, as well. For the creation of one morphological model with 90 compartments the time requirement for the user is about 30 minutes.

Figure 2.21 shows the resulting morphological model created by this Matlab program. Panel A is the Type 9 ON cone bipolar cell from Figure 2 in (Euler and Wässle 1995). In B the calculated morphological model of this cell is shown from the same perspective. Panels C and D show a view from below and a lateral view, respectively. The morphological model consists of 91 compartments. Radius of the soma is $5.4\ \mu\text{m}$, axonal $0.76\ \mu\text{m}$, dendritic in average $0.72\ \mu\text{m}$, and synaptic in average $0.61\ \mu\text{m}$. The total length of the cell (y-dimension) is $85.6\ \mu\text{m}$. According to (Euler and Wässle 1995) the axon of cell stratifies in stratum 5 of the IPL.

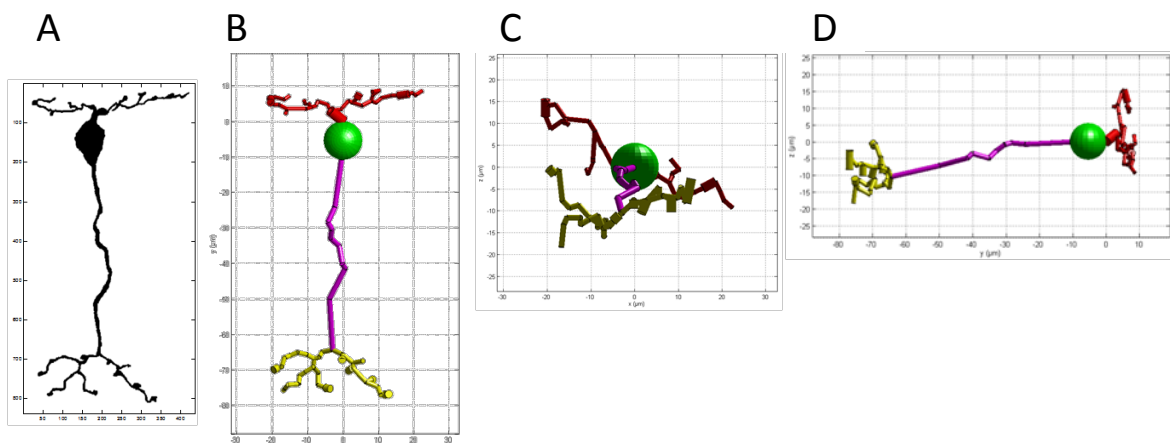


Figure 2.21 Morphological 3D model of a type 9 on cone bipolar cell

from (Euler and Wässle 1995)(A). The model was created using a custom made Matlab program. View from below (C) and side (D). The extent into the z-dimension (depth) is randomly generated.

The use of this more realistic morphological model has several advantages. Apart from the evident higher level of detail at which influence of cellular morphology can be investigated, the fact that this model has a rather high number of compartments reduces the potential computational numeric errors made during the simulation (see Figure 2.13). Furthermore, for addressing questions on preferential stimulation of ON or OFF cone bipolar cells, realistic morphological models are required

since ON and OFF differ in their shape, especially in length and soma sizes (Saito 1987, Euler and Wässle 1995, Ghosh et al. 2004), due to the different layers of axon stratification in the IPL.

As a model for an OFF bipolar cell, the type 2 OFF cone BP cell from (Euler and Wässle 1995), Figure 2, see Figure 2.22. The original black and white image of the type 2 OFF cone bipolar cell is shown in panel A. Panels B shows the resulting model, viewed from the same perspective as in A. Panels C and D show the model of the cell with bottom and lateral view, respectively. This morphological model consists of 78 compartments. The somatic compartment has a radius of $4.7 \mu\text{m}$. In average, the radius of axonal compartments is $0.48 \mu\text{m}$, dendritic radii average to $0.38 \mu\text{m}$, and synaptic radius is $0.54 \mu\text{m}$ in average. This cell has a total length of $46.8 \mu\text{m}$, and stratifies in stratum 1 of the IPL (Euler and Wässle 1995).

Figure 2.23 shows different time-courses of V_m calculated for a 0.5 ms rectangular 0.5 V cathodic stimulation pulse the ON cell (A) and OFF cell (B). The cell is equipped with passive membrane properties, identical to the passive properties in previous simulations with BP1. The resting voltage is set to -41 mV .

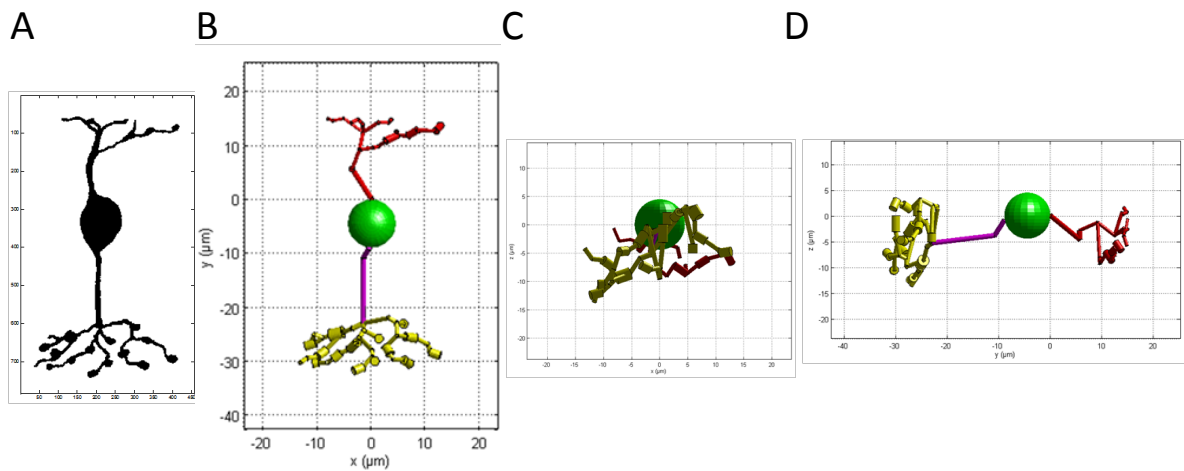


Figure 2.22

Morphological 3D model of a type 2 OFF cone bipolar cell

from Euler and Wässle 1995. (A). View from below (C) and side (D). The extent into the z-dimension (depth) is randomly generated.

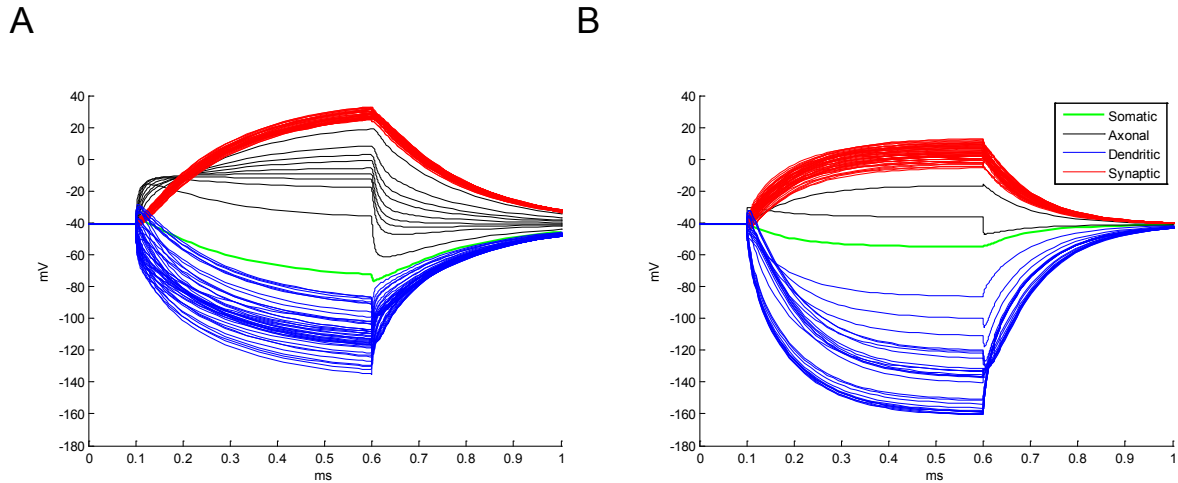


Figure 2.23

Time-courses of V_m in the realistic ON-type (A) and OFF-type (B) cone bipolar cells. The y-axis shows transmembrane potential V_m in mV. The 0.5 ms rectangular anodic 0.5 V stimulation pulse is initiated after a 0.1 ms delay.

The results for the ON cell yielded a maximal change in V_m from its resting potential of -41 mV to 33 mV in the synaptic compartments, thus maximal positive $\Delta V_m = 74$ mV. The maximal negative deflection of V_m occurred in the dendritic compartments located in close proximity to the stimulating electrode, in this case peaking at -134 mV, therefore the maximal negative $\Delta V_m = -93$ mV.

2.3.2 Multi-Electrode Simulations

The following step in advancement of the model was incorporation of arrays containing multiple electrodes. Following initial simulations with single electrodes, the model included simulation of multiple electrodes to obtain a better approximation to the BC response during stimulation with the Tübingen subretinal implant, which utilizes an array containing 1500 electrodes. In this section, the dependency of the elicited transmembrane potential on the size of the electrode array and the location of the current return was investigated. Array sizes range from 1x1 electrode to 11x11 (121) electrodes. Additionally, differences in stimulation paradigms with distant (monopolar) and local (dipolar) return electrode configurations were compared. However, realization of the distant return electrode was not done according to electrode configurations 1 and 2 as described in chapter 2.2.3. Instead, local return of current was implemented by creating a checkerboard stimulation pattern. In a checkerboard pattern representing the stimulation array, white fields correspond to electrodes generating a positive potential, while black fields correspond to electrodes that were subjected to a negative potential. The flow of current was determined by the gradient of these potential differences.

2.3.2.1 Monopolar Stimulation

With the initial design of the Tübingen subretinal implant all electrodes in the array are addressed simultaneously and potentials between 0 V and 2 V are generated on each electrode surface. Cross-talk between electric fields of neighboring electrodes is unavoidable, and dependent on the inter-electrode distance as well as the total number of electrodes (Stett et al. 2007). For the purpose of simplicity and computation speed most simulations are run with single electrode setups. In order to be able to transfer these results to a situation with multi-electrode-arrays (MEA), in this section the model was calculated using increasing square array sizes. In the clinical study, the current return sink is a large electrode which is attached to the implant and located in a position distant to the stimulating array (Zrenner et al. 2009). As a consequence, current from the electrodes flows unidirectionally away from the stimulating electrodes. This setup was represented in the model by turning the outer border of the retinal layer (see Figure 2.2) in the FEM model geometry into a current sink. This resulted in a unidirectional current flow from the electrodes towards the retinal borders and in the isopotential planes shown in Figure 2.24.

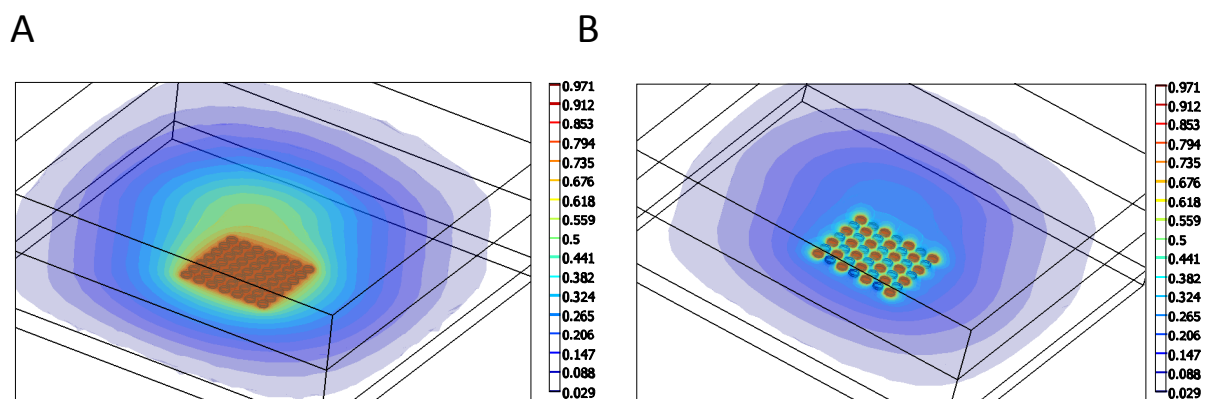


Figure 2.24

Multi-electrode arrays with distant current return. A: Full field stimulation. In this simulation all 49 electrodes (array of 7x7) simultaneously generated a potential of 1 V at their surface, the outer boundary acted as return electrode. B: Checkerboard unipolar stimulation. The 49 electrodes were activated in a checkerboard pattern, leaving every second electrode at 0 V. As in the full field stimulation, the retinal outer boundary acted as a large return electrode. Colors represent V_e .

2.3.2.2 Dipolar Stimulation

Dipolar electrical stimulation was simulated by using a checkerboard pattern where each positive electrode had four neighboring negative electrodes. The stimulation pattern and the resulting isopotential planes can be seen in Figure 2.25.

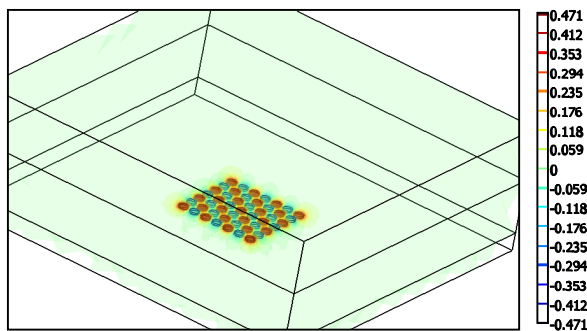


Figure 2.25

Checkerboard dipolar stimulation. In this simulation, the electrodes previously set to 1 V now were set to 0.5 V, while at the electrodes previously at 0 V were set to -0.5 V, thus acting as local return electrodes. Colors represent V_e .

2.3.2.3 Electrode Arrays

Results are given in maximal depolarization from resting potential ΔV_m . Full field (I): 2x2 electrodes yielded 59 mV depolarization, with increasing numbers of electrodes, ΔV_m decreased to 17 mV for 11x11 electrodes. In this simulation, maximal depolarization occurred in synaptic compartments. Checkerboard unipolar (II): ΔV_m decreased from 55 mV for 2x2 electrodes to 32 mV for 11x11 electrodes. The synaptic depolarization was slightly lower, ranging from 43 mV for 2x2 electrodes to 18 mV for 11x11 electrodes. Checkerboard dipolar (III): Here ΔV_m ranged from 32 mV for 2x2 electrodes to 30 mV for 11x11 electrodes. Synaptic compartments displayed some decrease in depolarization, 14 mV for 2x2 electrodes decreasing to 9 mV for 11x11 electrodes.

When comparing 2x2 and 11x11 electrodes, decrease in membrane depolarization was 71% for "I", 42% for "II" and 7% for "III". When considering synaptic compartments only, the decrease was 71%, 59% and 35%, respectively.

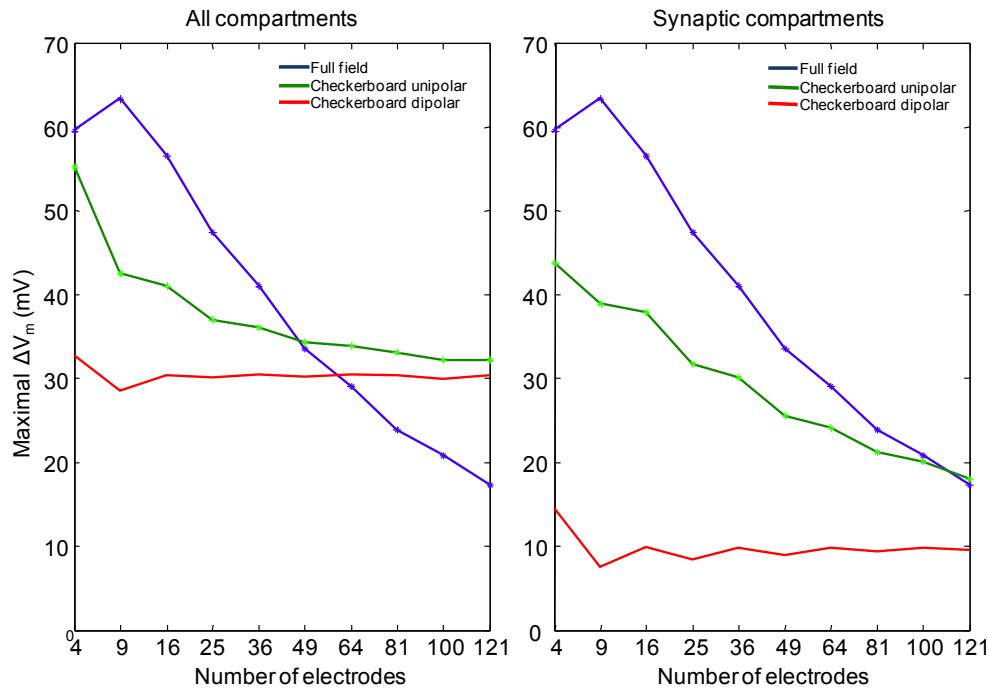


Figure 2.26 Increasing array sizes

Results of the simulations (in mV transmembrane potential change from -41 mV resting potential) with increasing array sizes, ranging from 4 electrodes (2x2 array) up to 121 electrodes (11x11 array). A 0.5 ms rectangular 1 V stimulus was applied in all simulations. Left panel: Maximal depolarization of the entire cell during the entire stimulation period. With small array sizes, full field stimulation causes a larger amplitude (blue), which decreases and falls below both checkerboard paradigms for array larger than 8x8. Unipolar checkerboard stimulation displays a similar, but decreasing dependency to array size (green). During all dipolar simulations, the depolarization remained at ~30 mV and showed no apparent dependency to array size and number of electrodes. Right panel: Maximal depolarization of the synaptic compartments in the simulated bipolar cell. With full field stimulation, the curve is equal to the left panel. Using unipolar checkerboard stimulation again a weaker dependency to array size is observed, while again the dipolar checkerboard stimulation has no apparent dependency to the electrode number. For the synaptic potentials, the curve for monopolar stimulations does not cross dipolar results for array sizes of up to 121 electrodes.

2.4 Discussion

The main purpose of this chapter was the presentation of necessary methods to prepare the reader for the applications of the active membrane model in the next chapter. It has been shown, that finite element simulations and passive membrane models allow simulation of the processes occurring during extracellular stimulation with an electrode or electrode array from the subretinal space. The investigation of these processes may combine and deepen the insights gained in the Tübingen subretinal implant project by *in-vitro* experiments and clinical studies.

The model presented here calculates transmembrane potential for arbitrary electrode configurations and neuronal morphologies. It is able to simulate the effect of different positions a target bipolar cell

may have relative to the stimulating electrode. The effect of crosstalk caused by multiple overlaying electrical fields was shown.

Furthermore, a Matlab tool was developed allowing the creation of three-dimensional neuronal morphologies based on two-dimensional images from traced neurons. Possible inaccuracies can be corrected by the investigator. In the case of retinal bipolar cell, where online databases offer no information on morphologies, this can be a helpful tool.

The computational efficiency of the model is high and allows simulations in the time span of ms, depending on the accuracy of the membrane model and the neuronal morphology.

3 The Active Model

3.1 Introduction

The passive model of retinal bipolar cell (BC) responses to external electrical stimulation elaborated in the previous chapter primarily served testing and evaluation purposes. Responses of passive membrane models can be conceived in a mathematically linear fashion. Therefore, the correctness of responses and sensitivity to parameter alterations can be verified more easily. Historically, retinal BCs were initially assumed to be passively responding neurons. However, during the last two decades, successive new discoveries of active, voltage-gated ion channels in the membrane of retinal BCs have been made, which will be discussed in more detail in section 3.2. The membrane potential responses of cones and rods to natural light stimulation are sustained and slower than the behavior of spiking neurons in the central nervous system (CNS) (Baylor 1987), yet retinal ganglion cells (RGC) can yield much more transient responses and convey neuronal information to the lateral geniculate nucleus (LGN) with spiking action potentials. In 1989 it was suggested, that this conversion from sustained responses in the outer retina to transient responses in the inner retina occurs mainly in retinal BCs, spurring renewed interest in identifying active ion channels in BCs (Maguire et al. 1989).

Most electrophysiological studies on bipolar cell channels before 2000 were conducted on lower vertebrates, revealing voltage-activated Ca^{++} currents, Ca^{++} -activated K^+ and Cl^- currents, outward K^+ currents and hyperpolarization-activated currents (Kaneko and Tachibana 1985, Lasater 1988, Tessier-Lavigne et al. 1988, Kaneko et al. 1989, Maguire et al. 1989, Karschin and Wässle 1990, Heidelberger and Matthews 1992, Okada et al. 1995, Connaughton and Maguire 1998). Consequently, while the first evidence for the presence of voltage-gate T-type Ca^{++} channels in higher vertebrates was found in 1989 (Kaneko et al. 1989) most other studies on voltage-gated ion channels in BCs of higher vertebrates followed only after the year 2000, where the increasing quality of dissection and identification techniques allowed the first evidence for the presence of voltage-gated Na^+ currents in mammalian cone bipolar cells of the rat (Pan and Hu 2000).

3.2 Literature Review

In the following section, a comprehensive overview of literature available to date on the ion channel equipment of cone bipolar cells (CBC) of the rat is presented. Data from the rat was used due to better availability. The apparent differences between ON-type and OFF-type CBCs will be elaborated and summarized in a form that can be incorporated into a computational representation of ON-type

and OFF-type CBCs. Because cell type specificity within this literature has improved significantly over the years, this review will be organized chronologically rather than exclusively by channel type.

3.2.1 Explanation of Common Methods

The relevant results from the literature reviewed here are achieved using two different methodologies: whole-cell patch-clamp measurements of a cell's electrophysiology and immunocytochemistry to reveal a cell's morphology. Patch-clamp measurements serve to create data describing the biophysical properties of a cell's ion channels. With immunocytochemistry it is possible to determine the subcellular position of specific ion channel types within the cell and verify their presence using specifically targeted antibodies. While some of the articles employ both methods, others use only patch-clamp measurements or only immunocytochemistry. In many but not all studies reviewed here, the authors were able to identify the specific type (Euler and Wässle 1995) of an electrophysiologically recorded CBC.

3.2.1.1 Whole-Cell Patch-Clamp Electrophysiology

To be able to reproduce the electrophysiological properties of retinal BCs in a computational model, information on the electric properties of various voltage-gated ion channels known to exist in these cells is required. The patch-clamp technique is the most widespread experimental method for studying these neuronal properties. It was originally developed by Neher and Sakmann (Neher and Sakmann 1976) to record from single ion channels. The main principle is that a micropipette containing an electrode and having a very small opening in the μm range is placed at the neuronal membrane - in this case covering a patch of membrane containing only a single ion channel - and creates a high resistance seal against the surrounding external solution. This setup allows investigations on the electrical excitability of neuronal membranes. Two different electrical setups can be realized, voltage-clamp and current-clamp.

Voltage Clamp vs. Current Clamp

In voltage-clamp measurements the transmembrane voltage is kept constant while the current required for realizing this constant voltage is measured. By convention, current flowing into the cell is treated as negative current and outward current is defined as positive (Neher and Sakmann 1976). By measuring the current flow through the membrane at different holding voltages, the voltage-dependent activation state of ion channels can be determined (see *Step-Clamp vs. Ramp-Clamp*, below).

In the current-clamp setup the membrane current is held constant while the changes in transmembrane voltage are measured. The potential (usually in the range mV) is generally measured in terms of intracellular minus extracellular potential, therefore a negative value implies a lower intracellular potential. The current-clamp paradigm allows voltage to vary, uncovering dynamic voltage-dependent processes such as the action potential.

Whole-Cell Patch-Clamp

In whole-cell patch-clamp measurements (Hamill et al. 1981), the micropipette does not cover a single ion channel, but instead perforates the neuronal membrane (Figure 3.1), usually at the soma. Using this technique all currents in the perforated cell can be measured simultaneously. The technique therefore does not give direct information on where in the measured cell these currents were initiated, with respect to different cellular regions such as dendrites, soma, axon or axon terminals. It also is not specific to single ion types. Mostly, the investigators pharmacologically block channels susceptible to other ions contained in the extracellular solution or manipulate the intra- and extracellular ion concentrations to be able to record e.g. only Na^+ or only K^+ currents. When whole-cell measurements are performed on isolated cells, some cells may lose their axons, distal dendrites or axon terminals during the isolation procedure (Hu et al. 2009). It may be possible to conclude channel locations by comparing current traces of cells that retained their axons and cells that did not retain their axons. Such cells are in a shock-like situation and therefore, conclusions have to be treated with caution. Another restriction of this method are space clamp issues, which arise due to the fact that implementing a voltage clamp or current clamp at one single location of the cell will most likely not have an homogeneous impact on the entire cell. Cellular charges exist in the form of free ions and organic molecules carrying positive or negative charges. The transport of these charges (current) is not instantaneous and therefore dependent on space and time.

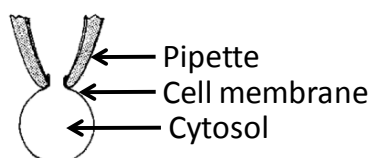


Figure 3.1

Schematic drawing of a whole-cell patch clamp setup. Modified from (Hamill et al. 1981)

Step-Clamp vs. Ramp-Clamp

During a typical voltage clamp (or step-clamp) experiment (Figure 3.2), the cell is first held at a certain holding potential, then a rectangular voltage pulse is applied to either depolarize or hyperpolarize the cell, bringing the cell to a more positive or more negative constant testing potential, respectively. The currents caused by this change in potentials are then measured. Finally, the voltage is returned to the initial holding potential, currents evoked by this step are called tail

currents. In a series of experiments, different testing potentials are applied to a cell and the currents evoked by each potential are recorded. Such experiments allow an insight into how the cellular currents depend on transmembrane potential. If each testing potential is applied for a sufficient time allowing the resulting currents to reach a steady state, the amplitude of these steady-state currents can be plotted versus the potentials to create a steady-state current-voltage characteristic or I-V curve.

It is further possible to apply a voltage ramp (or ramp-clamp), see Figure 3.2. In this case, the voltage applied by the electrode is constantly in-/decreased from the holding potential in a time-dependent manner, for example at a speed of 100 mV/s to a final potential. Voltage ramp experiments allow a more convenient creation of I-V curves by conducting a single measurement instead of an entire series of experiments. These I-V plots created in voltage-ramp experiments describe a quasi-steady-state if the voltage is not increased too quickly. Furthermore, they are based on the assumption that channels do not inactivate, which is not necessarily always the case.

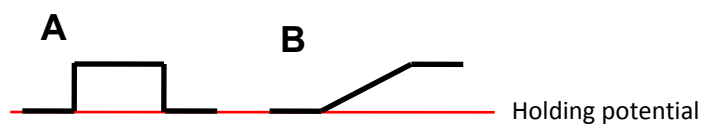


Figure 3.2

Electrode potential during (A) voltage clamp and (B) voltage-ramp experiments.

3.2.1.2 *Immunochemistry*

Additional to the biophysical properties of voltage-gated ion channels, information on their subcellular distribution and location is required for the creation of a realistic multi-compartment model. Immunostaining methods and electron microscopy can experimentally reveal if and where specific ion channels are located within a given cell. Some of the studies reviewed in this chapter applied immunostaining methods to retinal tissue samples (immunohistochemistry) or to single isolated cells (immunocytochemistry). Here, primary antibodies known to bind specifically to a molecule of interest are used as markers in tissue or cell preparations. In a second step, species-specific fluorescence-conjugated antibodies are then used to detect the primary antibodies. The fluorogenic sample can then be investigated using light-microscopy. The intensity of the measured fluorescence is proportional to the concentration of the targeted molecule. Unfortunately, in the available literature on ion channels in rat CBCs, immunostaining has only been applied to hyperpolarization-activated cyclic nucleotide-gated (HCN) channels (reviewed below). A more detailed explanation of the method can be found in (Ramos-Vara 2005).

3.2.2 First Evidence of Voltage-Gated Na⁺ Currents in Mammalian Cone Bipolar Cells

In a study from 2000, Cone bipolar cells of the rat were dissected and electrophysiologically investigated for the presence of voltage-gated Na⁺- and Ca⁺⁺-currents (Pan and Hu 2000). Recordings were made in whole-cell configuration at 20° C- 25° C.

Na⁺-currents with amplitudes >300pA were found and identified by reversible blocking with Tetrodotoxin (TTX), a known Na⁺ channel blocker (Figure 3.3 A). The currents were activated at membrane potentials around -50 mV to -40 mV and peaked at -20 mV to 0 mV (Figure 3.3 C). They also displayed rapid recovery from inactivation (Figure 3.3 B), suggesting that a brief hyperpolarization may remove Na⁺-inactivation.

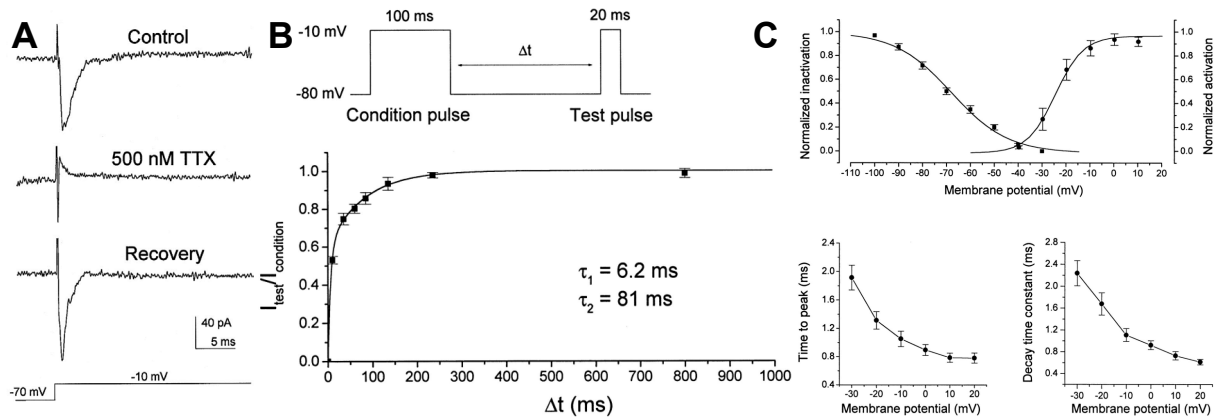


Figure 3.3

Na⁺ currents in rat CBCs. (A) Reversible blocking of Na⁺ channel using TTX had measurable effects on membrane currents. (B) Upper panel: Test-pulse conditions for time-dependent Na⁺ channel inactivation. Lower panel: Time-dependence of normalized Na⁺-inactivation. (C) Normalized activation and inactivation kinetics of Na⁺ currents (obtained by subtraction of TTX current from control current). From: (Pan and Hu 2000).

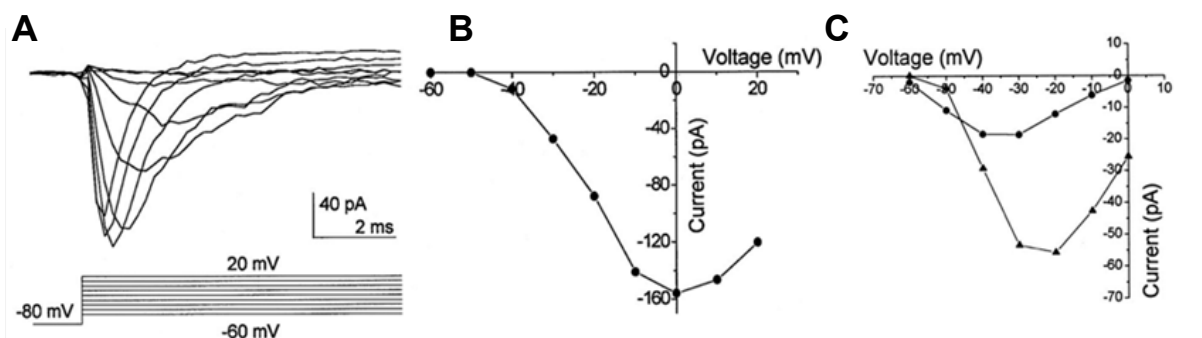


Figure 3.4

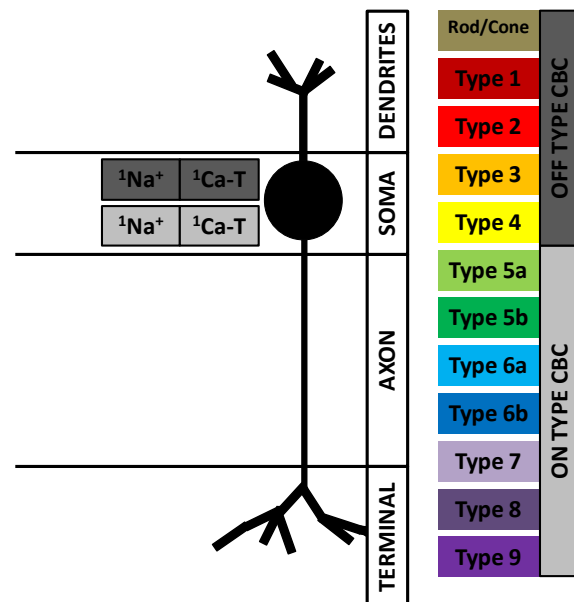
Currents measured under high Ca⁺⁺ concentration. Left panel: Current traces. Middle panel: resulting current-voltage (I-V) relationship of the voltage-activated transient inward peak currents. Right panel: I-V plot for peak currents of Na⁺ (triangle) and Ca⁺⁺ (circle) in high Ca⁺⁺ solution. From: (Pan and Hu 2000).

Additionally, low-voltage-activated (LVA) T-type Ca^{++} currents were found in these CBCs in conjunction with the Na^+ current (Figure 3.4). The Ca^{++} currents were blocked with Co^{++} . Both ON and OFF CBCs showed evidence for voltage-activated Na^+ -currents. However it was noted, that Na^+ currents appeared more frequently in cells with slightly smaller soma and longer axons. Since the dissection procedure mostly lead to the complete loss of the axon terminals, it was concluded, that most of the Na^+ current originated from the soma of these cells. These cells also were capable of generating action potentials, both electrode-driven and spontaneous. It was argued, that due to their biophysical properties and bipolar cell membrane potentials around -40 mV to -45 mV these Na^+ channels may be inactive in the dark state of the retina, but light evoked hyperpolarization may partially remove this inactivation. A large number of rod bipolar cells were further tested for Na^+ currents, however, none were detected. The preceding facts as they impact in the present modeling study are summarized in Figure 3.5.

Figure 3.5

Summarized visual representation of currents in cone bipolar cells of the rat suggested in ¹(Pan and Hu 2000)

The colors used in this type of figure represent all known cone bipolar cell types of the rat. Additionally, dark gray represents generic OFF-type CBCs while bright gray represents generic ON-type CBCs. The schematic of a bipolar cell is separated into four segments (dendrites, soma, axon and axon terminal). Each current is assigned to one or more of these segments throughout chapter 3. The superscript numbers from 1 to 7 refer to the seven journal articles reviewed in section 3.2.



3.2.3 Kinetics of K^+ Currents in Rat Retinal Bipolar Cells

In a detailed investigation of voltage-gated outward K^+ currents of rat bipolar cells (Hu and Pan 2002) it was found, that K^+ currents generally were larger in CBCs than in rod bipolar cells (RBC, Figure 3.6 and Figure 3.7). The study was performed on acutely isolated cells in whole-cell mode at room temperature. Most of the CBCs lost their axon and/or axon terminal during dissection, therefore the reported currents are best attributed to the soma. The cells were held at -60 mV and received test pulses with a duration of 2 s and potentials ranging from -50 mV to +30 mV. At +30 mV the peak K^+ current in RBCs was ~ 700 pA, while ~ 1700 pA were measured in CBCs. The whole cell capacitance of CBCs was ~ 2.5 pF.

A close investigation of activation and inactivation kinetics of K^+ channels in CBCs lead to the distinction of two groups: fast (CBC_F) and slow (CBC_S), referring to the speed of steady-state inactivation. As shown in Figure 3.6 B and C the I-V relationship of voltage-dependent channel activation differ only slightly in CBC_F and CBC_S , while during steady state inactivation (Figure 3.7 B and C) the I-V plot had a much steeper slope in CBC_F . Cells from these two groups were tested for their response to kainite and L-AP4 (Slaughter and Miller 1981) to determine whether they were OFF-type or ON-type bipolar cells. However, a correlation of CBC_F or CBC_S to ON-type and OFF-type bipolar cells was not found. The authors assumed that the K^+ currents they described in this study were a mixture of voltage-gated K^+ currents ($I_{K(V)}$) and Ca^{++} -dependent K^+ currents ($I_{K(Ca)}$), Figure 3.8.

The inactivation kinetics of $I_{K(V)}$ were then investigated using Co^{++} to block Ca^{++} currents. It was shown, that voltage-gated K^+ channels were differentially sensitive to 4-aminopyridine (4-AP) and the authors concluded, that the level of sensitivity correlates to K^+ channel subunits Kv1.1, Kv1.2 and Kv1.3. The results, however, were only conclusive for rod bipolar cells and different K(v) channel subunits had been shown before in the rod bipolar cells of the mouse (Klumpp et al. 1995). It was noted, that overall K^+ inactivation kinetics of rat bipolar cells appear similar to those of the axolotl (Tessier-Lavigne et al. 1988), and that these were A-type (inactivating) K^+ currents.

The functional relevance of K^+ channels in retinal bipolar cells remained unclear. The authors argued that they may contribute to shaping the response waveform and potentially play a more significant role in ON-type CBCs due to their commonly more positive membrane potential. It has been proposed that they oppose light induced depolarization in rod bipolar cells (Klumpp et al. 1995). In fish, however, K^+ channels of ON- and OFF-type CBCs have been found to not differ significantly (Lasater 1988) . In a later study from the same group evidence was presented for a role of K^+ channels in setting the different membrane operating ranges in retinal bipolar cells (Ma et al. 2005).

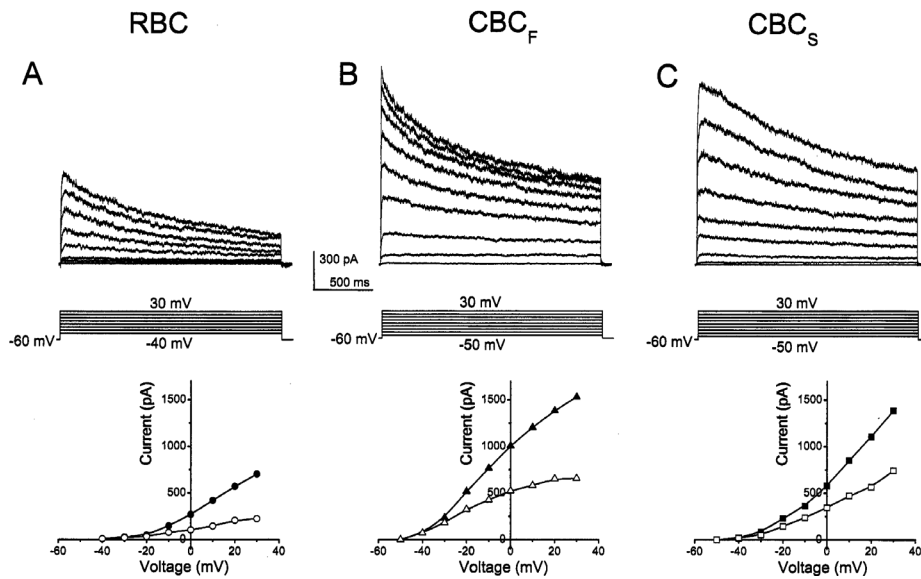


Figure 3.6
 K^+ activation kinetics. Total outward K^+ currents (upper panels) during 2 s test pulses and voltage-dependent activation kinetics (lower panels) during peak current (closed symbols) and at the end of the test pulse (open symbols). Figure from (Hu and Pan 2002).

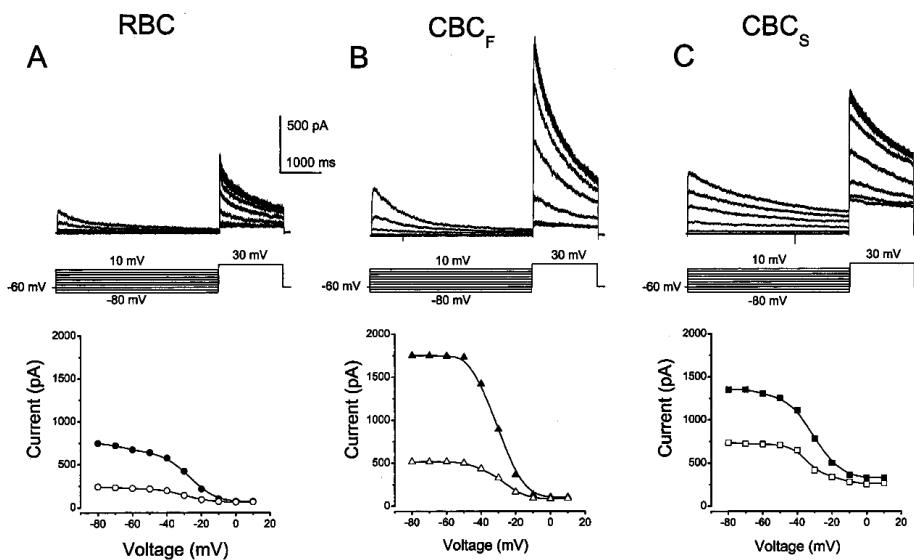
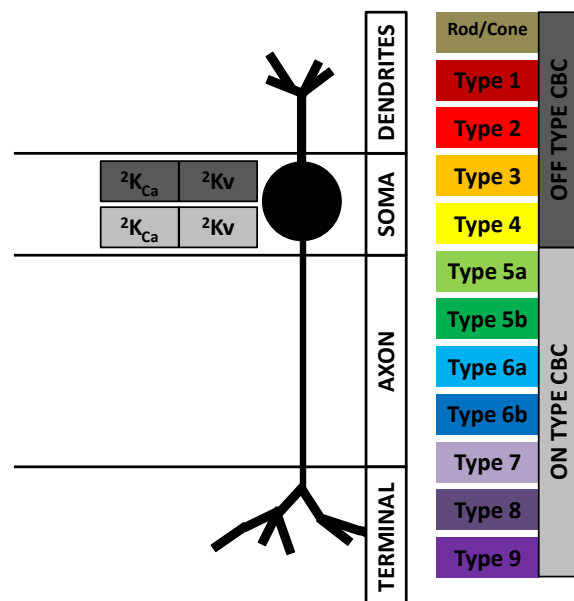


Figure 3.7
 K^+ inactivation kinetics. Total K^+ currents measured during a 2 s conditioning pulse and a following test pulse (upper panels), as well as the resulting steady-state inactivation kinetics (lower panel) during peak current (closed symbols) and at the end of the test pulse (open symbols). Figure from (Hu and Pan 2002).

Figure 3.8
 Summary of currents in cone bipolar cells of the rat suggested in ²(Hu and Pan 2002)



3.2.4 Detection of Differentially Expressed HCN Channels in Rat Retinal Bipolar Cells

In a later study (Müller et al. 2003) several hyperpolarization-activated cyclic nucleotide-gated HCN channels with heterogeneous distributions among bipolar cell types were found and electrophysiologically recorded. The highest concentrations of HCN channels in the rat retina were found at the synaptic terminals of photoreceptors and bipolar cells of the rat retina.

Using immunohistochemical methods, HCN2 channels were detected across several bands in the IPL. Only a very small number was found in bipolar cell bodies, but they were highly concentrated in their axon terminals. A type of bipolar cells that contained HCN4 in its axon terminal could be identified as type 3 CBCs, which are OFF-type CBCs (Figure 3.9). Type 2 CBCs were found to not contain any traces of HCN4 currents. The HCN4 currents in type 3 CBCs reached a steady-state only during hyperpolarization ($V_m = -100$ mV) and displayed slowly decaying tail currents when V_m was returned to the holding potential of -50 mV. The fitting parameters for this current during hyperpolarization were two exponentials with time constants $\tau_1 = 430$ ms and $\tau_2 = 2654$ ms. The currents were reversibly blocked by intracellular Cs^+ indicating that these are in fact HCN currents. The density of these channels was higher at the axon terminal than at the soma.

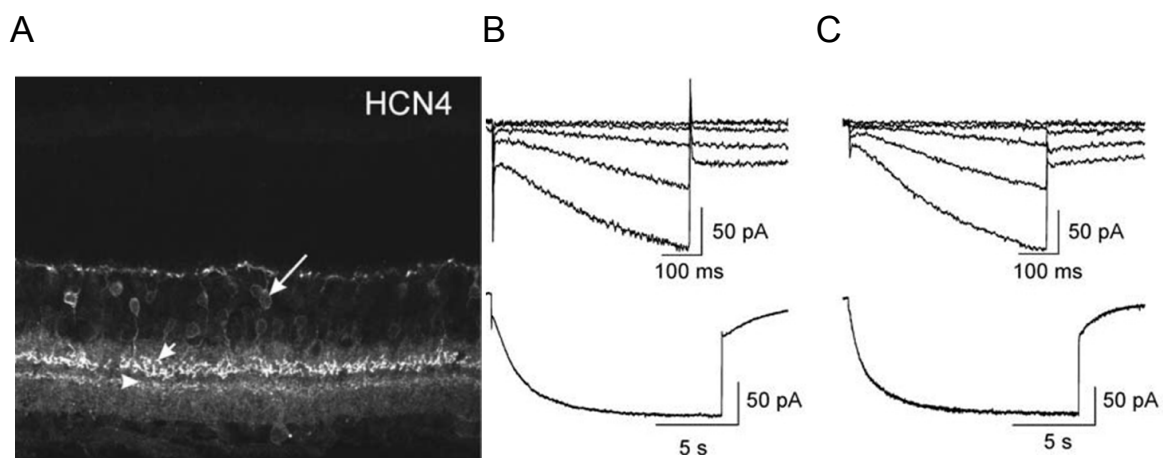


Figure 3.9

HCN4 channels and currents in type 3 cone bipolar cells. A: Immunohistochemical localization of HCN4 in the OFF-sublamina (arrowhead) of the IPL. Arrows show different bipolar cell types. B: HCN4 currents recorded in a HEK293 cell (HCN1 gene added by cDNA transfection). C: HCN currents in a type 3 CBC. Modified from (Müller et al. 2003)

An ON-type CBC identified as type 5 CBC was found to be positive for HCN1 and HCN4 channel staining at its axon terminal (Figure 3.10). It is currently assumed, that two subclasses of this type exist, type 5a and type 5b CBCs (Fyk-Kolodziej and Pourcho 2007). HCN1 channels, however, were only found in type 5b CBCs, therefore these type 5 CBCs will be referred to as type 5b CBCs. Additionally, it was investigated whether these channels form hetero-oligomers. The authors,

however, could not confirm this hypothesis. Fitting of HCN currents in type 5b CBCs required three exponentials, $\tau_1 = 63$ ms (HCN1), $\tau_2 = 379$ ms and $\tau_3 = 2945$ ms (HCN4). It was concluded that HCN1 channels contribute to 80% of the type 5b CBC HCN currents and 20% are contributed by HCN4 channels. The HCN2 specific antibody signal was found across the entire inner IPL. It was mentioned that all bipolar cells stratifying in that sublamina may express HCN2. However, they were only able to demonstrate conclusively that type 8 CBCs and rod bipolar cells have HCN2 channels in their axon terminal (Figure 3.11).

In photoreceptors HCN currents have a function of counteracting the hyperpolarizing response to high light intensities (Fain et al. 1978). The HCN1 channel, which has the fastest temporal properties, may be suited to serve a similar purpose in bipolar cells. The localization of HCN channels as relates to the present modeling study is summarized in Figure 3.12.

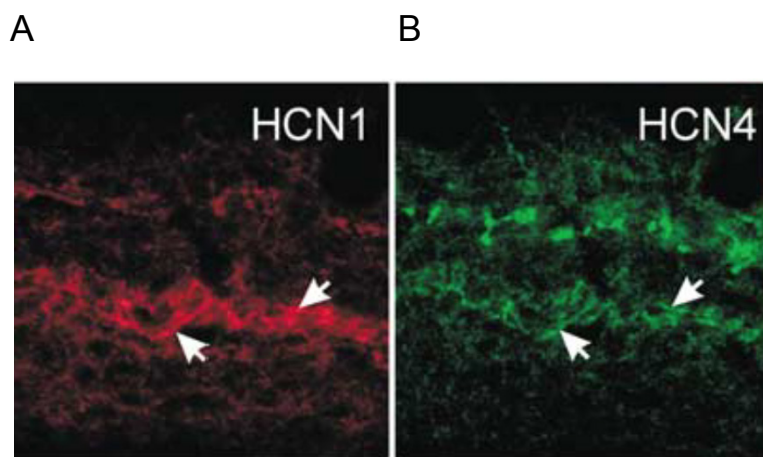


Figure 3.10

Type 5b CBC express HCN1 and HCN4. Double immunolabeling showed that HCN1 (A) and HCN4 (B) channels in type 5 CBC were colocalized (not shown). Modified from (Müller et al. 2003).

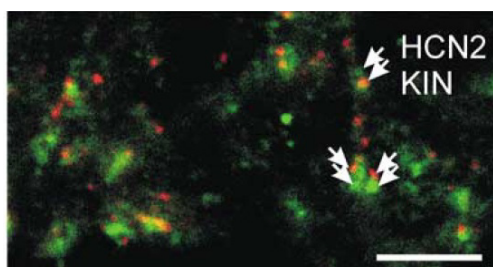
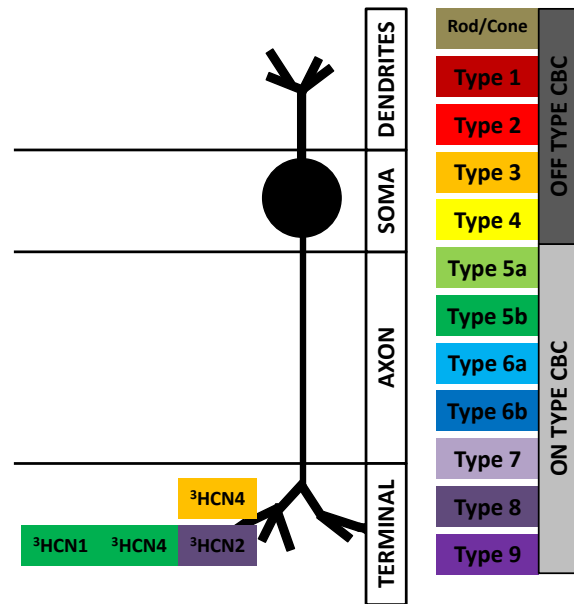


Figure 3.11

HCN2 channels localized at ribbon synapses. Double immunostaining with an antibody to Kinesin in these cells showed its colocalization to HCN2 channels (arrows). From (Müller et al. 2003)

Figure 3.12

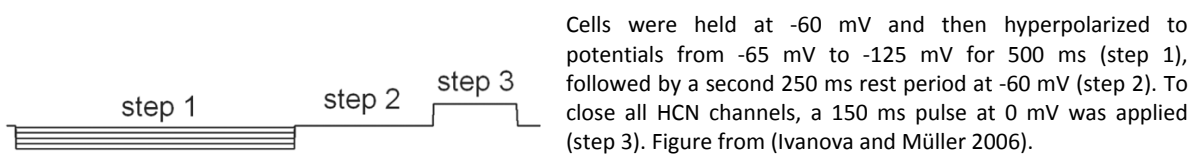
Summarized visual representation of currents in cone bipolar cells of the rat suggested in ³(Müller et al. 2003)



3.2.5 An Inventory of Retinal Cone Bipolar Cell Ion Channels in the Rat

A study in 2006 (Ivanova and Müller 2006) in adult rats suggested that the heterogeneous distribution of HCN channels in bipolar cells may be used as a kind of fingerprint for functional identification of bipolar cells using electrophysiology, in addition to the morphology-based identification introduced previously (Euler and Wässle 1995). This approach was used to identify a new ON-type CBC. The different HCN channels were distinguished based on the time-constants of the exponential fit. Figure 3.13 describes the electrophysiological patch-clamp paradigms applied in this study.

Figure 3.13



Cells were held at -60 mV and then hyperpolarized to potentials from -65 mV to -125 mV for 500 ms (step 1), followed by a second 250 ms rest period at -60 mV (step 2). To close all HCN channels, a 150 ms pulse at 0 mV was applied (step 3). Figure from (Ivanova and Müller 2006).

All ON CBCs and rod bipolar cells (RBC) expressed HCN2 channels at their axon terminal - as suggested in the previously reviewed study (Müller et al. 2003) - and HCN channels in general were found to be rather concentrated at the axon terminal. On the other hand, type 5 CBCs and type 6 CBCs expressed the HCN1 and HCN4 isoforms. Voltage-gated Ca^{++} and K^+ currents were found in all cells, but were not closely investigated in each cell type. In the following paragraphs, the electrophysiologically analyzed currents are described.

The HCN currents in type 5 CBCs were large and initially developed readily, but did not reach steady state during the 500 ms hyperpolarizing stimulation (Figure 3.15). Previously, type 5 CBCs have been

suggested to be either OFF-cells (Euler et al. 1996) or ON-cells (Hartveit 1997). This work presents evidence, that type 5 CBCs contact type All amacrine cells via gap junctions using the immunocytochemical marker CabP5 for type 5 CBCs (Haeseleer et al. 2000) and glycine for ON-CBCs (Vaney et al. 1998), therefore suggesting that type 5 CBCs are ON-cells. The transient component of the current recorded in type 5 CBCs could be blocked with Co^{++} and thus may be a T-type Ca^{++} current. Type 5 CBCs had the largest HCN currents (HCN1 and HCN4) in this investigation and the authors assumed that the cell showing large HCN currents in (Ma et al. 2003) was one of this type. Immunocytochemistry further identified HCN2 channels in type 5 CBCs but this could not be confirmed by electrophysiological recordings. Another group (Fyk-Kolodziej and Pourcho 2007) later differentiated type 5 CBCs into two new subtypes 5a and 5b (see the next section). In that work type 5a CBCs only expressed HCN4 channels, whereas type 5b CBCs expressed HCN isoforms 1, 2 and 4. It is therefore possible, that the present authors investigated only type 5b and not type 5a CBCs. This assumption is underlined by the finding that type 5b CBCs have more diffuse and less narrow axon terminals than type 5a, because the type 5 CBC shown in Figure 3.14 also has a rather broad, diffuse axon terminal.

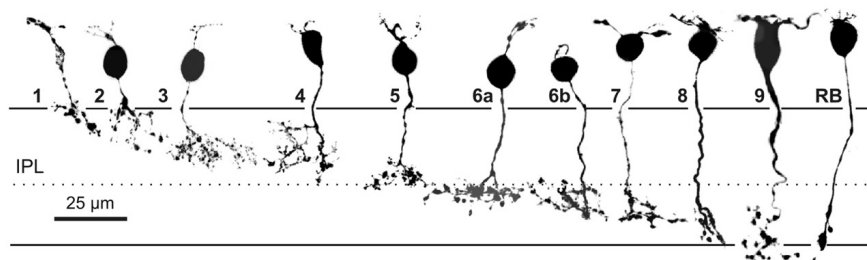


Figure 3.14

Identified rat bipolar cells filled with Lucifer-Yellow. On cholinergic band is shown by dotted line. Axons terminate in different depths of the IPL. From (Ivanova and Müller 2006).

The authors identified a new CBC type which resembles type 6 CBCs but has a more diffuse axon terminal and distinct electrophysiological properties, type 6b. Type 6 CBCs (Euler and Wässle 1995) are subsequently named type 6a CBCs. The different current traces of these two cell types are shown in Figure 3.15.

The exponentials used to fit current recordings from type 6a CBCs were typical for HCN1 and HCN4 channels. Additionally, T-Type Ca^{++} were found to be the main source of Ca^{++} influx, but small L-Type Ca^{++} currents could also be observed. In a later study (Hu et al. 2009) it was suggested that in CBCs with more prominent T-type Ca^{++} and less prominent L-type Ca^{++} currents (so-called T-rich cells), the T-type channels would be located at the soma and L-type channels at the axon terminal. Experiments were conducted, which showed that the recorded instantaneously active inward current in type 6a CBCs is caused by Ca^{++} -activated Cl^- channels. These channels had not previously been described in mammalian bipolar cells.

Type 6b CBCs also showed evidence for T-Type Ca^{++} channels. Their characteristic recordings had large instantaneous currents, probably caused by inward rectifying K^+ currents (Ma et al. 2003), followed by small time-dependent HCN2 currents.

All detected ON-CBCs were stratifying close to the ganglion cell layer (GCL) and expressed only the HCN2 channel isoform, which was concentrated at their axon terminals. Those were types 6b, 7, 8, 9 CBCs as well as RBCs.

In type 7 CBCs, in addition to HCN2, a relatively large instantaneous inward current was suggested to be I_{Kir} (inward rectifying K^+ current), see (Ma et al. 2003). The currents recorded upon depolarization to -60 mV probably originated from T-Type Ca^{++} channels which had been showed previously (Pan 2000).

Type 8 and type 9 CBCs differed only slightly in electrophysiological recordings. Type 8 CBCs showed larger HCN2 currents during hyperpolarization compared to type 9 CBCs. Inward currents following depolarization were completely blocked by Cs^+ (blocks HCN currents) in type 8 but only 50% blocked in type 9 CBCs. It was not clarified however, what type of channel caused the remaining 50%.

Rod bipolar cells stratify approximately at the same depth as type 9 CBCs in the inner plexiform layer (IPL). Here, the only HCN currents in RBCs appeared to be caused by HCN2 channels. From recordings of complete cells, cells that had lost the entire axon and cells without an axon terminal it could be shown, that 43% of HCN2 channels were located at the axon terminals of RBCs, 35% at the axon and 22% were distributed on the dendritic tree and the soma.

The authors also discovered a heterogeneous distribution of HCN channels in OFF-CBCs (Figure 3.16). Type 1 CBCs showed only small hyperpolarization-activated currents that could not be further investigated and the applied cellular imaging techniques exhibited no overlay of type 1 CBCs and HCN channels. Type 1 CBCs, however indicated strong outward currents.

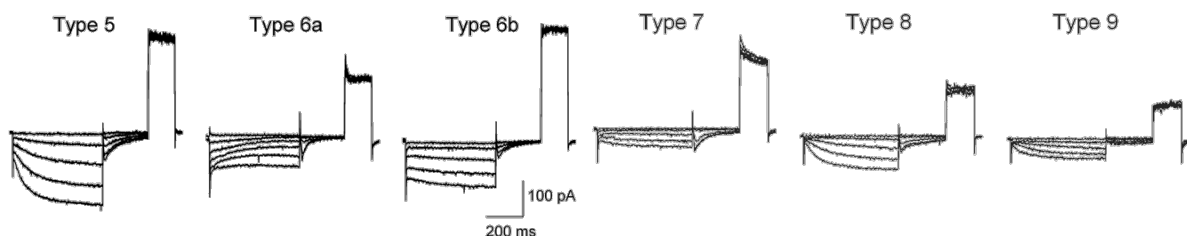


Figure 3.15

Current traces of ON-type bipolar cells. Experiments were made with the 3-step stimulation paradigm (see Figure 3.13). From (Ivanova and Müller 2006).

In type 2 CBCs, the detected hyperpolarization-activated currents were slightly larger than in type 1, but their origin could not be identified due to the rare occurrence of type 2 CBCs in this study.

The only OFF-type bipolar cell which showed strong evidence for HCN channels were type 3 CBCs (Figure 3.16). Those currents were fit with exponentials typical for slow kinetics of HCN4 channels. In agreement with a previous report (Müller et al. 2003), they showed strong outward currents, a sustained L-type Ca^{++} current, a very small transient T-type Ca^{++} current and another current which may be attributed to Na^+ channels. The differential expression of L-type and T-type Ca^{++} channels could suggest that type 3 CBCs may be L-rich cells (Hu et al. 2009) where L-type currents may come from the soma and T-type currents from the axon terminals.

In summary, type 1 and type 4 CBCs were the only bipolar cells that did not express HCN channels, whereas type 3 CBCs were the only OFF-type bipolar cell type in which HCN channels could be identified. A complete summary of the present study is provided in Figure 3.17.

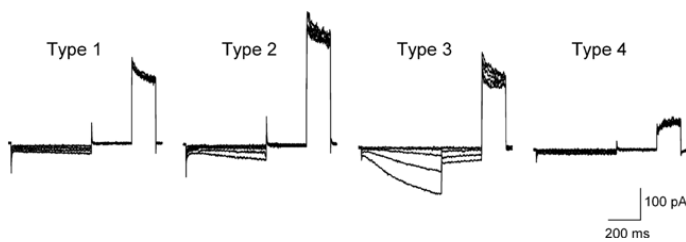
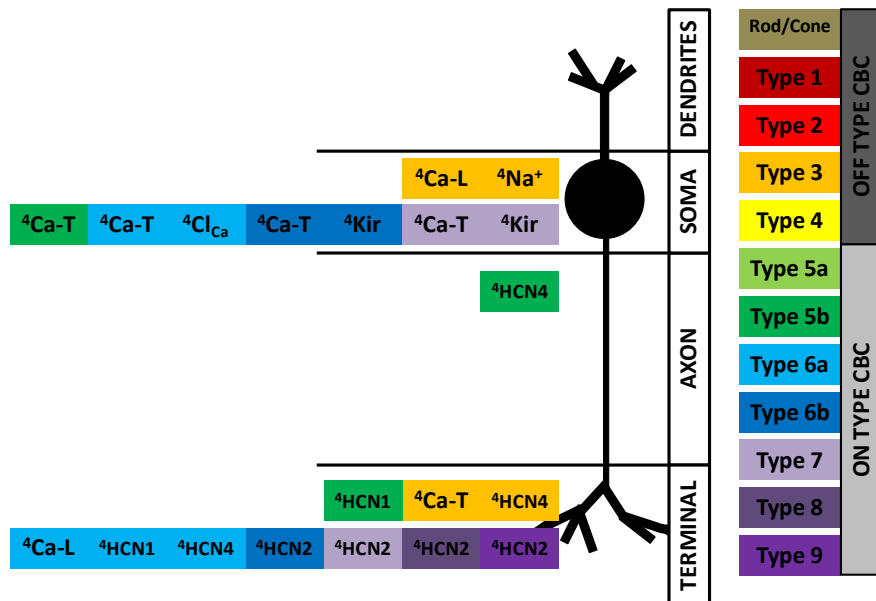


Figure 3.16

Recordings of OFF-type bipolar cells. The 3-step voltage protocol was applied (See Figure 3.13). Only type 3 CBC displayed large hyperpolarization-activated currents. Figure from (Ivanova and Müller 2006).

Figure 3.17

Summarized representation of currents in cone bipolar cells of the rat suggested in (Ivanova and Müller 2006)



3.2.6 Localization of HCN Channels in the Rat Retina

The distribution of HCN channels in cone bipolar cells of the rat retina could be used to present evidence for the existence of two subclasses of CBCs (Fyk-Kolodziej and Pourcho 2007). The authors differentiated the previously suggested (Euler and Wässle 1995, Hartveit 1997) type 5 CBCs into two new subclasses, type 5a and type 5b, based on the morphology of the axon terminal and absence or presence of certain HCN channels.

Immunoelectron microscopy revealed HCN1 channels in the OPL in dendritic processes of bipolar cells with mixed rod/cone input (Figure 3.18). These bipolar cells have been described in the rodent retina as OFF type CBCs (Hack et al. 1999). Furthermore, expression of HCN2 and HCN4 was detected in dendrites of type 3 OFF-CBCs which also contained HCN4 channels in their axon terminals (Figure 3.18). The dominant HCN current in type 3 CBCs however, has been shown to originate from HCN4 channels (Ivanova and Müller 2006). HCN4 had also previously been found in dendrites and axon terminal of the mouse retina (Feigenspan et al. 2004).

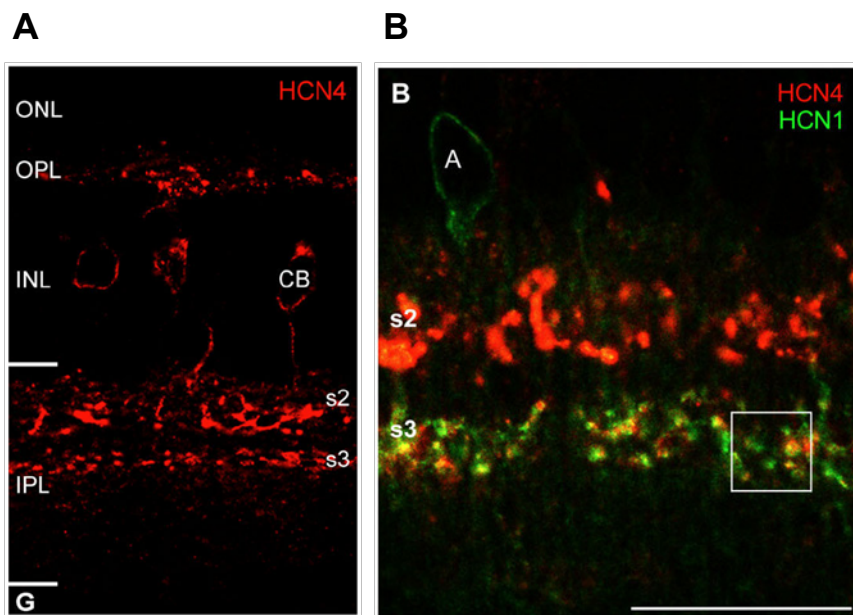


Figure 3.18

Expression HCN4 channels in the retina. (A) Results of immunocytochemical staining in a retinal slice in the rat. HCN4 channels were colocalized with cell bodies and processes of cone bipolar cells.

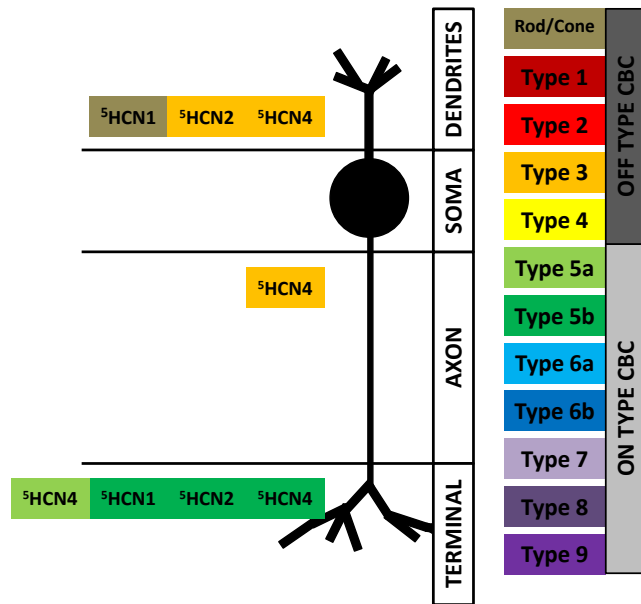
(B) Colocalization of HCN1 and HCN4 in the IPL. Sublamina 3 of the IPL was found to contain both HCN1 and HCN4, while in sublamina 2 only HCN2 channels were expressed. From (Fyk-Kolodziej and Pourcho 2007).

Another type of CBC, an ON-CBC morphologically identified as type 5b, expressed HCN isoforms 1, 2 and 4 in the axon terminal. Additionally, a morphologically similar cell, type 5a, with more narrowly stratifying and not so diffuse axon terminals expressing only HCN2 channels was found.

In both type 3 and type 5 CBCs large voltage-dependent Na^+ -current have been found (Cui et al. 2005). Figure 3.19 summarizes the relevant conclusions of this study.

Figure 3.19

Summarized visual representation of currents in cone bipolar cells of the rat suggested in ⁵(Fyk-Kolodziej and Pourcho 2007)



3.2.7 Two Types of Cone Bipolar Cells Express Voltage-Gated Na⁺ Channels in the Rat Retina

It was suggested that only two types of CBCs in the rat retina contain voltage driven Na⁺-channels (Cui and Pan 2008). In this study, immunohistochemical imaging and electrophysiological recordings were conducted in retinal slice preparations.

In contrast to previous studies, the authors establish a novel nomenclature system based on the layer of the IPL in which the identified cone bipolar cells stratify. Three types are discussed here, CB2 which stratifies in IPL sublamina 2, as well as CB3a and CB3b which stratify in sublamina 3. Furthermore, the authors argued that CB2 probably is a type 3 CBC following established naming schemes (Euler and Wässle 1995), and therefore an OFF-type cell.

Both CB3a and CB3b are initially assumed to be type 5 CBCs following the same scheme. Based on morphological classification (Euler and Wässle 1995), CB3a should correspond to type 5 CBCs. However, based on properties of hyperpolarization-activated currents, CB3a more closely resembled type 6b CBCs reported in (Ivanova and Müller 2006). Meanwhile, type 5 CBCs (Ivanova and Müller 2006) resemble CB3b cells and appeared to express HCN1 channels, in agreement with immunocytochemical staining patterns of type 5b as reported before (Fyk-Kolodziej and Pourcho 2007). The authors of this study (Cui and Pan 2008) assume that the discrepancy may be due to subjective differences in morphological classification of the cell types. In the following paragraphs, CB3a will be referred to as type 6b CBCs and CB3b as type 5b CBCs, because the physiological differences are more relevant for the purpose of this thesis and were uncovered more recently. Both CBC types 5b and 6b were shown to be ON-type bipolar cells.

Type 6b CBC (CB3a):

Cells were held at -80 mV and voltage pulses ranging from -60 mV to +10 mV were applied. Upon stimulation, fast transient inward Na^+ currents were detected (Figure 3.20 A) having an average peak inward current of 131.6 pA (Figure 3.21 A). The current showed “a sign of escape from voltage control”, therefore the authors claimed that the Na^+ channels in these cells are located primarily at the axon terminals or across distal dendrites, but not the soma. These cells were shown to be capable of generating Na^+ -dependent action potentials, in most cases in bursts of multiple spikes, but occasionally spontaneous spikes were recorded as well. The currents in type 6b CBCs exhibited an additional component with slower activation and inactivation kinetics than Na^+ currents. This component could be blocked by Co^{++} addition and was therefore identified to be caused by Ca^{++} influx. Based on the temporal properties of this Ca^{++} current and in context of later data published by the same group (Hu et al. 2009) this appeared to be a T-type Ca^{++} current (Figure 3.20 B). Its time-to-peak delay was slightly shorter than the ones found later, therefore it is very unlikely to be a sustained L-type current. Furthermore, hyperpolarization-activated currents were examined by application of pulses from -70 mV to -120 mV. The recorded inward current consisted of two components, a smaller time-dependent current and a larger time-independent instantaneous current (Figure 3.22 A and Figure 3.23 A). It is argued, that the time-dependent component is likely to be I_h originating from HCN2 channels and the time-independent an inward rectifying K^+ current I_{Kir} , as had been shown previously (Ma et al. 2003) .

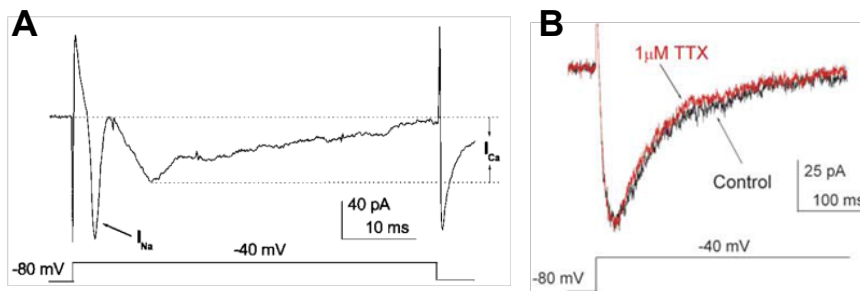


Figure 3.20

(A) Voltage-gated Na^+ and Ca^{++} currents in a type 6b CBC (Cui and Pan 2008). (B) T-type Ca^{++} current in a T-rich CBC with the same stimulation pulse. From (Hu et al. 2009)

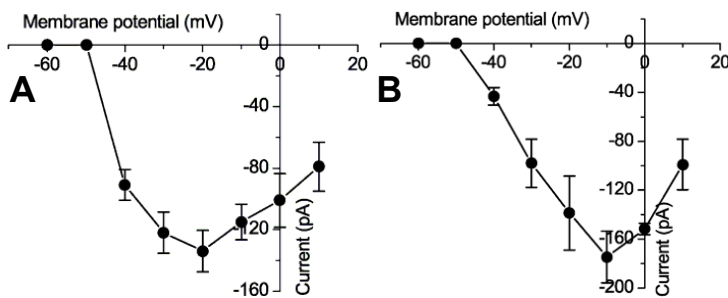


Figure 3.21

I-V relationships of TTX-sensitive Na^+ currents in (A) type 6b and (B) type 3 CBC. From (Cui and Pan 2008)

Type 5b CBC (CB3b):

Another bipolar cell, type 5b CBC, with axon terminal stratification similar to type 6b CBCs was identified, but in the electrophysiological recordings no Na^+ current was apparent as treatment with TTX did not have any effects. Additionally, only a few samples of this cell type indicated voltage-gated Ca^{++} currents, which then were of smaller amplitude than in Type 6b and had an average peak inward current of -16 pA. No action potentials could be elicited in these cells. Like type 6b, type 5b CBCs had hyperpolarization-activated current, however, in type 5b cells the time-dependent I_h component (probably HCN1 channels) was of larger amplitude than the time-independent I_{kir} (Figure 3.22 B and Figure 3.23 B).

Type 3 CBC (CB2):

The second bipolar cell type, that exhibited voltage-gated Na^+ currents at pulses above -50 mV, stratified in sublamina 2 and was an OFF-type cell. The average peak Na^+ inward current was measured at 165 pA (Figure 3.21 B). These cells were also capable of generating Na^+ -dependent action potentials, but multiple spiking was not observed in 11 out of 12 recordings. The Na^+ channels appeared to be located at the soma, and the cell did not generate spontaneous spikes. There was also no prominent Ca^{++} inward current observed, but the cells did have time-dependent (I_h , probably HCN4) and time-independent (I_{kir}) hyperpolarization-activated currents (Figure 3.22 C and Figure 3.23 C). The I_h component was larger than in type 5b CBCs.

In conclusion, the bipolar cell types with Na^+ channels had largely similar Na^+ currents but differed in their complement of other voltage-gated ion channels such as Ca^{++} and hyperpolarization-activated channels. These conclusions are summarized schematically in Figure 3.24.

Functional implications

The middle section of the IPL is where more transient retinal signals are processed (Awatramani and Slaughter 2000). Due to the fast activation and inactivation kinetics of its channels Na^+ may play a central role in enhancing transient responses in retinal ganglion cells. This has already been shown in the tiger salamander (Ichinose et al. 2005). Furthermore, axon terminals of type 3 and type 5b CBCs partially overlap with the processes of starburst amacrine cells, which have been shown to be important for direction selectivity (Yoshida et al. 2001, Borst and Euler 2011). Therefore, voltage-gated Na^+ channels could also play a role in direction selectivity of the retina.

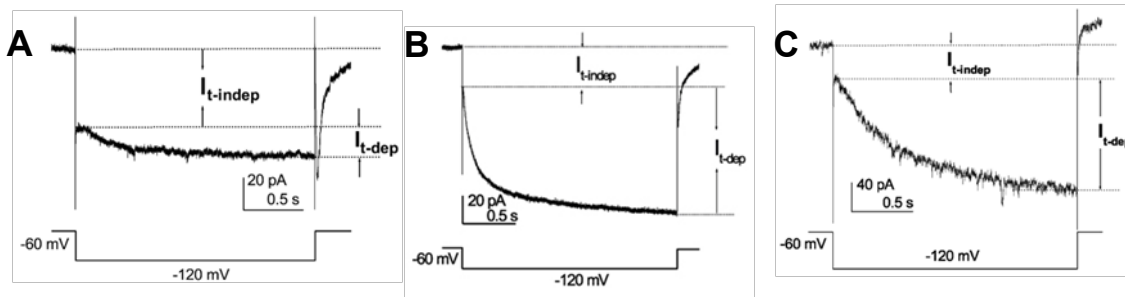


Figure 3.22

Hyperpolarization-activated currents in (A) type 6b, (B) type 5b and (C) type 3 CBC. Contributions of instantaneous current $I_{t-indep}$ (probably I_{Kir}) and sustained current I_{t-dep} (probably I_h from HCN channels) in response to a hyperpolarizing test pulse from -60 mV holding potential to -120 mV. From (Cui and Pan 2008)

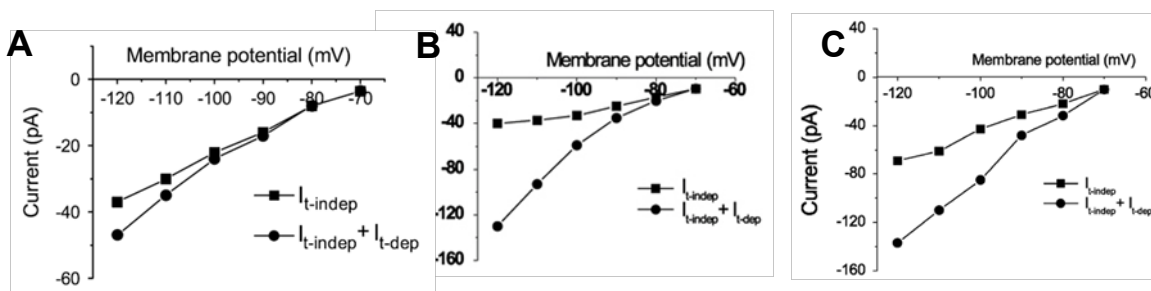
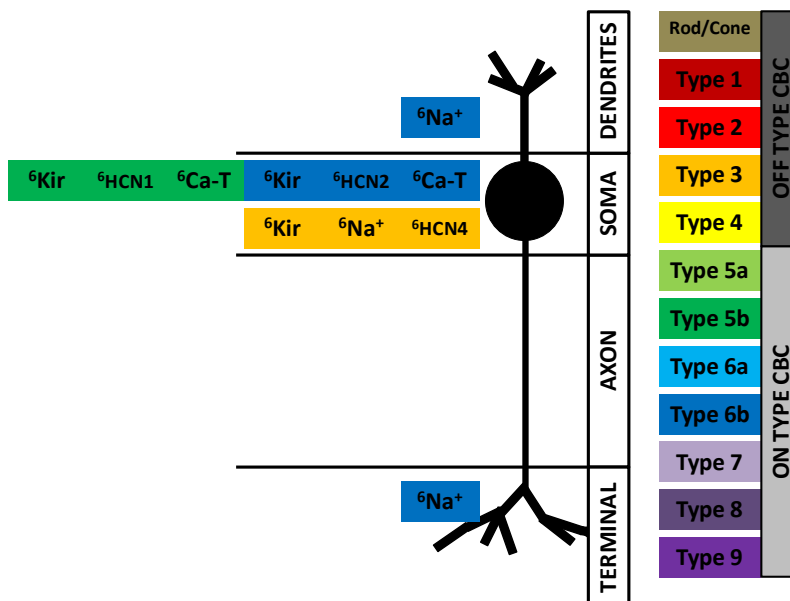


Figure 3.23

I-V relationships of all ($I_{t-indep} + I_{t-dep}$) and instantaneous ($I_{t-indep}$) hyperpolarization-activated currents in (A) type 6b, (B) type 5b and (C) type 3 CBC. From (Cui and Pan 2008)

Figure 3.24

Summarized visual representation of currents in cone bipolar cells of the rat suggested in (Cui and Pan 2008)



3.2.8 T-Type Ca⁺⁺ Channels in Rat Retinal Bipolar Cells

The next study reviewed here (Hu et al. 2009) closely investigated the differential distribution of various Ca⁺⁺ channels in cone bipolar cells of the rat. Currents were recorded from dissociated cells in whole-cell patch clamp mode. The majority of the cells lost their axon terminal during preparation. Cells were held at -80 mV; then an increasing voltage ramp from -80 mV to +40 mV was applied at a rate of 100 mV/s (Figure 3.25).

Mainly T-type (transient) and L-type (long-lasting) Ca⁺⁺ currents were observed. The T-type channels were activated at around -60 mV and their current peaked close to -40 mV. Different cells appeared to express different T-type channels and three groups of T-type channels were identified. Identification depended on the time required by a channel reached to reach its peak current amplitude. The three channel types had a time-to-peak of approximately 20 ms (group 1), 25 ms (group 2) and 35 ms (group 3). The average current generated by T-type channels was ~40 pA with a peak current of ~130 pA. Furthermore, T-type channels were able to generate low-threshold spikes or regenerative potentials. L-type Ca⁺⁺ channels required a voltage between -40 mV and -30 mV for activation and peaked at -20 mV to -10 mV. The average and peak currents were ~50 pA and ~160 pA, respectively.

Most of the cells could be differentiated into one of two groups, one with more prominent T-type Ca⁺⁺ currents which had smaller L-type currents (T-rich cells) with a whole-cell capacitance of 2.2 ± 1.9 pF (n=783) and a second group with larger L-type and smaller T-type currents (L-rich cells) with whole-cell capacitance of 3.1 ± 2.1 pF (n=990) and were generally larger in size. Due to the fact, that most of the cells which exhibited prominent T-type in conjunction with L-type Ca⁺⁺ currents were cells that had retained their axon terminals it was concluded, that T-rich CBCs have T-type channels mainly in the soma, whereas L-type channels are found across their dendrites and axon terminal. Conversely, L-rich CBCs mostly expressed L-type Ca⁺⁺ channels at their soma and T-Type channels along distal dendrites and axon terminal.

It was shown previously that the spike-like potentials were not caused by Na⁺ (TTX had no effect) and were sensitive to the drug Mibefradil, a T-type Ca⁺⁺ channel blocker (Figure 3.26 C). Transient and sustained Ca⁺⁺ currents may play a role in shaping the different waveforms of bipolar cell responses. Also, it had been shown before that activation of T-type Ca⁺⁺ channels may trigger transmitter release at bipolar cell axon terminals (Pan 2000), but these findings were not discussed in the context of L-rich and T-rich cells. The same study further measured Ca⁺⁺ currents in the axon of CBCs, however, because of a temporal delay, the authors assumed that Ca⁺⁺ had diffused from the axon terminal.

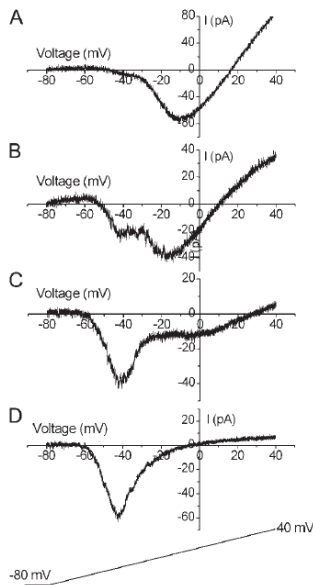


Figure 3.25

I-V Relationships of T-type and L-type currents.

(A) CBC primarily displaying L-type currents

(B) CBC with prominent L- and T-type currents

(C & D) CBC with larger T-type currents

Figure from (Hu et al. 2009).

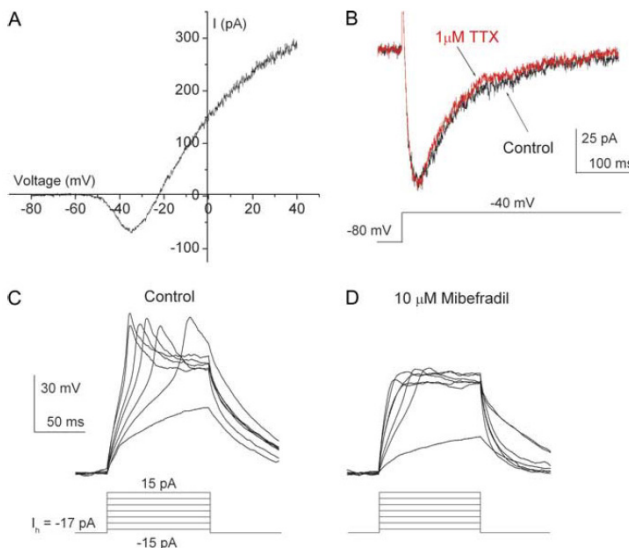


Figure 3.26

Ca⁺⁺ spikes in bipolar cells. Electrophysiological recordings were made in a 2.5mM Ca⁺⁺ solution.

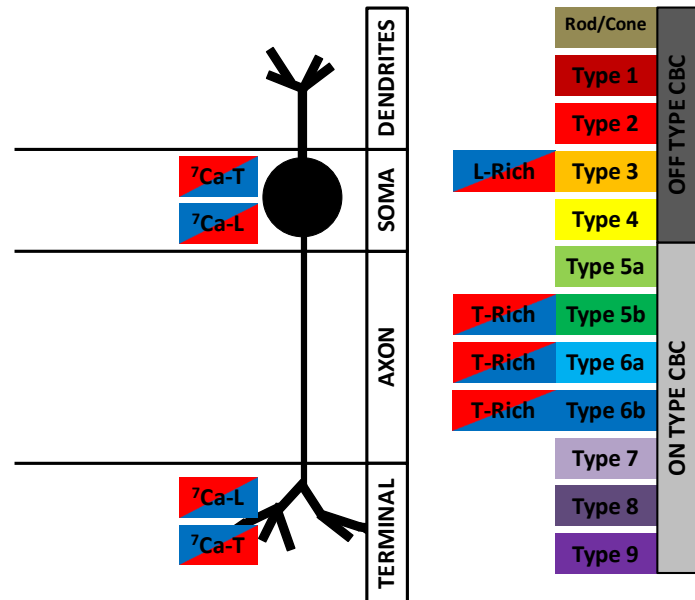
(A) I-V relationship, voltage was increased from -80 mV to +40 mV. (B) Blocking Na⁺ by TTX showed no significant effect. (C) Regenerative potentials recorded in current clamp configuration. (D) 10 μM Mibefradil (T-type Ca⁺⁺ channel blocker) blocked the regenerative potentials. From (Hu et al. 2009).

The question, of whether these T-rich and L-rich CBCs correspond to different functional bipolar cell types was not addressed in this study. However, strong T-type Ca⁺⁺ currents in type 5b, type 6a and type 6b CBCs had been found previously (Ivanova and Müller 2006), therefore CBCs types 5b, 6a and 6b CBCs appear to be T-rich type CBCs. All of these were ON-types. The authors (Ivanova and Müller 2006) did not encounter any L-type Ca⁺⁺ channels in dendrites and axon terminals of those cell types, but this may be caused by the fact that most cells had lost their axons during the dissociation procedure. Furthermore, very weak T-type Ca⁺⁺ currents were reported in type 3 CBCs, an OFF-type CBC. The type 3 CBC in Figure 3.16 also appears to produce L-type Ca⁺⁺ currents after the depolarization step. Thus, type 5b, 6a and 6b CBCs could be T-rich cells and type 3 CBCs could be L-rich. Based on this information it was not possible to make general conclusions for all ON-type and OFF-type CBCs in rat, since the ON-type CBC in the computational model developed in this thesis was

a T-rich cell and the OFF-type CBC was an L-rich cell. There is no evidence in other literature that would suggest the presence of L-type or T-type Ca^{++} channels in the dendrites of rat CBCs. Therefore, it will be assumed that T-rich cells have T-type Ca^{++} channels in their soma and a low density of L-type Ca^{++} channels at the axon terminals. Analogously, L-rich cells will be assumed to express L-type Ca^{++} channels at their soma and less prominent T-type Ca^{++} channels at their axon terminal (Figure 3.36).

Figure 3.27

Summarized visual representation of currents in cone bipolar cells of the rat suggested in ⁷(Hu et al. 2009). These Ca^{++} currents cannot be definitively attributed to specific CBC types, accordingly, they are assigned a unique color scheme to reflect this fact.



3.2.9 Literature Summary

3.2.9.1 Table of Identified Ion Channels

All ion channels discussed in section 3.2 are summarized in Table 3.1. Additional to the name of each specific ion channel and the study in which it was described in the rat retina, other information such as the cell type in which it was found is added, when this information was available. Other fields indicate whether the CBCs were an ON-type or OFF-type cells, which type of ions were mainly transported by the channel, in which cellular region (dendrites, soma, axon or axon terminal) the channels may be located and comments where appropriate.

Name	BP-Type	ON/OFF	Ion	Compartment	Comment	Reference
Na ⁺	ON CBC	ON	Na ⁺	Soma	more often if soma small	Pan and Hu, 2000
Na ⁺	OFF CBC	OFF	Na ⁺	Soma		Pan and Hu, 2000
Ca ⁺⁺	ON CBC	ON	Ca ⁺⁺	Soma	in Na ⁺ bearing CBC	Pan and Hu, 2000
Ca ⁺⁺	OFF CBC	OFF	Ca ⁺⁺	Soma	in Na ⁺ bearing CBC	Pan and Hu, 2000
KCa	ON CBC	ON	K ⁺	Soma	K(Ca) and Kv added	Hu and Pan 2002
Kv	ON CBC	ON	K ⁺	Soma	K(Ca) and Kv added	Hu and Pan 2002
KCa	OFF CBC	OFF	K ⁺	Soma	K(Ca) and Kv added	Hu and Pan 2002
Kv	OFF CBC	OFF	K ⁺	Soma	K(Ca) and Kv added	Hu and Pan 2002
HCN4	type 3	OFF	cation	Terminal		Müller et al., 2003
HCN1	type 5b	ON	cation	Terminal	contribute 80%	Müller et al., 2003
HCN4	type 5b	ON	cation	Terminal	contribute 20%	Müller et al., 2003
HCN2	type 8	ON	cation	Terminal	also RBC, maybe all CBC	Müller et al., 2003
HCN4	type 3	OFF	cation	Terminal	only OFF-type HCN	Ivanova and Müller, 2006
Ca-T	type 3	OFF	Ca ⁺⁺	Soma	very small current	Ivanova and Müller, 2006
Na	type 3	OFF	Na ⁺	Soma	not clear	Ivanova and Müller, 2006
HCN1	type 5b	ON	cation	Terminal	larger HCN	Ivanova and Müller, 2006
HCN4	type 5b	ON	cation	Terminal	smaller HCN	Ivanova and Müller, 2006
Ca-T	type 5b	ON	Ca ⁺⁺	Soma		Ivanova and Müller, 2006
HCN1	type 6a	ON	cation	Terminal		Ivanova and Müller, 2006
HCN4	type 6a	ON	cation	Terminal		Ivanova and Müller, 2006
Ca-T	type 6a	ON	Ca ⁺⁺	Soma	stronger	Ivanova and Müller, 2006
Ca-L	type 6a	ON	Ca ⁺⁺	Soma	small	Ivanova and Müller, 2006
CaCl	type 6a	ON	Cl ⁻	Soma	first report in mammals	Ivanova and Müller, 2006
HCN2	type 6b	ON	cation	Terminal	small, time-dependent	Ivanova and Müller, 2006
Ca-T	type 6b	ON	Ca ⁺⁺	Soma		Ivanova and Müller, 2006
Kir	type 6b	ON	K ⁺	Soma	large	Ivanova and Müller, 2006
HCN2	type 7	ON	cation	Terminal	see Ma et al. 2003	Ivanova and Müller, 2006
Ca-T	type 7	ON	Ca ⁺⁺	Soma	see Pan et al. 2000	Ivanova and Müller, 2006
Kir	type 7	ON	K ⁺	Soma	relatively large	Ivanova and Müller, 2006
HCN2	type 8	ON	cation	Terminal	larger than in type 9	Ivanova and Müller, 2006
HCN2	type 9	ON	cation	Terminal	smaller than in type 8	Ivanova and Müller, 2006
HCN1	rod/cone	OFF	cation	Dendrites	OFF-cell	Fyk-Kolodziej and Pourcho 2007
HCN2	type 3	OFF	cation	Dendrites		Fyk-Kolodziej and Pourcho 2007
HCN4	type 3	OFF	cation	Dendrites		Fyk-Kolodziej and Pourcho 2007
HCN4	type 3	OFF	cation	Axon	dominant in type 3 CBC	Fyk-Kolodziej and Pourcho 2007
HCN1	type 5b	ON	cation	Terminal	diffuse axon terminal	Fyk-Kolodziej and Pourcho 2007
HCN2	type 5b	ON	cation	Terminal	diffuse axon terminal	Fyk-Kolodziej and Pourcho 2007
HCN4	type 5b	ON	cation	Terminal	diffuse axon terminal	Fyk-Kolodziej and Pourcho 2007
HCN4	type 5a	ON	cation	Terminal	narrow axon terminal	Fyk-Kolodziej and Pourcho 2007
Na ⁺	type 6b	ON	Na ⁺	Terminal	mainly, spiking	Cui and Pan, 2008
Na ⁺	type 6b	ON	Na ⁺	Dendrites	possibly	Cui and Pan, 2008
Ca ⁺⁺	type 6b	ON	Ca ⁺⁺	Soma		Cui and Pan, 2008
HCN2	type 6b	ON	cation	Soma	I _h , t-dep, smaller	Cui and Pan, 2008
Kir	type 6b	ON	K ⁺	Soma	I _{Kir} , t-indep, larger	Cui and Pan, 2008
Ca ⁺⁺	type 5b	ON	Ca ⁺⁺	Soma	small	Cui and Pan, 2008
HCN1	type 5b	ON	cation	Soma	I _h , t-dep, larger	Cui and Pan, 2008
Kir	type 5b	ON	K ⁺	Soma	I _{Kir} , t-indep, smaller	Cui and Pan, 2008
Na ⁺	type 3	OFF	Na ⁺	Soma	some spiking	Cui and Pan, 2008
HCN4	type 3	OFF	cation	Soma	I _h , t-dep, larger than in 5b	Cui and Pan, 2008
Kir	type 3	OFF	K ⁺	Soma	I _{Kir} , t-indep	Cui and Pan, 2008
Ca-T	T-rich CBC	N.A.	Ca ⁺⁺	Soma	low threshold Ca ⁺⁺ spikes	Hu,Bi and Pan 2009
Ca-L	T-rich CBC	N.A.	Ca ⁺⁺	Dendrites		Hu,Bi and Pan 2009
Ca-L	T-rich CBC	N.A.	Ca ⁺⁺	Terminal		Hu,Bi and Pan 2009
Ca-L	L-rich CBC	N.A.	Ca ⁺⁺	Soma		Hu,Bi and Pan 2009
Ca-T	L-rich CBC	N.A.	Ca ⁺⁺	Dendrites		Hu,Bi and Pan 2009
Ca-T	L-rich CBC	N.A.	Ca ⁺⁺	Terminal		Hu,Bi and Pan 2009

Table 3.1 Summary of all ion channels found in the literature reviewed, ordered by appearance section 3.2.

3.2.9.2 Ion Channel Equipment of ON Cone Bipolar Cells

Figure 3.28 illustrates the combined findings on ON-CBCs from this section. Due to the methodological restrictions of whole-cell patch-clamp measurements, it was not always possible to clearly determine the subcellular location of certain channels. Additionally, in most of the studies no imaging data from immunostaining experiments was available to deduce ion channel locations. In these cases, considering that the micropipettes were measuring from the soma, it was assumed that the ion channels are located at the soma. Thus, the soma area in Figure 3.28 is the cellular region with the highest variability in terms of different ion channel types. The literature review revealed that the somatic membrane of ON-CBCs of the rat may contain T-type Ca^{++} , inward rectifying K^+ , Cl^- -dependent Ca^{++} , Ca^{++} -dependent K^+ , voltage-gated K^+ , HCN1 and HCN2 channels^{1,2,4,6,7}(Pan and Hu 2000, Hu and Pan 2002, Ivanova and Müller 2006, Cui and Pan 2008, Hu et al. 2009). The differential distribution (T-rich and L-rich) of T-type and L-type Ca^{++} channels is displayed as suggested by⁷(Hu et al. 2009) for ON- and OFF-CBCs. In⁶(Cui and Pan 2008) it was argued that ON-CBCs may have Na^+ channels in their dendrites and/or axon terminals. The only voltage-gated ion channels that were attributed to the axon of an ON-CBCs were HCN4 channels⁴(Ivanova and Müller 2006). It is likely, however, that some of the ion channels attributed to the soma in Figure 3.28 actually are located at least partly on the axon or axon hillock. Due to the morphological closeness of these areas however, this was difficult to determine.

Apart from possible Na^+ and L-type Ca^{++} channels, the axon terminal of all ON-CBCs were equipped with at least one type of HCN channel, in many cases HCN1, HCN2 and HCN4 could be attributed to this area^{3,4,5}(Müller et al. 2003, Ivanova and Müller 2006, Fyk-Kolodziej and Pourcho 2007). Hyperpolarization-activated currents were both electrophysiologically measured and localized using immunostaining methods in several studies. Most information was available for type 5b CBCs and type 6B CBCs, when compared to other ON-type CBCs.

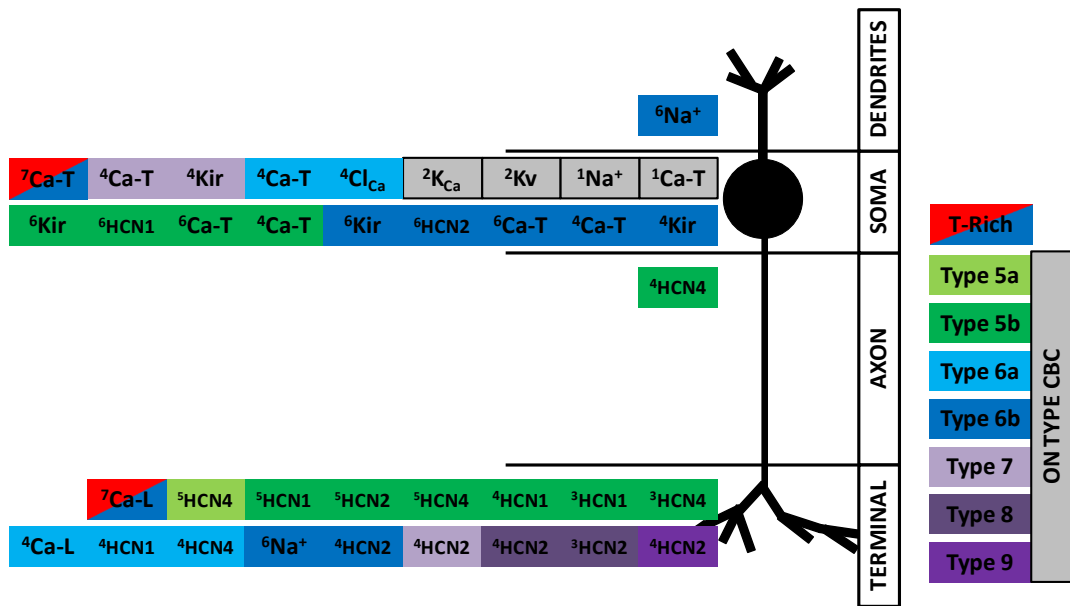


Figure 3.28

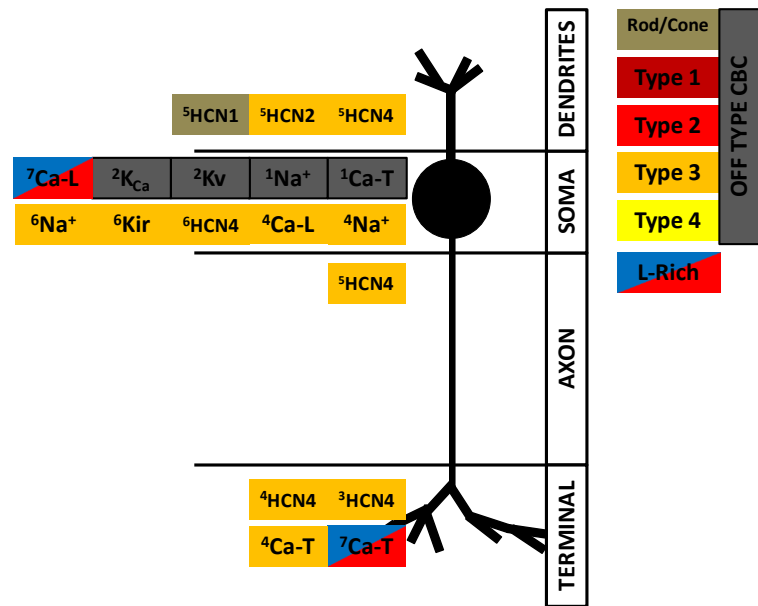
Voltage-dependent ion channels in rat ON-type CBC described in the reviewed literature.

3.2.9.3 Ion Channel Equipment of OFF Cone Bipolar Cells

The combined findings on the ion channel equipment of OFF-type CBCs are presented in Figure 3.29. The distribution of L-type Ca^{++} and T-type Ca^{++} channels in this figure is displayed in agreement with the conclusion made from section 3.2.8 that the modeled OFF-type CBC should be an L-rich cell. Immunostaining methods showed that the dendritic membrane of OFF-type CBCs contain HCN channels⁵(Fyk-Kolodziej and Pourcho 2007): HCN2 and HCN4 were found in type 3 CBCs, whereas bipolar cells with mixed rod/cone input (also considered OFF-type) displayed HCN1 channels. Ca^{++} -dependent K^+ and voltage-gated K^+ channels could not be clearly assigned to only ON- or OFF-type CBCs and may therefore be present in the soma of OFF-type CBCs²(Hu and Pan 2002) and ON-type CBCs. Furthermore, two studies found Na^+ , inward rectifying K^+ , HCN4 and T-type Ca^{++} channels in type 3 CBCs^{4,6}(Ivanova and Müller 2006, Cui and Pan 2008), which were attributed to the somatic region. The only voltage-gated ion channel type found in the axonal region of OFF-type CBCs was the HCN4 channel in type 3 CBCs⁵(Fyk-Kolodziej and Pourcho 2007). HCN4 channels were also the only channels described in the axon terminal of OFF-type CBC with immunocytochemical evidence, again shown only in type 3 CBCs^{3,4}(Müller et al. 2003, Ivanova and Müller 2006).

Figure 3.29

Voltage-dependent ion channels in rat OFF-type CBC described in the reviewed literature.



3.2.9.4 Differences in the Ion Channel Equipment of ON and OFF Cone Bipolar Cells

For OFF CBC types 1, 2 and 4 no specific information on ion channel equipment could be found in the literature. In contrast, at least one type of voltage-gated ion channels could be attributed to each ON-type CBC. In general, more information was available in the literature for ON-type CBCs. This discrepancy was not addressed in any of the reviewed studies. However, it may result from the smaller morphological size of OFF-type CBCs. This may make them less accessible during the experimental procedures of patch-clamp electrophysiology, where cells need to be targeted with high precision.

The differences between the ion channels in ON-type and OFF-type CBCs are compared in Figure 3.30. For each neuronal area, both ON and OFF-type are displayed with the ion channels unique to them. Ion channels found in a specific region of ON-type CBCs but not in the same region of OFF-type CBCs will be defined as ON-specific channels and, analogously, the opposite will be defined as OFF-specific channels.

In most studies that investigated voltage-gated Ca⁺⁺ currents (Ivanova and Müller 2006, Cui and Pan 2008) ON-type CBCs (types 5b,6a and 6b) were T-rich cells with prominent T-type currents in the soma and smaller L-type currents, probably in the axon terminal (Hu et al. 2009), while OFF CBCs type 3 were L-rich cells with stronger L-type currents in the soma and smaller T-type currents in the axon terminal.

In the dendritic region, at the outer plexiform layer of the retina, HCN1, HCN2 and HCN4 channels were OFF-specific. Evidence for the presence of voltage-gated Na⁺ channels in the dendrites was only available for ON-type CBCs. In the soma, however, Na⁺ channels have been shown only in OFF-type CBCs, the same applies to HCN3 channels. Somatic HCN1 and HCN2 channels, as well as L-type Ca⁺⁺ and Ca⁺⁺-activated Cl⁻ channels were ON-specific. The axons had no difference in this respect. Finally, while no HCN channels in the axon terminal were OFF-specific, several HCN channels in the axon terminal of ON-type CBCs were ON-specific. Additional to voltage-gated Na⁺ currents, this was the case for HCN1, HCN2 and HCN4.

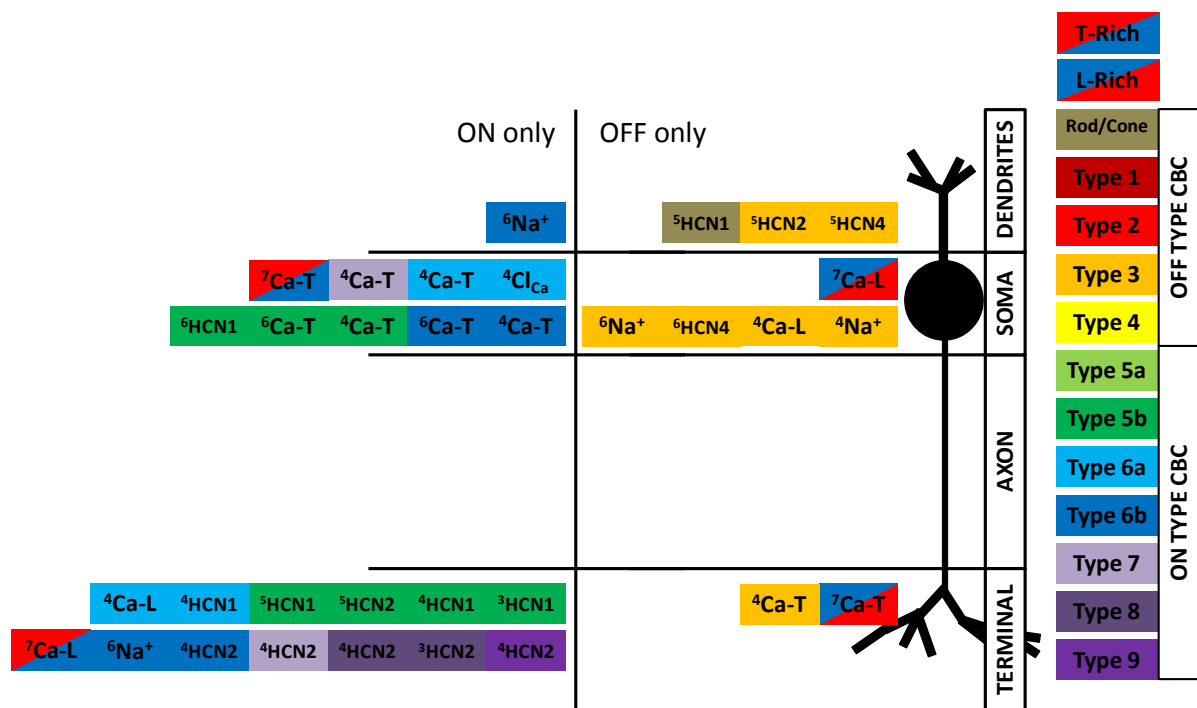


Figure 3.30

Differences in the ion channel equipment of ON-type and OFF-type CBC. Ion channels unique to ON-type CBC are shown in the left panel, channels described only in OFF-type CBC are shown in the right panel. The distribution of hyperpolarization-activated HCN channels is a main differentiator between ON and OFF CBC.

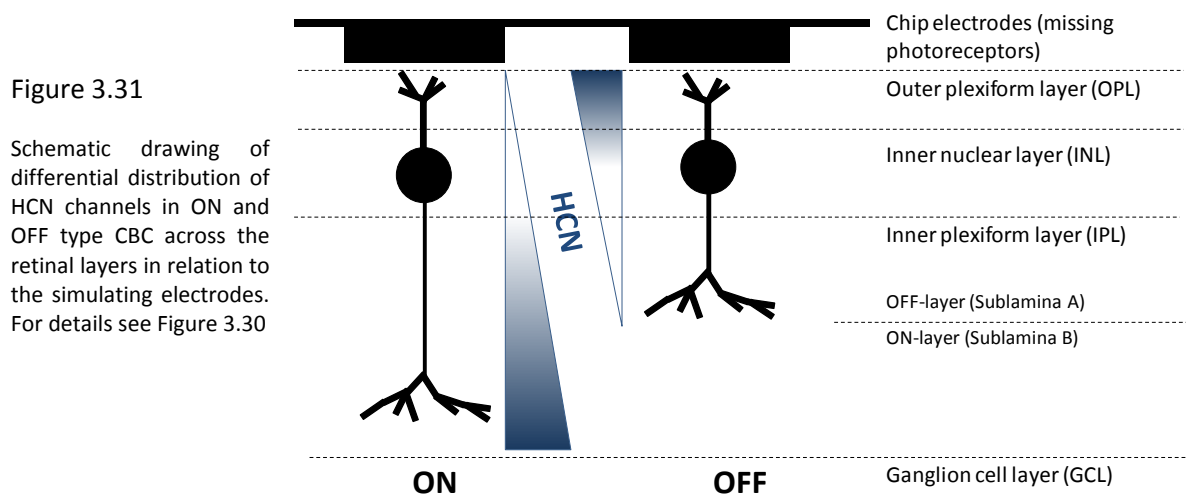
3.2.10 Conclusions for the Active Bipolar Cell Model

Taken together, the studies presented here show that a significant amount of information on the ion channel equipment of most CBC types in the rat is available. However, the picture remains incomplete because there was no study that aimed at finding all ion channels in all CBCs types.

Especially in earlier studies, the voltage-gated ion channels were not assigned to specific CBC types (Pan and Hu 2000, Hu and Pan 2002), but this was also the case in more recent investigations (Hu et al. 2009). Only one of the studies (Ivanova and Müller 2006) made an attempt at mapping ion channels in all CBC types and while this group could identify different ion channels in most CBC types,

the main focus of the study was on HCN channels. Thus, even this study could not reveal a complete picture for voltage-gated ion channels in CBCs of the rat.

As shown in Figure 3.30, the distribution of HCN channels in the different regions of ON-type CBCs differed significantly from OFF-type CBCs. While OFF-specific HCN channels were located in the dendrites or the soma, various ON-specific HCN channels were located mainly in the axon terminals. Figure 3.31 schematically depicts this differential distribution of ON- and OFF-specific HCN channels in relation to the different retinal layers and their distance from the stimulating electrodes of the subretinal implant. OFF-specific HCN channels were mostly located in the outer plexiform layer, close to the stimulating electrodes. On the other hand, ON-specific HCN channels were more prominent in sublamina B of the inner plexiform layer, close to the ganglion cell layer and therefore more distant to the stimulating electrodes.



This heterogeneous distribution of ON-specific and OFF-specific HCN channels, especially in respect to their distance from the stimulating electrodes, could potentially be a significant factor in achieving a differential or selective stimulation of ON-type and OFF-type bipolar cells with the subretinal implant in blind patients. HCN channels operate on a rather slow timescale (up to several 100 ms for most and more than 1000 ms for HCN4) when compared to the timescale of rectangular voltage pulses used with the Tübingen subretinal implant, which is on the order of a few milliseconds. However, in contrast to K^+ channels and Na^+ channels, which were also found to be ON-specific or OFF-specific (Figure 3.30), reliable information on the subcellular distribution of HCN channels was available from the literature reviewed in this section, since several studies used immunostaining methods to detect the localization of HCN channels (Müller et al. 2003, Ivanova and Müller 2006, Fyk-Kolodziej and Pourcho 2007, Cui and Pan 2008). Indeed, conservation of a channel type across different cell types suggests that it plays a crucial role in cell function.

A realistic model of ON-type CBCs and OFF-type CBCs, however, cannot include only ion channels which are ON-specific or OFF-specific, respectively. Several types of ion channels appeared in both neuronal classes and should not be left out, since they are likely to serve a physiological function in the according neurons even if the functional purposes of all ion channels have not yet been experimentally clarified.

It is the general objective of this modeling study to make statements about the electrical excitability of ON-type CBCs versus OFF-type CBCs. Ideally, a separate model should be developed for each type of CBC (1-9), and then correlations within the group of ON-type CBCs could be contrasted with correlations of all OFF-type CBCs. However, as mentioned previously, none of the reviewed studies performed a complete analysis of all ion channels in a given CBC type. Even merging the combination of all results presented in these studies does not guarantee that all functionally relevant ion channels are included in each CBC-type model. As already pointed out, for some CBC types (1, 2 and 4) no cell-type specific information is available. Therefore, creating a model for a single CBC type would be based on sparse information. An alternative and more feasible approach is the development of two models, one for a generic ON-type CBC and a second model for a generic OFF-type CBC. This approach allows the convergence of all information available on ON-type or OFF-type CBCs into one representative model for each class, which will be referred to as “ideal” ON-model and “ideal” OFF-model. These ideal ON and OFF models comprise nearly all information that is available for their respective class, ON or OFF. Allowing these models to include most common (see below for exclusions) and all unique (ON-specific / OFF-specific) ion channels found for CBCs is the best possible starting point for finding differences that apply to the excitability of ON-type or OFF-type CBCs in general.

The ion channel equipment shown in Figure 3.32 was used in the ideal ON-type CBC model of this thesis. Most channels summarized in Figure 3.28 were included. However, Na^+ channels were not assigned to the soma of ON-type CBC model, since there is evidence that they are located either in dendrites or axon terminals of ON-type CBCs, but not in the soma (Cui and Pan 2008). Ca^{++} -activated Cl^- channels were not included in the ideal ON model because no quantitative data for the amplitudes of this current in rat CBCs is available. As elaborated in section 3.2.8, ON-type CBCs in the reviewed literature appear to be T-rich cells. Thus, the ideal ON model was created with stronger somatic T-type Ca^{++} currents and weaker L-type Ca^{++} currents in the axon terminal region.

Therefore, the following currents were calculated for the ideal ON-cell: I_{Na} , $I_{\text{Ca,T}}$, I_{Kir} , I_{HCN1} , I_{HCN2} , $I_{\text{K(Ca)}}$, I_{Kv} , I_{HCN4} , $I_{\text{Ca,L}}$ and a leak current I_{L} . The nature of each of these currents will be specified in detail later in the exact model description in section 3.3.

Figure 3.32

Ion channel equipment used for the ideal ON-type CBC in the computational model. Somatic Na^+ channels and Ca^{++} -activated Cl^- channels and were left out. (For details see text)

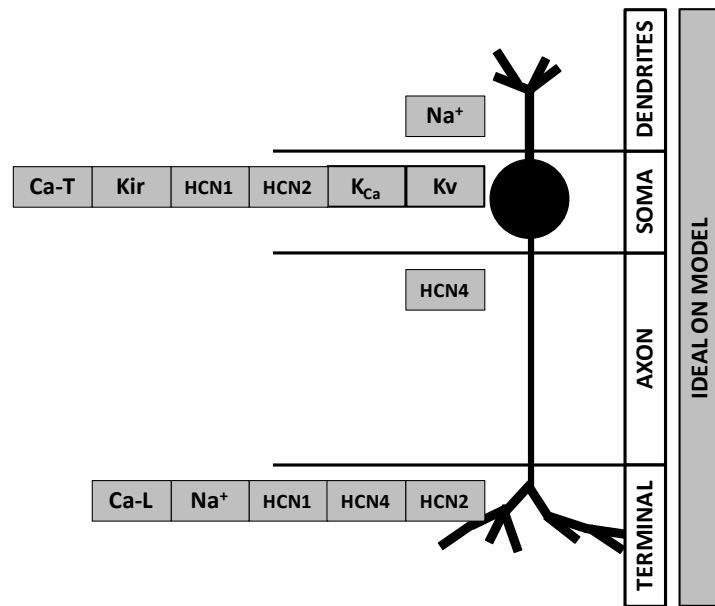
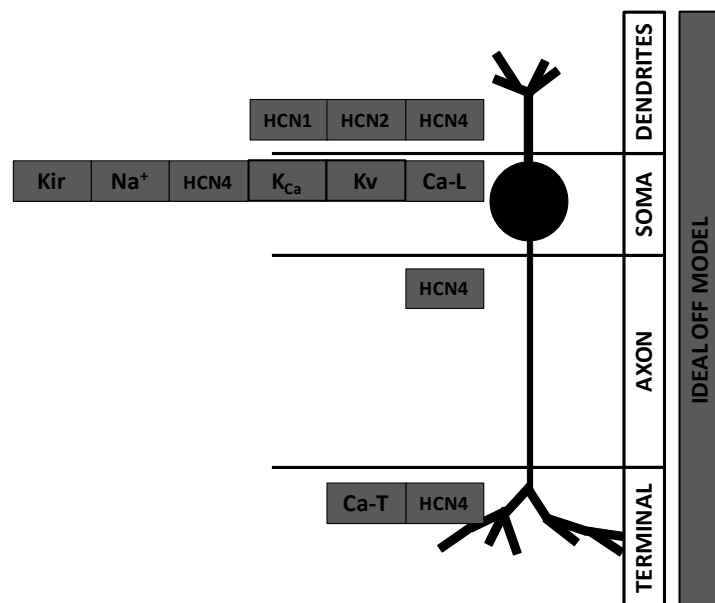


Figure 3.33 shows the ion channels that were assigned to the model of an ideal OFF-type CBC which was based on the channel equipment shown in Figure 3.29. As suggested in section 3.2.9.3, the ideal OFF-CBC model was realized as an L-rich cell (Hu et al. 2009) with larger L-type currents in the somatic region and smaller T-type currents in the axon terminal. The model also contained all different HCN channels shown in Figure 3.29 which constituted a significant difference to the distribution of HCN channels in the ideal ON model.

Figure 3.33

Ion channel equipment used for the ideal OFF-type CBC in the computational model.



3.3 Ion Channel Modeling

This section describes the computational modeling of all ionic currents which have been found in rat CBCs as presented in section 3.2. The biophysical reproduction of current flow through voltage-gated ion channels can be implemented with “active” ion channel models based on differential equations governing the conductance of ion flow and the resulting current through these channels.

Different numerical methods are available to solve this problem. The first who presented a formalism that was able to reproduce neuronal membrane excitability were Alan Lloyd Hodgkin and Andrew Fielding Huxley in their groundbreaking publication from 1952 (Hodgkin and Huxley 1952). The Hodgkin-Huxley (HH) model will be explained in more detail below. Other approaches to the modeling of neuronal excitation are thermodynamic models or Markov models. While Hodgkin and Huxley determined the rate constants of ion flow through the channels by fitting appropriate functions to experimental data, thermodynamic models deduce functions describing the voltage dependence of current flow using known thermodynamic principles (Tsien and Noble 1969, Hill and Chen 1972). Another method for the numerical formulation of membrane biophysics during excitation uses Markov models. Hodgkin and Huxley based their work on the assumption that Na⁺ channel activation and inactivation were statistically independent processes. However, several more recent studies have shown that in fact activation and inactivation of Na⁺ channels are coupled processes (Armstrong 1981, Aldrich et al. 1983). Markov models allow the formulation of possibly dependent statistical processes using different states which can depend on each other, but do not have to. A more detailed comparison of HH-like models, thermodynamic models and Markov models for neural excitation can be found in the literature (Destexhe and Huguenard 2001).

In this study, all models of current flow through voltage-gated ion channels were based on the formalism developed by Hodgkin and Huxley. Even though the HH model may have certain limitations, it is the most widely used approach. Many research groups formalize their experimental data by fitting it to equations based on or similar to the differential equations described by Hodgkin and Huxley. Also, several databases in the internet collecting various ion channel models mostly provide parameters for HH-like equations.

In the next section the original HH model will be explained, followed by a detailed description of the models used for ion channels in rat retinal bipolar cells and how they differ from the original HH model.

3.3.1 Hodgkin Huxley Model

In order to examine the generation of an action potential, Hodgkin and Huxley (Hodgkin and Huxley 1952) conducted a series of experiments in the giant axon of the squid. The diameter of this axon (1mm) allowed rather exact electrophysiological investigations with the methods available in 1952. Based on the data collected in these experiments a biophysical model was developed describing the nonlinear behavior of conductance changes, current flow and resulting voltage changes during neuronal excitation. For their developments, Hodgkin and Huxley were awarded the Nobel Prize for Physiology or Medicine in 1963. The neuronal cell membrane is a phospholipid bilayer and in addition to many other molecules several different voltage-gated ion channels are embedded in it. Like other ion channels, voltage-gated ion channels are transmembrane proteins that span the entire membrane and create a connection between the extracellular and intracellular space. They can be selectively permeable to ions with a certain charge (positive or negative) or e.g. to Na^+ ions mainly. However, voltage-gated ion channels do not allow ions to pass through continuously. Instead, they are equipped with a gating mechanism that can close the channel. The state of this gating mechanism, from fully open to fully closed, is controlled by the transmembrane voltage gradient. The ion flow through voltage-gated channels is therefore limited by the speed at which an ion can pass the channel, the state of the channel and by the density of voltage-gated ion channels in the neuronal membrane. These limitations constitute a resistance; therefore this ion flow is an Ohmic current. Each type of voltage-dependent ion channels can have different preferences in respect to the transmembrane potential. In some channels the gating mechanisms open at lower voltages, others at higher voltages (activation threshold). Certain channels open the gates upon depolarization of the membrane, others after membrane hyperpolarization. Additional to current through voltage-gated ion channels the membrane also acts as a capacitor which can load up with charge and then discharge with a temporal delay. Thus, the membrane currents can be divided into a capacitive component and an Ohmic component through voltage-gated ion channels.

$$i = C_m \frac{dV}{dt} + i_{ion} \quad (3.1)$$

where i is the total membrane current density ($\mu\text{A}/\text{cm}^2$, by convention inward current is considered positive), C_m is the membrane capacitance ($\mu\text{F}/\text{cm}^2$), V is the displacement from the resting membrane potential (mV), t is the time and i_{ion} is the current density for all ionic currents ($\mu\text{A}/\text{cm}^2$). The original model accounted for two different specific ionic currents, sodium (i_{Na}) and potassium (i_{K}). All other ionic currents including chloride currents, currents through voltage independent channels and through less selective channels were lumped into one variable called leak current (i_{L}). Based on their observations, Hodgkin and Huxley assumed that sodium channels contain three

activation gates and one inactivation gate, represented by the stochastic gating variables m and h , respectively ($0 \leq m \leq 1$, $0 \leq h \leq 1$). A sodium channel would be fully open to ions if $m^3h = 1$. For the model of potassium channels, a mechanism containing four gates of only one type (activating) was sufficient for, represented by the stochastic gating variable n . The potassium channel, then, is open if $n^4 = 1$ ($0 \leq n \leq 1$). The gating variables denote the opening probability of the respective gate in an ion channel.

The sum of all ionic current densities i_{ion} in the squid axon was therefore described by:

$$i_{ion} = i_{Na} + i_K + i_L \quad (3.2)$$

At any given time point, the ionic current flowing through a voltage-gated ion channel in the neuronal membrane is dependent on the difference between transmembrane voltage ($V_m = V_i - V_e$) and the equilibrium potential of the ion (E_{ion}), the conductance of the membrane for the ion (g_{ion} , given in mS/cm²), and on the actual state of those channels, open or closed (gating variables m , n , h). The transmembrane voltage can be measured using metal electrodes inside and outside the cell. If the ion concentrations inside and outside of the cell are known as well as the temperature, the equilibrium potential E_{ion} (mV) of a specific ion can be calculated using the Nernst equation:

$$E_{ion} = 1000 \frac{RT}{zF} \ln \frac{[ion]_i}{[ion]_o} \quad (3.3)$$

where R is the ideal gas constant (joules per Kelvin per mole), T is the temperature (°K), z is the charge of the ion (+1 for Na⁺), F is the Faraday constant (coulombs per mole), and $[ion]_i$ and $[ion]_o$ are intracellular and extracellular molar concentrations of the ion (mole), respectively. Multiplication by a factor of 1000 yields E_{ion} in mV, which are convenient for most electrophysiological data.

Thus, in the HH model the three different ionic currents were obtained by the equations:

$$i_{Na} = g_{Na}(V_m - E_{Na}) \quad (3.4)$$

$$i_K = g_K(V_m - E_K) \quad (3.5)$$

$$i_L = g_L(V_m - E_L) \quad (3.6)$$

By subtracting the resting membrane potential V_r at which all neuronal currents are in a steady state from V_m Hodgkin and Huxley introduced the reduced voltage $V = V_m - V_r$, where V_r was assumed to -70 mV in the squid axon. This simplifies the calculations in the model and yields:

$$V_{Na} = E_{Na} - V_r \quad (3.7)$$

$$V_K = E_K - V_r \quad (3.8)$$

$$V_L = E_L - V_r \quad (3.9)$$

furthermore, $i_{Na} = g_{Na}(V - V_{Na}) \quad (3.10)$

$$i_K = g_K(V - V_K) \quad (3.11)$$

$$i_L = g_L(V - V_L) \quad (3.12)$$

The reduced membrane voltage allows the model equations to be initialized with the boundary condition of $V(t) = 0$ for $t = 0$. Additionally, the voltages are then measured as displacements from the resting transmembrane potential at steady state.

The ionic conductance g_{ion} can be expressed in the form of conductance/cm² based on the assumption that the combined effects of all single voltage-gated ion channels in the cell membrane are handled as a continuous conductance for an entire neuronal compartment. A higher ion channel density leads to a greater value of conductance for a given ion.

If the extracellular or intracellular potential is changed during stimulation, the conductance g_{ion} of voltage-gated ion channels can also change in a time-dependent manner. The changes in g_{ion} result from changes of the current state (open/closed) of activation and/or inactivation gates which are present in these channels.

Specifically, the conductance for sodium and potassium during excitation in the HH model was described by

$$g_{Na} = \bar{g}_{Na}m^3h \quad (3.13)$$

$$g_K = \bar{g}_Kn^4 \quad (3.14)$$

where \bar{g}_{ion} is a constant describing the maximal ion conductance per unit area given in mS/cm². The conductance of the leak current g_L is assumed to remain constant throughout the process of excitation.

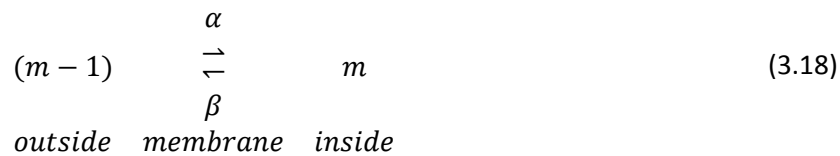
The gating variables m , h and n solve the first order kinetic equations:

$$\frac{dm}{dt} = \alpha_m(1 - m) - \beta_m m \quad (3.15)$$

$$\frac{dh}{dt} = \alpha_h(1 - h) - \beta_h h \quad (3.16)$$

$$\frac{dn}{dt} = \alpha_n(1 - n) - \beta_n n. \quad (3.17)$$

These ordinary differential equations contain the ion transfer rates α (outside to inside) and β (inside to outside, see also Figure 3.18), which are functions of the reduced voltage V and are given in $\frac{1}{ms}$. Equations 3.15 – 3.17 can be multiplied with a factor k in order to adjust for the difference in temperature, since Hodgkin and Huxley conducted their experiments in a solution at 6.3°C which has an effect on the temporal dependency of ion flow ($k = 3^{0.1(T-6.3)}$, where T is the target temperature in °C). The following will be explained only for the stochastic variable m , but is equally valid for the other stochastic variables h and n . The kinetic basis of this set of equations can be explained by assuming that m represents the fraction of a given ion species (e.g. K^+) at the intracellular side of the membrane and $(1 - m)$ denotes the fraction of ions at the extracellular side of the membrane. In this case, α is the transfer rate of ions from outside to inside, and β is the transfer rate of ions from inside to outside as shown in the kinetic equation 3.18.



During the resting state, at which $V = 0$, as pointed out above m represents the portion of ions that can flow from the intracellular cytoplasm to the extracellular space, thus it can be written as

$$m_{rest} = \frac{\alpha_{m_{rest}}}{\alpha_{m_{rest}} + \beta_{m_{rest}}} \quad (3.19)$$

A sudden change of V requires α_m and β_m to adapt to this change instantaneously. The following boundary conditions apply for time t :

$$m = m_{\infty} - (m_{\infty} - m_{rest})e^{-\frac{t}{\tau_m}} \quad (3.20)$$

$$\text{with } m_{\infty} = \frac{\alpha_m}{\alpha_m + \beta_m} \text{ and } \tau_m = \frac{1}{\alpha_m + \beta_m} \text{ ms}$$

where m_∞ is the value that can ultimately be achieved by m and τ_m is the time constant for m . Using this formalism α_m , β_m and the transfer rates for the other gates (h , n) can be determined by fitting appropriate functions to the conductance data and inactivation data obtained from electrophysiological experiments. Hodgkin and Huxley chose Boltzmann equations for this purpose, since these describe the behavior of particles not in a thermodynamic equilibrium. They obtained:

$$\alpha_m = \frac{0.1(V+25)}{e^{\left(\frac{V+25}{10}\right)+1}} \quad \beta_m = 4e^{\left(\frac{V}{18}\right)} \quad (3.21)$$

$$\alpha_h = \frac{0.01(V+10)}{e^{\left(\frac{V+10}{10}\right)-1}} \quad \beta_h = 0.125e^{\left(\frac{V}{80}\right)} \quad (3.22)$$

$$\alpha_n = 0.07e^{\left(\frac{V}{20}\right)} \quad \beta_n = \frac{1}{e^{\left(\frac{V+30}{10}\right)+1}} \quad (3.23)$$

The following parameters complete the HH model:

$$\bar{g}_{Na} = 120 \frac{mS}{cm^2}, \quad \bar{g}_K = 36 \frac{mS}{cm^2}, \quad g_L = 0.3 \frac{mS}{cm^2},$$

$$V_{Na} = -115 mV, \quad V_K = 12 mV, \quad V_L = 0.3 mV$$

$$C_m = 1 \frac{\mu F}{cm^2}.$$

The models used in this thesis for the simulation of voltage-gated ion channels were based on the formalism introduced by Hodgkin and Huxley. The models employed stochastic gating variables and voltage-dependent transfer rates. The transfer rates and conductances used in the models described below, however, have been fitted to data from electrophysiological recordings of rat retinal cone bipolar cells. If experimental data for the activation (conductance data) and inactivation for a specific ion channel species was available, an algorithmic fitting procedure was used to determine the required parameters for the recreation of current measurements. However, in most cases sufficient data from rat CBCs was not available. In these cases, published models were adapted to recreate the qualitative behavior of ion channels in rat CBCs. The adaptation of model parameters was done on a subjective basis and compared with experimental data in an iterative process until the currents generated by all modeled ion channels sufficiently reproduced the behavior of experimentally measures currents in rat CBCs. In this way, while the chosen parameters may not be precisely correct, they can reasonably be expected to regulate model behavior within acceptable limits since they accurately reproduce the available empirical data.

3.3.2 Sodium Channels - I_{Na}

As shown in Figure 3.32 of section 3.2.10, the ideal ON-type CBC contains voltage-gated Na^+ channels in dendritic and axon terminal membranes (Cui and Pan 2008). In a previous study the same group (Pan and Hu 2000) conducted a series of voltage-step experiments with the primary goal of isolating Na^+ currents (Figure 3.34 A) and produced the I-V relationship shown in Figure 3.34 B. The very short time to peak is a characteristic of Na^+ current (Figure 3.34 A). Usually the inward current peaks only a few milliseconds after onset, followed by a slightly slower decrease of the current. The data for Na^+ conductance (activation) and inactivation (Figure 3.3 C, upper panel) is the target for the fitting of ion channel transfer rates (α, β). The following equations and parameters were found to be able to sufficiently reproduce the behavior of voltage-gated Na^+ channels in rat CBCs:

$$g_{Na} = \bar{g}_{Na} m^3 h \quad (3.24)$$

$$\alpha_m = 0.271 e^{\left(\frac{V}{30.075}\right)} \quad \beta_m = \frac{10}{e^{\left(\frac{V+25.2619}{10.1191}\right)} + 1} \quad (3.25)$$

$$\alpha_h = 0.3898 e^{\left(\frac{1.6482-V}{12.2978}\right)} \quad \beta_h = \frac{0.6624}{e^{\left(\frac{-44.9996-V}{40}\right)} + 1} \quad (3.26)$$

$$\text{For ON-type CBC:} \quad E_{Na} = 57.016 \text{ mV}, \quad \bar{g}_{Na} = 2.22858 \frac{\text{mS}}{\text{cm}^2}$$

$$\text{For OFF-type CBC:} \quad E_{Na} = 57.016 \text{ mV}, \quad \bar{g}_{Na} = 5.2749 \frac{\text{mS}}{\text{cm}^2}$$

Using these equations together with the ordinary differential equations 3.15 and 3.16, it is possible to recreate the electrophysiological *in-vitro* experiments of Pan and Hu *in-silico*. The value for E_{Na} was based on a concentration gradient that yielded values reasonable close to the HH mode, and other literature while it also facilitated the recreation of data from Pan and Hu. Since the reviewed literature presented no evidence for different amplitudes of Na^+ currents in ON- and OFF-type CBC, the goal was to create currents with similar amplitudes for both ON and OFF. Two different values for \bar{g}_{Na} were required to reach this goal, because the models were based on different morphologies. Figure 3.34 C shows the results of the simulated voltage-step experiments in comparison to the original data (Figure 3.34 A). The cell is first fixed at a holding potential of -80 mV, then test pulses from -60 mV to 20 mV in steps of 10 mV are applied. Plotting the peak current of each of the applied testing voltages against the appropriate voltage yields the I-V plot of this experiment (Figure 3.34 B). Below (Figure 3.34 D) the I-V plot of the *in-silico* experiments is shown. The close agreement of the two current time-courses and the two I-V curves is taken as justification for further use of the chosen gating parameters.

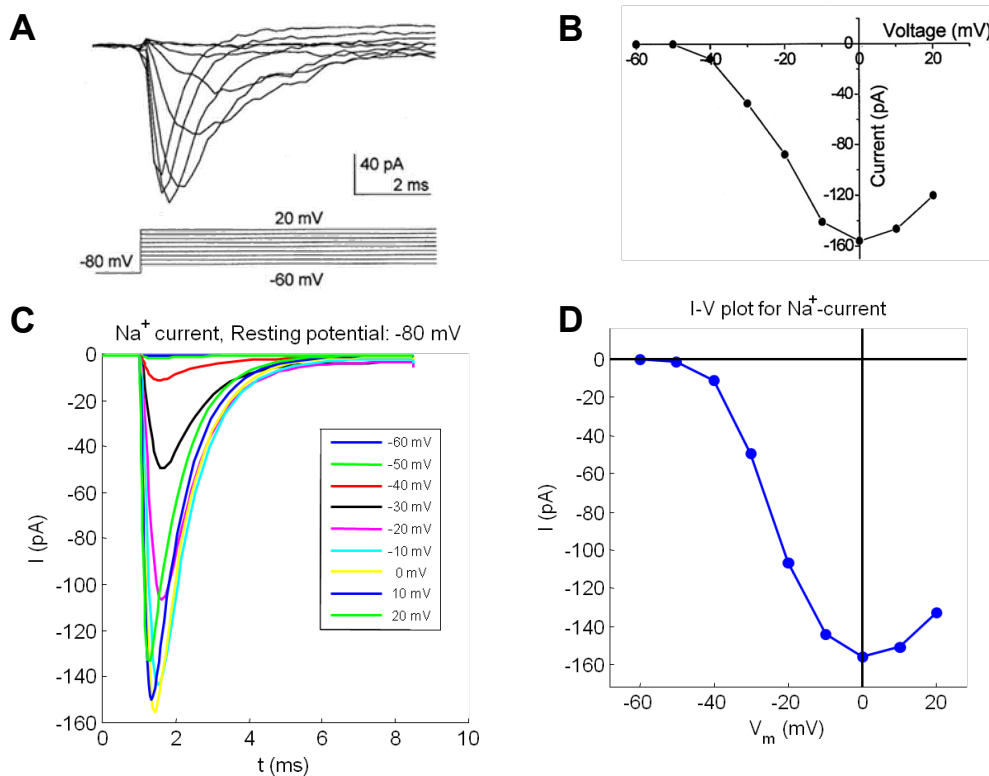


Figure 3.34

Comparison of whole-cell Na⁺ current traces from voltage step experiments (A) and the resulting I-V curve for the peak current (B) (Figures from (Pan and Hu 2000)) with simulated voltage-step experiments for the ideal ON-type CBC model (C) and the resulting I-V curve (D) for peak current. The membrane was held at -80 mV, then depolarizing pulses from -60 mV to +20 mV were applied for 8 ms. The abscissae for A,C and B,D have identical scaling.

3.3.3 Potassium Channels - I_{KV}

As pointed out in section 3.2.10, both the ideal ON-type CBC and the ideal OFF-type CBC modeled here were equipped with voltage-gated K⁺ channels (K_v, see Figure 3.32 and Figure 3.33). Two other types of K⁺ channels, the inward rectifying K⁺ channel (K_{ir}) and Ca⁺⁺-activated K⁺ channels (K_{Ca}), will be addressed in a later section. K_{ir} will be grouped with other hyperpolarization-activated currents (section 3.3.4) because most hyperpolarization experiments include traces of K_{ir} currents. K_{Ca} currents will be grouped with Ca⁺⁺ currents, since they depend on the intracellular Ca⁺⁺ concentration which will be explained in more detail in section 3.3.5.

In contrast to K⁺ currents described by Hodgkin and Huxley in the squid axon (categorized as transient outward K⁺ current), the K⁺ currents measured in rat CBCs are A-Type K⁺ currents, also called inactivating K⁺ currents or transient outward K⁺ currents. These inactivating K⁺ currents have a considerably slower timescale than Na⁺ currents in CBCs, but their amplitude is larger. Inactivating K⁺ currents had been previously described in retinal bipolar cells (Kaneko and Tachibana 1985).

Qualitatively, the K^+ currents measured in rat CBCs (Hu and Pan 2002) (see also Figure 3.35 A) closely resemble the inactivating K^+ currents measured in auditory neurons by (Desai et al. 2008), who also created a model describing the K^+ currents through inactivating K^+ channels (Kv3.3 channel). This model was adapted here to be used with rat CBCs.

$$g_K = \bar{g}_K m^2 h$$

$$m_\infty = \frac{1}{1 + e^{\left(\frac{V-50}{-12.3}\right)}} \quad \tau_m = 2.0304 + \frac{27.913114}{1 + e^{\left(\frac{V-27.4141}{55.704638}\right)}} \text{ ms} \quad (3.27)$$

$$h_\infty = 0.05 + \frac{0.95}{1 + e^{\left(\frac{V-23.2939}{19.385636}\right)}} \quad \tau_h = 199.78 + 2776.11 e^{\left(\frac{-V-5}{55}\right)} \text{ ms} \quad (3.28)$$

$$\text{with } \frac{dm}{dt} = \frac{m_\infty - m}{\tau_m} \quad \frac{dh}{dt} = \frac{h_\infty - h}{\tau_h} \quad (3.29)$$

$$\text{For ON-type CBC: } E_K = -58 \text{ mV}, \bar{g}_K = 14.3357 \frac{\text{mS}}{\text{cm}^2}$$

$$\text{For OFF-type CBC: } E_K = -58 \text{ mV}, \bar{g}_K = 23.8928 \frac{\text{mS}}{\text{cm}^2}$$

The resulting current traces from inactivating K^+ channels by simulated voltage-step experiments are shown in Figure 3.35 C (compare to electrophysiological data shown in Figure 3.35 A). A series of testing pulses ranging from -50 mV to +30 mV in steps of 10 mV was applied after holding the membrane potential at a value of -60 mV. The I-V curve of peak currents and currents at the end of stimulation are shown in Figure 3.35 B for the electrophysiological experiments and in Figure 3.35 D for the simulations.

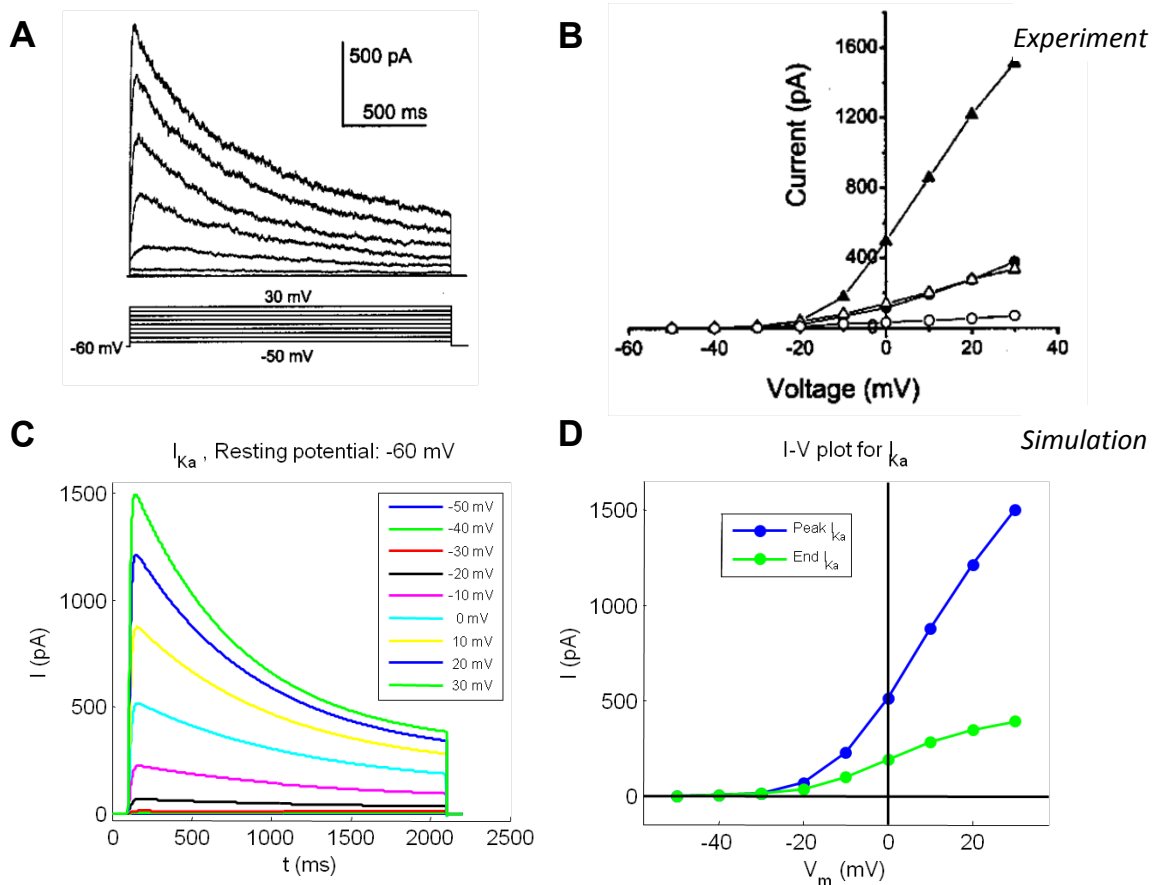


Figure 3.35

Comparison of inactivating K^+ whole-cell current traces (A-type) from voltage step experiments (A) and the resulting I-V curve (B) at the peak of the current trace (filled triangles) and at the end of stimulation (empty triangles) (Figures from (Hu and Pan 2002)) with simulated voltage-step experiments for the ideal ON-type CBC model (C) and the resulting I-V curve (D) at the peak of the current trace (blue line) and at the end of stimulation (green line). The membrane was held at -60 mV, then depolarizing pulses from -50 mV to $+30$ mV in steps of 10 mV were applied for 2000 ms. The abscissae for A,C and B,D have identical scaling.

3.3.4 Hyperpolarization-Activated Channels – I_{HCN1} , I_{HCN2} , I_{HCN4} , I_{Kir}

As elaborated in section 3.2.10 ON-type CBCs and OFF-type CBCs have significantly different complements of hyperpolarization-activated cyclic nucleotide-gated (HCN) channels (also compare Figure 3.32 and Figure 3.33). Additionally, the hyperpolarization-activated inward-rectifying K^+ (Kir) channel has been found in both ON and OFF CBCs of the rat.

HCN channels differ in their temporal properties, but in general have rather slow kinetics compared to most other voltage-gated ion channels. Their time-to-peak can be up to several seconds (Ivanova and Müller 2006). HCN channels create an inward current of positively charged anions after hyperpolarization. It is therefore assumed that one of their main functions is to bring the membrane back to its resting potential.

Moosmang (Moosmang et al. 2001) measured HCN currents in cardiac neurons and fitted Boltzmann equations to their electrophysiological data to create an HCN channel model. The parameters of this model were adapted to reproduce the current traces of HCN 1, 2 and 4 channels in rat CBCs.

3.3.4.1 Inward Rectifying K^+

In the literature reviewed in section 3.2 most experiments with hyperpolarizing voltage pulses elicited instantaneously activated Kir currents simultaneously with HCN currents (Ivanova and Müller 2006, Cui and Pan 2008). Cui et al. separated their analysis of hyperpolarization-activated currents into putative instantaneous Kir currents (called $I_{t\text{-indep}}$ by the authors) as well as putative time-dependent HCN currents (called $I_{t\text{-dep}}$) and created accompanying I-V plots (Figure 3.36 B and Figure 3.38 E).

Kir currents in rat bipolar cells have been found to be non-inactivating (Ma et al. 2003), therefore a Hodgkin-Huxley like model adapted from (Simoes de Souza and De Schutter 2011) with an activating component and no inactivating component was fitted to the electrophysiological data from type 5b (ON) and type 3 CBCs (OFF) in the rat (Cui and Pan 2008), see Figure 3.36 B,D.

$$g_{Kir} = \bar{g}_{Kir} m \quad (3.30)$$

$$\alpha_m = 0.13289 e^{\left(\frac{V-8.94}{-6.3902}\right)} \quad \beta_m = 0.16994 e^{\left(\frac{V-48.94}{27.714}\right)} \quad (3.31)$$

$$\text{For ON-type CBC:} \quad E_{Kir} = E_K, \quad \bar{g}_{Kir} = 0.175 \frac{mS}{cm^2}$$

$$\text{For OFF-type CBC:} \quad E_{Kir} = E_K, \quad \bar{g}_{Kir} = 0.33 \frac{mS}{cm^2}$$

3.3.4.2 HCN1

HCN1 currents in rat have been described in several different CBC types, see Figure 3.28 and Figure 3.29. Cui et al. conducted a detailed analysis of the I-V relationship in type 5b CBCs during hyperpolarization and divided the current traces into contributions from time-independent and time-dependent currents, which most likely arise from Kir and HCN channels, respectively. Moreover, the HCN currents in type 5b CBCs closely resemble typical HCN1 current traces (Ivanova and Müller 2006). Therefore, these measurements were the basis for fitting the amplitude of the HCN1 current in the model (Figure 3.36). Ivanova et al. (Ivanova and Müller 2006), however, gathered HCN current traces from type 5b CBCs which had faster kinetics and saturated in shorter periods of time, more in agreement with the typical HCN1 channel kinetics, but they did not create I-V plots for this current.

Therefore, the temporal aspects of the HCN1 channel model were fitted to the recordings from Ivanova et al. All HCN channel models (HCN1, HCN2 and HCN4) used in the present thesis were based on a previously developed model for HCN channels of cardiac pacemaker and retinal cells from mice (Moosmang et al. 2001) and adapted to the rat CBC data. Identical equilibrium potentials were used for all HCN channels, since HCN channels are cation selective.

$$g_{HCN1} = \bar{g}_{HCN1} m$$

$$m_{\infty} = \frac{1}{1 + e^{\left(\frac{V-39}{6.6}\right)}} - 0.0027 \quad \tau_m = 60 \text{ ms} \quad (3.32)$$

$$\text{with } \frac{dm}{dt} = \frac{m_{\infty} - m}{\tau_m} \quad (3.33)$$

$$\text{For ON-type CBC: } E_{HCN1} = -45 \text{ mV}, \bar{g}_{HCN1} = 0.1128 \frac{\text{mS}}{\text{cm}^2}$$

$$\text{For OFF-type CBC: } E_{HCN1} = -45 \text{ mV}, \bar{g}_{HCN1} = 0.068 \frac{\text{mS}}{\text{cm}^2}$$

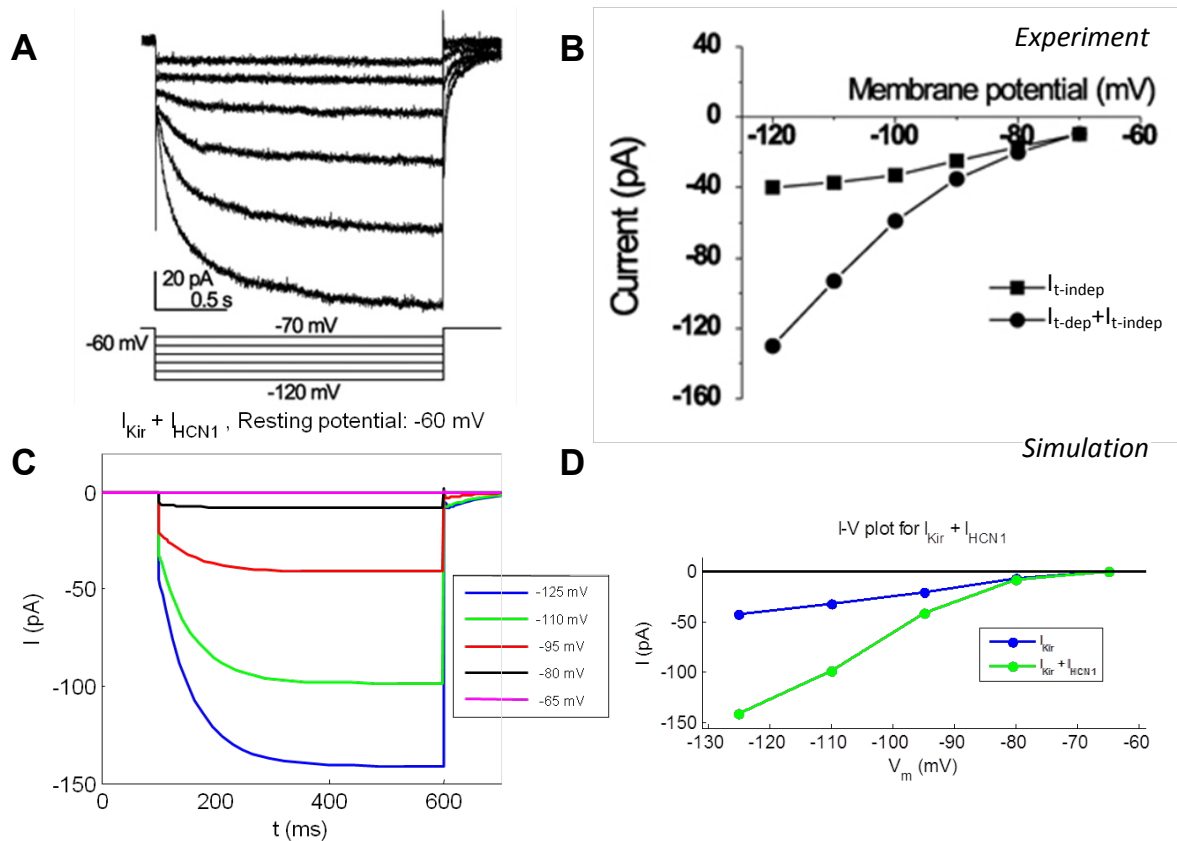


Figure 3.36

Comparison of experimental and modeled whole-cell hyperpolarization-activated currents. Voltage step experiments (cell held at -60 mV, then pulses from -70 mV to -120 mV were applied in steps of 10 mV) in type 5b CBC (A) with the resulting I-V curve (B) for the I_{Kir} component only (squares) and both $I_{Kir} + I_{HCN1}$ component (circles). Figures adapted from (Cui and Pan 2008). Current traces (C) of hyperpolarization-activated (HCN1 and I_{Kir}) currents during voltage step simulations and the corresponding I-V curve (D) with breakdown into contributions of HCN1 and I_{Kir} currents. The abscissae for B and D have identical scaling.

3.3.4.3 HCN2

According to the literature reviewed in section 3.2 the HCN2 channel appears to be the only hyperpolarization-activated ion channel in type 8 CBCs (Ivanova and Müller 2006). The current traces evoked by hyperpolarizing voltage steps elicited no apparent instantaneous currents and the time-course agreed with that of typical HCN2 channels. Therefore, the HCN2 model used here has been fitted to match data from type 8 CBCs.

$$g_{HCN2} = \bar{g}_{HCN2} m$$

$$m_{\infty} = \frac{1}{1 + e^{\left(\frac{V+42}{6.2}\right)}} \quad \tau_m = 120 \text{ ms} \quad (3.34)$$

$$\text{with } \frac{dm}{dt} = \frac{m_{\infty} - m}{\tau_m} \quad (3.35)$$

$$\text{For ON-type CBC: } E_{HCN2} = -45 \text{ mV}, \bar{g}_{HCN2} = 0.1 \frac{\text{mS}}{\text{cm}^2}$$

$$\text{For OFF-type CBC: } E_{HCN2} = -45 \text{ mV}, \bar{g}_{HCN2} = 0.2531 \frac{\text{mS}}{\text{cm}^2}$$

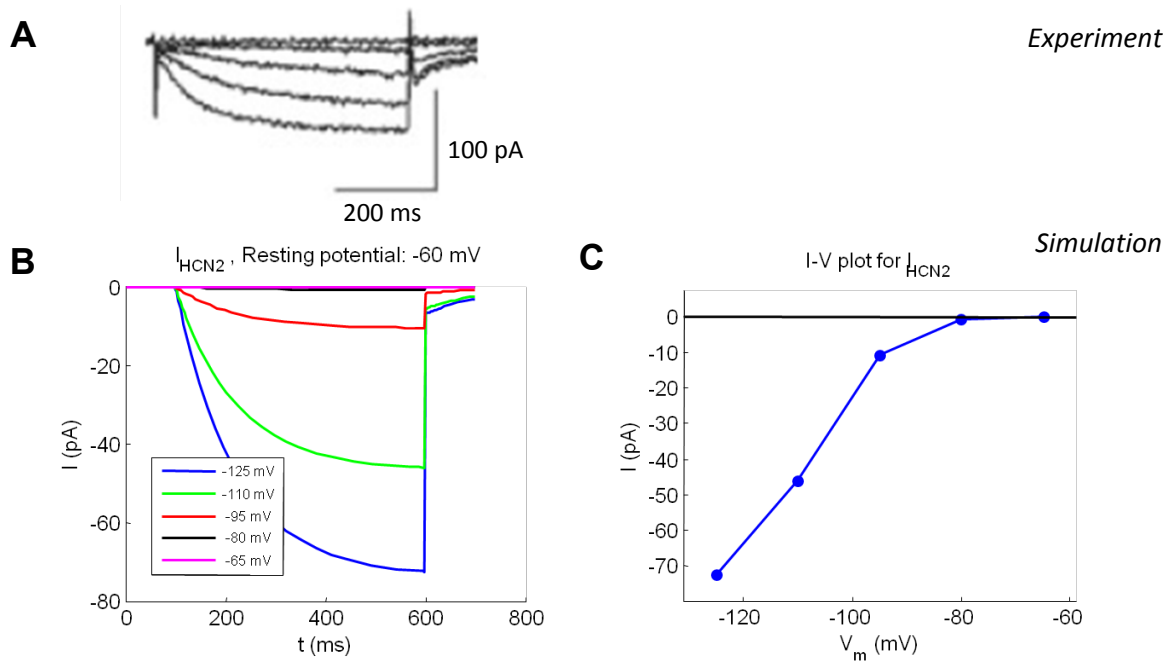


Figure 3.37

Comparison of experimental and simulated whole-cell HCN2 currents. Voltage step experiments (cell held at -60 mV, then 500 ms pulses from -65 mV to -125 mV were applied in steps of 15 mV) in type 8 CBC (A, Figure adapted from (Ivanova and Müller 2006)). Results of simulated voltage step experiments (B) with the same stimulation paradigm and the accompanying I-V curve.

3.3.4.4 HCN4

In the literature reviewed in section 3.2 type 3 CBCs (OFF-type) are the only cells which expressing HCN4 channels but not HCN1 or HCN2. The publication reviewed in section 3.2.5 (Ivanova and Müller 2006) presents current traces of type 3 CBCs after hyperpolarization which appear to be generated only by HCN4 channels (Figure 3.38 A). Furthermore, (Cui and Pan 2008) collected data from type 3 CBCs in a similar stimulation paradigm in which the current recordings also exhibited an instantaneous, time-independent component, most likely caused by Kir channels (Figure 3.38 C). The associated I-V plot also was created (Figure 3.38 E). The parameters of the HCN4 model were fitted such that a sufficient reproduction of the experiments conducted in both of these studies was possible. The results are shown in Figure 3.38 B, D and E.

$$g_{HCN4} = \bar{g}_{HCN4} m$$

$$m_{\infty} = \frac{1}{1 + e^{\left(\frac{V+60}{9.6}\right)}} \quad \tau_m = 46.1 \text{ ms} \quad (3.36)$$

$$\text{with } \frac{dm}{dt} = \frac{m_{\infty} - m}{\tau_m} \quad (3.37)$$

$$\text{For ON-type CBC: } E_{HCN4} = -45 \text{ mV}, \bar{g}_{HCN4} = 0.176 \frac{\text{mS}}{\text{cm}^2}$$

$$\text{For OFF-type CBC: } E_{HCN4} = -45 \text{ mV}, \bar{g}_{HCN4} = 0.2914 \frac{\text{mS}}{\text{cm}^2}$$

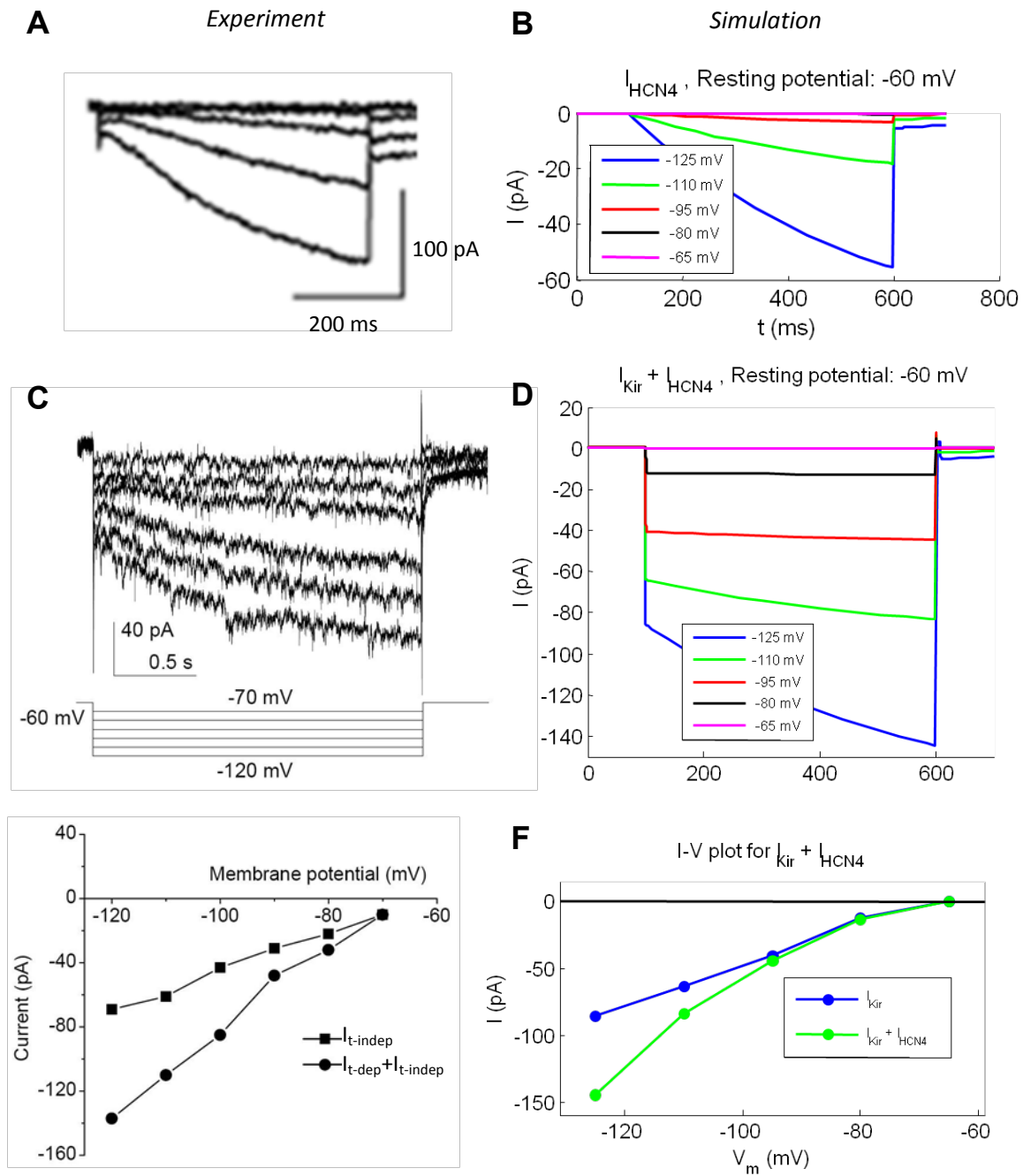


Figure 3.38

Comparison of experimental and simulated whole-cell HCN4 currents. Experimental HCN4 current traces from a type 3 CBC without instantaneous Kir currents (A, stimulation as in Figure 3.37 A, figure adapted from (Ivanova and Müller 2006)). Simulated HCN4 currents during identical stimulation (B). Current traces from a type 3 CBC with instantaneous Kir currents (C, stimulation as in Figure 3.36 A) and simulated HCN4 + Kir currents at similar hyperpolarization steps (D). E shows the I-V relationship of the experiment in A for peak amplitudes of Kir currents (squares) and Kir+HCN4 currents (circles). F shows the I-V relationship for the simulations shown in D for peak amplitudes of Kir currents (blue) and Kir+HCN4 currents (green). C and E are adapted from (Cui and Pan 2008).

3.3.5 Ca^{++} Concentration, Ca^{++} Channels and Ca^{++} -activated Channels – $I_{\text{Ca,T}}$, $I_{\text{Ca,L}}$, $I_{\text{K(Ca)}}$

Calcium ions serve numerous functions in a neuron. Not only do Ca^{++} currents through ion channels contribute to the transmembrane potential, but amongst other functions Ca^{++} also acts as second messenger for metabotropic receptor pathways (Yamashita and Wässle 1991, Nawy 2000). Furthermore, the intracellular Ca^{++} concentration ($[\text{Ca}^{++}]_i$) in the axon terminal controls the speed of synaptic glutamate vesicle release into the synaptic cleft and therefore inter-neuronal signal transduction from CBCs to GCs (Heidelberger and Matthews 1994, Morgans 2000). Compared to most other functional ions, $[\text{Ca}^{++}]_i$ is maintained at very low levels through endogenous buffers (Neher and Augustine 1992). Concentrations of $\sim 0.1 \mu\text{M}$ have been measured in bipolar cell synaptic terminals with increases to levels above $1 \mu\text{M}$ during stimulation by depolarization through elevation of extracellular K^+ concentration levels (Heidelberger and Matthews 1992). Other studies measured up to $10 \mu\text{M}$ $[\text{Ca}^{++}]_i$ using different techniques (Tachibana 1999). Due to the special role of Ca^{++} , the $[\text{Ca}^{++}]_i$ was not treated as a constant but instead was modeled dynamically. $[\text{Ca}^{++}]_i$ influences Ca^{++} currents by alteration of the cellular equilibrium potential for Ca^{++} currents (E_{Ca} , see equation 3.3) and Ca^{++} -dependent currents such as Ca^{++} -dependent K^+ currents ($I_{\text{K(Ca)}}$) because the state (open/closed) of these ion channels depends directly on $[\text{Ca}^{++}]_i$. Another factor requires consideration when modeling currents through Ca^{++} channels. Even though Ca^{++} channels are highly selective and have a ~ 1000 -fold preference to Ca^{++} ions compared to K^+ ions (Lee and Tsein 1982), the very low $[\text{Ca}^{++}]_i$ creates an additional effect: because the normal intracellular K^+ concentration in general is ~ 1 million that of Ca^{++} , the majority of outward current through Ca^{++} channels is caused by K^+ ions. Therefore, although the thermodynamic equilibrium potential of Ca^{++} is in the range of $+120 \text{ mV}$, due to the relatively low $[\text{Ca}^{++}]_i$, the reversal potential of Ca^{++} channels is experimentally observed at less positive values, closer to E_{K} ($E_{\text{K}} = -58 \text{ mV}$ in this model). Therefore, this reversal potential was modeled as a weighted combination of the thermodynamic equilibrium potentials of both Ca^{++} and K^+ . Different weights were used for T-type and L-type Ca^{++} channels.

3.3.5.1 Intracellular Ca^{++} Concentration

In a publication from Usui et al. (Usui et al. 1996) a model of ionic currents in bipolar cells of the lower vertebrate retina was presented. The ionic current model also included complex model for the calculation of $[\text{Ca}^{++}]_i$ in vertebrate bipolar cells, based on a model which had been developed previously for cardiac cells (DiFrancesco and Noble 1985) and later adapted to rod outer segments (Forti et al. 1989). This model differentiated each morphological compartment into two new compartments, one for the submembrane space and another for the deeper intracellular space (Figure 3.39). For each of these spaces, a low-affinity and a high-affinity Ca^{++} buffer was modeled

along with to two separate Ca^{++} concentrations. Furthermore, for the extrusion of intracellular Ca^{++} into the extracellular space a Na^+-Ca^{++} exchanger and a Ca^{++} -ATPase ion pump were modeled. This $[Ca^{++}]_i$ model was implemented in the development of this theses and the results were compared with a simpler $[Ca^{++}]_i$ model used by (Resatz 2005) which was first introduced by (Fohlmeister et al. 1990). The differences (data not shown) appeared to be small in consideration of the additional complexity, number of parameters and computational effort. Therefore, the less complex model was used in this thesis.

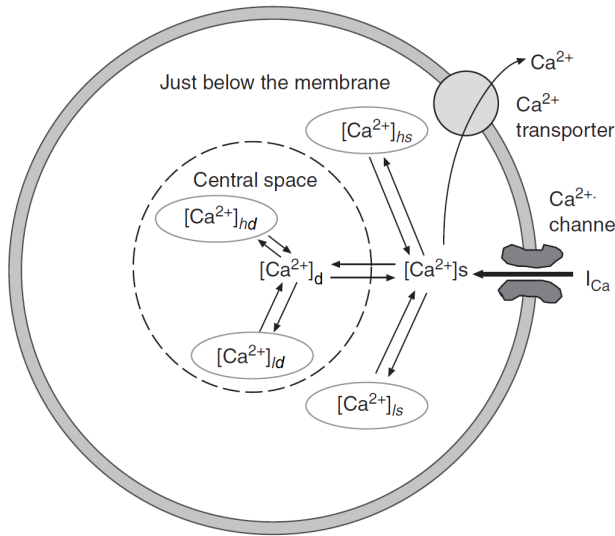


Figure 3.39

Complex model for Ca^{++} concentration changes in retinal bipolar cells. The intracellular space is divided into one compartment just below the membrane (submembrane, s) and the deeper central space compartment (deep, d). For each compartment, the concentration of free Ca^{++} and Ca^{++} bound to high- and low-affinity buffers is modeled. Ca^{++} transporters (ion pumps) extrude free Ca^{++} from the submembrane compartment to the extracellular space. Figure modified from (Usui et al. 1996)

Simplified Calcium concentration model (Resatz 2005):

$$\frac{d[Ca^{++}]_i}{dt} = -\frac{-si_{Ca}}{2vF} - \frac{[Ca^{++}]_i - [Ca^{++}]_{res}}{\tau}$$

Parameters of the Calcium concentration model in bipolar cells

F	96489 C/M, Faraday constant
$[Ca^{++}]_{res}$	0.15 μM , minimal residual Ca^{++} concentration level
s	dm^3 , surface of the compartment
v	dm^2 , submembrane volume
τ	1.5 ms, time constant

Initial values:

For ON-type CBC: $[Ca^{++}]_i = 0.1501 \mu M$

For OFF-type CBC: $[Ca^{++}]_i = 0.15002 \mu M$

For all CBCs: $[Ca^{++}]_o = 1800 \mu M$ extracellular Ca^{++} concentration, constant

These different values for $[Ca^{++}]_i$ were assumed by the model cells independently of the starting values after they had reached a steady state in test-simulations.

3.3.5.2 T-Type Ca^{++} Currents

T-type Ca^{++} currents have been found in ON- and OFF-type CBCs with different subcellular distributions. As elaborated in section 3.2.10 the model of an ideal ON-type CBC was equipped with T-type Ca^{++} currents in the soma, while the ideal OFF-type CBC model had T-type Ca^{++} channels in its presynaptic axon terminals. A detailed analysis of T-type Ca^{++} currents in rat CBCs can be found in (Hu et al. 2009). However, as pointed out in section 3.2.8, the cells measured electrophysiologically in this study could not be clearly identified and it remains unclear whether they were ON- or OFF-type CBCs.

A computational model for simulation of T-type currents in bipolar cells of higher vertebrates was not available. However, a model developed previously for T-type currents measured in HEK-293 cells (Human Embryonic Kidney Cells) transiently expressing human Cav3.3 (a T-type Ca^{++} channel) subunits (Traboulsie et al. 2007) could be adapted for use in this thesis. For the recreation of T-type Ca^{++} currents, one activating gate and one inactivating gate were used in the ion channel model.

$$g_{CaT} = \bar{g}_{CaT} m h \quad (3.38)$$

$$m_{\infty} = \frac{1}{1 + e^{\left(\frac{V - 37.5456}{-3.073015}\right)}} \quad \tau_m = 1.358 + \frac{21.675}{1 + e^{\left(\frac{V_m - 39.9596}{4.110392}\right)}} \text{ ms} \quad (3.39)$$

$$h_{\infty} = \frac{1}{1 + e^{\left(\frac{V - 8.968}{8.416382}\right)}} \quad \tau_h = 65.8207 + 0.0023 e^{\left(\frac{V - 80}{4.781719}\right)} \text{ ms} \quad (3.40)$$

$$\text{with } \frac{dm}{dt} = \frac{m_{\infty} - m}{\tau_m} \quad \frac{dh}{dt} = \frac{h_{\infty} - h}{\tau_h} \quad (3.41)$$

$$E_{CaT} = \text{Nernst}(Ca^{++}) \frac{45}{100} + E_K \frac{55}{100} \quad (3.42)$$

$$\text{For ON-type CBC (T-rich): } \bar{g}_{CaT} = 2.715 \frac{\text{mS}}{\text{cm}^2}$$

$$\text{For OFF-type CBC (L-rich): } \bar{g}_{CaT} = 0.212 \frac{\text{mS}}{\text{cm}^2}$$

Figure 3.40 A shows the inward T-type Ca^{++} current elicited in a T-rich CBC during a depolarizing pulse at 40 mV after the cell was held at -80 mV (Hu et al. 2009). The current trace simulated under identical conditions is shown for comparison in Figure 3.40 C. The I-V curve presented in Figure 3.40 B was not composed of peak voltages in multiple voltage-step experiments, but instead was recorded during a single voltage-ramp experiment with an initial holding potential of -80 mV and an increase in applied voltage at 100 mV/s from -80 mV to +40 mV (Hu et al. 2009). Again, the results of a simulation under identical circumstances (Figure 3.40 D) are shown below.

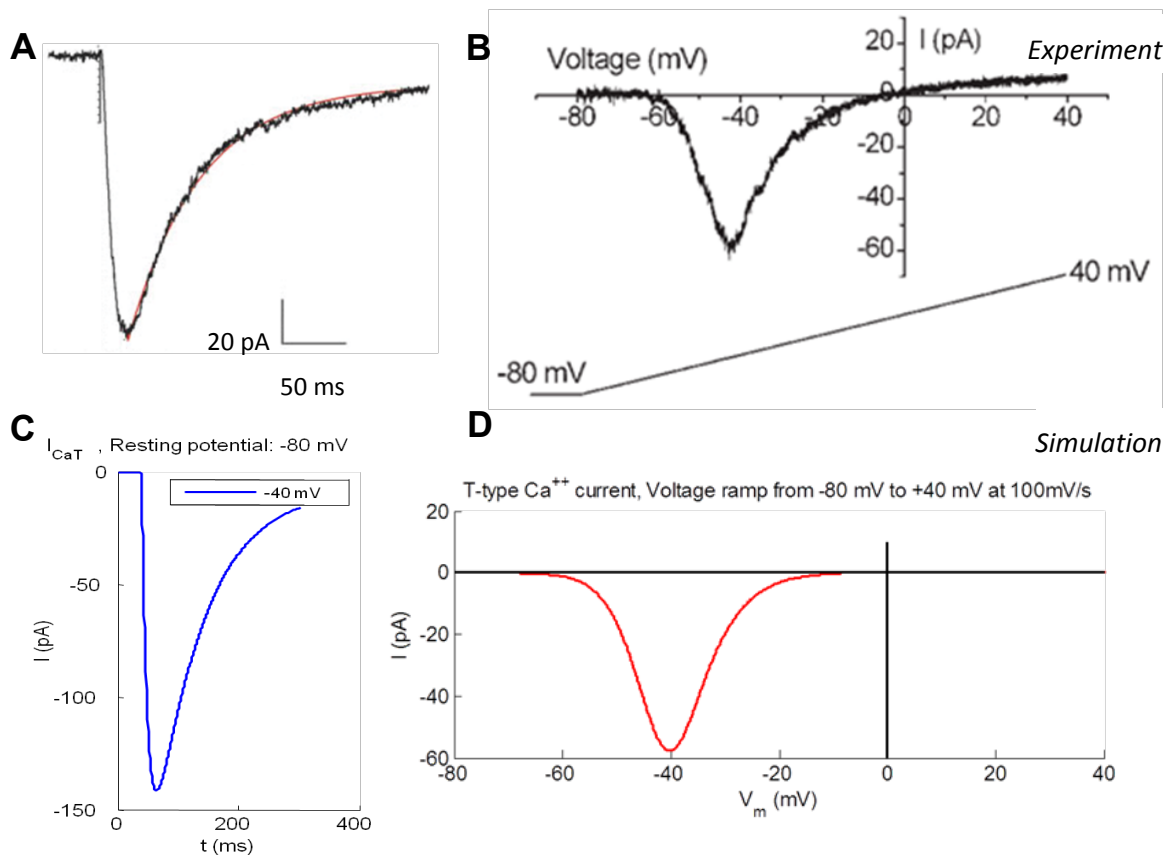


Figure 3.40

Comparison of experimental and simulated whole-cell T-type Ca^{++} currents. T-type Ca^{++} currents during a test-pulse of -40 mV after a holding potential of -80 mV from an experiment (A) and during simulations (C). I-V curve of an T-rich CBC measured with a voltage-ramp experiment from -80 mV holding potential up to -40 mV at a speed of 100 mV/s (B). I-V curve under identical conditions in a voltage-ramp simulation (D). Figures A and B adapted from (Hu et al. 2009).

3.3.5.3 L-Type Ca^{++} Currents

Similar to T-type Ca^{++} currents, L-type Ca^{++} currents have been traced in ON- and OFF type CBCs with heterogeneous subcellular distributions. The ideal model used for ON-type CBCs carried L-type channels in the axon terminal region, while these channels were located in the soma of the ideal OFF-type model. Again, a computational model for simulation of L-type currents in bipolar cells of higher vertebrates was not available. However, a model developed previously for L-type currents in feline retinal ganglion cells (RGC) (Benison et al. 2001) could be used in part. The formula for activation of L-type Ca^{++} channels could be adapted from this model to generate satisfactory reproductions of L-type currents in rat CBCs. The inactivation of L-type Ca^{++} channels could be modeled most effectively using an adapted form of a model created for rat hippocampal CA3 pyramidal neurons (Avery and Johnston 1996). The L-type Ca^{++} channel model used here was simulated using two activating gates and one inactivating gate.

$$g_{CaL} = \bar{g}_{CaL} m^2 h \quad (3.43)$$

$$\alpha_m = 0.427 \frac{V_m - 63}{1 - e^{\left(\frac{-(V_m - 63)}{10.5}\right)}} \quad \beta_m = 0.0406 e^{\left(\frac{70 - V_m}{12}\right)} \quad (3.44)$$

$$h_\infty = \frac{1}{1 + e^{\left(\frac{V_m}{66.4}\right)}} \quad \tau_m = 292 \text{ ms} \quad (3.45)$$

$$\text{with } \frac{dh}{dt} = \frac{h_\infty - h}{\tau_h} \quad (3.46)$$

$$E_{CaL} = \text{Nernst}(Ca^{++}) \frac{32}{100} + E_K \frac{68}{100} \quad (3.47)$$

$$\text{For ON-type CBC (T-rich): } \bar{g}_{CaL} = 0.4352 \frac{mS}{cm^2}$$

$$\text{For OFF-type CBC (T-rich): } \bar{g}_{CaL} = 12.6269 \frac{mS}{cm^2}$$

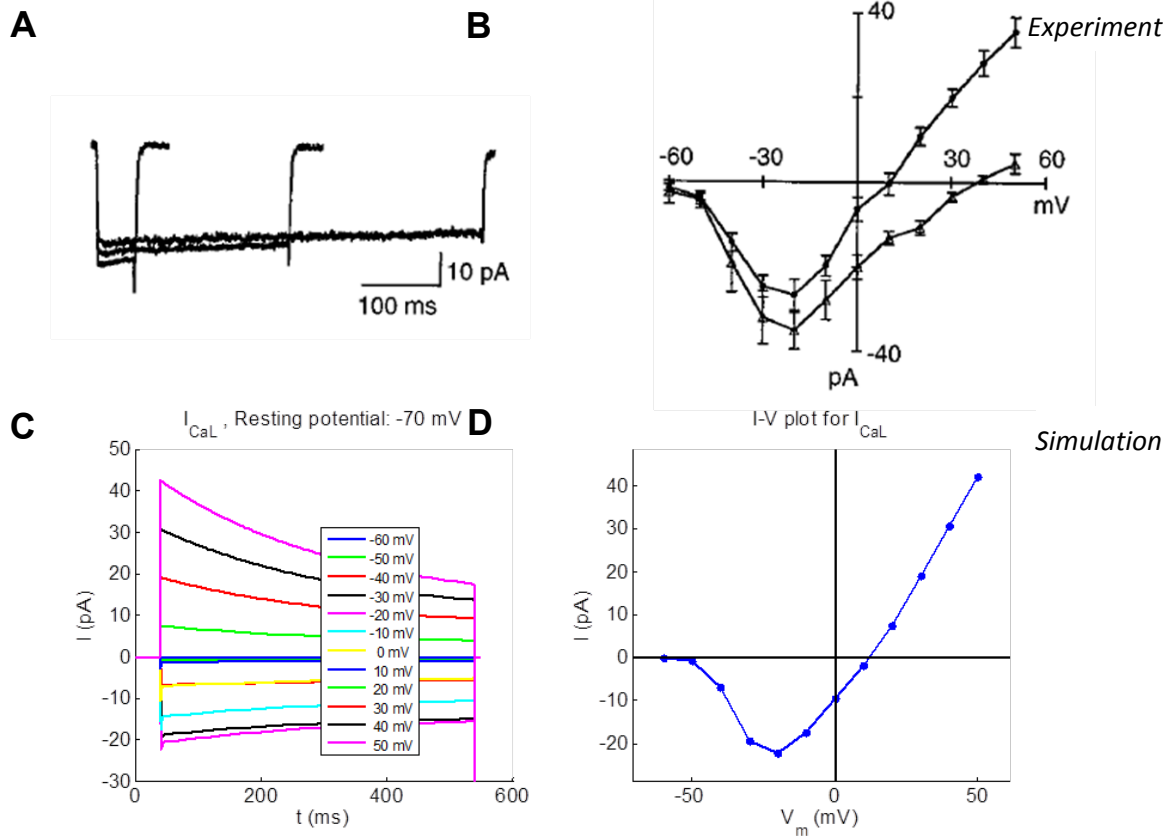


Figure 3.41

Comparison of experimental and simulated whole-cell L-type Ca⁺⁺ currents. The weak inactivation is shown by three L-type Ca⁺⁺ current traces elicited in a rat rod bipolar cell (A) with depolarizing pulses of -20 mV, durations of 50, 250 and 500 ms, holding potential was -70 mV. Current traces from voltage-step simulations (C) for an L-rich CBC model, pulse duration of 500 ms. I-V curve (B, filled circles) from peak L-type Ca⁺⁺ currents of voltage step experiments in rod bipolar cells depolarized (-70 mV holding voltage) with pulses from to -60 mV to +60 mV in steps of 15 mV. I-V curve for the voltage-step simulations (D) of the L-rich CBC model. Figures A and B adapted from (Protti and Llano 1998).

3.3.5.4 Ca^{++} -Dependent K^+ Currents

Calcium-activated K^+ currents also have been found in rat CBCs and have been added to the models of ideal ON- and OFF-type CBC. Unfortunately, there is no data available for direct measurements of K_{Ca} currents in rat CBCs. However, Hu and Pan (Hu and Pan 2002) collected data of K^+ currents in extracellular solutions with high Ca^{++} and low Ca^{++} concentrations. These measurement yielded current traces with different amplitudes. For this model it is assumed, that the majority of this difference is due to the absence and presence of K_{Ca} currents. The difference in amplitude between these measurements has been estimated and was used here as an approximate value for the amplitude of K_{Ca} currents in OFF-type rat CBCs in the K_{Ca} current model. Due to this lack of more direct measurements, the quality of K_{Ca} current reproductions is less precise than that of the other ion channel models in this thesis.

A previously published model (Usui et al. 1996) used for Ca^{++} -dependent K^+ currents in retinal BCs of lower vertebrates has been used here. Only the conductivity value $\bar{g}_{K(Ca)}$ was changed to adapt the model to rat CBCs. The model incorporates dependencies on the reduced transmembrane voltage V and to the submembrane Ca^{++} concentration $[Ca^{++}]_s$.

$$g_{K(Ca)} = \bar{g}_{K(Ca)} m^2 \left(\frac{[Ca^{++}]_s}{[Ca^{++}]_s + 0.2} \right) \quad (3.48)$$

$$\alpha_m = 100 \frac{230-V}{e^{\left(\frac{230-V}{52}\right)} - 1} \quad \beta_m = 120 e^{\left(\frac{-V}{95}\right)} \quad (3.49)$$

$$\text{For ON-type CBC:} \quad \bar{g}_{K(Ca)} = 360 \frac{mS}{cm^2}$$

$$\text{For OFF-type CBC:} \quad \bar{g}_{K(Ca)} = 91.44 \frac{mS}{cm^2}$$

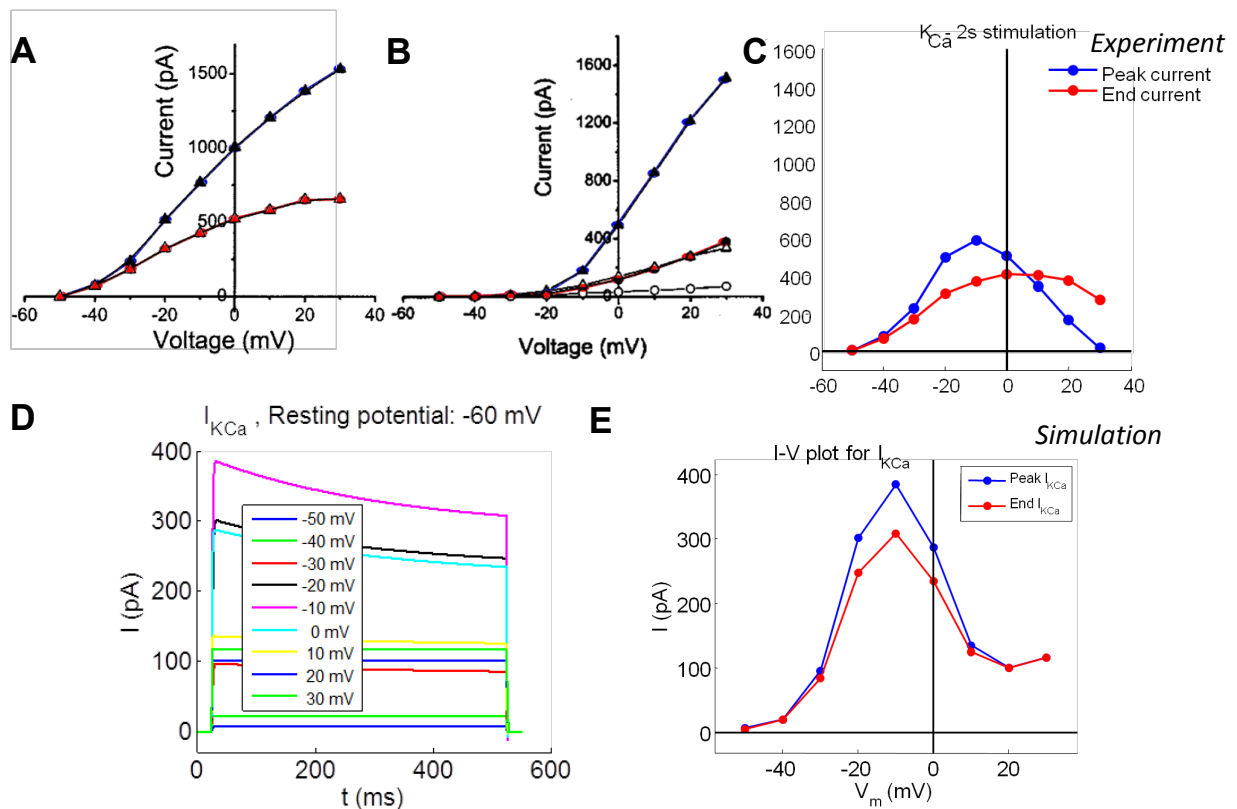


Figure 3.42

Experimental and simulated whole-cell Ca^{++} -dependent K^+ currents (KCa) currents. I-V curve for K^+ currents under high (A) and low (B) Ca^{++} concentrations. The difference (C, derived from A and B) is assumed to be an upper bound for KCa currents. Simulated currents traces (D) and the resulting I-V curve (E) for modeled peak KCa currents and currents at end of simulation. The peak amplitude was set to be 65% of the differences measured in A. Figures A and B modified from (Hu and Pan 2002).

3.4 Simulations and Results

At this stage, all required parameters for the active cone bipolar cell (CBC) model with voltage-gated ion channels have been introduced. Realistic morphologies for two different CBCs, one ON-type and one OFF-type CBC were presented in section 2.3.1.4. Following a review of literature on voltage-gated ion channels in rat CBCs in section 3.2, the appropriate Hodgkin-Huxley based models were developed and fitted to experimental electrophysiological recordings of these ion channels (section 3.3). Additionally, a model for changes of $[Ca^{++}]_i$ was included into the model.

In the following sections, whole-cell ionic current traces and I-V relationships were simulated for demonstration of the behavior these ideal ON- and OFF-type CBCs would have under voltage-clamp conditions. Then, different types of voltage-controlled pulses (see overview in Table 3.2) from external MPDA electrodes were applied to the models of ideal ON-type and ideal OFF-type CBCs. The resulting membrane potentials, ionic currents and synaptic Ca^{++} concentrations in the axon terminal

are reported. During the course of the clinical study the stimulus waveforms were either monophasic cathodic or biphasic anodic-first pulses. Therefore, anodic (hyperpolarizing) and cathodic (depolarizing) pulses were simulated, as well as combinations of these and trains of several consecutive stimuli. Furthermore, the effects of dipolar stimulation with local return electrodes were simulated (see section 2.3.2.2). The default pulse-length used in simulations of subretinal stimulation is 0.5 ms, as this is also the most common pulse length in the clinical trial (Zrenner et al. 2010). The default stimulation amplitude was 1 V, since stimulation amplitudes with the Tübingen subretinal implant typically range between 0 V – 2 V and maximally reach 2.5 V to prevent tissue damage (Sachs et al. 2005). The choice of 1 V rather than a value closer to the charge injection limit leaves additional room for further optimizations. In all simulations, a resting membrane potential of -53.08 mV is assumed, which is also set to be the equilibrium potential of leak currents. Leak currents were modeled with a conductivity of $g_L = 0.0417 \text{ mS/cm}^2$ in all simulations. The distance from the soma to the electrode surface is retained at 45 μm during simulations. Through sections 3.4.1 and 3.4.2 very little text is provided. Instead, important features are identified in the legend. A more complete discussion of these simulations is then presented in section 3.5.

	ON-type CBC		OFF-type CBC
I	Figure 3.45 Voltage clamp, 0.5 ms pulse from -53 mV to -103 mV	Hyperpolarizing	Figure 3.58 Voltage clamp, 0.5 ms pulse from -53 mV to -103 mV
II	Figure 3.46 Subretinal implant, 0.5 ms pulse at -1 V		Figure 3.59 Subretinal implant, 0.5 ms pulse at -1 V
III	Figure 3.47 Subretinal implant, 0.5 ms pulse at -2 V		Figure 3.60 Subretinal implant, 0.5 ms pulse at -2 V
IV	Figure 3.48 Voltage clamp, 0.5 ms pulse from -53 mV to -3 mV	Depolarizing	Figure 3.61 Voltage clamp, 0.5 ms pulse from -53 mV to -3 mV
V	Figure 3.49 Subretinal implant, 0.5 ms pulse at +1 V		Figure 3.62 Subretinal implant, 0.5 ms pulse at +1 V
VI	Figure 3.50 Subretinal implant, 0.5 ms pulse at +2 V		Figure 3.63 Subretinal implant, 0.5 ms pulse at +2 V
VII	Figure 3.51 Cathodic-first, 1 ms pulse at 1 V	Biphasic	Figure 3.64 Cathodic-first, 1 ms pulse at 1 V
VIII	Figure 3.52 Anodic-first, 1 ms pulse at 1 V		Figure 3.65 Anodic-first, 1 ms pulse at 1 V
IX	Figure 3.53 Five 0.5 ms pulses at +1 V with 0.5 ms pause	Stimulus Bursts	Figure 3.66 Five 0.5 ms pulses at +1 V with 0.5 ms pause
X	Figure 3.54 Five 0.5 ms pulses at +1 V with 4.5 ms pause		Figure 3.67 Five 0.5 ms pulses at +1 V with 4.5 ms pause
XI	---		Figure 3.68 Five 0.5 ms pulses at +1 V with 9.5 ms pause
XII	---		Figure 3.69 Five 0.5 ms pulses at +1 V with 19.5 ms pause
XIII	---		Figure 3.70 Five 0.5 ms pulses at +1 V with 39.5 ms pause
XIV	Figure 3.55 Monophasic 0.5 ms pulse with 2 V (-1 V & +1 V)	Dipolar	Figure 3.71 Monophasic 0.5 ms pulse with 2 V (-1 V & +1 V)

Table 3.2 Overview of simulations performed in sections 3.4.1 and 3.4.2

Simulations I and IV were conducted in voltage-clamp mode, while all other simulations were based on extracellular stimulation from the subretinal stimulation space.

3.4.1 ON Cone Bipolar Cell

For the model of an ideal ON-type CBC (see sections 3.2.9.2 and 3.2.10) the morphological 3D structure of a type 9 rat CBC was used (see also section 2.3.1.4). The reference morphology (Figure 3.43 A) was selected from the bipolar cells identified by (Euler and Wässle 1995).

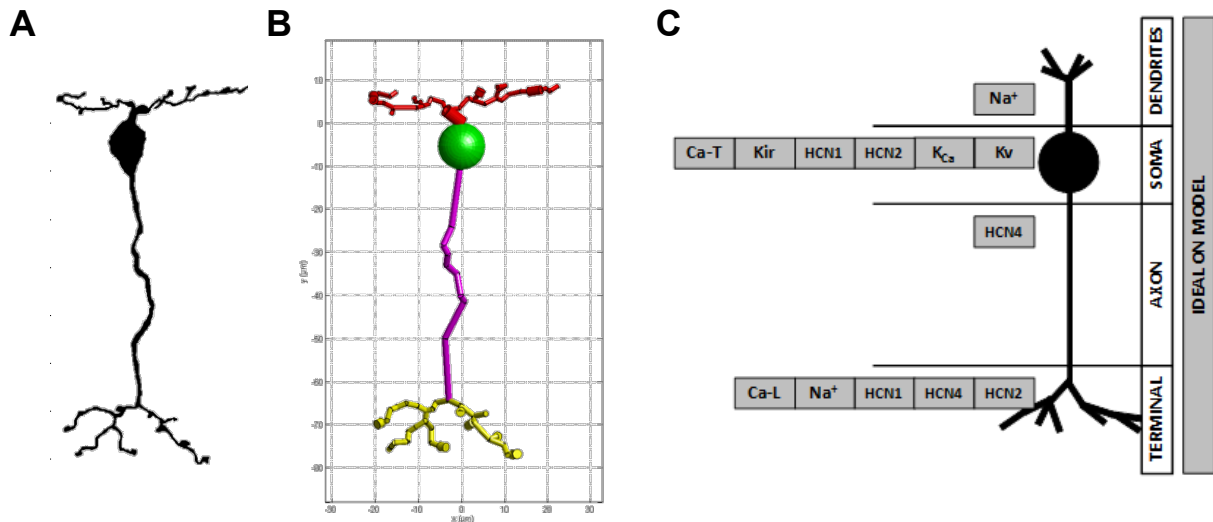


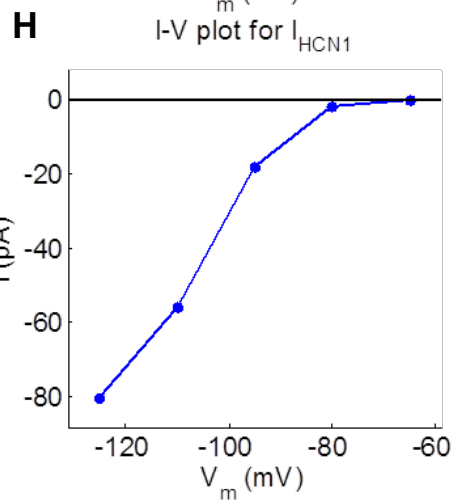
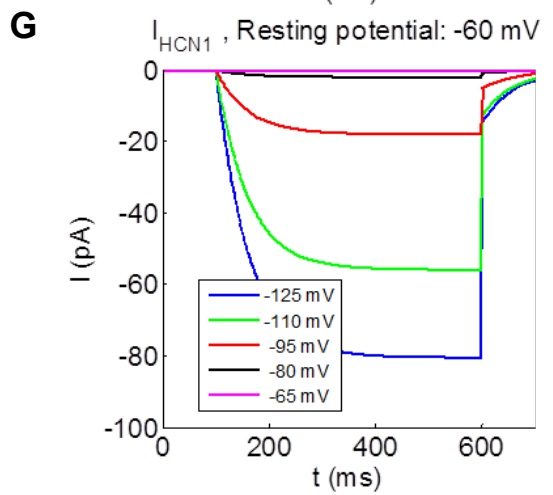
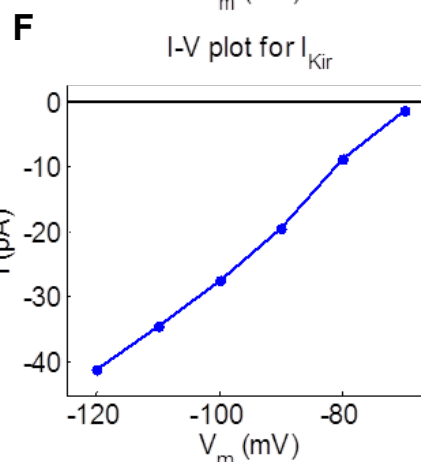
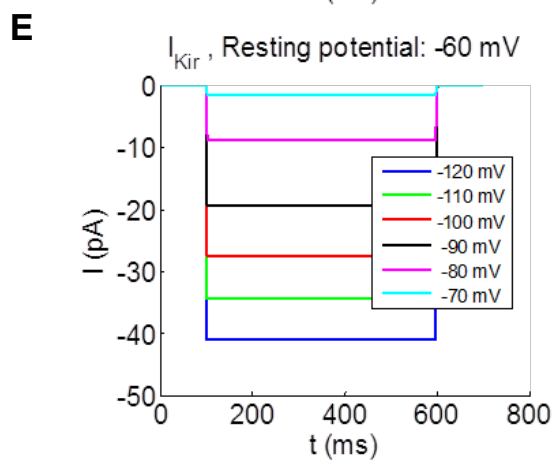
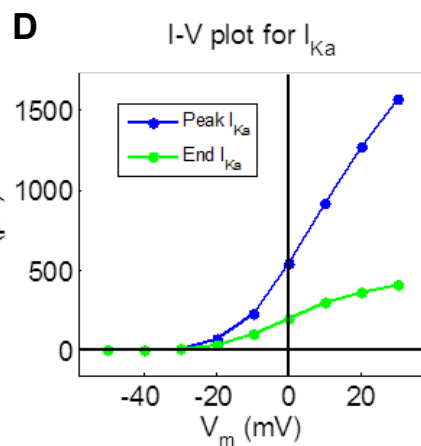
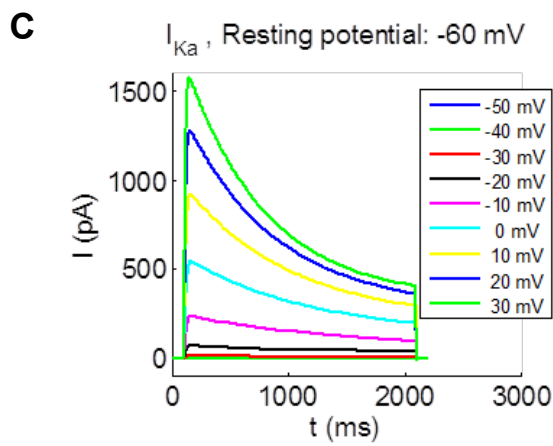
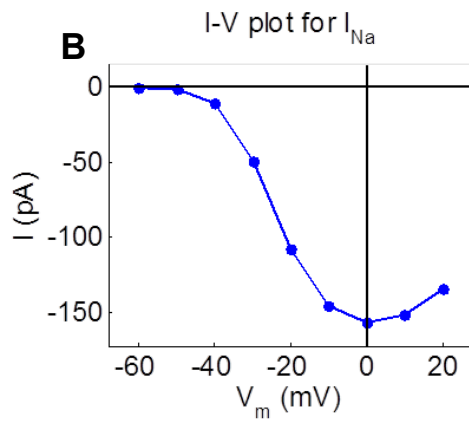
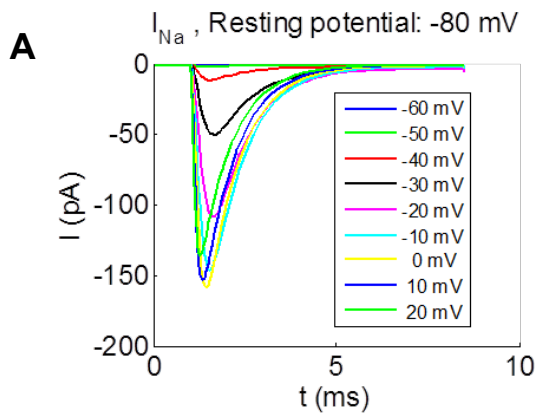
Figure 3.43

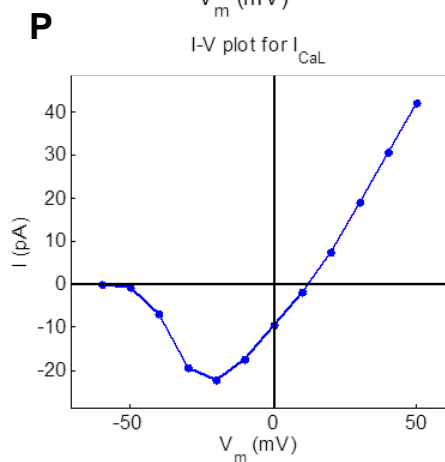
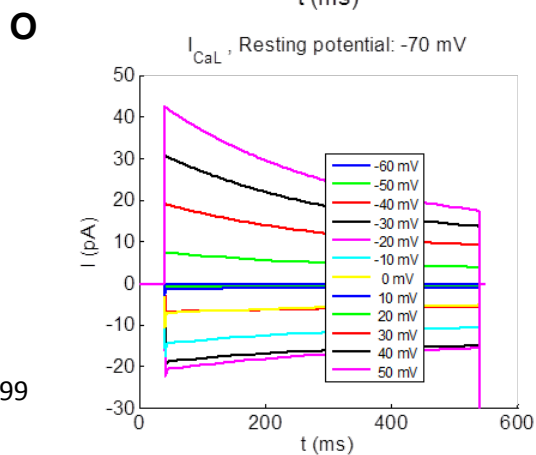
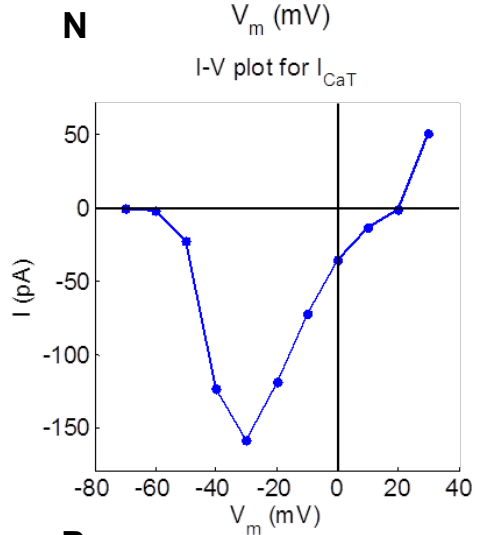
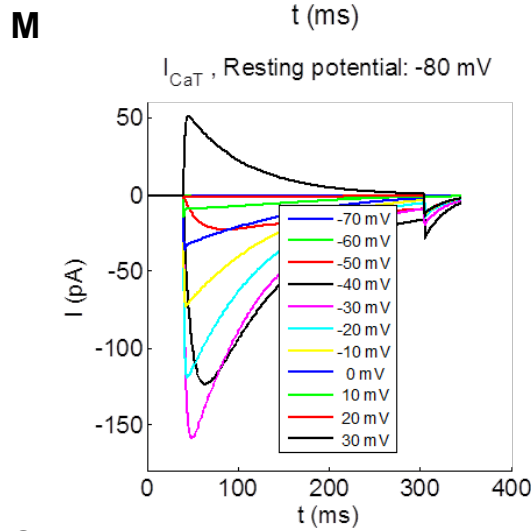
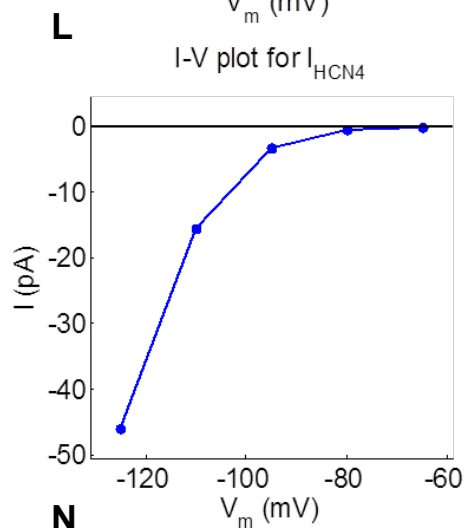
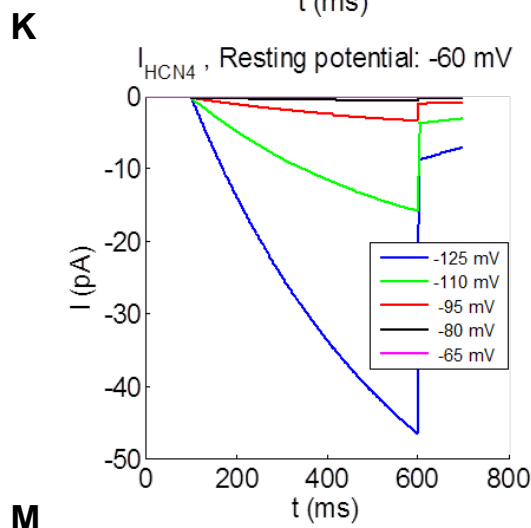
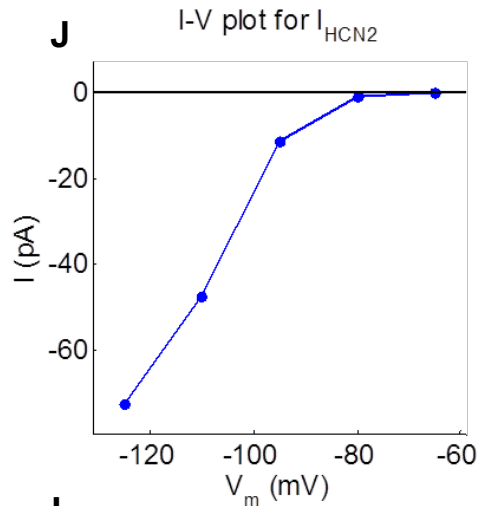
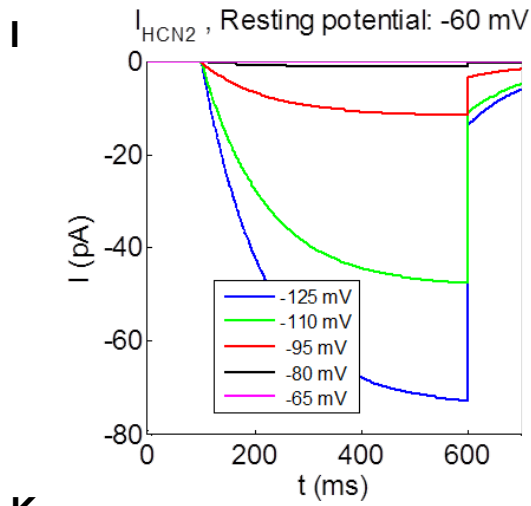
Type 9 rat CBC used (A) used as morphological reference for the ideal ON-type CBC model. Image modified from (Euler and Wässle 1995). Three dimensional morphological model (B) generated for the reference cell. Colors represent different neuronal regions, red: dendrites, green: soma, purple: axon, yellow: axon terminal. Ion channel equipment (C) assumed for the ideal ON-type CBC model.

Based on this 2D image, a 3D morphology (Figure 3.43 B) with 91 compartments was generated using a custom made Matlab program. This 3D morphology and the ion channels equipment shown in Figure 3.43 C complete the ideal ON-type CBC model.

3.4.1.1 Whole-Cell Voltage Clamp Currents

The exact behavior of all ion channel types used in the ideal ON-type CBC model under voltage-clamp conditions is shown in Figure 3.44. The amplitudes were adjusted according to information from the literature reviewed in section 3.2.





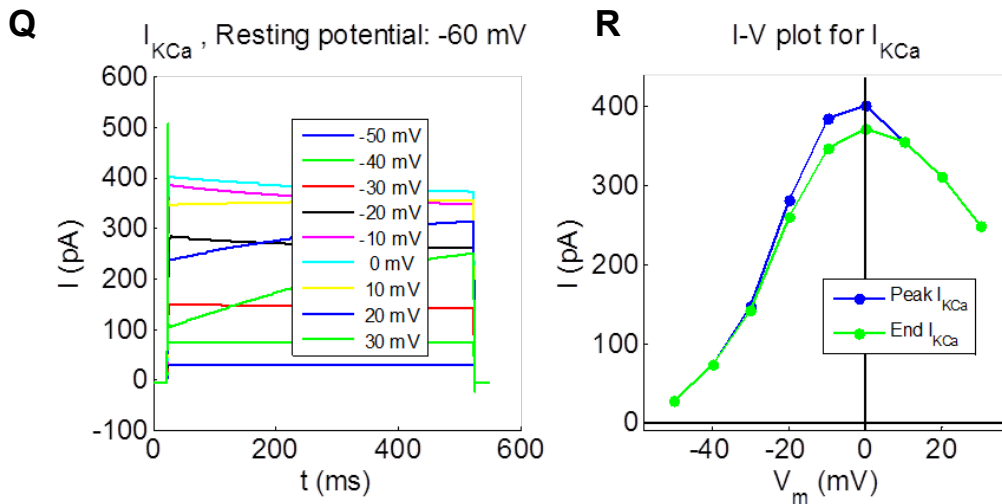


Figure 3.44

A-R: Whole-cell amplitudes of all currents used in the ideal ON-type CBC under voltage-clamp (step-clamp) conditions. The left panels show the time-courses of whole-cell currents, right panels show peak amplitudes of these current traces plotted against holding voltage (For I_{KCa} and $I_{K(Ca)}$ the current amplitude at the end of the voltage-step pulse is also plotted into the right panel).

3.4.1.2 Hyperpolarizing Pulses

A series of simulations of hyperpolarizing pulses was conducted. The first figure here shows the results of a hyperpolarizing voltage-step simulation (Figure 3.45), followed by two simulations of stimulation with an extracellular electrode as used in the Tübingen subretinal implant with -1 V (Figure 3.46) and -2 V (Figure 3.47). Intracellular Ca^{++} concentrations did not change significantly using hyperpolarizing pulses and showed only slight decreases from their initial resting value of $0.1501 \mu M$.

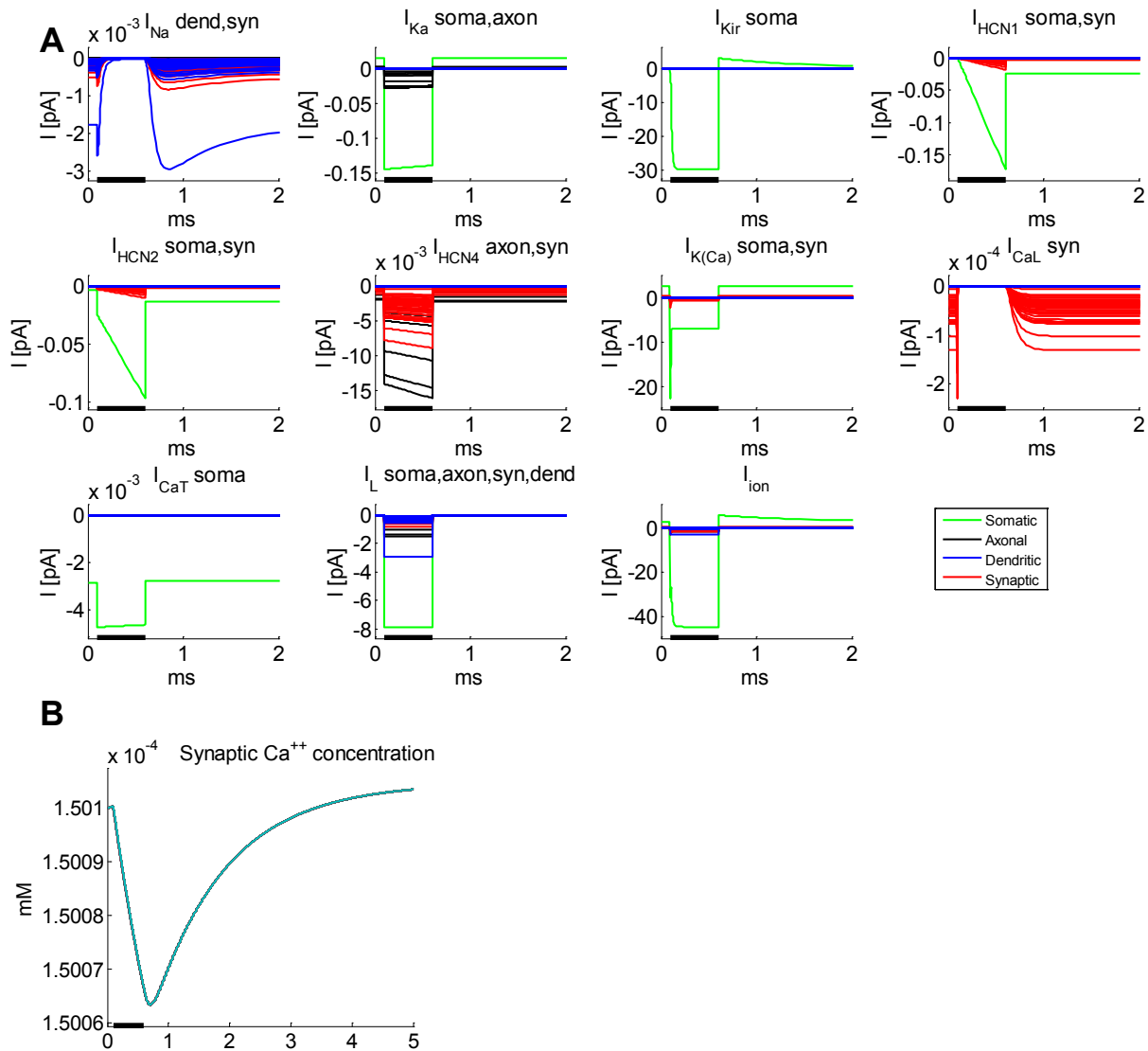


Figure 3.45 Voltage clamp, 0.5 ms pulse from -53 mV to -103 mV

All figures in sections 3.4.1 and 3.4.2 follow the same scheme. The first panel (A) shows the time-courses for all single compartments for all voltage-dependent ion channels, leak currents and the sum of all ionic currents (I_{ion}). The current trace of each compartment is plotted in a color representing its neuronal region (soma, axon, dendrite or synaptic axon terminal). Each plot title mentions the channel type, and in which neuronal region this specific channel type was present in the model. In each plot, a black bar at the bottom x-axis depicts the timing of the stimulus. The second panel (B) here shows the intracellular concentration of Ca^{++} ions, which was always initiated at 0.0001501 mM in the ON-CBC model. This concentration decreased only slightly during the hyperpolarizing pulse from -53 mV resting potential to -103 mV and recovered to its original value after several ms. Although not readily apparent in this figure, time-courses of multiple synaptic compartments are overlaid using the same color. In other figures showing results of extracellular stimulation, panel B would show the transmembrane voltage (V_m), however, in this voltage-clamp stimulation, V_m is dictated by the control pulse.

Please note, that all y-axes have different scaling in order to maximize the observable behavior of current time-courses. Furthermore, y-axes can have exponents such as $x10^{-3}$ or $x10^{-4}$.

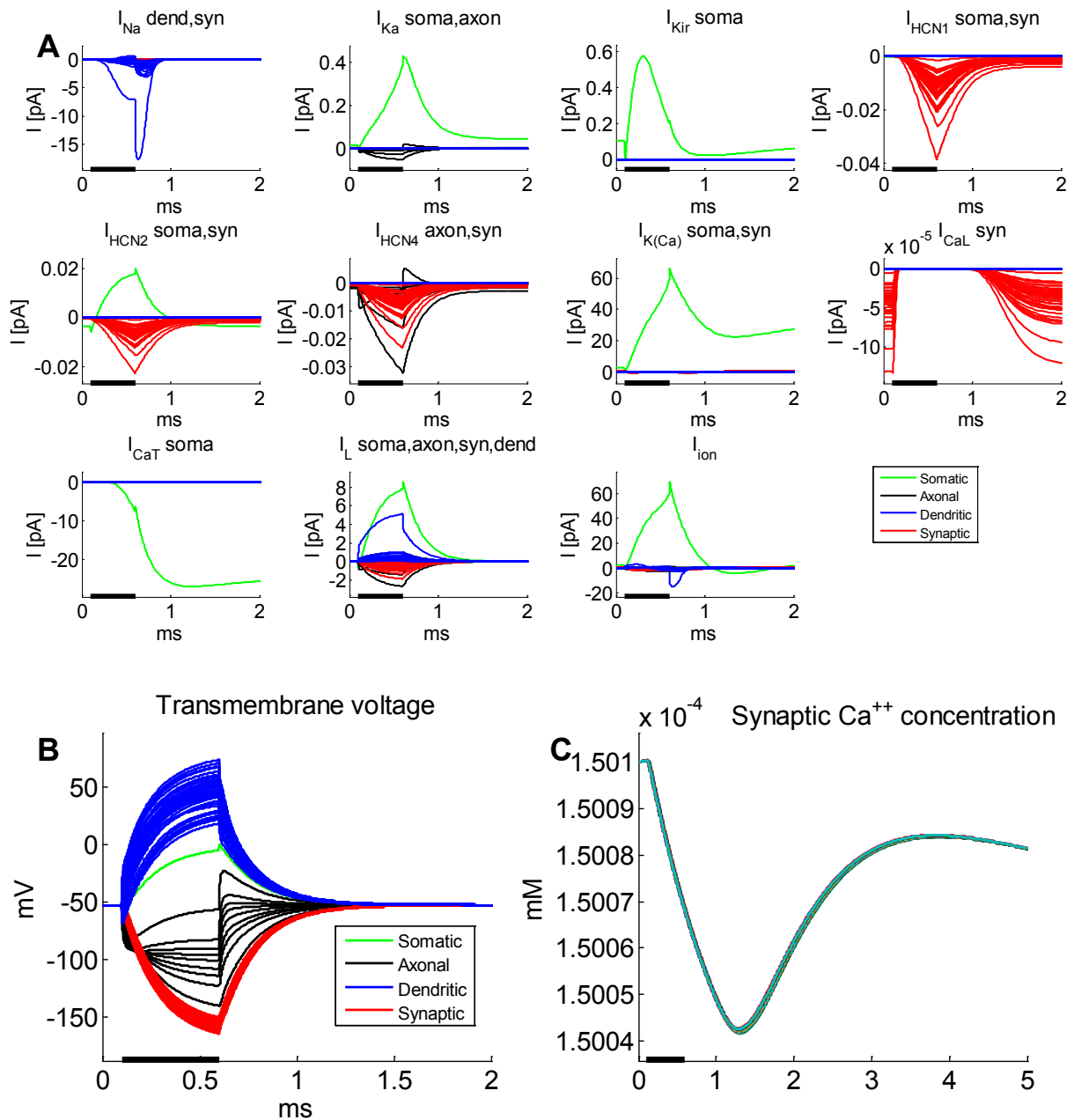


Figure 3.46 Subretinal implant, 0.5 ms pulse at -1 V

Single compartment current time-courses (A) during a -1 V hyperpolarizing pulse from the subretinal space. In the synaptic compartments only inward currents could be observed. In all other compartments, both inward and outward currents resulted from this simulation. V_m (B) increased mostly in dendritic compartments and decreased in axonal and synaptic compartments, reaching its starting value approximately 1 ms after end of stimulation. The Synaptic Ca^{++} concentration at the axon terminal (C) decreased slightly during the pulse and the following 1 ms.

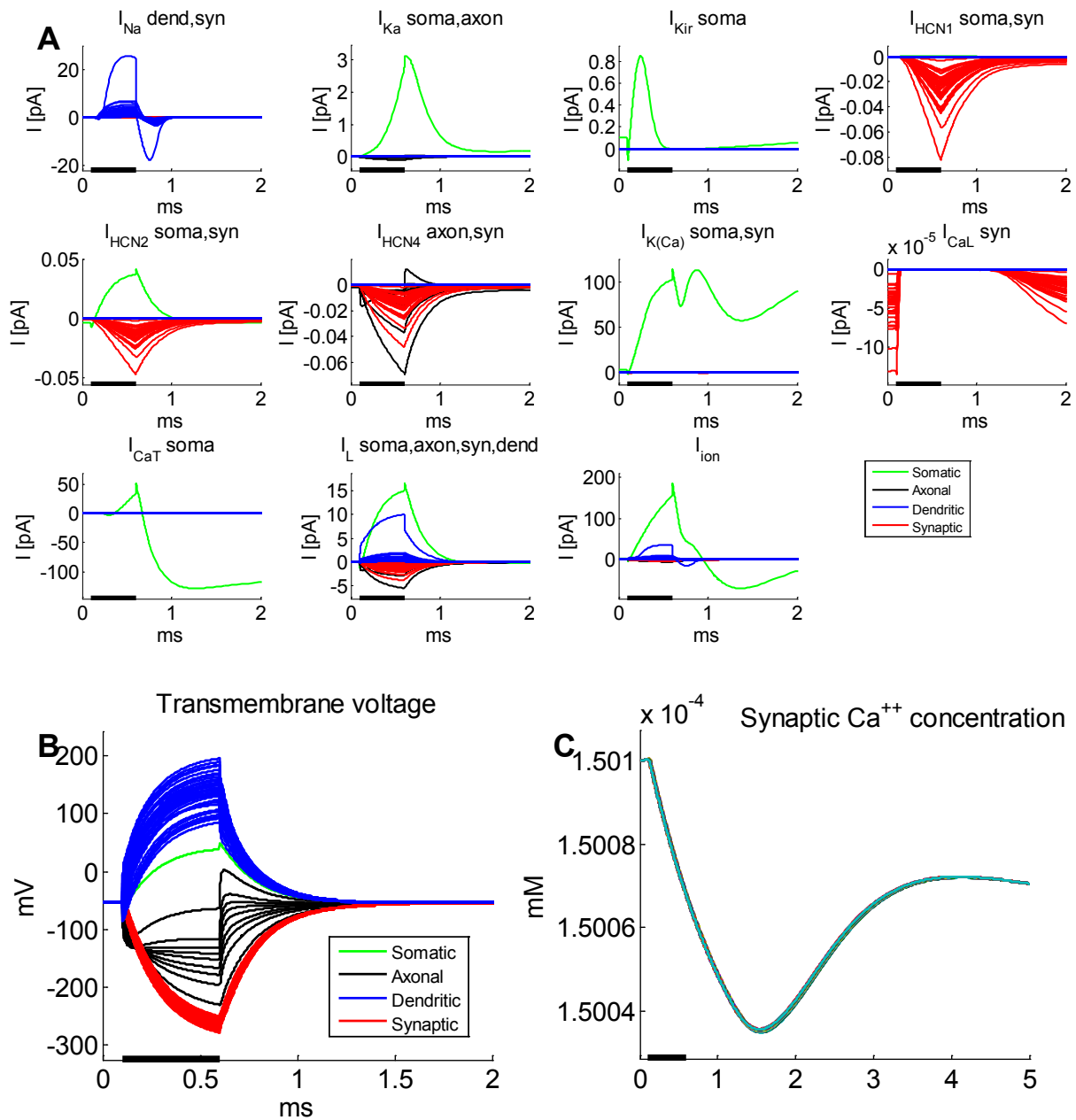


Figure 3.47 Subretinal implant, 0.5 ms pulse at -2 V

Single compartment current time-courses (A) during a -2 V hyperpolarizing pulse from the subretinal space. Most currents exhibited behavior qualitatively similar to a -1 V stimulation with some larger amplitudes, although I_{Na} showed some dendritic outward currents. Relative to the -1 V stimulation, V_m (B) showed an increase in dendritic and a decrease in synaptic compartments. The Synaptic Ca^{++} concentration (C) decreased slightly.

3.4.1.3 Depolarizing Pulses

The stimuli used for simulation of the results in this section differ from the previous section only in the polarity of the stimulus, but were otherwise identical.

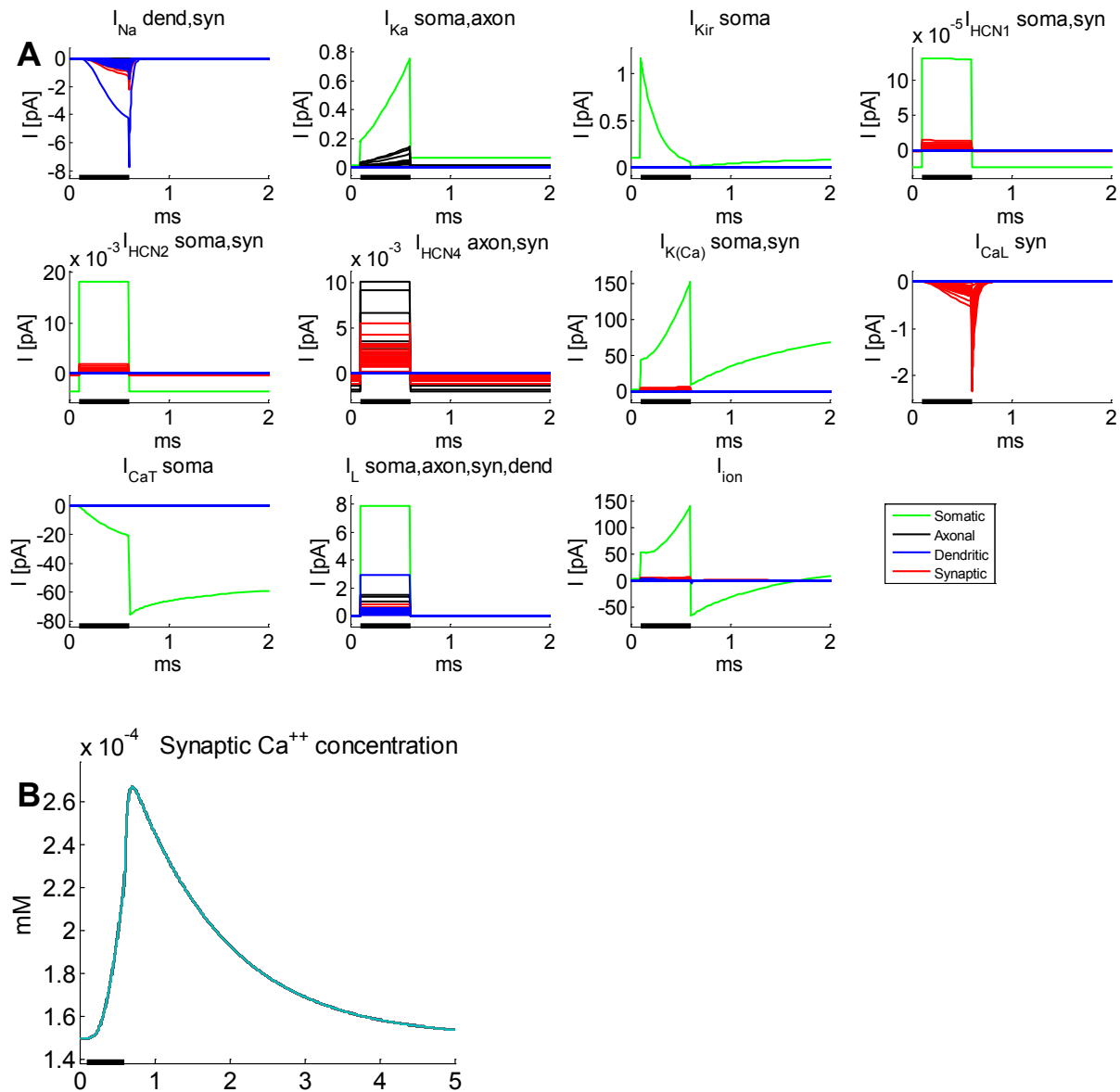


Figure 3.48 Voltage clamp, 0.5 ms pulse from -53 mV to -3 mV

Single compartment current traces (A) during a depolarizing voltage-clamp simulation. Most somatic, axonal and synaptic currents were outward with the exception of most Na^+ and Ca^{++} currents, which were inward across all compartment types. Somatic inward T-type Ca^{++} currents were elicited by the stimulus and persisted throughout the course of the simulation. The synaptic Ca^{++} concentration (B) increased by approximately 75% during the depolarizing pulse.

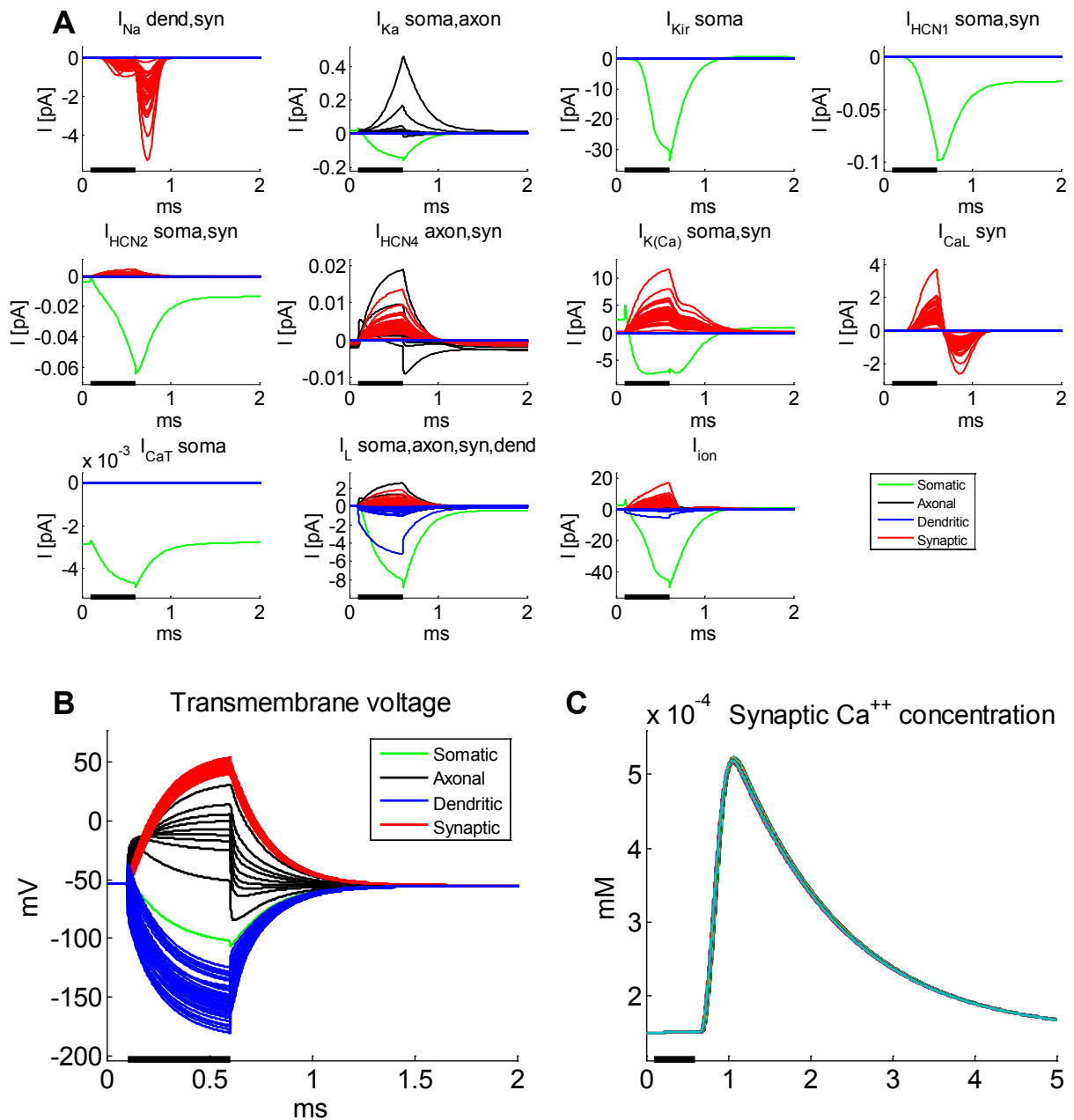


Figure 3.49 Subretinal implant, 0.5 ms pulse at +1 V

Single compartment current traces (A). All synaptic and somatic currents went outward with the following exceptions. Inward Na^+ currents occurred at the synaptic compartments, whereas L-type Ca^{++} currents were outward during stimulation and reversed their direction after the end of the stimulus. V_m reached appr. +50 mV in synaptic compartments (B). The stimulation led to a 250% increase of synaptic $[Ca^{++}]_i$ (C) from 0.15 μM to 0.52 μM .

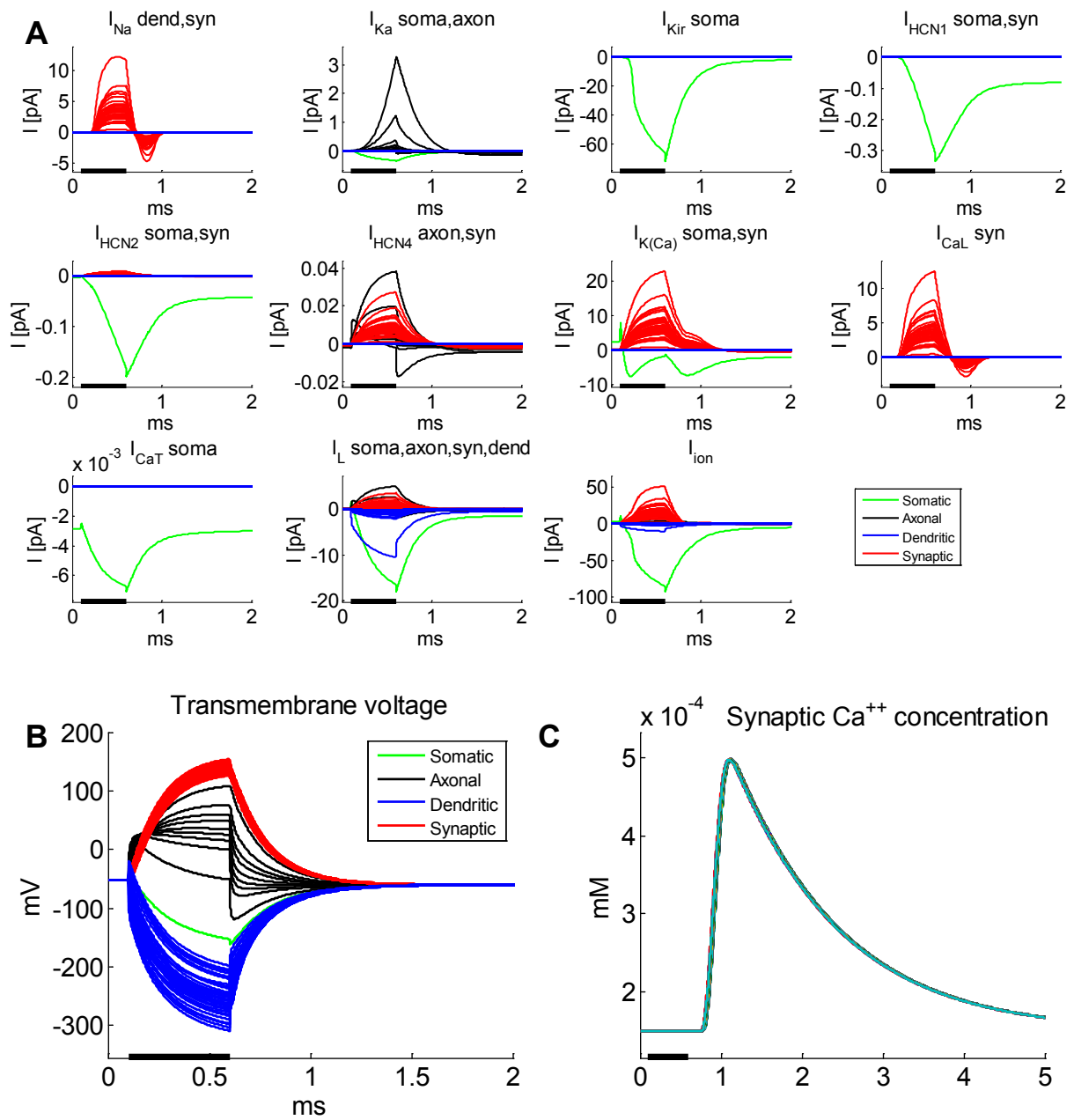


Figure 3.50 Subretinal implant, 0.5 ms pulse at +2 V

Current time-courses (A) at +2 V caused inward somatic dendritic currents and largely outward axonal and synaptic currents. Synaptic transmembrane voltage (V_m) reached values of appr. +150 mV (B). as in the previous figure, synaptic $[Ca^{++}]_i$ (C) increased to appr. 0.5 μM .

3.4.1.4 Biphasic Pulses

The following simulations were performed with symmetric cathodic-first and anodic-first biphasic pulses at 1 V. Each phase had a duration of 0.5 ms.

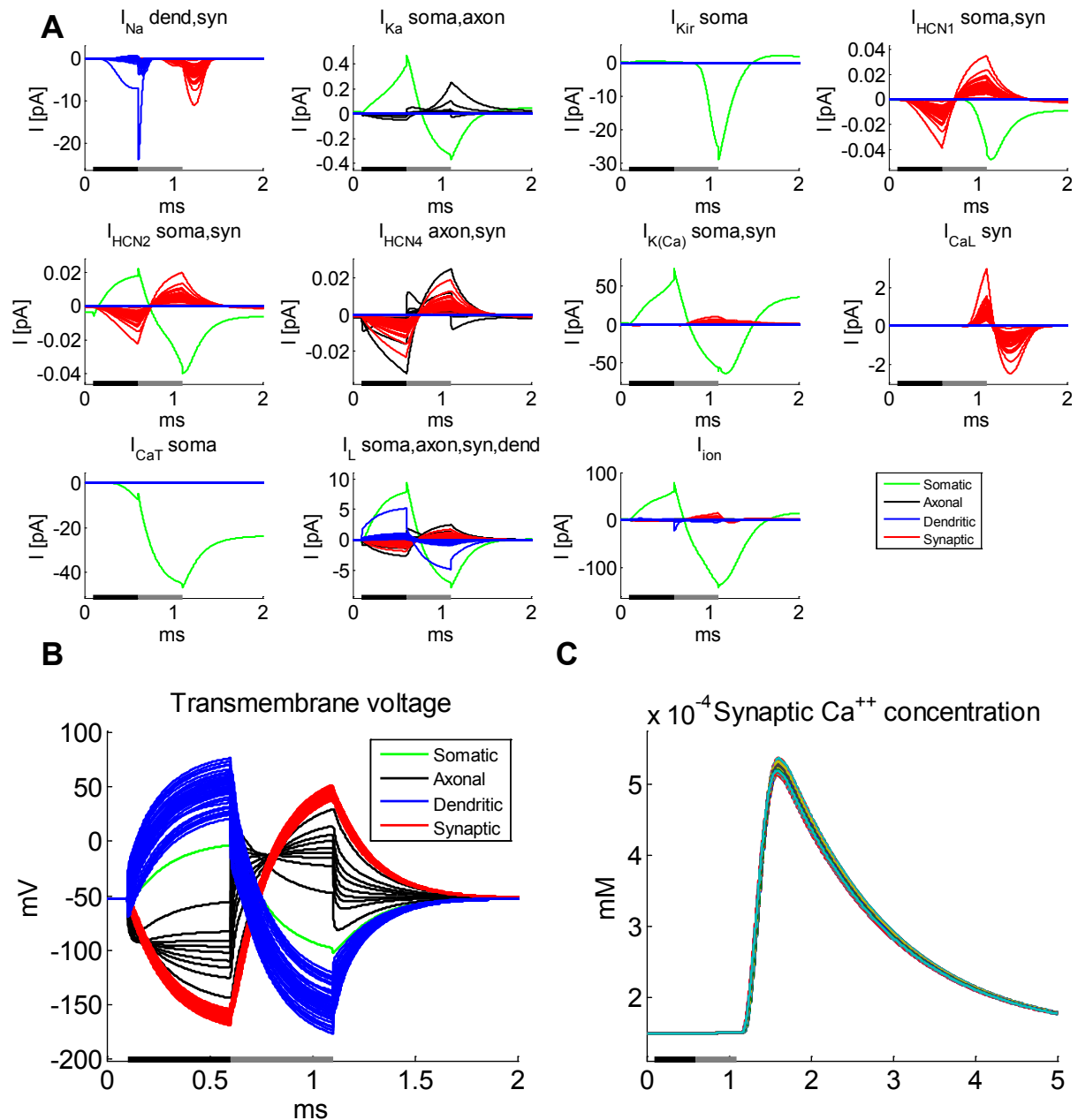


Figure 3.51 Cathodic-first, 1 ms pulse at 1 V

Simulation of a cathodic-first biphasic pulse. Most synaptic and dendritic currents (A) reversed their direction (inward or outward) in response to the reversed potential of the stimulus (black bar at bottom of plot: first phase, grey bar: second phase). Synaptic Na^+ and L-type Ca^{++} currents were initiated at the end of stimulation. The transmembrane voltage (B) also responded according to potential reversal, leading to a depolarization of synaptic V_m at appr. +50 mV at the end of the stimulus. Synaptic $[Ca^{++}]_i$ at axon terminals (C) were increased from 0.15 μM to appr. 5.3 mM 1 ms after end of stimulation.

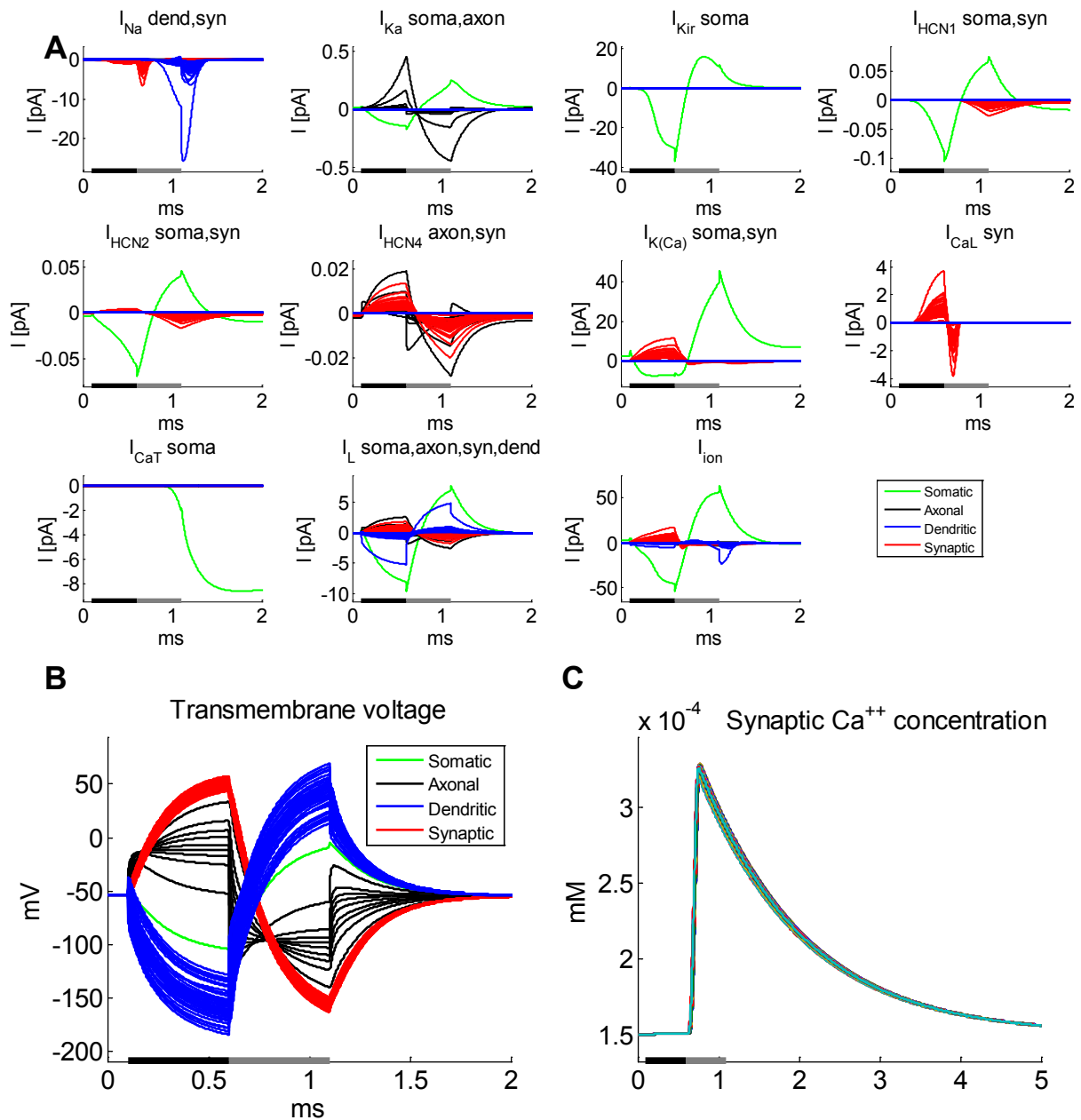


Figure 3.52 Anodic-first, 1 ms pulse at 1 V

Single compartment current traces (A) during an anodic-first biphasic pulse were mostly the opposite of currents during cathodic-first stimulation, however, synaptic outward L-type Ca^{++} currents initiated during the anodic phase and inward somatic T-type Ca^{++} currents initiated after the cathodic phase. Synaptic V_m (B) was at appr. -150 mV at the end of the stimulus. $[Ca^{++}]_i$ (C) increased after the anodic phase and reached appr. 0.33 μM .

3.4.1.5 Stimulus Bursts

The following section presents results from simulation of 5 consecutive rectangular anodic stimuli forming a stimulus burst. Different inter-stimulus intervals (ISI) were used to investigate different stimulation frequencies. Anodic pulses were used due to their stronger influence on $[Ca^{++}]_i$.

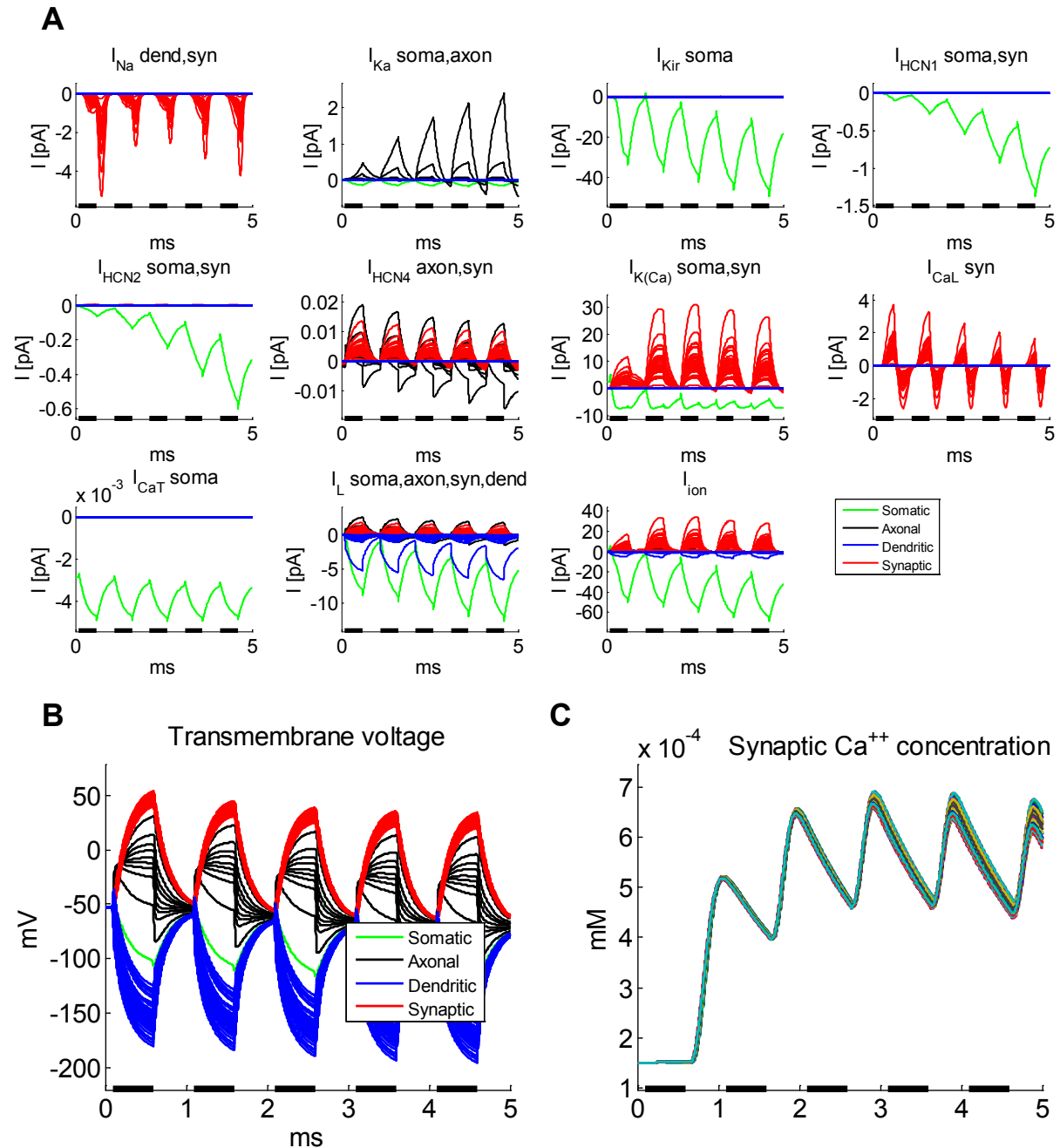


Figure 3.53 Five 0.5 ms pulses at +1 V with 0.5 ms pause

Current traces (A) during five repetitions of depolarizing pulses. Synaptic Na^+ , L-type Ca^{++} and HCN4 currents decreased in the course of the five stimuli. Somatic Kir , HCN1 and HCN2 currents as well as axonal Ka and synaptic $K(Ca)$ currents increased compared to the first pulse. V_m (B) exhibited a trend towards more negative potentials, retaining appr. the same difference between maximal and minimal amplitudes while synaptic compartments remained depolarized most of the time. Synaptic $[Ca^{++}]_i$ (C) increased between the first and second stimuli to $0.52 \mu M$, reached appr. $0.7 \mu M$ before the onset of the other stimuli and did not return to its initial resting value throughout the simulation.

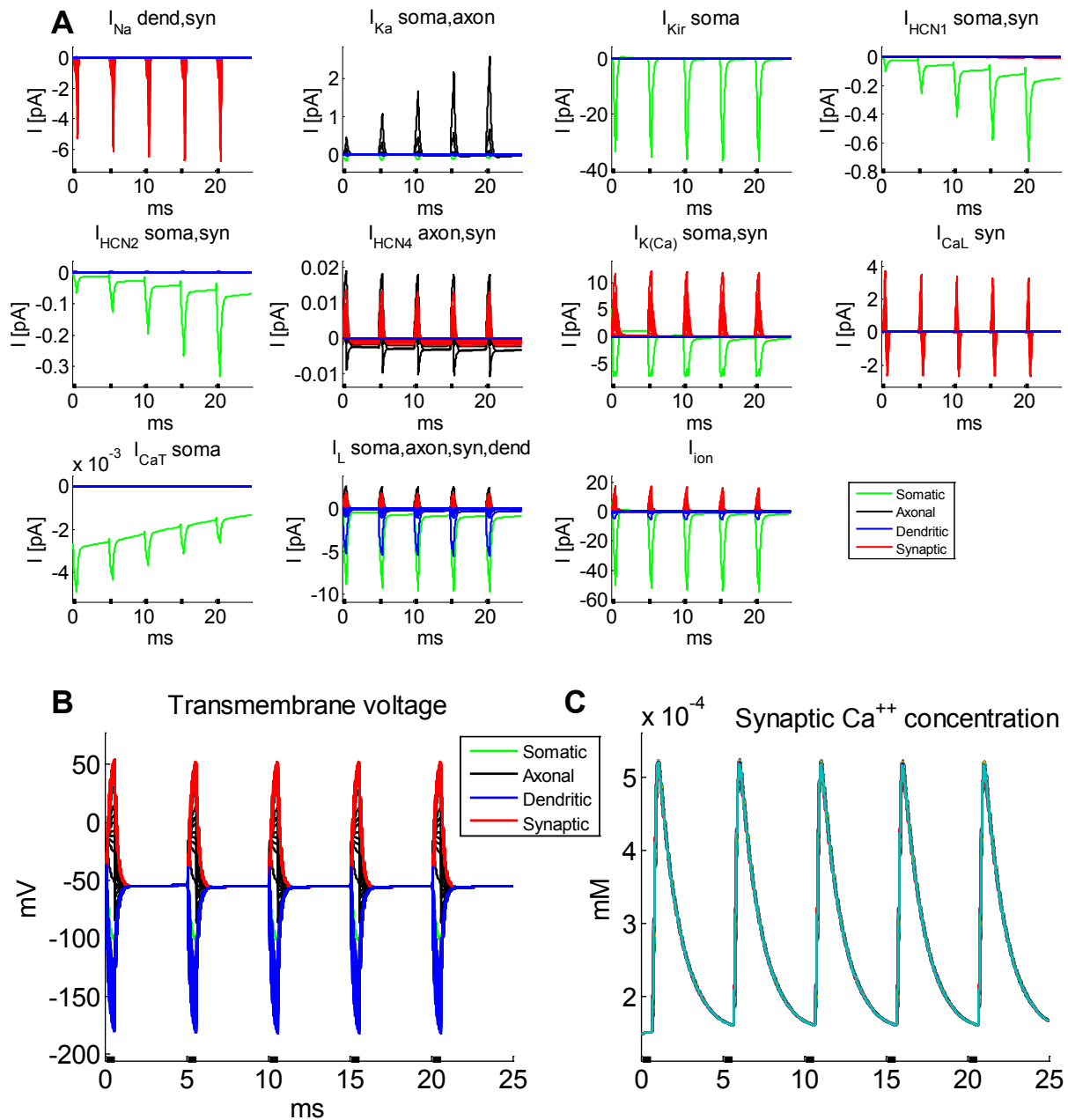


Figure 3.54 Five 0.5 ms pulses at +1 V with 4.5 ms pause

Five repetitions of +1 V pulses with 5 ms between stimulus onsets. Most currents (A) were stable throughout the time-course. Somatic HCN1 and HCN2 as well as axonal K_a current amplitudes increased during stimulations. Somatic T-type currents showed a decreasing trend. Both V_m (B) and synaptic $[Ca^{++}]_i$ (C) returned to their resting values before onset of the next stimulus.

3.4.1.6 Dipolar Stimulation

This section contains a simulation using the dipolar electrode configuration with a ring electrode for local current return around the central disk electrode.

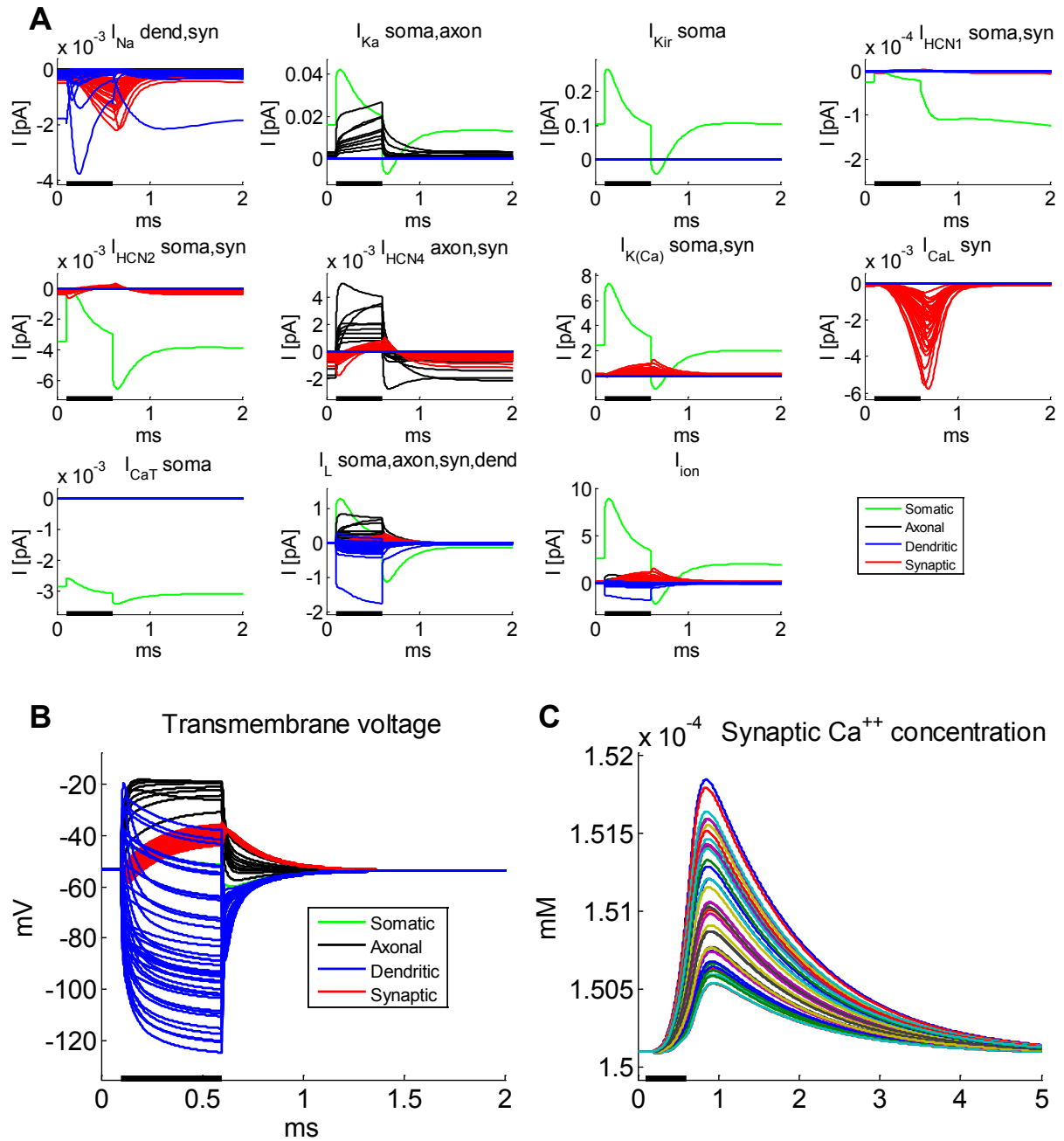


Figure 3.55 Monophasic 0.5 ms pulse with 2 V (-1 V & +1 V)

Current time-courses during dipolar stimulation (A) at 2 V were considerably smaller than during monopolar stimulation, most had amplitudes below 1 pA. Synaptic compartments were depolarized (B) from -53 mV to appr. -40 mV. Synaptic $[Ca^{++}]_i$ (C) showed slight increases.

3.4.2 OFF Cone Bipolar Cell

The morphological properties of the ideal OFF-type CBC model were based on a type 2 rat CBC (Figure 3.56 A). The type 2 CBC was chosen to maximize the difference between ON and OFF cell lengths in the model while still representing a stereotypical OFF bipolar cell. This cell has originally been identified by (Euler and Wässle 1995). An swc-file (see section 2.3.1.1) was generated for this cell in order to create a three-dimensional morphological model (Figure 3.56 B), which was then equipped with the appropriate ion channels (Figure 3.56 C, see also sections 3.2.9.3 and 3.2.10).

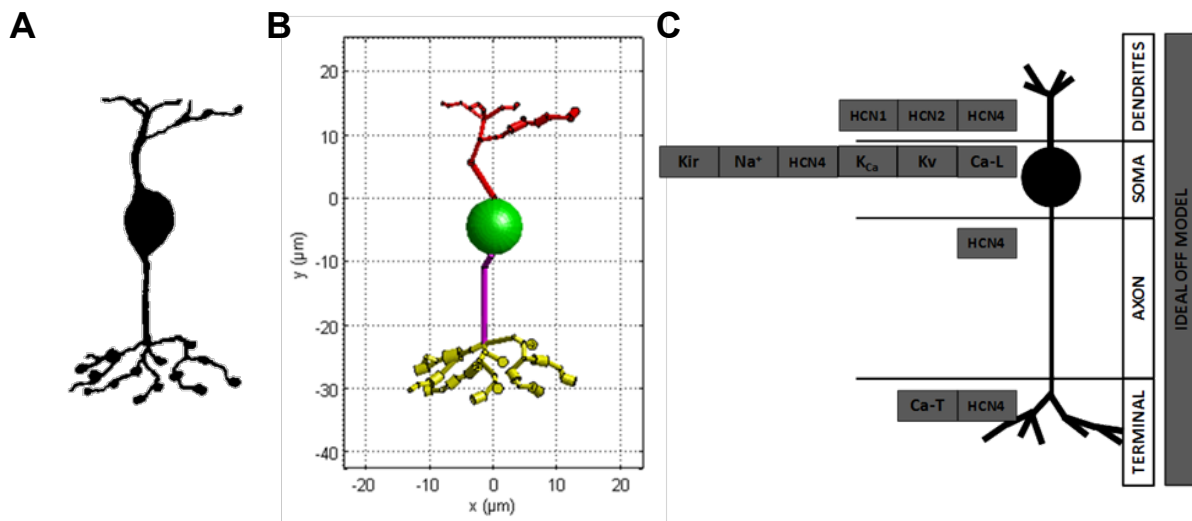
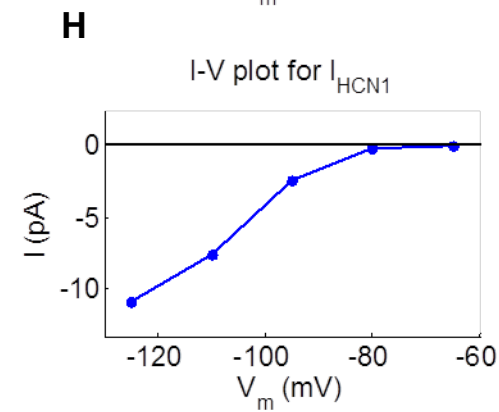
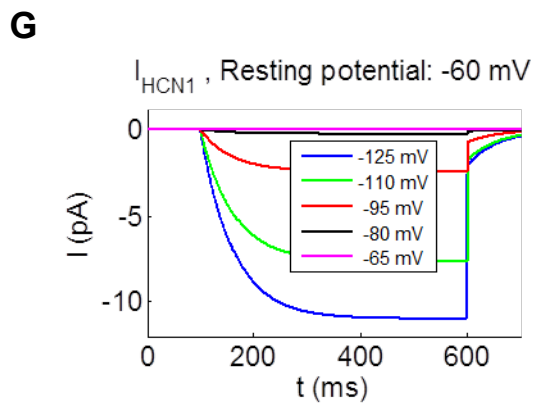
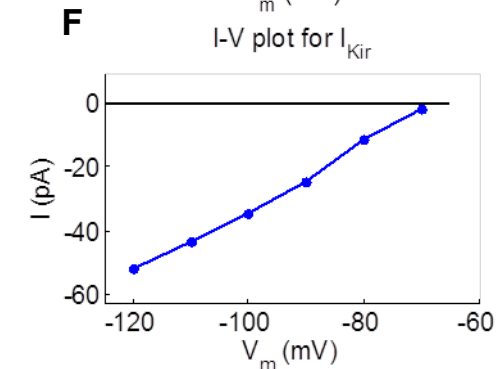
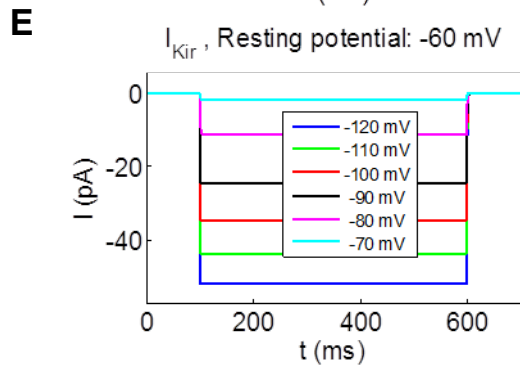
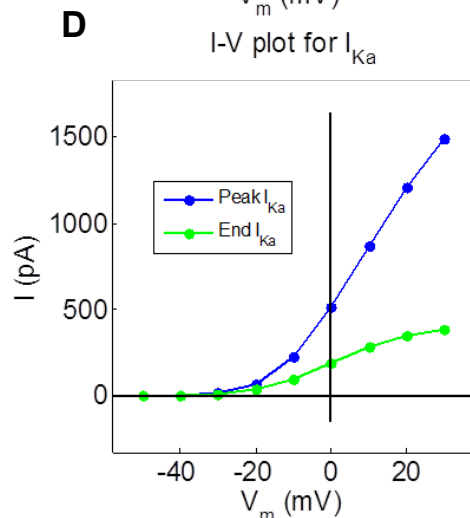
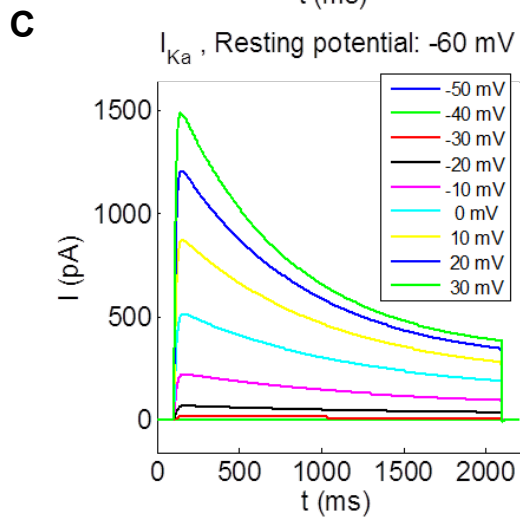
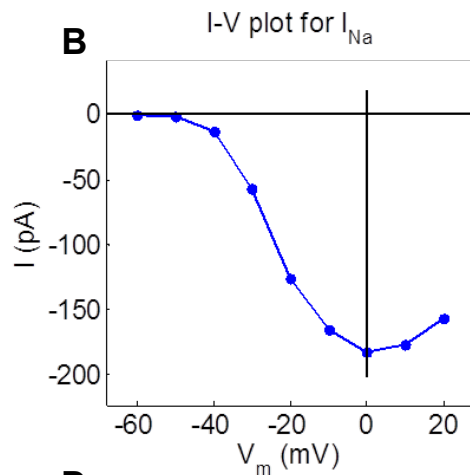
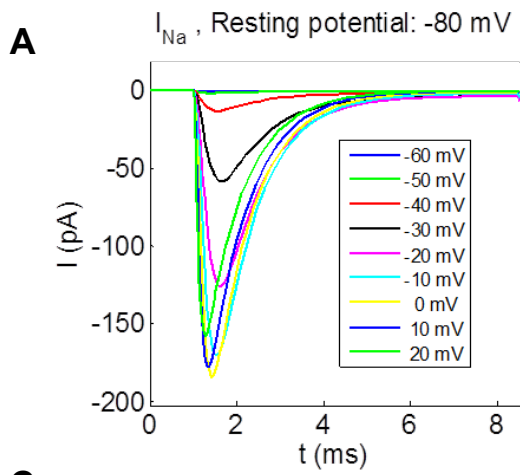
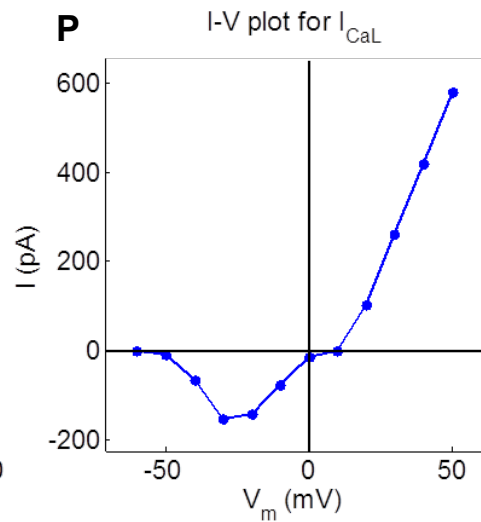
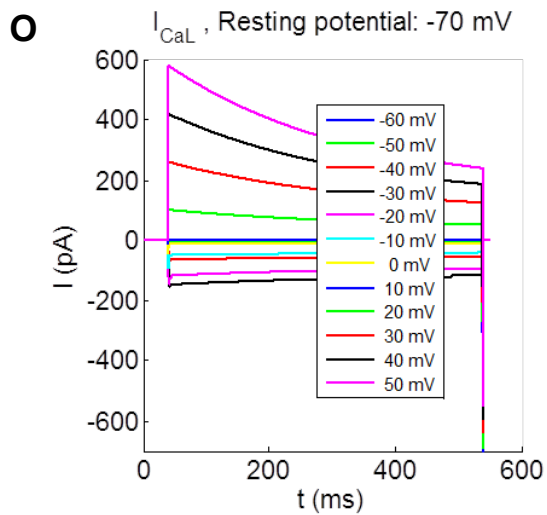
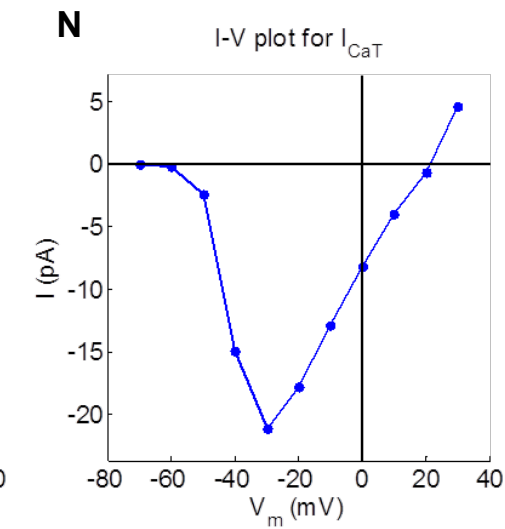
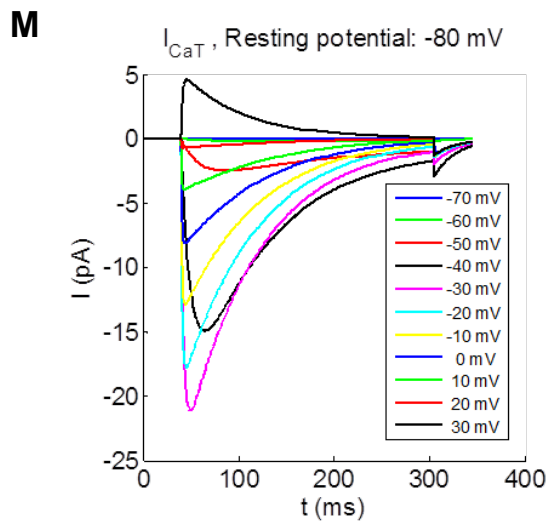
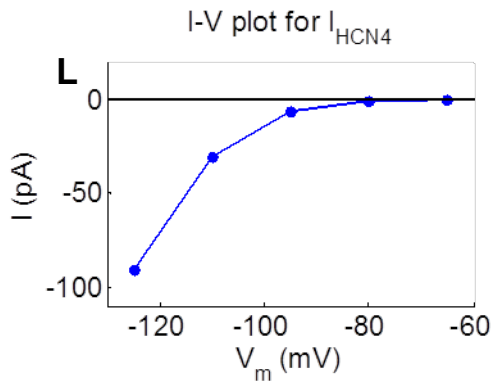
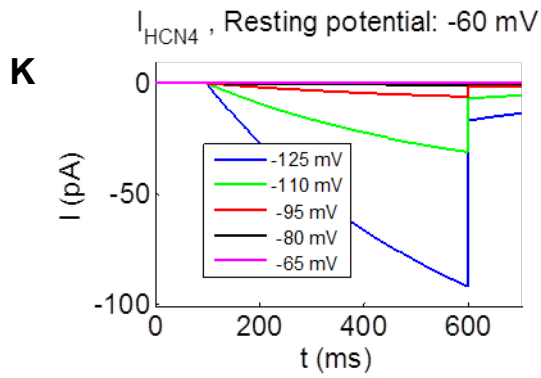
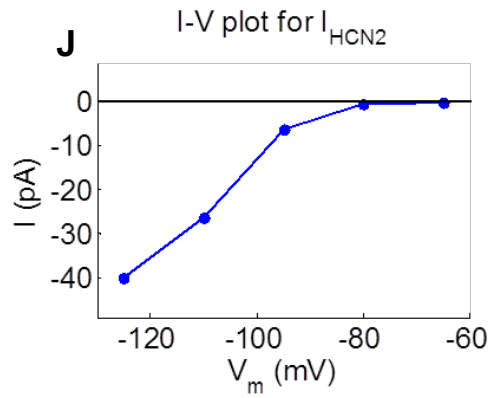
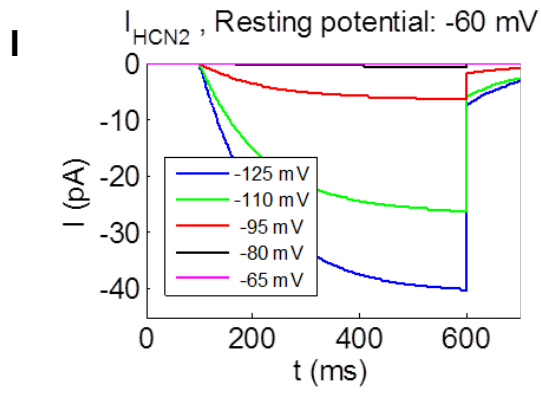


Figure 3.56

Type 2 rat CBC used (A) as morphological reference for the ideal OFF-type CBC model. Image modified from (Euler and Wässle 1995). Three dimensional morphological model (B) generated for the reference cell. Colors represent different neuronal regions, red: dendrites, green: soma, purple: axon, yellow: axon terminal. Ion channel equipment (C) assumed for the ideal OFF-type CBC model.

The amplitudes of the currents generated by these ion channels and their current-voltage relationships are demonstrated in Figure 3.57. They differ from the ionic currents of the ideal ON-type CBC both in relation to their subcellular neuronal localizations (dendrites, soma, axon, synaptic axon terminal) and quantitatively by their amplitudes due to different conductivities.





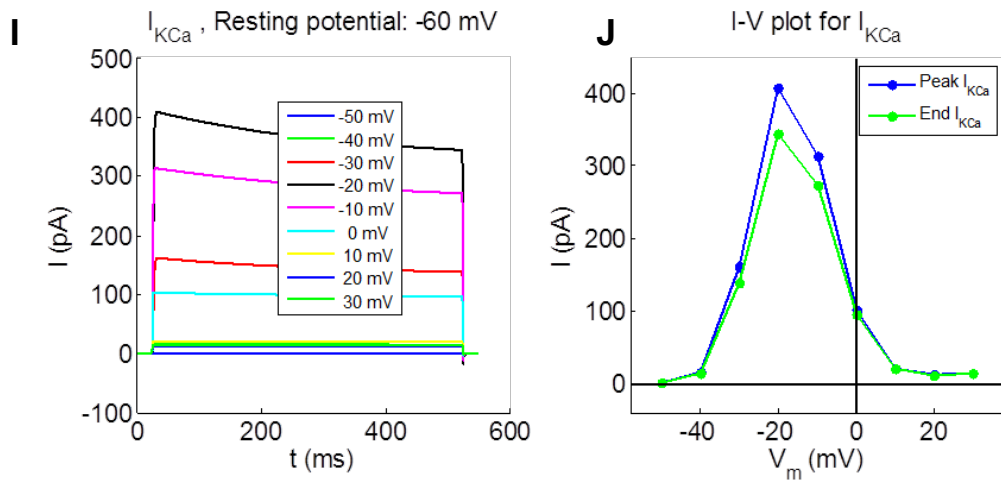


Figure 3.57

A-R: Whole-cell amplitudes of all currents used in the ideal OFF-type CBC under voltage-clamp (step-clamp) conditions. In the left panels, time-courses of whole-cell currents during different voltage-steps are shown. The right panels show the peak amplitudes of these current traces plotted against each holding voltage of the voltage-step. For I_{KCa} and $I_{K(Ca)}$ the current amplitude at the end of the voltage-step pulse was also plotted additionally in the right panel.

3.4.2.1 Hyperpolarizing Pulses

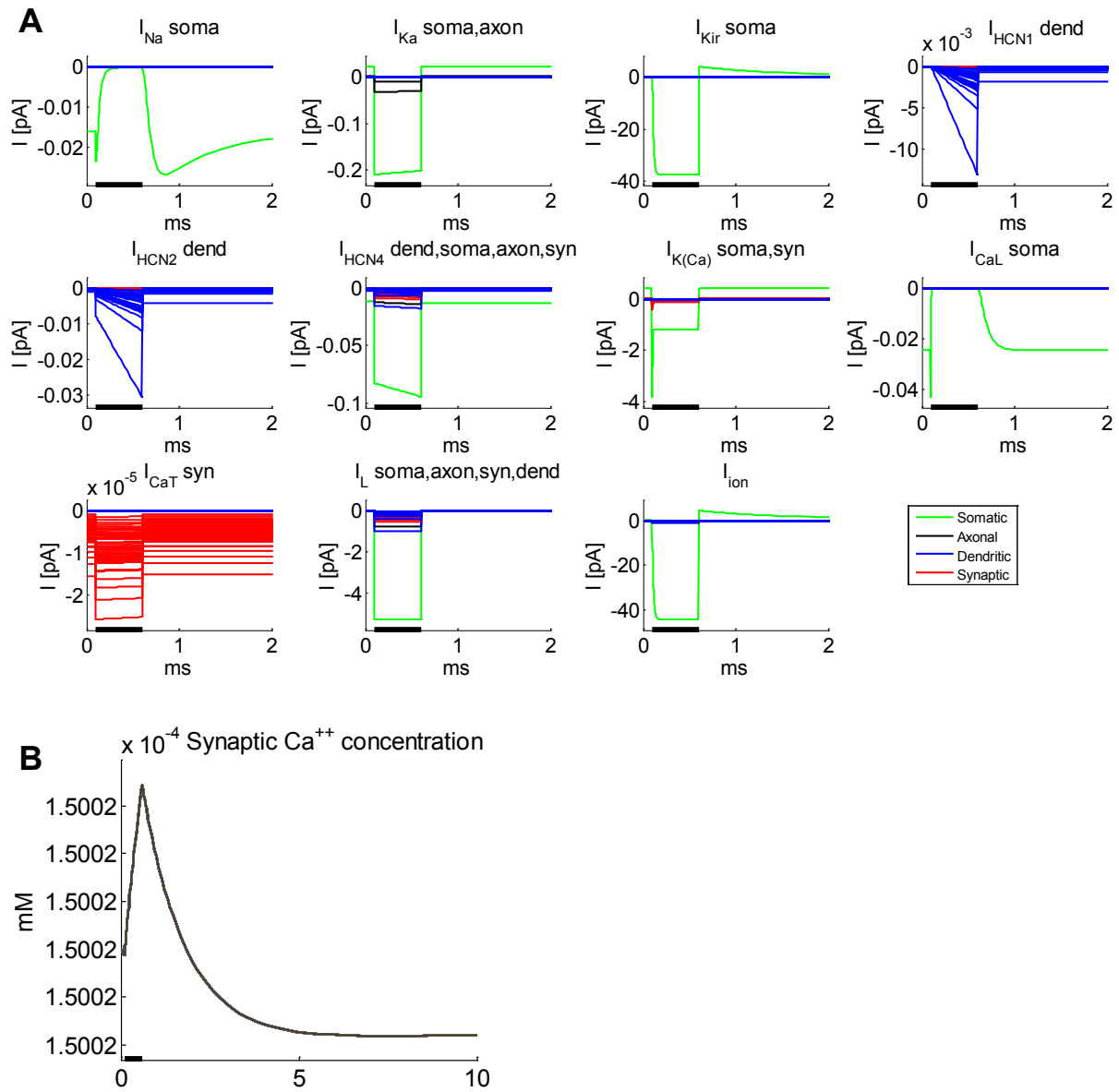


Figure 3.58 Voltage clamp, 0.5 ms pulse from -53 mV to -103 mV

Single compartment current traces (A) in the ideal OFF-type CBC model from a hyperpolarizing voltage-clamp simulation. The majority of currents in all compartments were negative and therefore inward currents. The synaptic $[Ca^{++}]_i$ (B) had negligible increases.

Note that a longer time axis is used to depict Ca^{++} concentration changes for all OFF cell figures relative to the preceding ON cell figures.

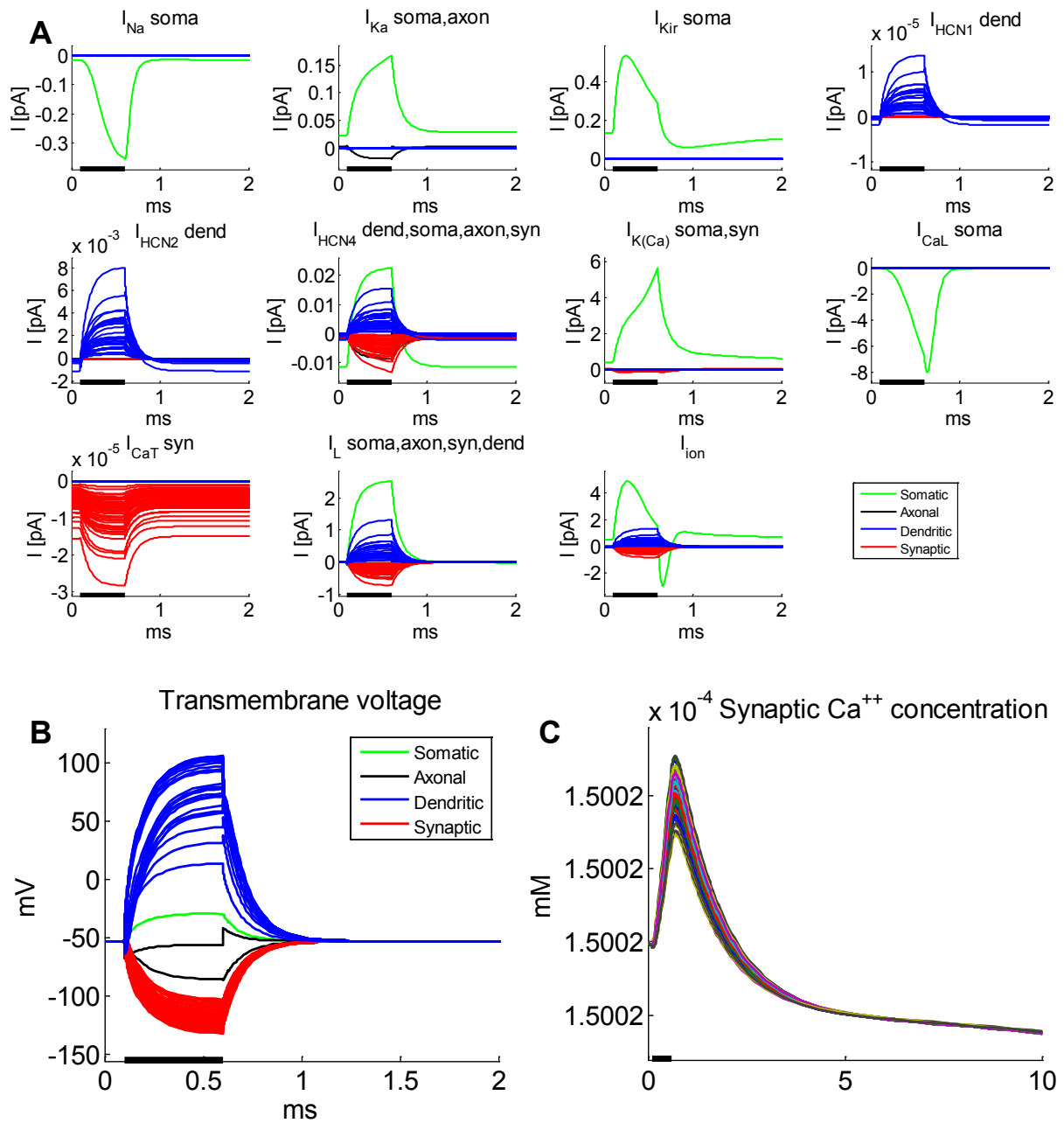


Figure 3.59 Subretinal implant, 0.5 ms pulse at -1 V

OFF-CBC current traces (A) during a -1 V subretinal stimulation. Dendritic currents were mostly outward while synaptic currents mostly went inward. Both directions could be observed for somatic currents, which usually peaked at the end of the stimulus. The transmembrane voltage (V_m) plot (B) showed dendritic depolarization and synaptic hyperpolarization. The synaptic $[Ca^{++}]_i$ at axon terminal (C) showed small changes.

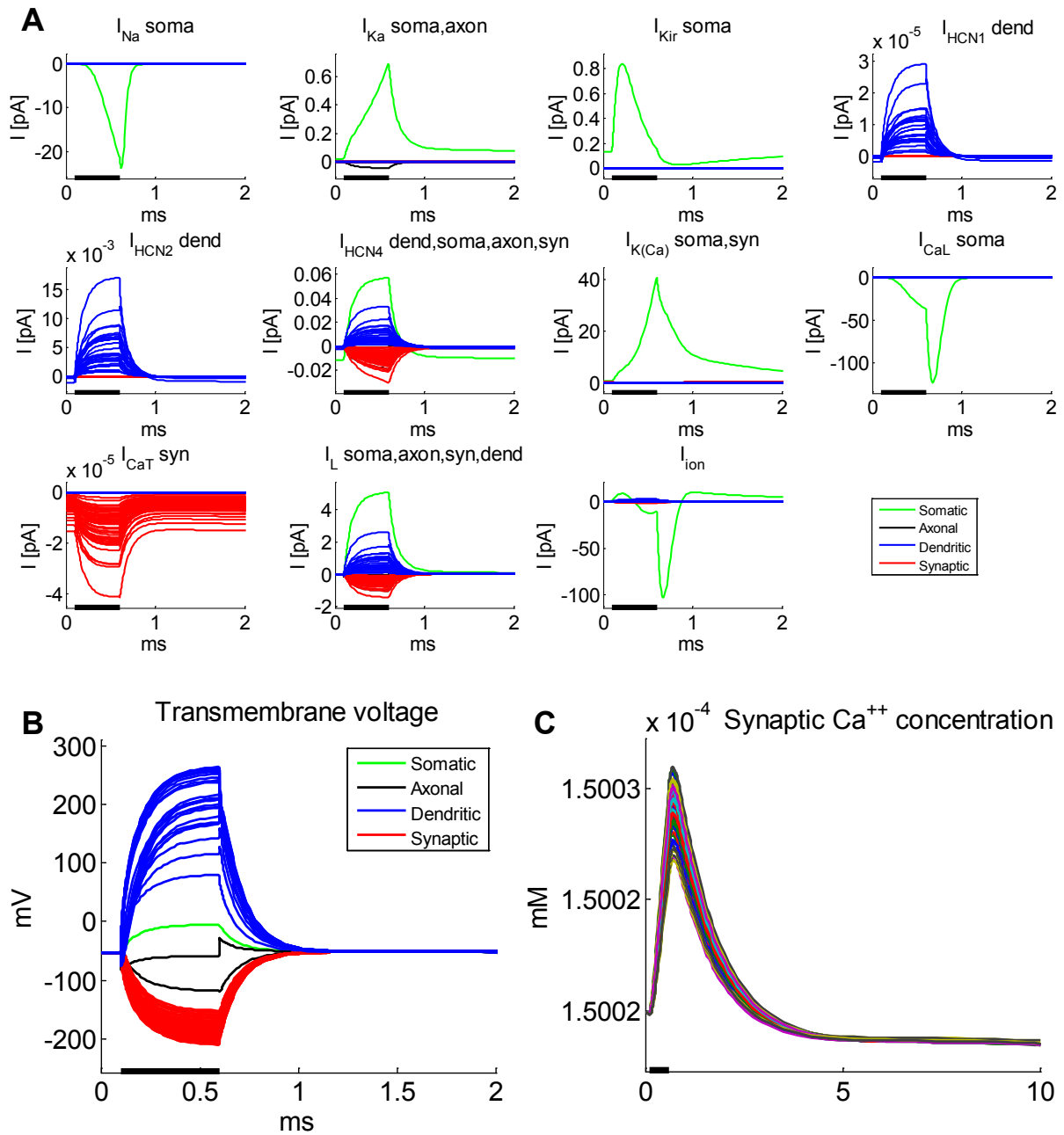


Figure 3.60 Subretinal implant, 0.5 ms pulse at -2 V

Simulation of a -2 V subretinal stimulation resulted in current time-courses (A) and V_m (B) qualitatively very similar to stimulation with -1 V but with larger amplitudes. $[Ca^{++}]_i$ at the synaptic terminals (C) did not increase significantly.

3.4.2.2 Depolarizing Pulses

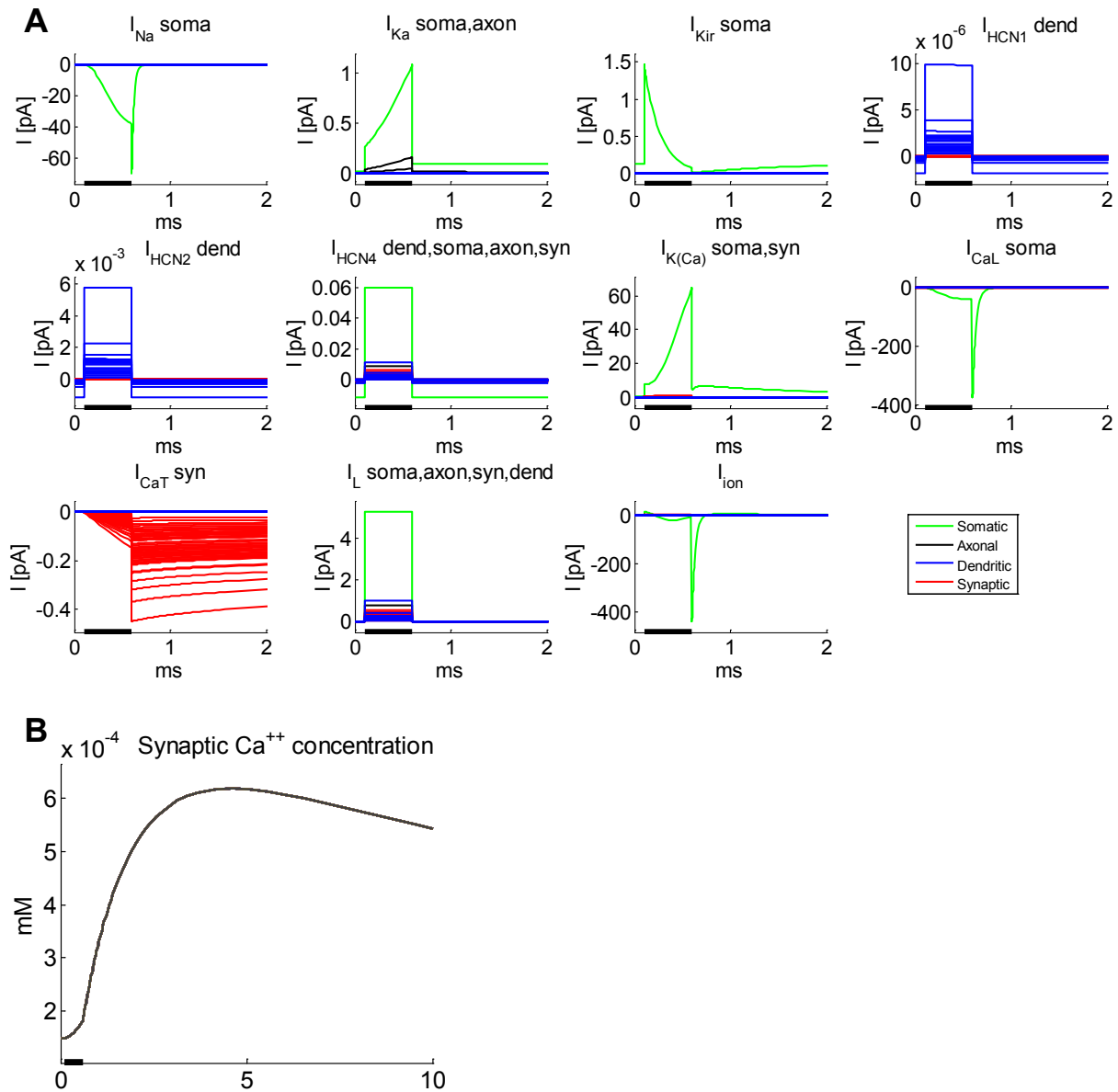


Figure 3.61 Voltage clamp, 0.5 ms pulse from -53 mV to -3 mV

Current-traces from a depolarizing voltage-clamp simulation (A) exhibited strong somatic inward L-type currents up to -400 pA at the end of the simulation. The synaptic Ca^{++} concentration at axon terminal (B) increased during the voltage pulse and the following 4 ms. $[Ca^{++}]_i$ (C) did not return to its resting value within the 10 ms simulation period.

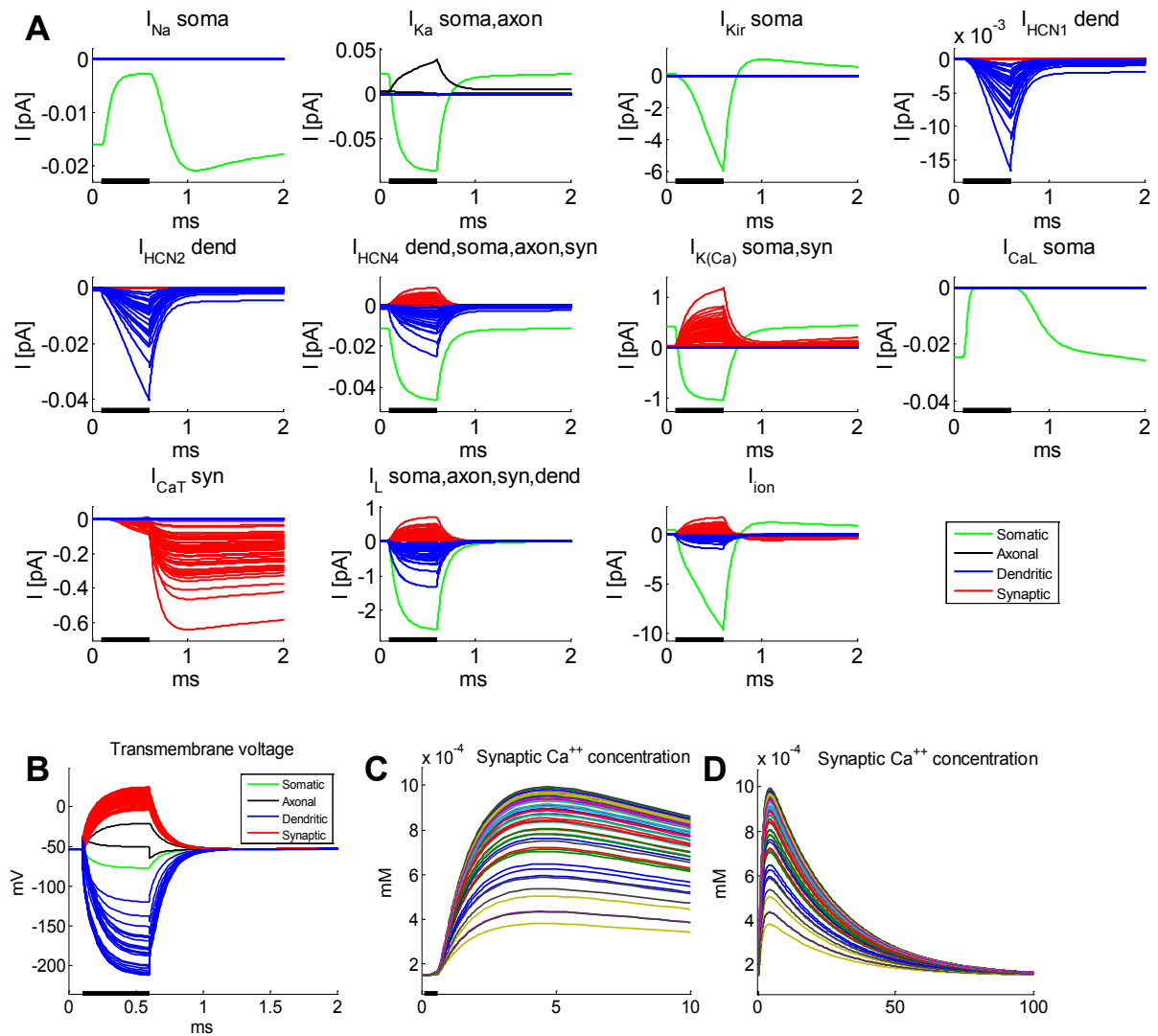


Figure 3.62 Subretinal implant, 0.5 ms pulse at +1 V

A +1 V extracellular stimulus led to inward synaptic T-type Ca^{++} currents (A). Inward dendritic currents also resulted for the other ion channels. V_m (B) was increased from -53 mV to appr. +25 mV in synaptic compartments. V_m returned to its resting potential in all compartments within 1 ms of end of stimulation. Synaptic $[Ca^{++}]_i$ (C) peaked at 1 μ M appr. 5 ms after stimulus onset and required up to 100 ms to return to resting values (D). In contrast to the ON model, $[Ca^{++}]_i$ varied significantly across the different synaptic compartments.

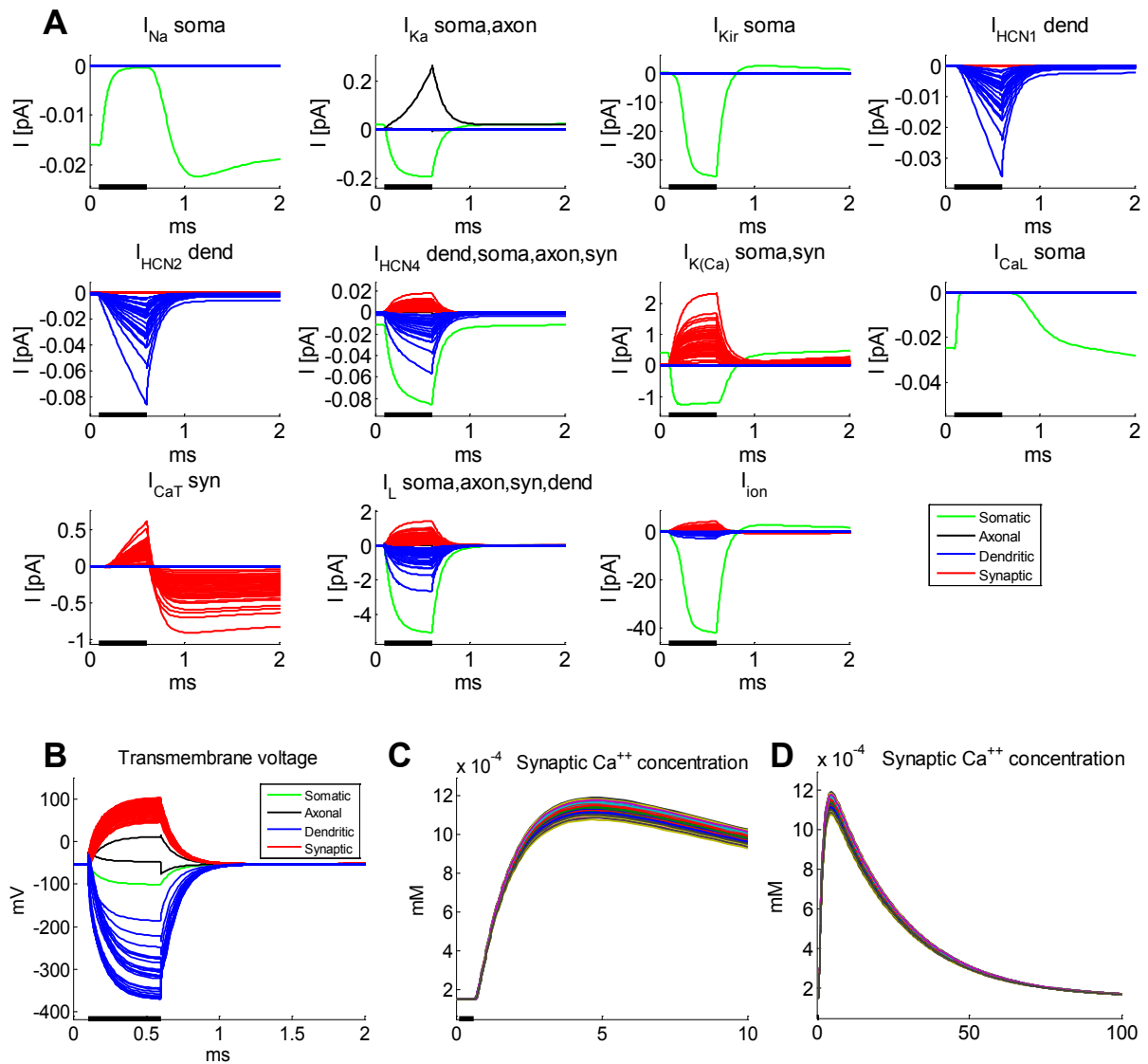


Figure 3.63 Subretinal implant, 0.5 ms pulse at +2 V

Single-compartment current traces (A) were mostly similar to +1 V stimulation. All dendritic ion channels produced inward currents. Synaptic T-type Ca^{++} currents showed an initial inward direction and changed the direction after the end of the stimulus. The synaptic membrane was depolarized from its resting potential up to +100 mV (B). $[\text{Ca}^{++}]_i$ in synaptic terminal compartments reached values of 1.2 μM (C), the decrease to resting values required approximately 100 ms.

3.4.2.3 Biphasic Pulses

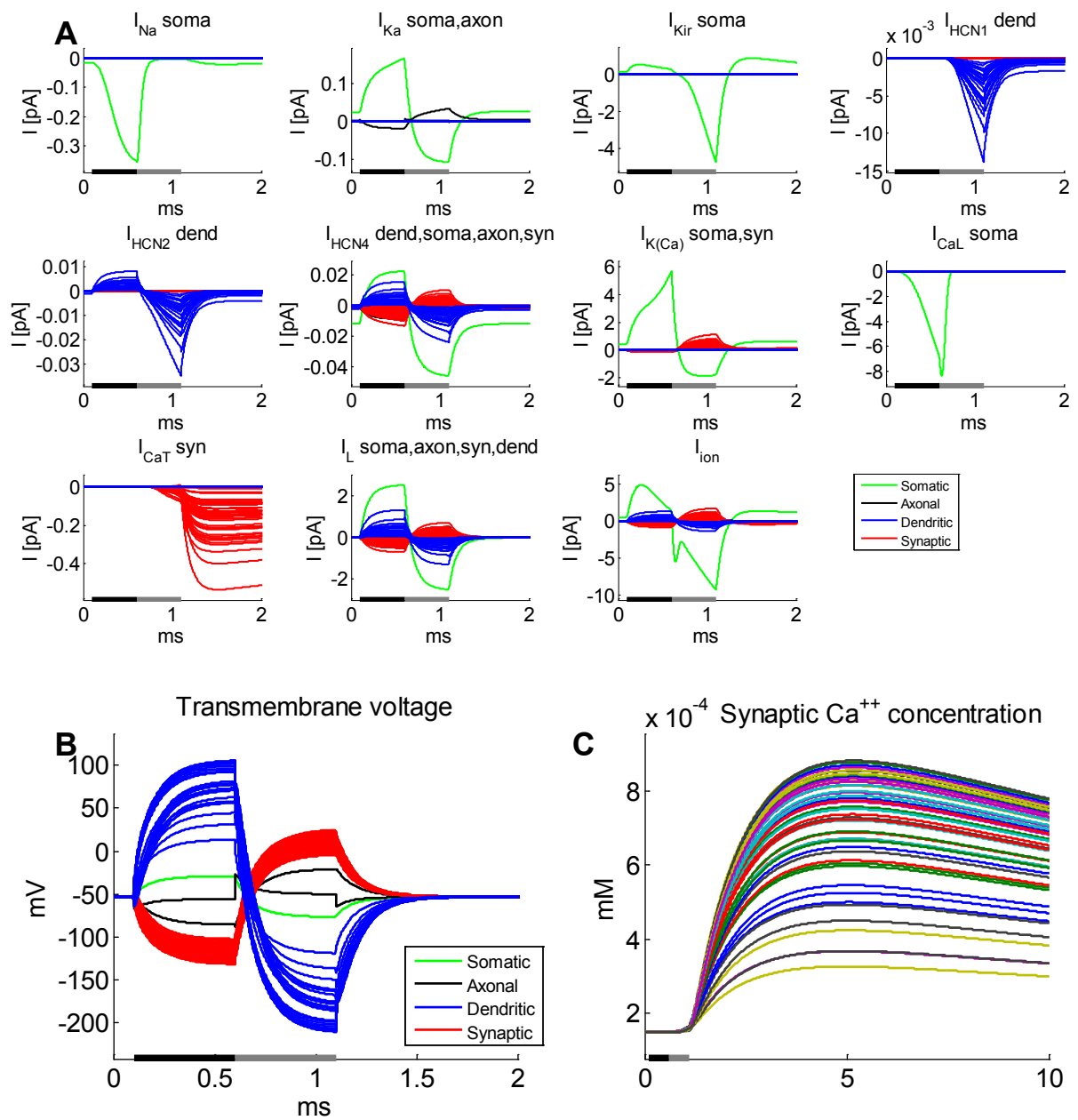


Figure 3.64 Cathodic-first, 1 ms pulse at 1 V

Cathodic-first biphasic pulse at 1 V. The direction (inward or outward) of HCN2, HCN4, K(Ca) and leak currents (A) changed with the polarity of the stimulating voltage pulse. Somatic L-type and synaptic T-type Ca^{++} were inward only and initiated during the cathodic or anodic phase, respectively. The resulting voltage time-course (B) showed synaptic depolarization of appr. +25 mV at the end of stimulation. $[Ca^{++}]_i$ in axon terminals (C) started to increase after the stimulation and peaked at appr. $0.9 \mu M$ 5 ms after the end of stimulation. It did not decrease significantly within the 10 ms simulation period.

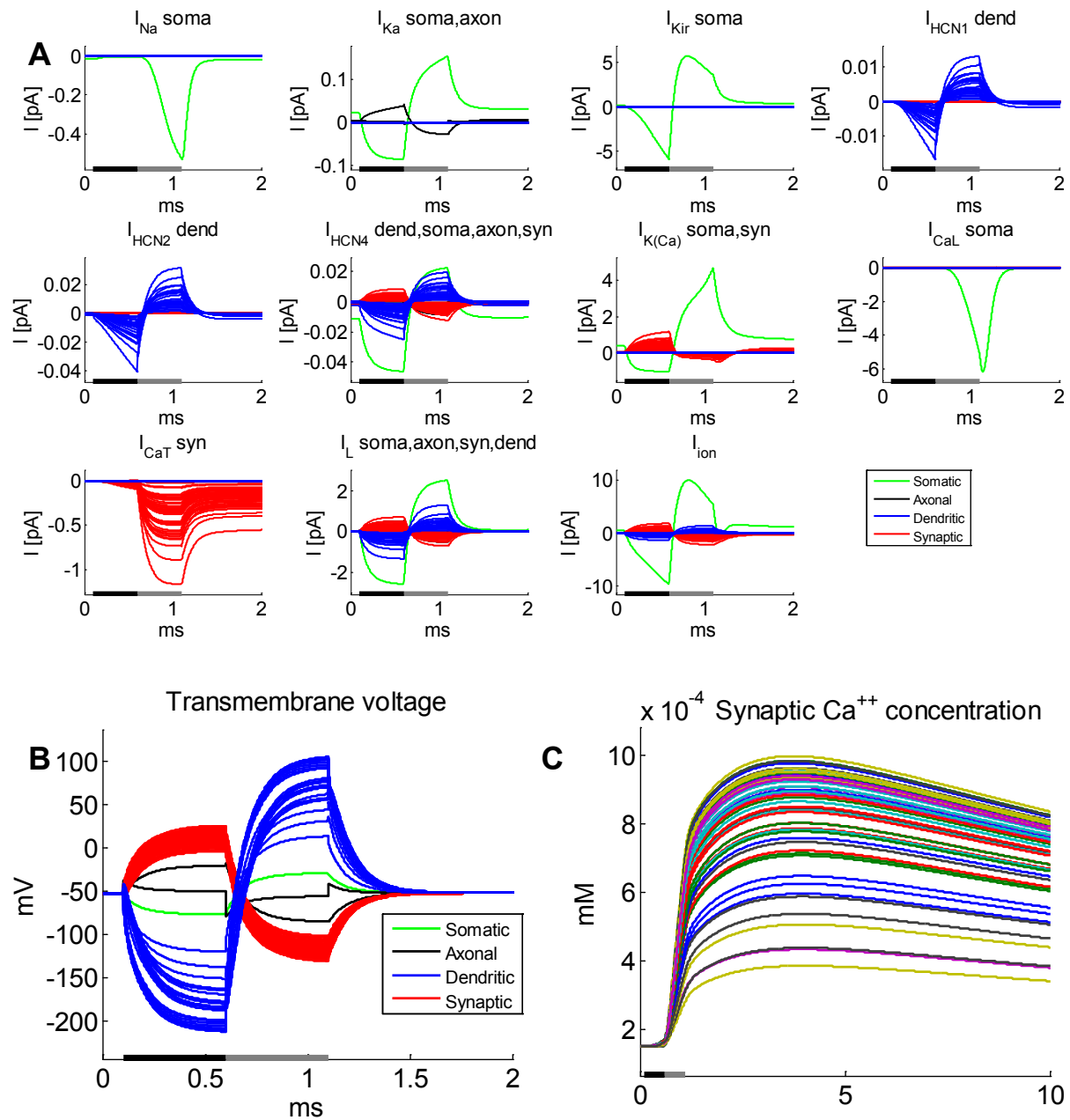


Figure 3.65 Anodic-first, 1 ms pulse at 1 V

Biphasic anodic-first stimulation. The ionic currents (A) mostly changed from inward to outward with changing stimulus polarity. All synaptic compartments showed inward Ca^{++} currents which were retained during the 10 ms simulation period. Resulting V_m curves for all compartments (B). The synaptic $[Ca^{++}]_i$ (C) started to increase with initiation of the cathodic pulse phase, followed by a steep rise up to 1 μM and a decrease to appr. 80% of the peak value after 10 ms.

3.4.2.4 Stimulus Bursts

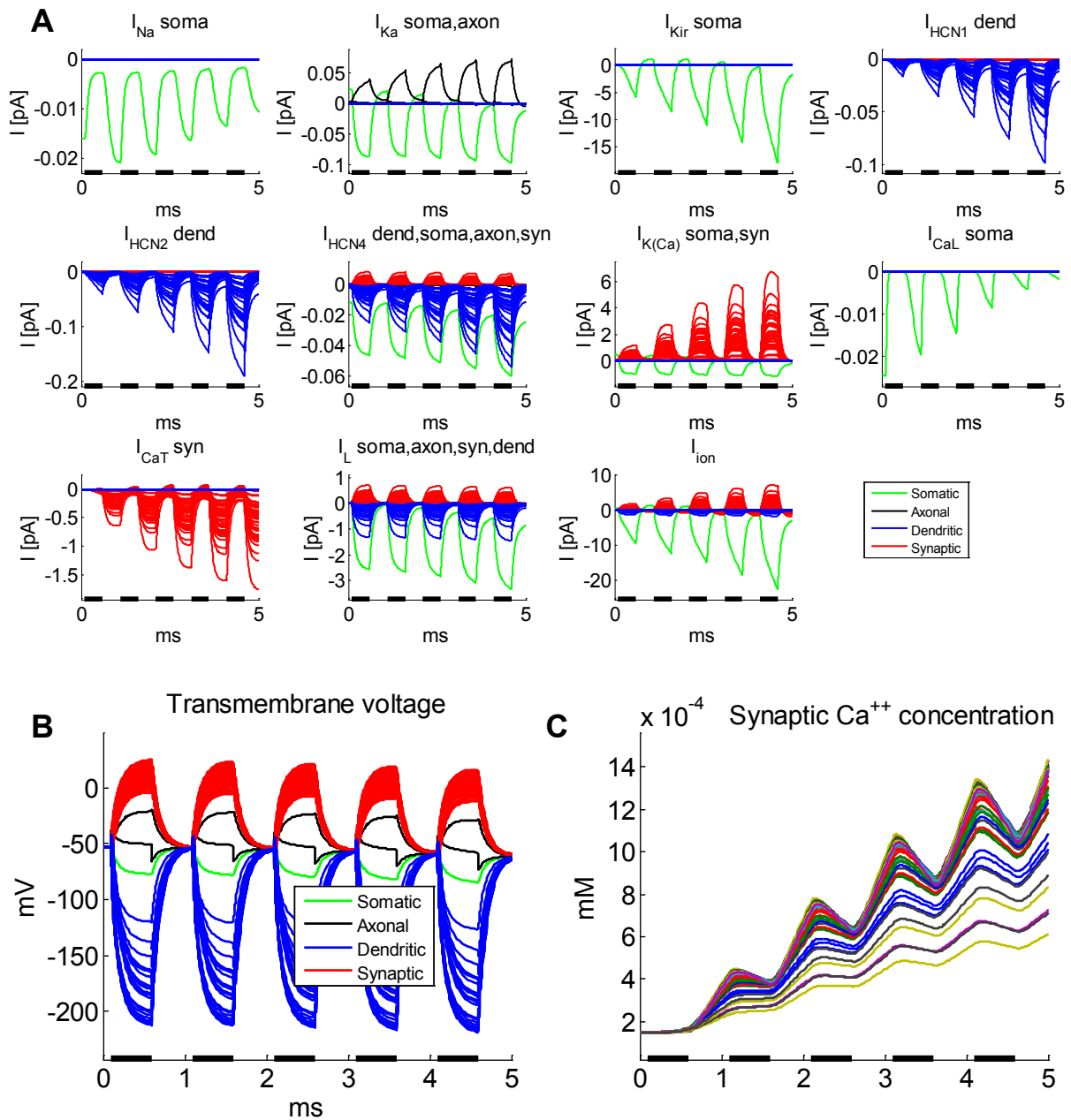


Figure 3.66 Five 0.5 ms pulses at +1 V with 0.5 ms pause

During 5 repetitions of the same 1 V stimulus Kir, HCN1, HCN2, K(Ca) and T-type Ca^{++} currents increased with each additional pulse. Amplitudes of somatic Na^+ and L-type Ca^{++} currents decreased. The sum of all ionic currents (i_{ion}) showed a net increase for inward and outward currents throughout 5 stimulations. Transmembrane voltage (B) remained mostly stable, with slight decreases of maximal synaptic depolarization. Synaptic $[\text{Ca}^{++}]_i$ (C) increased during non-stimulation phases and were reduced when the stimulus was active (black bars at bottom of plots). The concentration increases were larger than the decreases, resulting in a cumulative addition with each additional stimulus.

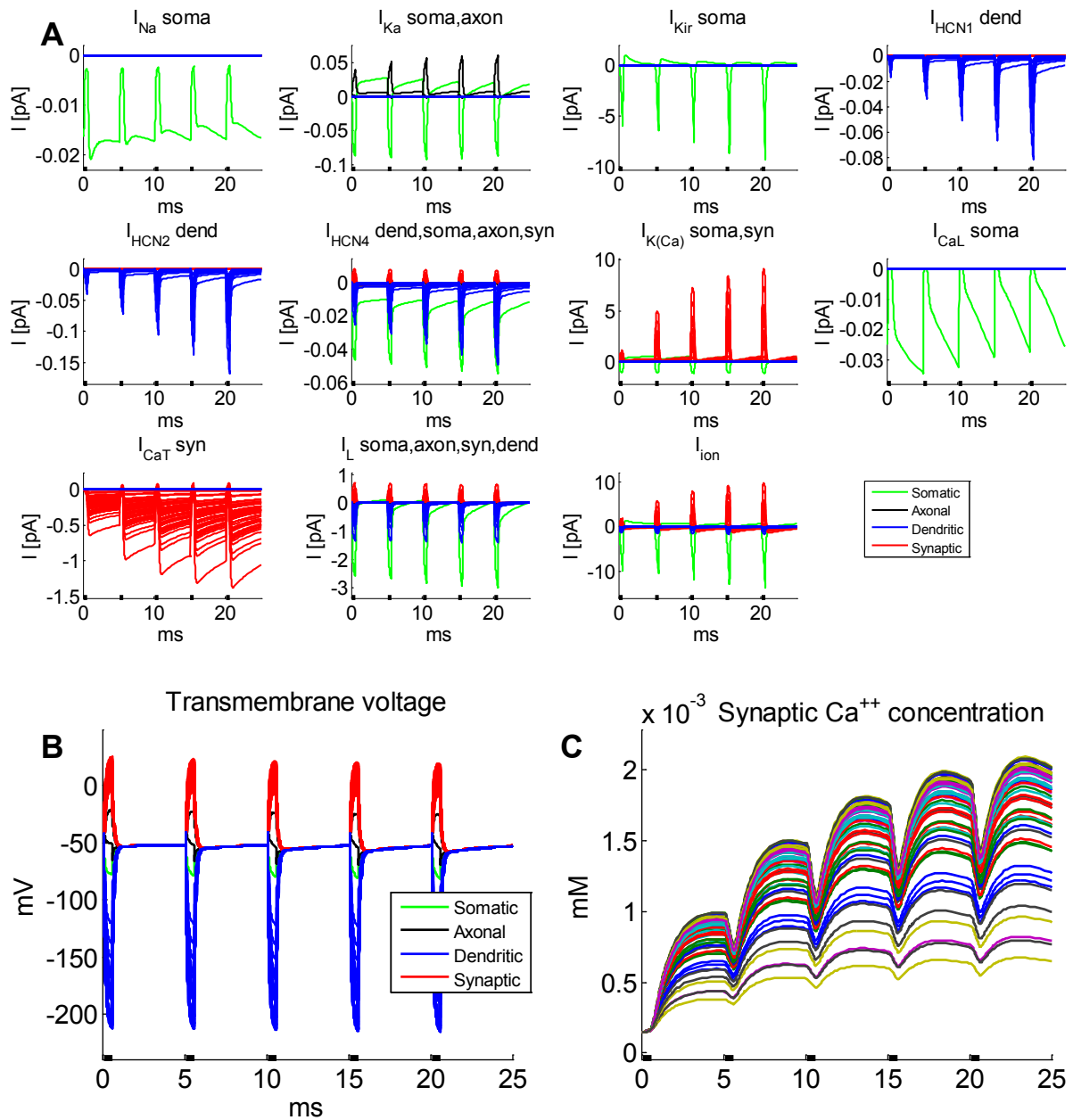


Figure 3.67 Five 0.5 ms pulses at +1 V with 4.5 ms pause

Repetition of 5 pulses with pause intervals of 5 ms. The behavior of ionic currents (A) was qualitatively similar to the previous higher frequency simulation, but the relative changes of maximal amplitudes were less pronounced. V_m showed no significant changes within the 5 stimulations, but in the phases between stimulations a slight trend towards more positive potentials could be observed (B). $[Ca^{++}]_i$ at the axon terminals (C) showed accumulated increases after each additional stimulation, with a tendency to reach an overall saturation level. The concentrations peaked appr. 3-4 ms after end of stimulation followed by a gradual decrease. During the actual stimulation, the concentration decreased more quickly, but did not return to resting levels.

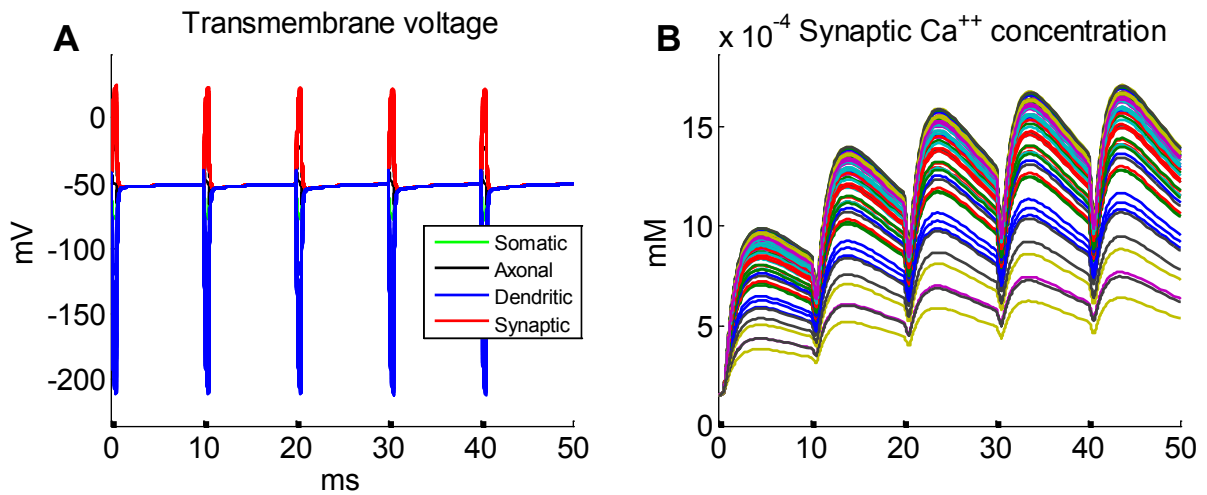


Figure 3.68 Five 0.5 ms pulses at +1 V with 9.5 ms pause

Transmembrane voltage (B) of the ideal OFF-type CBC during five pulses at 1 V with 10 ms inter-stimulus interval (ISI). Synaptic $[Ca^{++}]_i$ (C) increased after the end of each stimulation (black bars at bottom), peaked appr. 3-4 ms later and then started to decrease but did not return to the initial values, resulting in an asymptotic increase of Ca^{++} concentration.

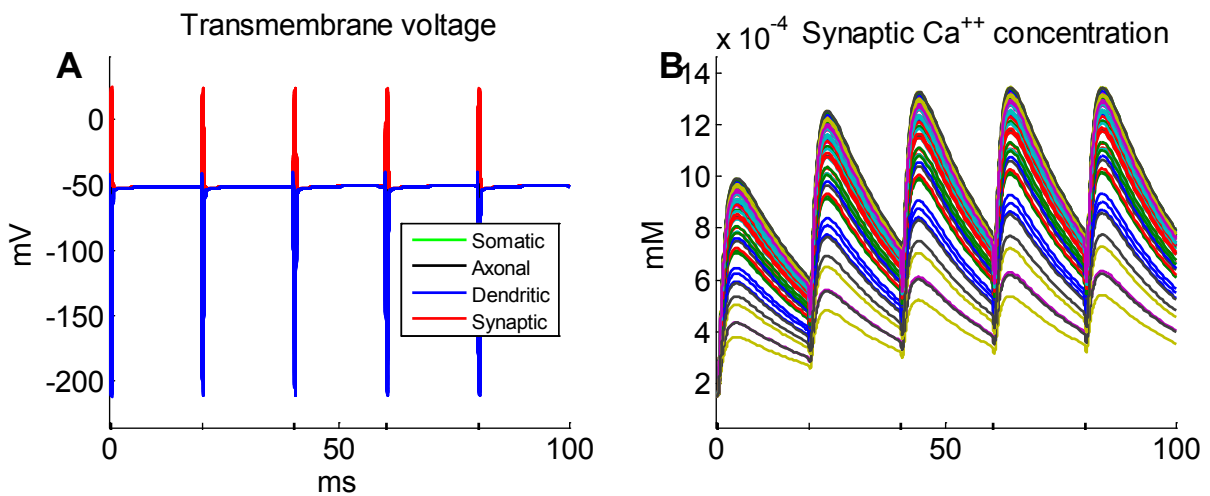


Figure 3.69 Five 0.5 ms pulses at +1 V with 19.5 ms pause

Five repetitions of the same pulse with 20 ms intervals. Transmembrane potentials (A) exhibited a slight depolarizing trend between stimulations. Synaptic $[Ca^{++}]_i$ (C) did not return to initial resting values, but the peak value did stabilize within 4 pulses.

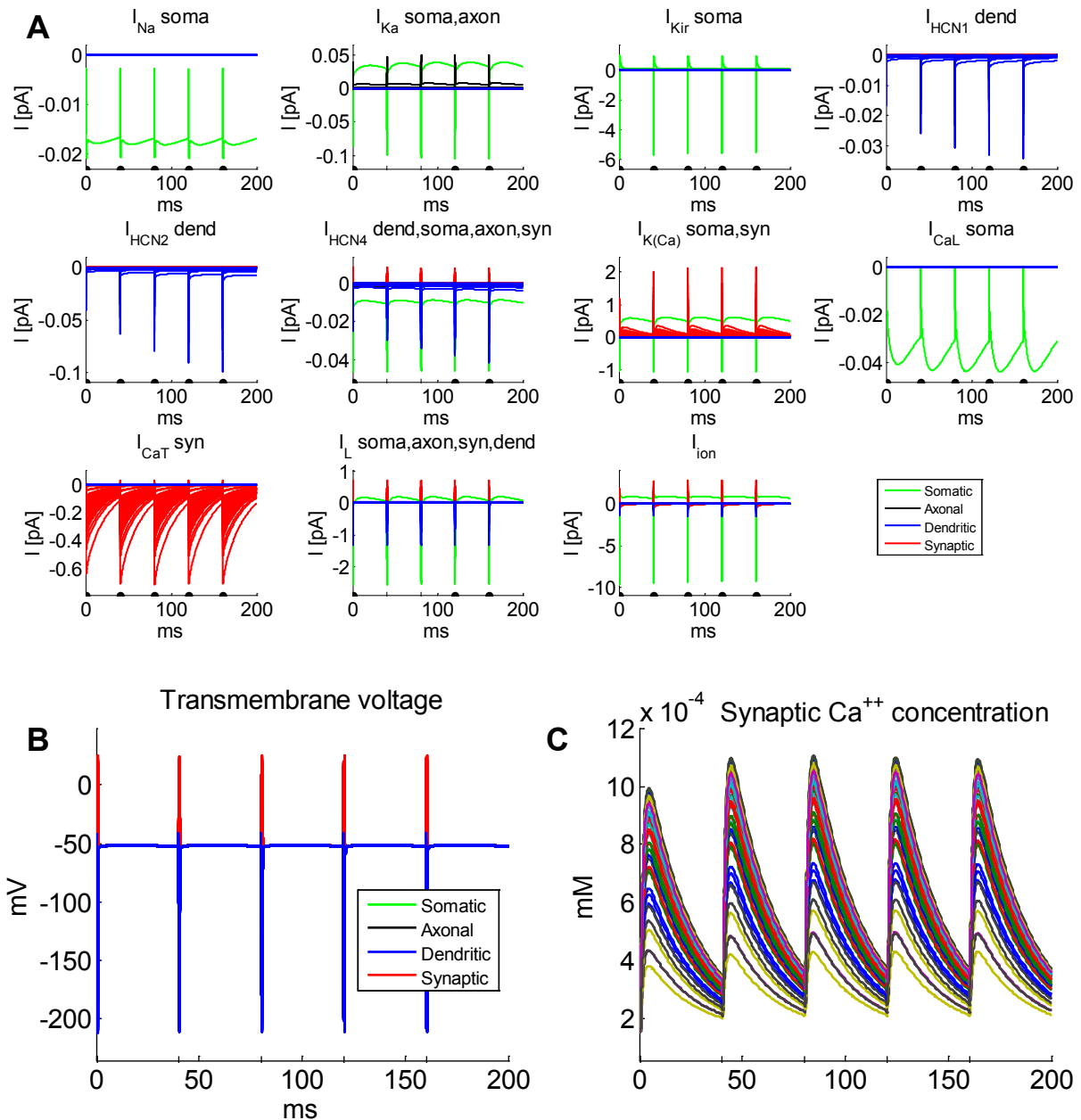


Figure 3.70 Five 0.5 ms pulses at +1 V with 39.5 ms pause

Five repetitions with 40 ms intervals. Except for HCN1,2 and 4, all ion channels produced similar current time-courses (A) during and after each stimulus presentation. Synaptic inward T-type Ca^{++} currents returned to very small values before the next stimulus was initiated. V_m of this simulation (B) showed no positive trends between stimulations. The increases of synaptic $[Ca^{++}]_i$ (C) were larger for the second pulse compared to the first pulse, but remained constant throughout the following stimulations and nearly reached their resting values before the next stimulation.

3.4.2.5 Dipolar Stimulation

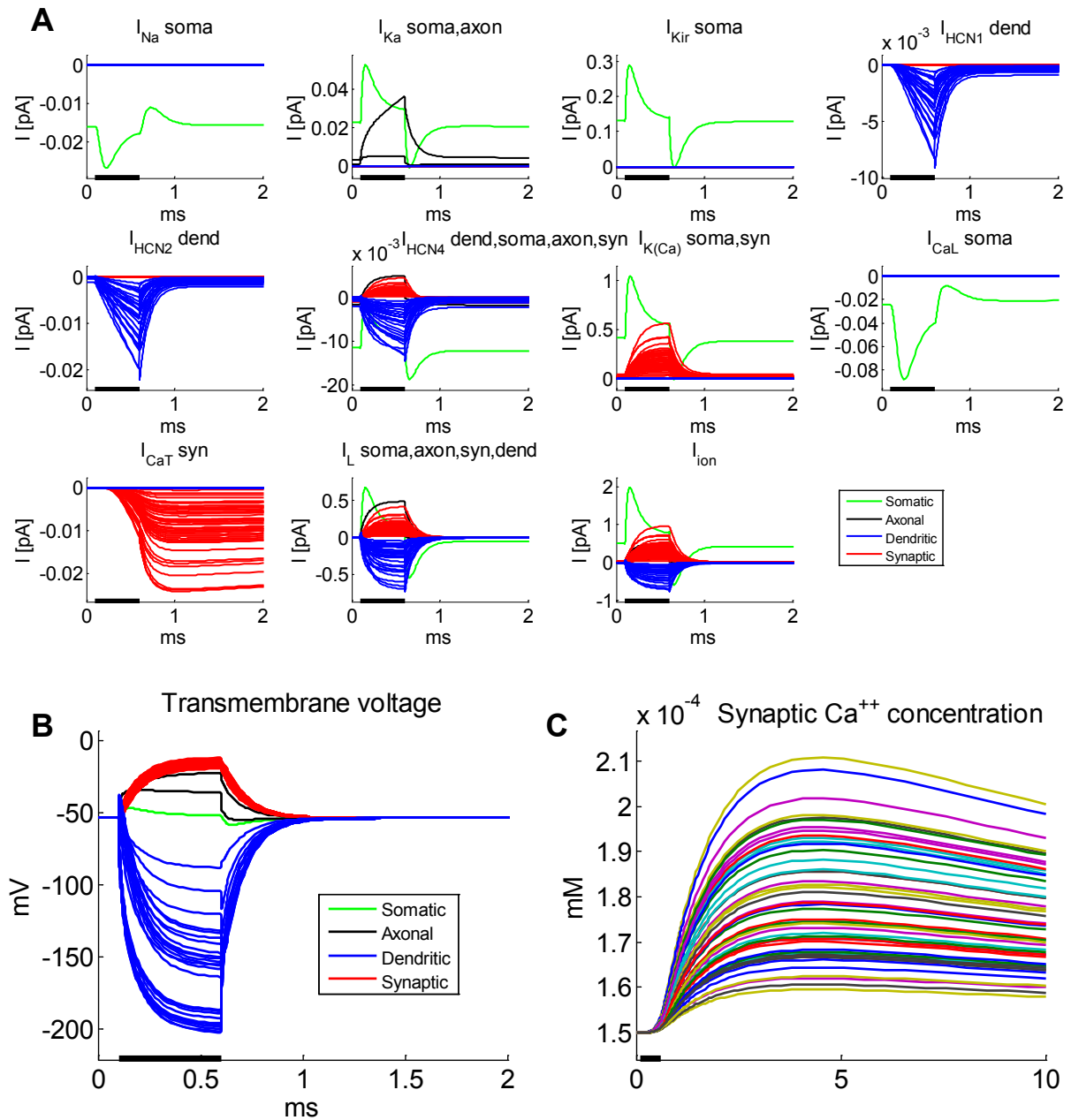
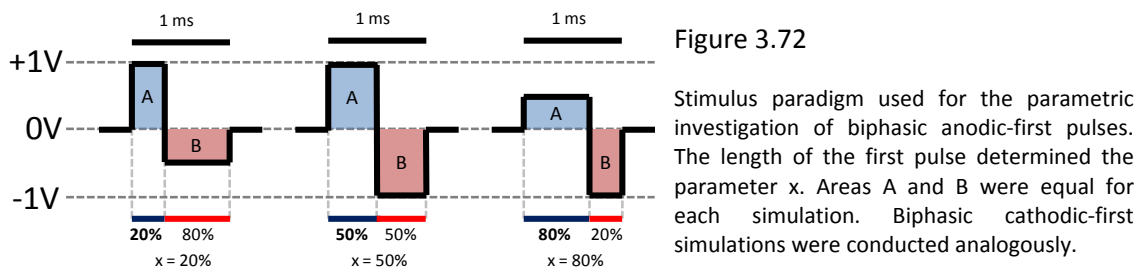


Figure 3.71 Monophasic 0.5 ms pulse with 2 V (-1 V & +1 V)

Simulation of a dipolar 2 V stimulation with the resulting current-traces (A). V_m of synaptic compartments remained below 0 mV (B). Synaptic $[Ca^{++}]_i$ (C) showed a small increase.

3.4.3 Selective Stimulation of ON and OFF Bipolar Cells

A parametric investigation was conducted in order to exploit potential preferences of ON-type and OFF-type CBCs to certain forms of stimulations. This series of simulations used different biphasic voltage pulses which differed in respect to the temporal proportioning of the two phases (Figure 3.72). The duration of both phases together remained constant at 1 ms and the fraction allocated to the positive and negative pulses was varied. In an effort to approximate balanced charge delivery, the amplitude of the longer pulse was smaller than the amplitude of the shorter one (areas A and B were always for a given simulation). The larger amplitude was +1 V or -1 V in all simulations. The parameter describing a simulation was the proportional length of the first pulse in respect to the 1 ms stimulation period (Table 3.3). If the first pulse had a duration of 0.2 ms (20% of 1 ms), then $x = 20\%$. If the first and the second pulse both had a duration of 0.5 ms ($x = 50\%$), both had an amplitude of +1 V or -1 V.



$x =$	10%	20%	30%	40%	50%	60%	70%	80%	90%
First phase	100 μ s	200 μ s	300 μ s	400 μ s	500 μ s	600 μ s	700 μ s	800 μ s	900 μ s
	+1 V	+1 V	+1 V	+1 V	+1 V	+666 mV	+428 mV	+25 mV	+111 mV
Second phase	900 μ s	800 μ s	700 μ s	600 μ s	500 μ s	400 μ s	300 μ s	200 μ s	100 μ s
	-111 mV	-25 mV	-428 mV	-666 mV	-1 V	-1 V	-1 V	-1 V	-1 V

Table 3.3 Parameters used for simulation of different biphasic pulses

Values for anodic-first stimulation. For cathodic-first, the signs of all voltages were switched from - to + and vice versa.

Nine anodic-first and nine cathodic-first simulations were performed starting from $x = 10\%$ to $x = 90\%$ with the parameters shown in Table 3.3. The average synaptic $[Ca^{++}]_i$ resulting from this series of simulations are shown in Figure 3.73. In all simulations, the Ca^{++} concentration peak was largest with $x=40\%$, $x=50\%$ or $x=60\%$, probably partly due to more current being injected with these parameters (areas A and B were larger). The most notable observation was that at $x=30\%$ for cathodic-first stimulation the $[Ca^{++}]_i$ increases in the ideal ON-cell (Figure 3.73 A) were considerable (72.8 % increase), while only negligible increases (7.8 %) occurred in the OFF-cell model (Figure 3.73 B).

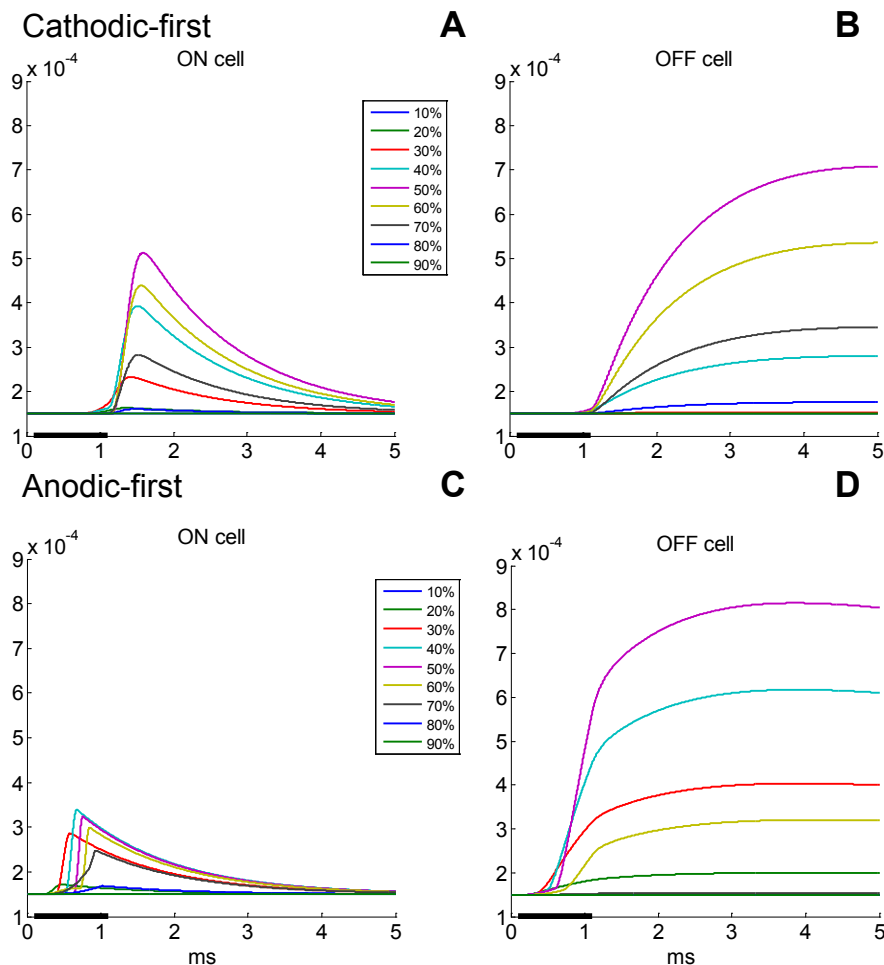


Figure 3.73

Synaptic Ca^{++} concentrations during different biphasic pulses (see Table 3.3). Cathodic-first stimulation of the ON-CBC (A) and OFF-CBC (B) model.

Anodic-first stimulation of the ON-CBC (C) and OFF-CBC (D) model.

Similar differential activation was found for $x=70\%$ in the anodic-first simulations (Figure 3.73 C for ON- and Figure 3.73 D for OFF-cell models). The detailed ionic current time-traces and the associated transmembrane potentials from $x=30\%$ cathodic-first pulses are shown in Figure 3.74 A for the ideal ON-type CBC, panel D shows the ideal OFF-type CBC. Furthermore, at $x=50\%$ the increases of synaptic $[Ca^{++}]_i$ were significantly larger in the OFF-cell than in the ON-cell for both cathodic and anodic-first pulses (Figure 3.73). At $x=40\%$, cathodic-first pulses led to higher $[Ca^{++}]_i$ peaks in ON cells, whereas anodic-first pulses with $x=40\%$ caused larger peaks in OFF-cells. However, due to the observable slower decrease of intracellular Ca^{++} in OFF-cells caused by the sustained synaptic inward T-type Ca^{++} currents (see Figure 3.74 D bottom left plot and Figure 3.64), the effect (vesicle release) of the larger $[Ca^{++}]_i$ peak could be less divergent between the ideal ON- and OFF-type CBC models during cathodic-first pulses. In both cells, inward T-type Ca^{++} currents built up during stimulation. However, in the ideal ON-model these channels were restricted to the soma and therefore had no effect on synaptic $[Ca^{++}]_i$.

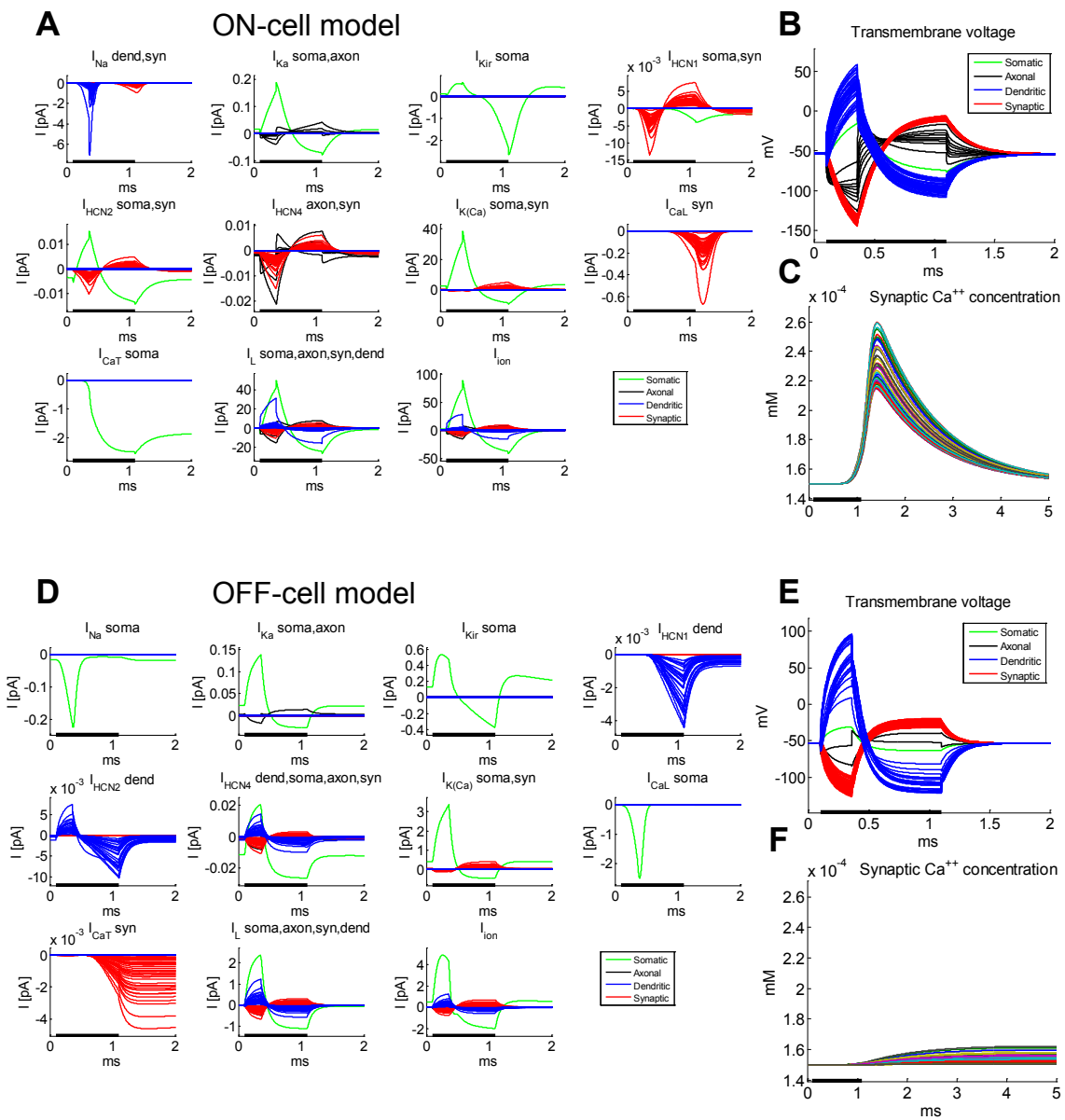


Figure 3.74

Detailed results of biphasic cathodic-first stimulation with $x=30\%$ (0.3 ms pulse at -1 V then a 0.7 ms pulse at 0.428 mV). The same pulse form was applied to both cells. Current time courses of the ON-cell (A) show transient synaptic L-type Ca^{++} and sustained somatic T-type Ca^{++} currents. The resulting transmembrane potentials of all compartments (B). Synaptic $[Ca^{++}]_i$ in the ON-cell (C) increased from 0.15 μM to 0.2596 μM . Inward Ca^{++} currents in the OFF-cell (D) were transient at the soma and sustained in synaptic compartments. Resulting transmembrane voltage for the OFF-cell (E). Synaptic $[Ca^{++}]_i$ in the OFF-cell (F) increased from 0.15 μM to 0.162 μM .

3.5 Discussion

Several different simulations have been conducted with the active models of retinal ON- and OFF-type CBCs. In order to bridge from electrophysiological experiments in neurons to extracellular stimulation from the subretinal space, voltage-clamp currents were presented first as whole-cell currents for all individual ion channels in the ideal ON-type and ideal OFF-type CBC models followed by a presentation of single-compartment voltage-clamp currents in both models. The stimuli applied by the subretinal MPDA typically have short durations and were therefore tested with a pulse length of 0.5 ms for monophasic pulses and 1 ms for biphasic pulses. These short timescales did not allow most ion channels present in retinal bipolar cells to develop a behavior similar to that from electrophysiological experiments, since the pulse-lengths in these experiments are usually considerably longer (Hu and Pan 2002, Ivanova and Müller 2006), sometimes even lasting for several seconds. Such long stimulation periods, however, are not feasible for a subretinal implant due to limitations of safe charge injection (McCreery et al. 1990). Na⁺ channels had the fastest activation kinetics of all modeled ion channels with peak currents reached within less than 1 ms.

Hyperpolarizing and depolarizing pulses were then applied in extracellular stimulation mode to both ON- and OFF-cell models at ± 1 V and ± 2 V. As it was also the case with the passive model (see section 2.3), a negative electrode potential led to depolarization of the compartments close to the electrodes (dendrites, soma) and to hyperpolarization of more distant neuronal regions (axon, synaptic axon terminal). However, both T-type and L-type Ca⁺⁺ channels in this model were not activated by hyperpolarization, and therefore the activation of synaptic voltage-dependent Ca⁺⁺ channels was minimal. Consequently, synaptic [Ca⁺⁺]_i changes remained in the range of less than 1% using monophasic negative pulses.

The application of monophasic depolarizing pulses with 1 V or 2 V amplitude had inverse effects, causing hyperpolarization of dendrites/soma and depolarization of the membrane potential in the axon and synaptic axon terminals. Thus, considerably more inward currents through synaptic voltage-dependent Ca⁺⁺ channels resulted from depolarization than from hyperpolarization, leading to large increases of synaptic [Ca⁺⁺]_i up to 350% in the ON model and more than 600% in the OFF model at 1 V during depolarizing pulses.

Why did the Ca⁺⁺ concentration in the ON model not differ between +1 V and +2 V pulses?

Synaptic L-type currents in the ON model at +1 V (Figure 3.49) were outward currents up to 4 pA during the stimulating pulse and became inward currents up to 2.2 pA after the stimulus was deactivated. In the +2 V simulation (Figure 3.50), the amplitude of the outward currents was

increased to up to 11 pA, but the maximal amplitude of inward currents after end of stimulation was very similar to the +1 V stimulation. Since the model was always initiated at $[Ca^{++}]_i$ levels close to the minimal Ca^{++} concentration $[Ca^{++}]_{res}$, different outward current amplitudes did not affect $[Ca^{++}]_i$ as much as different inward Ca^{++} current amplitudes.

Why did the Ca^{++} concentration decrease slower in the OFF model?

While the synaptic compartments of the ideal ON-type CBC were equipped with L-type Ca^{++} channels (T-rich cell), the synaptic compartments of the ideal OFF-type CBC contained T-type Ca^{++} channels instead (L-rich cell).

Figure 3.75 A shows the synaptic L-type Ca^{++} currents which resulted from the +1 V extracellular stimulation in the ON model. Even though L-type (L=long lasting) Ca^{++} currents are sustained and have rather slow inactivation kinetics (see Figure 3.41), they stopped about 1 ms after the end of the stimulus (black bar). However, de-activation not inactivation was responsible for this decrease of outward and inward currents. Figure 3.75 B shows the voltage dependence of L-type Ca^{++} channel activation (the x-axis shows the reduced potential V which, by definition, is zero at the resting potential). The transmembrane potentials of all compartments in this simulation are shown in Figure 3.75 C. In the synaptic compartments, V_m peaked at $t=0.6$ ms and then returned to the resting potential within 1 ms. This decrease of V_m caused L-type channel activation to return to the value it had at $V = 0$, which is nearly 0 as well. Therefore, L-type Ca^{++} channels were de-activated when synaptic V_m returned to rest. Since no significant inward Ca^{++} currents in the synaptic compartments of the ideal ON-cell persisted more than 1 ms beyond the stimulus pulse, Ca^{++} pumps returned $[Ca^{++}]_i$ back to its initial value within 4-5 ms.

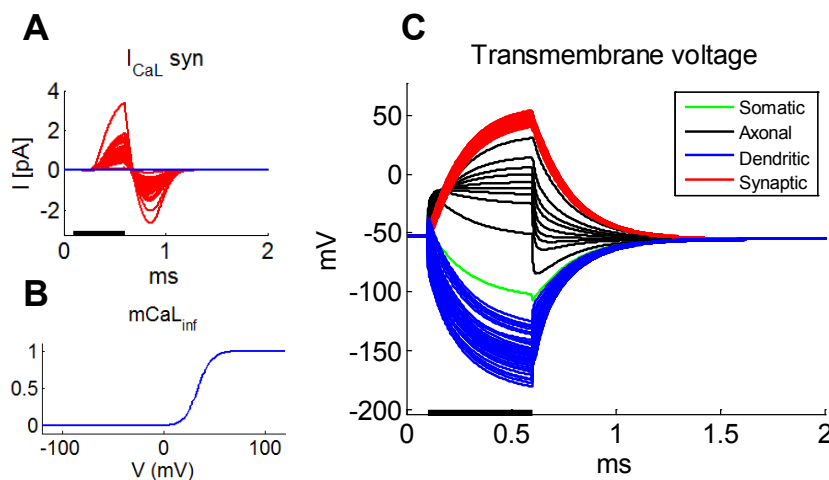


Figure 3.75

Synaptic L-type Ca^{++} currents in the ON model during a 0.5 ms +1 V depolarizing stimulus. Voltage dependence of L-type Ca^{++} channel activation (V , the reduced potential is zero at the resting potential). V_m in the ideal ON-type CBC during the +1 V stimulation.

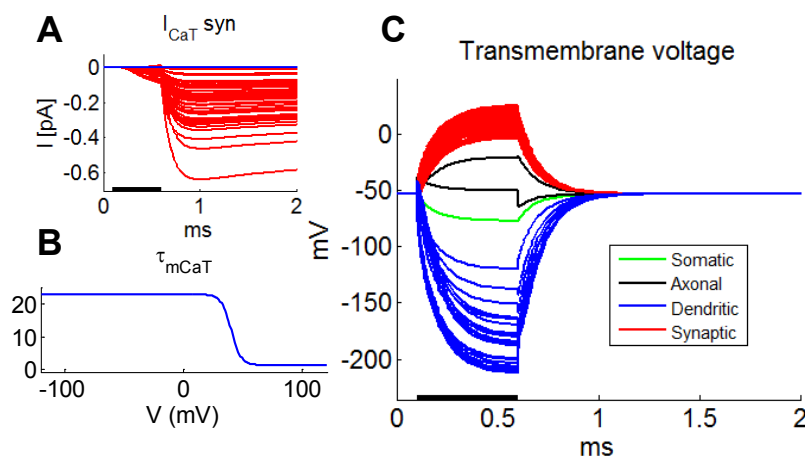


Figure 3.76

Synaptic T-type Ca^{++} currents in the OFF model during a 0.5 ms +1 V depolarizing stimulus. Voltage dependence of T-type Ca^{++} channel activation time constant $\tau_{m\text{CaT}}$. V_m in the ideal OFF-type CBC during the +1 V stimulation.

Figure 3.76 A shows synaptic T-type Ca^{++} currents in the OFF model during a +1 V depolarizing extracellular stimulation. In Figure 3.76 B it can be seen that the time constant of T-type Ca^{++} channel activation ($\tau_{m\text{CaT}}$) depends on the reduced potential V . Synaptic V_m (Figure 3.76 C) increased during the stimulation (black bar), causing inward T-type Ca^{++} currents. After the end of stimulation, the cell returned to its resting potential, which led to larger values for $\tau_{m\text{CaT}}$. A larger activation time constant results in slower changes of activation, therefore the amplitude of T-type Ca^{++} currents decreased only slowly. Due to the sustained inward Ca^{++} current, $[\text{Ca}^{++}]_i$ could not be returned to its initial value within the same timeframe as in the ON model.

The results from the simulation of biphasic pulses (cathodic-first and anodic-first) can be explained with the same mechanism. In the ON model, transient synaptic inward L-type Ca^{++} currents were initiated after the anodic phase of the cathodic-first stimulation at the end of the stimulus duration and after the anodic phase of the anodic-first stimulation in the middle of the stimulus duration. The biphasic cathodic-first stimulation of the OFF model caused synaptic inward T-type Ca^{++} currents during and after the anodic phase, which were de-activated only slowly after the stimulus had ended. In the anodic-first stimulation these inward currents were also initiated during and after the anodic phase, however, the following cathodic phase caused a smaller value for $\tau_{m\text{CaT}}$ such that T-type channel de-activation occurred more rapidly than in the cathodic-first stimulation of the OFF model. As shown in Figure 3.65, the synaptic $[\text{Ca}^{++}]_i$ peaked earlier in the anodic-first stimulation than in the cathodic-first (Figure 3.64). Consequently, the maximal peak $[\text{Ca}^{++}]_i$ was higher during the anodic-first stimulation. A more detailed observation of different combinations of biphasic pulses was conducted in section 3.4.3 and will be discussed below.

How did ON and OFF models react to repetitive stimulation?

Five repetitions of monophasic depolarizing pulses were applied to the ideal ON-type and OFF-type CBC models. In the ON model, the pause phases between two consecutive stimulations were 0.5 ms and 4.5 ms, therefore the inter-stimulus interval (ISI) was 1 ms (1000 Hz stimulation) and 5 ms (200 Hz stimulation). Similar stimulus bursts have been used in the clinical pilot study (Zrenner et al. 2010), where single stimuli were replaced with up to five consecutive stimuli, followed by a longer pause phase (depending on the stimulation frequency) before the next stimulus burst was initiated. The predictions of the ON model showed that an ISI of 1 ms led to a cumulative increase in synaptic $[Ca^{++}]_i$ (Figure 3.53), with higher concentrations after the second and third pulse than after the first one. The consequence of this relation is difficult to assess. Most importantly, these results were obtained under a large number of different assumptions and therefore may not reflect the actual events in bipolar cell synapses. The first stimulus led to an $[Ca^{++}]_i$ increase of more than 300%, a level that would be sufficient to drive synaptic signaling from bipolar cell to the retinal ganglion cell layer (Zhou et al. 2006). It can be assumed that the qualitative model predictions may be more accurate than the quantitative predictions. If the actual increase in $[Ca^{++}]_i$ is smaller, a cumulative increase in synaptic $[Ca^{++}]_i$ during repeated stimuli may result in a more effective stimulation of the retinal network by reaching higher synaptic activation levels. On the other hand, excessive increases of $[Ca^{++}]_i$ may lead to synaptic vesicle depletion, which has been discussed as one of the main reasons for retinal adaptation to electrical stimulation (Jensen and Rizzo III 2007). The simulation of lower frequency bursts with an ISI of 5 ms (200 Hz, Figure 3.54) suggested that - in retinal ON-type CBCs - synaptic $[Ca^{++}]_i$ may be able to return to their initial values within this interval and that no cumulative increase of $[Ca^{++}]_i$ would occur in this case.

As elaborated above, synaptic $[Ca^{++}]_i$ levels in the ideal OFF-type CBC model required more time to return to their initial values. When repetitive stimulus bursts were applied to the OFF model, this fact led to larger cumulative increases of $[Ca^{++}]_i$ with each additional stimulus. Additional simulations of repetitive bursts with ISI = 10 ms, 20 ms or 40 ms were conducted in the OFF model. It has been shown in Figure 3.62 D, that Ca^{++} pumps required up to 100 ms to return $[Ca^{++}]_i$ to resting values. Therefore, a repetitive stimulation with ISI = 40 ms did not allow $[Ca^{++}]_i$ to return fully to initial values, however, $[Ca^{++}]_i$ did return to values which allowed a repetitive +1 V stimulation of the OFF model with largely equivalent increases of $[Ca^{++}]_i$ during each of the stimuli.

Effects of dipolar stimulation

A simulation of extracellular stimulation with a dipolar ring electrode (see section 2.3.2.2) was conducted with the models of ideal ON- and ideal OFF-type CBCs. In the dipolar stimulation, a central disc electrode was activated with a certain voltage (e.g. +1 V) while a second ring electrode was set to a negative potential (e.g. -1 V) and acted as a return electrode: This is in contrast to monopolar stimulation where the return electrode is located relatively distant from the stimulating electrode and has a free floating potential. As a consequence, most of the current in this setup flowed directly from the positive to the negative electrode without deeply entering into retinal tissue. Therefore, higher potentials were required for achievement of neuronal activations comparable to monopolar stimulation. This effect was demonstrated in Figure 3.55 (ON model) and Figure 3.71 (OFF model). In both cases, a 2 V dipolar stimulation (+1 V and -1 V) was applied, but led to an $[Ca^{++}]_i$ increase of 1.2% in the ideal ON-type CBC model and 39% in the OFF model. Both of these increases were below levels that had been achieved with monopolar stimulation at 1 V. Further effects of dipolar subretinal stimulation have been discussed elsewhere (Gerhardt et al. 2010).

To which type of stimulation did ON and OFF models respond differentially?

In the biphasic pulse simulations conducted in sections 3.4.1.4 and 3.4.2.3 the model results suggested that synaptic $[Ca^{++}]_i$ increases would be more rapid during the anodic-first stimulations. This was an important observation especially for the OFF model, as it displayed equally slow increases and decreases of $[Ca^{++}]_i$ during all other simulations (see above). The reason for this difference in synaptic $[Ca^{++}]_i$ kinetics is displayed in Figure 3.77.

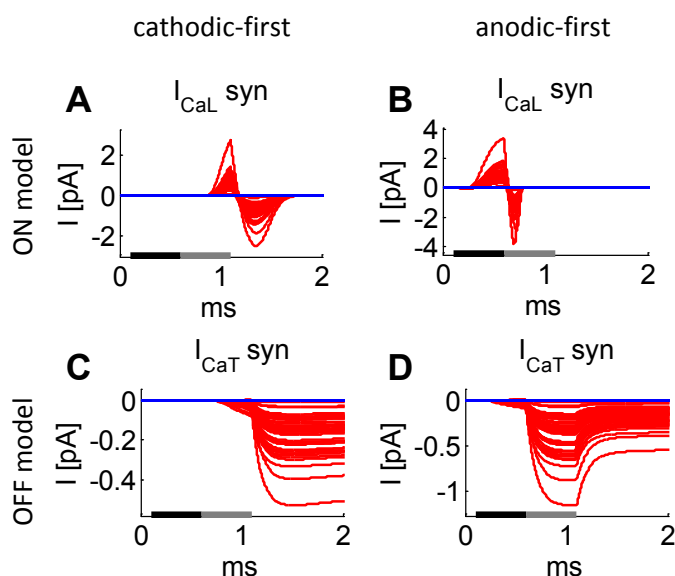


Figure 3.77

Synaptic Ca^{++} currents during biphasic cathodic-first and anodic-first stimulation at 1 V. The bars at the bottom of each plot indicate the stimulus phases (black: first phase, grey: second phase). In the ON model (A, B), synaptic L-type Ca^{++} currents were initiated during the anodic phase and ended maximally 1 ms after end of the anodic phase. In the OFF model (C, D), synaptic T-type Ca^{++} currents also were initiated during the anodic phase. In the cathodic-first stimulation, T-type Ca^{++} currents were sustained and decreased gradually after the end of the anodic phase (C). In the anodic-first simulation, the decay of T-type currents was accelerated after the cathodic phase which followed the anodic phase (D).

In both biphasic simulations, cathodic-first and anodic-first, synaptic Ca^{++} currents were initiated during the anodic phase. For the ON model (Figure 3.77 A, B), the anodic-first stimulation caused the L-type Ca^{++} currents to return to zero slightly faster than in the cathodic-first stimulation. Investigation of the synaptic Ca^{++} currents of the OFF model (Figure 3.77 C, D), however, showed that T-type currents, which de-activated very slowly in all other simulations, were forced to toward zero in a step-like form after the cathodic phase of the anodic-first stimulation. This observation motivated the design of a parametric study on different biphasic pulses, which was conducted in section 3.4.3. It could be shown, that the model predictions for synaptic $[\text{Ca}^{++}]_i$ increases differed significantly between the ideal ON-type and OFF-type CBC models. A combination of a short, strong negative pulse and a longer, weaker positive pulse was found to preferentially activate the ON model and showed only very low $[\text{Ca}^{++}]_i$ increases in the OFF model. This was true for any order of both phases, anodic-first and cathodic-first. This series of biphasic pulse simulations further showed, that temporally balanced biphasic pulses (0.5 ms cathodic and 0.5 ms anodic or vice versa) would preferentially activate the ideal OFF-type CBC model. However, significant $[\text{Ca}^{++}]_i$ increases were also predicted for the ideal ON-type CBC model, leading to a less pronounced difference.

A preliminary experiment with explanted *wild type* (*wt*) mouse retinae was conducted using biphasic stimuli with $x = 30\%$ and $x = 70\%$ (see Table 3.3) that elicited significantly different synaptic $[\text{Ca}^{++}]_i$ increases in the ideal ON and OFF models (Figure 3.73). Measurements and stimulations were performed with a 64-channel multielectrode array (Multi Channel Systems, Reutlingen). Interleaved with electrical stimulation, light stimuli were used for identification of ON and OFF cells on the array. Following electrical stimulation with the aforementioned biphasic pulses, the spiking activity of OFF RGCs during light stimulation appeared to be reduced in comparison to ON RGCs. The preliminary nature of this experiment should be underlined; a more complete analysis of the data is pending. Nevertheless, these results give rise to the need for further experiments using this stimulus form for a deeper understanding of the phenomenon.

4 Conclusions

The cellular processes occurring during extracellular stimulation under *in-vivo* conditions, for example in retinal implant patients, are inaccessible to currently available measurement techniques. A better understanding, especially of membrane currents and related biophysical events, is required for our ability to improve the stimulation strategies used today. The present thesis combined theoretic principles, experimental data and clinical experience into a computational model for simulations of these neuronal events and discussed their potential implications for the further development of the Tübingen subretinal implant.

A Finite Element Method (FEM) model was implemented for quantitative calculation of the extracellular electric potential (V_e) generated by electrodes or electrode arrays in a subretinal location. The inclusion of different electrode configurations (monopolar and dipolar) allowed the investigation of the currently used (Zrenner et al. 2010) monopolar microphotodiode-array (MPDA) configuration as well as theoretical considerations of the effect dipolar stimulation might have.

Using the calculated V_e , a multi-compartment model of linear, passive membrane potentials (V_m) was implemented. The theoretical basis for calculating the effects V_e has on the dynamics of V_m was provided by the activating function (Rattay 1999). Simulations with the passive model revealed the principal reaction of neuronal V_m to extracellular stimulation. In agreement with previous models (Resatz 2005), neuronal compartments close to an electrode were hyperpolarized and compartments distant from an electrode were depolarized during anodic rectangular voltage-controlled pulses. This principal was conserved for the active model which incorporated additional information on all active, voltage-gated ion channels currently known to be present in the membrane of rat cone bipolar cells (CBC). The inventory of ion channels was based on published electrophysiological and immunochemical data from all 11 types of rat CBCs. The fitting of appropriate Hodgkin-Huxley based (Hodgkin and Huxley 1952) models to this data facilitated a more realistic and detailed calculation of the CBC response to electrical stimulation and related ionic transmembrane currents as well as resultant intracellular Ca^{++} levels, especially in the synaptic axon terminals of CBCs.

The consideration of different ion channels complements for ON-type CBC and OFF-type CBC facilitated a differential investigation of the effects the subretinal implant has on retinal ON- and OFF-pathways. While both models were equipped with the same types of voltage-gated ion channels, their subcellular distribution and density differed strongly. Furthermore, realistic three-dimensional morphologies of identified rat ON-type and OFF-type CBCs (Euler and Wässle 1995) were generated for these models using a custom-made Matlab tool. Simulations of several different

stimulation paradigms were performed in order to investigate how present stimulation paradigms affect retinal CBCs, and to explore possible new stimulation paradigms which preferentially activate ON or OFF CBCs.

Repetitive electrical stimulation of the retinal network has exhibited limits in the clinical study. In many cases, patients experienced fading of their visual percepts once the stimulation frequency reached levels above 10 Hz (Zrenner et al. 2010). The results of this modeling study support theories suggesting that synaptic vesicle depletion may be one of the main reasons for this limitation (Jensen and Rizzo III 2007), as repetitive stimuli were often found to prevent synaptic Ca^{++} concentrations from returning to their resting levels. It is likely, however, that other limiting factors may also have to be considered, since repetitive stimulation with neither 5 ms inter stimulus interval (200 HZ, ON-model) nor 40 ms (25 Hz, OFF-model) has appeared to be sustainable in the clinical study, whereas synaptic Ca^{++} concentrations under these conditions were fully restored to baseline in the model. These values refer to stimulation with rectangular pulses. Such repetitive bursts of stimuli may cause neuronal adaptation in OFF cells faster than in ON cells due to the differences predicted by the model for their Ca^{++} concentration kinetics (more sustained high Ca^{++} concentration may cause earlier synaptic vesicle depletion). The use of sinusoidal stimulus waveforms may have different effects and has been discussed elsewhere (Freeman et al. 2010).

Except for Na^+ channels, most ion channels have kinetic properties and activation time ranges which are considerably slower than the stimulus durations of the Tübingen subretinal implant and other neuroprosthetic devices. Therefore, the differences between HCN channels in ON and OFF cells could not be exploited in respect to possible preferential stimulation of ON and OFF pathways. One speculative possibility may be the enhancement of Na^+ channel expression in ON-type or OFF-type CBCs to increase the active responsivity of these CBCs to subretinal stimulation. Transfection of ON-type CBCs with the Channelrhodopsin-2 gene has been performed previously and the required promoters are available (Lagali et al. 2008).

The model results suggested that monophasic cathodic pulses and dipolar stimulation within safety limits may not be able to initiate sufficient increases of synaptic Ca^{++} concentration levels in any CBCs.

The simulation of biphasic pulses, on the other hand, elicited sufficient heterogeneous responses in the ON-type and OFF-type CBC models to support differential activation of these two pathways. A parametric simulation study on biphasic pulses demonstrated that preferential stimulation of the ideal ON-type CBC model may be possible, and preliminary *in-vitro* experiments conducted with the

appropriate stimuli appeared to elicit differential spiking responses in ON-type and OFF-type mouse retinal ganglion cells (data not shown). Any conclusions based on the predictions of the model must appreciate that these predictions are based on a number of assumptions and simplifications. Nonetheless, the results can help in pointing out new directions for further experimental and clinical research. The model made the assumption, that ON-type CBCs were T-rich cells and OFF-type CBCs were L-rich cells (Hu et al. 2009). This may not be the case. However, L-rich and T-rich cells do exist and are likely to serve different retinal signaling functions. The model indicated, under the assumptions made, that differential stimulation of L-rich and T-rich cells is possible. Rather than the ON and OFF pathways, these two types may functionally correlate more appropriately to CBCs with sustained and transient responses, to different chromatic pathways in the retina, or to midget and parasol cells.

The model did not incorporate any retinal network properties or neuron-to-neuron connections. Such extensions could be the subject of further projects based on this model, leading up to the representation of several retinal layers and a more complete retinal model.

In conclusion, the model demonstrated that transmembrane depolarization V_m of CBCs may not be sufficient as the only indicator for determination of CBC activation levels during extracellular electrical stimulation. Synaptic Ca^{++} concentration changes which control vesicle release, and by extension communication with the retinal ganglion cell layer may, not be linearly correlated to V_m .

5 References

- Aldrich, R. W., D. P. Corey and C. F. Stevens (1983). "A reinterpretation of mammalian sodium channel gating based on single channel recording." Nature **306**(5942): 436-441.
- Armstrong, C. M. (1981). "Sodium channels and gating currents." Physiological Reviews **61**(3): 644-683.
- Ascoli, G. A., D. E. Donohue and M. Halavi (2007). "NeuroMorpho.Org: A Central Resource for Neuronal Morphologies." The Journal of Neuroscience **27**(35): 9247-9251.
- Avery, R. B. and D. Johnston (1996). "Multiple Channel Types Contribute to the Low-Voltage-Activated Calcium Current in Hippocampal CA3 Pyramidal Neurons." The Journal of Neuroscience **16**(18): 5567-5582.
- Awatramani, G. B. and M. M. Slaughter (2000). "Origin of transient and sustained responses in ganglion cells of the retina." The Journal of neuroscience : the official journal of the Society for Neuroscience **20**(18): 7087-7095.
- Balazsi, A. G., J. Rootman, S. M. Drance, M. Schulzer and G. R. Douglas (1984). "The effect of age on the nerve fiber population of the human optic nerve." Am J Ophthalmol **97**(6): 760-766.
- Baylor, D. A. (1987). "Photoreceptor signals and vision. Proctor lecture." Invest Ophthalmol Vis Sci **28**(1): 34-49.
- Benav, H., R. Wilke, A. Stett and E. Zrenner (2008). "Simulation of Spatial and Temporal Characteristics of Perceptions Elicited by a Subretinal Implant." Invest. Ophthalmol. Vis. Sci. **49**(5): 3013-.
- Benison, G., J. Keizer, L. M. Chalupa and D. W. Robinson (2001). "Modeling temporal behavior of postnatal cat retinal ganglion cells." Journal of theoretical biology **210**(2): 187-199.
- Besch, D., H. Sachs, P. Szurman, D. Gulicher, R. Wilke, S. Reinert, E. Zrenner, K. U. Bartz-Schmidt and F. Gekeler (2008). "Extraocular surgery for implantation of an active subretinal visual prosthesis with external connections: feasibility and outcome in seven patients." Br J Ophthalmol **92**(10): 1361-1368.
- Bird, A. C., N. M. Bressler, S. B. Bressler, I. H. Chisholm, G. Coscas, M. D. Davis, P. T. de Jong, C. C. Klaver, B. E. Klein, R. Klein and et al. (1995). "An international classification and grading system for age-related maculopathy and age-related macular degeneration. The International ARM Epidemiological Study Group." Surv Ophthalmol **39**(5): 367-374.
- Borofsky, A. J. and J. Partridge (1963). Doping of Germanium Transistor Surfaces by Fluid-Base Encapsulant Systems. Symposium on Cleaning and Materials Processing for Electronics and Space Apparatus, ASTM: 165-181.
- Borst, A. and T. Euler (2011). "Seeing things in motion: models, circuits, and mechanisms." Neuron **71**(6): 974-994.
- Boycott, B., J. Dowling and H. Kolb (1969). "Organization of the Primate Retina: Light Microscopy " Philosophical Transactions of the Royal Society of London. Series B, Biological Sciences **255**(799): 91.
- Ciavatta, V. T., M. Kim, P. Wong, J. M. Nickerson, R. K. Shuler, G. Y. McLean and M. T. Pardue (2009). "Retinal Expression of Fgf2 in RCS Rats with Subretinal Microphotodiode Array." Investigative Ophthalmology & Visual Science **50**(10): 4523-4530.
- Clay, J. R. and L. J. DeFelice (1983). "Relationship between membrane excitability and single channel open-close kinetics." Biophysical journal **42**(2): 151-157.

Coburn, B. (1989). "Neural modeling in electrical stimulation." Critical reviews in biomedical engineering **17**(2): 133-178.

Coleman, P. A. and R. F. Miller (1989). "Measurement of passive membrane parameters with whole-cell recording from neurons in the intact amphibian retina." J Neurophysiol **61**(1): 218-230.

Connaughton, V. P. and G. Maguire (1998). "Differential expression of voltage-gated K⁺ and Ca²⁺ currents in bipolar cells in the zebrafish retinal slice." The European journal of neuroscience **10**(4): 1350-1362.

Cui, J., Y.-P. Ma and Z.-H. Pan (2005). "Characterization of Two Populations of Retinal Cone Bipolar Cells That Express Large Voltage-Dependent Na⁺ Currents in the Rat." Invest. Ophthalmol. Vis. Sci. **46**(5): 610-.

Cui, J. and Z.-H. Pan (2008). "Two types of cone bipolar cells express voltage-gated Na⁺ channels in the rat retina." Visual Neuroscience **25**(5-6): 635-645.

Dacey, D. M. and M. R. Petersen (1992). "Dendritic field size and morphology of midget and parasol ganglion cells of the human retina." Proceedings of the National Academy of Sciences **89**(20): 9666-9670.

Desai, R., J. Kronengold, J. Mei, S. A. Forman and L. K. Kaczmarek (2008). "Protein kinase C modulates inactivation of Kv3.3 channels." The Journal of biological chemistry **283**(32): 22283-22294.

Destexhe, A. and J. Huguenard (2001). Which Formalism to Use for Modeling Voltage-Dependent Conductances? Realistic Modeling for Experimentalists. D. E. Boca Raton, CRC Press.

DiFrancesco, D. and D. Noble (1985). "A model of cardiac electrical activity incorporating ionic pumps and concentration changes." Philosophical Transactions of the Royal Society of London. Series B, Biological Sciences **307**(1133): 353-398.

Dommel, N. B., Y. T. Wong, T. Lehmann, C. W. Dodds, N. H. Lovell and G. J. Suaning (2009). "A CMOS retinal neurostimulator capable of focussed, simultaneous stimulation." J Neural Eng **6**(3): 10.

Doslak, M. J., R. Plonsey and C. W. Thomas (1980). "The effects of variations of the conducting media inhomogeneities on the electroretinogram." IEEE transactions on bio-medical engineering **27**(2): 88-94.

Dreosti, E., F. Esposti, T. Baden and L. Lagnado (2011). "In vivo evidence that retinal bipolar cells generate spikes modulated by light." Nature Neuroscience **14**(8): 951-952.

Eckhorn, R., M. Wilms, T. Schanze, M. Eger, L. Hesse, U. T. Eysel, Z. F. Kisvarday, E. Zrenner, F. Gekeler, H. Schwahn, K. Shinoda, H. Sachs and P. Walter (2006). "Visual resolution with retinal implants estimated from recordings in cat visual cortex." Vision Res **46**(17): 2675-2690.

Euler, T., H. Schneider and H. Wässle (1996). "Glutamate responses of bipolar cells in a slice preparation of the rat retina." J Neurosci **16**(9): 2934-2944.

Euler, T. and H. Wässle (1995). "Immunocytochemical identification of cone bipolar cells in the rat retina." J Comp Neurol **361**(3): 461-478.

Fain, G. L., F. N. Quandt, B. L. Bastian and H. M. Gerschenfeld (1978). "Contribution of a caesium-sensitive conductance increase to the rod photoresponse." Nature **272**(5652): 466-469.

Feigenspan, A., U. Janssen-Bienhold, S. Hormuzdi, H. Monyer, J. Degen, G. Sohl, K. Willecke, J. Ammermuller and R. Weiler (2004). "Expression of connexin36 in cone pedicles and OFF-cone bipolar cells of the mouse retina." The Journal of Neuroscience **24**(13): 3325-3334.

Fernández, E., F. Pelayo, S. Romero, M. Bongard, C. Marin, A. Alfaro and L. Merabet (2005). "Development of a cortical visual neuroprosthesis for the blind: the relevance of neuroplasticity." Journal of Neural Engineering **2**(4): R1.

- Fetkenhour, C. L., E. Choromokos, J. Weinstein and D. Shoch (1977). "Cystoid macular edema in retinitis pigmentosa." Trans Sect Ophthalmol Am Acad Ophthalmol Otolaryngol **83**(3 Pt 1): OP515-521.
- Fohlmeister, J. F., P. A. Coleman and R. F. Miller (1990). "Modeling the repetitive firing of retinal ganglion cells." Brain research **510**(2): 343-345.
- Forti, S., A. Menini, G. Rispoli and V. Torre (1989). "Kinetics of phototransduction in retinal rods of the newt *Triturus cristatus*." The Journal of Physiology **419**: 265-295.
- Freeman, D. K., J. F. Rizzo III and S. Fried (2010). "Electric stimulation with sinusoids and white noise for neural prostheses." Frontiers in Neuroprosthetics: 5.
- Fujikado, T., T. Morimoto, H. Kanda, S. Kusaka, K. Nakauchi, M. Ozawa, K. Matsushita, H. Sakaguchi, Y. Ikuno, M. Kamei and Y. Tano (2007). "Evaluation of phosphenes elicited by extraocular stimulation in normals and by suprachoroidal-transretinal stimulation in patients with retinitis pigmentosa." Graefes Arch Clin Exp Ophthalmol **245**(10): 1411-1419.
- Fyk-Kolodziej, B. and R. G. Pourcho (2007). "Differential Distribution of Hyperpolarization-Activated and Cyclic Nucleotide-Gated Channels in Cone Bipolar Cells of the Rat Retina." Retina **903**: 891-903.
- Garcia-Martin, E., I. Pinilla, E. Sancho, C. Almarcegui, I. Dolz, D. Rodriguez-Mena, I. Fuertes and N. Cuenca (2012). "Optical Coherence Tomography In Retinitis Pigmentosa: Reproducibility and Capacity to Detect Macular and Retinal Nerve Fiber Layer Thickness Alterations." Retina Publish Ahead of Print.
- Geddes, L. A. and L. E. Baker (1967). "The specific resistance of biological material--a compendium of data for the biomedical engineer and physiologist." Med Biol Eng **5**(3): 271-293.
- Gerhardt, M. (2009). Verbesserung der Orts- und Zellselektivität der multilokalen Elektrostimulation durch raumzeitliche Feldmodulation, Universität Ulm. Ph.D. Thesis (German).
- Gerhardt, M., J. Alderman and A. Stett (2010). "Electric field stimulation of bipolar cells in a degenerated retina--a theoretical study." IEEE Trans Neural Syst Rehabil Eng **18**(1): 1-10.
- Ghosh, K. K., S. Bujan, S. Haverkamp, A. Feigenspan and H. Wassle (2004). "Types of bipolar cells in the mouse retina." The Journal of comparative neurology **469**(1): 70-82.
- Hack, I., L. Peichl and J. H. Brandstatter (1999). "An alternative pathway for rod signals in the rodent retina: rod photoreceptors, cone bipolar cells, and the localization of glutamate receptors." Proceedings of the National Academy of Sciences of the United States of America **96**(24): 14130-14135.
- Haeseleer, F., I. Sokal, C. L. Verlinde, H. Erdjument-Bromage, P. Tempst, A. N. Pronin, J. L. Benovic, R. N. Fariss and K. Palczewski (2000). "Five members of a novel Ca²⁺-binding protein (CABP) subfamily with similarity to calmodulin." The Journal of biological chemistry **275**(2): 1247-1260.
- Hamill, O. P., A. Marty, E. Neher, B. Sakmann and F. J. Sigworth (1981). "Improved patch-clamp techniques for high-resolution current recording from cells and cell-free membrane patches." Pflugers Archiv : European journal of physiology **391**(2): 85-100.
- Hartong, D. T., E. L. Berson and T. P. Dryja (2006). "Retinitis pigmentosa." The Lancet **368**(9549): 1795-1809.
- Hartveit, E. (1997). "Functional organization of cone bipolar cells in the rat retina." J Neurophysiol **77**(4): 1716-1730.
- Heidelberger, R. and G. Matthews (1992). "Calcium influx and calcium current in single synaptic terminals of goldfish retinal bipolar neurons." The Journal of Physiology **447**: 235-256.

- Heidelberger, R. and G. Matthews (1994). "Dopamine enhances Ca^{2+} responses in synaptic terminals of retinal bipolar neurons." Neuroreport **5**(6): 729-732.
- Hill, T. L. and Y.-D. Chen (1972). "On the Theory of Ion Transport Across the Nerve Membrane, VI. Free Energy and Activation Free Energies of Conformational Change." Proceedings of the National Academy of Sciences **69**(7): 1723-1726.
- Hille, B. (2001). Ion Channels of Excitable Membranes, Sinauer.
- Hines, M. L. and N. T. Carnevale (1997). "The NEURON simulation environment." Neural computation **9**(6): 1179-1209.
- Hines, M. L., T. Morse, M. Migliore, N. T. Carnevale and G. M. Shepherd (2004). "ModelDB: A Database to Support Computational Neuroscience." Journal of Computational Neuroscience **17**(1): 7-11.
- Hodgkin, A. and A. Huxley (1952). "A Quantitative Description of Membrane Current and its Application to Conduction and Excitation in Nerve." Journal of Physiology **117**: 500-544.
- Hornig, R., T. Laube, P. Walter, M. Velikay-Parel, N. Bornfeld, M. Feucht, H. Akguel, G. Rossler, N. Alteheld, D. Lutke Notarp, J. Wyatt and G. Richard (2005). "A method and technical equipment for an acute human trial to evaluate retinal implant technology." J Neural Eng **2**(1): S129-134.
- Hu, C., A. Bi and Z. H. Pan (2009). "Differential expression of three T-type calcium channels in retinal bipolar cells in rats." Visual Neuroscience **26**(2): 177-187.
- Hu, H. J. and Z. H. Pan (2002). "Differential expression of K^+ currents in mammalian retinal bipolar cells." Visual Neuroscience **19**(2): 163-173.
- Humayun, M. S. (2001). "Intraocular retinal prosthesis." Trans Am Ophthalmol Soc **99**: 271-300.
- Ichinose, T., C. R. Shields and P. D. Lukasiewicz (2005). "Sodium channels in transient retinal bipolar cells enhance visual responses in ganglion cells." J Neurosci **25**(7): 1856-1865.
- Ivanova, E. and F. Müller (2006). "Retinal bipolar cell types differ in their inventory of ion channels." Visual Neuroscience **23**(2): 143-154.
- Izhikevich, E. M. (2001). "Resonate-and-fire neurons." Neural networks : the official journal of the International Neural Network Society **14**(6-7): 883-894.
- Jensen, R. J. and J. F. Rizzo III (2007). "Responses of ganglion cells to repetitive electrical stimulation of the retina." J Neural Eng **4**(1): S1-S6.
- Kameneva, T., H. Meffin and A. N. Burkitt (2010). Differential stimulation of ON and OFF retinal ganglion cells: A modeling study. Engineering in Medicine and Biology Society (EMBC), 2010 Annual International Conference of the IEEE.
- Kaneko, A. (1973). "Receptive field organization of bipolar and amacrine cells in the goldfish retina." The Journal of Physiology **235**(1): 133-153.
- Kaneko, A., L. H. Pinto and M. Tachibana (1989). "Transient calcium current of retinal bipolar cells of the mouse." The Journal of Physiology **410**: 613-629.
- Kaneko, A. and M. Tachibana (1985). "A voltage-clamp analysis of membrane currents in solitary bipolar cells dissociated from *Carassius auratus*." The Journal of Physiology **358**: 131-152.
- Karschin, A. and H. Wässle (1990). "Voltage- and transmitter-gated currents in isolated rod bipolar cells of rat retina." Journal of Neurophysiology **63**(4): 860-876.
- Keizer, J. (1987). Statistical Thermodynamics of Nonequilibrium Processes, Springer.

- Klumpp, D. J., E. J. Song, S. Ito, M. H. Sheng, L. Y. Jan and L. H. Pinto (1995). "The Shaker-like potassium channels of the mouse rod bipolar cell and their contributions to the membrane current." The Journal of neuroscience : the official journal of the Society for Neuroscience **15**(7 Pt 1): 5004-5013.
- Klumpp, D. J., E. J. Song and L. H. Pinto (1995). "Identification and localization of K⁺ channels in the mouse retina." Visual Neuroscience **12**(6): 1177-1190.
- Kolb, H., E. Fernandez and R. Nelson (2005). "webvision.med.utah.edu."
- Kuffler, S. W. (1953). Discharge patterns and functional organization of mammalian retina. **16**: 37-68.
- Lagali, P. S., D. Balya, G. B. Awatramani, T. A. Munch, D. S. Kim, V. Busskamp, C. L. Cepko and B. Roska (2008). "Light-activated channels targeted to ON bipolar cells restore visual function in retinal degeneration." Nature Neuroscience **11**(6): 667-675.
- Lasater, E. M. (1988). "Membrane currents of retinal bipolar cells in culture." Journal of Neurophysiology **60**(4): 1460-1480.
- Lee, K. S. and R. W. Tsein (1982). "Reversal of current through calcium channels in dialysed single heart cells." Nature **297**(5866): 498-501.
- Li, L., M. Sun, P. Cao, C. Cai, X. Chai, X. Li, P. Chen and Q. Ren (2008). A visual prosthesis based on Optic Nerve Stimulation: In vivo Electrophysiological Study in Rabbits. 7th Asian-Pacific Conference on Medical and Biological Engineering. Y. Peng and X. Weng, Springer Berlin Heidelberg. **19**: 54-57.
- Ma, Y.-P., J. Cui and Z.-H. Pan (2005). "Heterogeneous expression of voltage-dependent Na⁺ and K⁺ channels in mammalian retinal bipolar cells." Visual Neuroscience **22**(02): 119-133.
- Ma, Y. P., J. Cui, H. J. Hu and Z. H. Pan (2003). "Mammalian retinal bipolar cells express inwardly rectifying K⁺ currents (I_{Kir}) with a different distribution than that of I_h." Journal of Neurophysiology **90**(5): 3479-3489.
- MacLaren, R. E. (2009). "An analysis of retinal gene therapy clinical trials." Curr Opin Mol Ther **11**(5): 540-546.
- MacNeil, M. A. and R. H. Masland (1998). "Extreme diversity among amacrine cells: implications for function." Neuron **20**(5): 971-982.
- Maguire, G., B. Maple, P. Lukasiewicz and F. Werblin (1989). "Gamma-aminobutyrate type B receptor modulation of L-type calcium channel current at bipolar cell terminals in the retina of the tiger salamander." Proceedings of the National Academy of Sciences of the United States of America **86**(24): 10144-10147.
- Major, G. (2001). Passive Cable Modelling - A Practical Introduction. Realistic Modeling for Experimentalists. E. De Schutter. Boca Raton, CRC Press: 229-253.
- Marc, R. E., B. W. Jones, C. B. Watt and E. Strettoi (2003). "Neural remodeling in retinal degeneration." Prog Retin Eye Res **22**(5): 607-655.
- Marc, R. E. and W. Liu (2000). "Fundamental GABAergic amacrine cell circuitries in the retina: nested feedback, concatenated inhibition, and axosomatic synapses." J Comp Neurol **425**(4): 560-582.
- Markram, H. (2006). "The Blue Brain Project." Nat Rev Neurosci **7**(2): 153-160.
- Masland, R. H. (2001). "The fundamental plan of the retina." Nature Neuroscience **4**(9): 877-886.
- Mathieson, K., J. Loudin, G. Goetz, P. Huie, L. Wang, T. I. Kamins, L. Galambos, R. Smith, J. S. Harris, A. Sher and D. Palanker (2012). "Photovoltaic retinal prosthesis with high pixel density." Nat Photon **6**(6): 391-397.

- McCreery, D. B., W. F. Agnew, T. G. Yuen and L. Bullara (1990). "Charge density and charge per phase as cofactors in neural injury induced by electrical stimulation." IEEE Trans Biomed Eng **37**(10): 996-1001.
- McNeal, D. R. (1976). "Analysis of a Model for Excitation of Myelinated Nerve." Biomedical Engineering, IEEE Transactions on BME-23(4): 329-337.
- Moosmang, S., J. Stieber, X. Zong, M. Biel, F. Hofmann and A. Ludwig (2001). "Cellular expression and functional characterization of four hyperpolarization-activated pacemaker channels in cardiac and neuronal tissues." European journal of biochemistry / FEBS **268**(6): 1646-1652.
- Morgans, C. W. (2000). "Neurotransmitter release at ribbon synapses in the retina." Immunol Cell Biol **78**(4): 442-446.
- Müller, F., A. Scholten, E. Ivanova, S. Haverkamp, E. Kremmer and U. B. Kaupp (2003). "HCN channels are expressed differentially in retinal bipolar cells and concentrated at synaptic terminals." The European journal of neuroscience **17**(10): 2084-2096.
- Nawy, S. (2000). "Regulation of the On Bipolar Cell mGluR6 Pathway by Ca^{2+} ." The Journal of Neuroscience **20**(12): 4471-4479.
- Naycheva, L., A. Schatz, T. Rock, G. Willmann, K. U. Bartz-Schmidt, E. Zrenner and F. Gekeler (2010). "Comparison of Electrically Evoked Phosphene Thresholds in Healthy Subjects and Patients With Retinal Diseases." Invest. Ophthalmol. Vis. Sci. **51**(5): 1058-.
- Neher, E. and G. J. Augustine (1992). "Calcium gradients and buffers in bovine chromaffin cells." J Physiol **450**: 273-301.
- Neher, E. and B. Sakmann (1976). "Single-channel currents recorded from membrane of denervated frog muscle fibres." Nature **260**(5554): 799-802.
- Nieto-Sampedro, M. and M. Nieto-Díaz (2005). "Neural plasticity: changes with age." Journal of Neural Transmission **112**(1): 3-27.
- Normann, R. A., B. Greger, P. House, S. F. Romero, F. Pelayo and E. Fernandez (2009). "Toward the development of a cortically based visual neuroprosthesis." J Neural Eng **6**(3): 035001.
- Okada, T., H. Horiguchi and M. Tachibana (1995). " Ca^{2+} -dependent Cl^- current at the presynaptic terminals of goldfish retinal bipolar cells." Neuroscience Research **23**(3): 297-303.
- Oltedal, L., M. L. Veruki and E. Hartveit (2009). "Passive membrane properties and electrotonic signal processing in retinal rod bipolar cells." J Physiol **587**(Pt 4): 829-849.
- Osterberg, G. (1935). Topography of the Layer of Rods and Cones in the Human Retina, Levin & Munksgaard.
- Pan, Z. H. (2000). "Differential expression of high- and two types of low-voltage-activated calcium currents in rod and cone bipolar cells of the rat retina." Journal of Neurophysiology **83**(1): 513-527.
- Pan, Z. H. and H. J. Hu (2000). "Voltage-dependent Na^+ currents in mammalian retinal cone bipolar cells." Journal of Neurophysiology **84**(5): 2564-2571.
- Pezaris, J. S. and R. C. Reid (2007). "Demonstration of artificial visual percepts generated through thalamic microstimulation." Proceedings of the National Academy of Sciences **104**(18): 7670-7675.
- Plonsey, R. (1974). "The active fiber in a volume conductor." IEEE transactions on bio-medical engineering **21**(5): 371-381.
- Polyak, S. L. (1941). The Retina. Chicago, University of Chicago Press.
- Protti, D. A., N. Flores-Herr and H. von Gersdorff (2000). "Light Evokes Ca^{2+} Spikes in the Axon Terminal of a Retinal Bipolar Cell." Neuron **25**(1): 215-227.

- Protti, D. A. and I. Llano (1998). "Calcium currents and calcium signaling in rod bipolar cells of rat retinal slices." The Journal of neuroscience : the official journal of the Society for Neuroscience **18**(10): 3715-3724.
- Ramon y Cajal, S. (1893). "La retine des vertebres." Cellule **9**: 119–255.
- Ramos-Vara, J. A. (2005). "Technical Aspects of Immunohistochemistry." Veterinary Pathology Online **42**(4): 405-426.
- Rattay, F. (1987). "Ways to approximate current-distance relations for electrically stimulated fibers." Journal of theoretical biology **125**(3): 339-349.
- Rattay, F. (1999). "The basic mechanism for the electrical stimulation of the nervous system." Neuroscience **89**(2): 335-346.
- Rattay, F., R. J. Greenberg and S. Resatz (2003). Neuron Modeling. Handbook of Neuroprosthetic Methods. P. LoPresti, CRC Press.
- Resatz, S. (2005). Analysis of retinal cell excitation with visual neuroprostheses. Institut für Analysis und Scientific Computing. Vienna, Technische Universität Wien. Ph.D Thesis.
- Resatz, S. and F. Rattay (2004). "A Model for the Electrically Stimulated Retina." Mathematical and Computer Modelling of Dynamical Systems: Methods, Tools and Applications in Engineering and Related Sciences **10**(2): 93 - 106.
- Resnikoff, S., D. Pascolini, D. Etya'ale, I. Kocur, R. Pararajasegaram, G. P. Pokharel and S. P. Mariotti (2004). "Global data on visual impairment in the year 2002." Bull World Health Organ **82**(11): 844-851.
- Rizzo III, J., S. Miller, T. Denison, T. Herndon and J. Wyatt (1996). "Electrically-evoked cortical potentials from stimulation of rabbit retina with a microfabricated electrode array." ARVO Abstracts Invest. Ophthalmol. Vis Sci **37**: S707.
- Sachs, H. G., U. Bartz-Schmidt, F. Gekeler, D. Besch, U. Brunner, B. Wilhelm, W. Wrobel, R. Wilke, V.-P. Gabel and E. Zrenner (2009). "The Transchoroidal Implantation of Subretinal Active Micro-Photodiode Arrays in Blind Patients: Long Term Surgical Results in the First 11 Implanted Patients Demonstrating the Potential and Safety of This New Complex Surgical Procedure That Allows Restoration of Useful Visual Percepts." Invest. Ophthalmol. Vis. Sci. **50**(5): 4742-.
- Sachs, H. G., F. Gekeler, H. Schwahn, W. Jakob, M. Kohler, F. Schulmeyer, J. Marienhagen, U. Brunner and C. Framme (2005). "Implantation of stimulation electrodes in the subretinal space to demonstrate cortical responses in Yucatan minipig in the course of visual prosthesis development." Eur J Ophthalmol **15**(4): 493-499.
- Saito, T. (1987). "Physiological and morphological differences between On- and Off-center bipolar cells in the vertebrate retina." Vision Res **27**(2): 135-142.
- Santos, A., M. S. Humayun, E. de Juan, Jr., R. J. Greenburg, M. J. Marsh, I. B. Klock and A. H. Milam (1997). Preservation of the inner retina in retinitis pigmentosa. A morphometric analysis. **115**: 511-515.
- Schiller, P. H. (1995). "The ON and OFF channels of the mammalian visual system." Progress in Retinal and Eye Research **15**(1): 173-195.
- Shampine, L. and M. Reichelt (1997). "The MATLAB ODE Suite." SIAM Journal on Scientific Computing **18**(1): 1-22.
- Shampine, L., M. Reichelt and J. Kierzenka (1999). "Solving Index-1 DAEs in MATLAB and Simulink." SIAM Review **41**(3): 538-552.

- Simoes de Souza, F. and E. De Schutter (2011). "Robustness effect of gap junctions between Golgi cells on cerebellar cortex oscillations." Neural Systems & Circuits **1**(1): 7.
- Slaughter, M. and R. Miller (1981). "2-amino-4-phosphonobutyric acid: a new pharmacological tool for retina research." Science **211**(4478): 182-185.
- Stett, A., W. Barth, S. Weiss, H. Haemmerle and E. Zrenner (2000). "Electrical multisite stimulation of the isolated chicken retina." Vision Res **40**(13): 1785-1795.
- Stett, A., A. Mai and T. Herrmann (2007). Retinal charge sensitivity and spatial discrimination obtainable by subretinal implants: key lessons learned from isolated chicken retina.
- Stiles, J. R. and T. M. Bartol (2001). Monte Carlo methods for simulating realistic synaptic microphysiology using MCell. Computational Neuroscience: Realistic Modeling for Experimentalists. E. De Schutter. Boca Raton, FL, CRC: 87-128.
- Tachibana, M. (1999). "Regulation of transmitter release from retinal bipolar cells." Prog Biophys Mol Biol **72**(2): 109-133.
- Taylor, W. R. (1996). "Response properties of long-range axon-bearing amacrine cells in the dark-adapted rabbit retina." Vis Neurosci **13**(4): 599-604.
- Tessier-Lavigne, M. (2000). Phototransduction and information processing in the retina. Principles of Neural Science. E. Kandel. **3**: 400-416.
- Tessier-Lavigne, M., D. Attwell, P. Mobbs and M. Wilson (1988). "Membrane currents in retinal bipolar cells of the axolotl." The Journal of general physiology **91**(1): 49-72.
- Traboulsie, A., J. Chemin, M. Chevalier, J.-F. Quignard, J. Nargeot and P. Lory (2007). "Subunit-specific modulation of T-type calcium channels by zinc." The Journal of Physiology **578**(1): 159-171.
- Tsien, R. W. and D. Noble (1969). "A transition state theory approach to the kinetics of conductance changes in excitable membranes." Journal of Membrane Biology **1**(1): 248-273.
- Usui, S., A. Ishihara, Y. Kamiyama and H. Ishii (1996). "Ionic current model of bipolar cells in the lower vertebrate retina." Vision Res **36**(24): 4069-4076.
- Vaney, D. I., J. C. Nelson and D. V. Pow (1998). "Neurotransmitter coupling through gap junctions in the retina." The Journal of neuroscience : the official journal of the Society for Neuroscience **18**(24): 10594-10602.
- Venter, J. C., M. D. Adams, E. W. Myers, P. W. Li, R. J. Mural, G. G. Sutton, H. O. Smith, M. Yandell, C. A. Evans, R. A. Holt, J. D. Gocayne, P. Amanatides, R. M. Ballew, D. H. Huson, et al. (2001). "The sequence of the human genome." Science **291**(5507): 1304-1351.
- Veraart, C., M. C. Wanet-Defalque, B. Gerard, A. Vanlierde and J. Delbeke (2003). "Pattern recognition with the optic nerve visual prosthesis." Artif Organs **27**(11): 996-1004.
- Wässle, H. (2004). "Parallel processing in the mammalian retina." Nat Rev Neurosci **5**(10): 747-757.
- Wässle, H. and B. B. Boycott (1991). Functional architecture of the mammalian retina. Physiol. Rev. **71**: 447-480.
- Wässle, H., C. Puller, F. Muller and S. Haverkamp (2009). "Cone contacts, mosaics, and territories of bipolar cells in the mouse retina." The Journal of Neuroscience **29**(1): 106-117.
- Werblin, F. S. and J. E. Dowling (1969). "Organization of the retina of the mudpuppy, *Necturus maculosus*. II. Intracellular recording." Journal of Neurophysiology **32**(3): 339-355.
- West, M. and P. J. Harrison (1997). Bayesian Forecasting and Dynamic Models. New York, Springer.
- WHO (2007). VISION 2020: The right to sight, World Health Organization.

- Yamashita, M. and H. Wässle (1991). "Responses of rod bipolar cells isolated from the rat retina to the glutamate agonist 2-amino-4-phosphonobutyric acid (APB)." The Journal of Neuroscience **11**(8): 2372-2382.
- Yamazaki, T., H. Ikeno, Y. Okumura, S. Satoh, Y. Kamiyama, Y. Hirata, K. Inagaki, A. Ishihara, T. Kannon and S. Usui (2011). "Simulation Platform: A cloud-based online simulation environment." Neural Networks **24**(7): 693-698.
- Yoshida, K., D. Watanabe, H. Ishikane, M. Tachibana, I. Pastan and S. Nakanishi (2001). "A key role of starburst amacrine cells in originating retinal directional selectivity and optokinetic eye movement." Neuron **30**(3): 771-780.
- Zhou, J. A., S. J. Woo, S. I. Park, E. T. Kim, J. M. Seo, H. Chung and S. J. Kim (2008). "A suprachoroidal electrical retinal stimulator design for long-term animal experiments and in vivo assessment of its feasibility and biocompatibility in rabbits." J Biomed Biotechnol **2008**: 547428-547421-547428-547410.
- Zhou, Z. Y., Q. F. Wan, P. Thakur and R. Heidelberger (2006). "Capacitance measurements in the mouse rod bipolar cell identify a pool of releasable synaptic vesicles." J Neurophysiol **96**(5): 2539-2548.
- Zrenner, E. (2002). "Will retinal implants restore vision?" Science **295**(5557): 1022-1025.
- Zrenner, E., K. U. Bartz-Schmidt, H. Benav, D. Besch, A. Bruckmann, V. P. Gabel, F. Gekeler, U. Greppmaier, A. Harscher, S. Kibbel, J. Koch, A. Kusnyerik, T. Peters, K. Stingl, et al. (2010). "Subretinal electronic chips allow blind patients to read letters and combine them to words." Proc R Soc B.
- Zrenner, E., A. Bruckmann, U. Greppmaier, G. Hoertdoerfer, C. Kernstock, I. Sliesoraityte, K. Stingl and B. Wilhelm (2011). "Improvement of Visual Orientation and Daily Skills Mediated by Subretinal Electronic Implant Alpha IMS in Previously Blind RP Patients." Invest. Ophthalmol. Vis. Sci. **52**(6): 457-
- Zrenner, E., K. Rütger and E. Apfelstedt-Sylla (1992). "Retinitis pigmentosa - Klinische Befunde, molekulargenetische Ergebnisse und Forschungsperspektiven." Der Ophthalmologe **89**: 5-21.
- Zrenner, E., A. Stett, S. Weiss, R. B. Aramant, E. Guenther, K. Kohler, K. D. Miliczek, M. J. Seiler and H. Haemmerle (1999). "Can subretinal microphotodiodes successfully replace degenerated photoreceptors?" Vision Res **39**(15): 2555-2567.
- Zrenner, E., R. Wilke, K. Bartz-Schmidt, H. Benav, D. Besch, F. Gekeler, J. Koch, K. Porubska, H. Sachs and B. Wilhelm (2009). "Blind Retinitis Pigmentosa Patients Can Read Letters and Recognize the Direction of Fine Stripe Patterns With Subretinal Electronic Implants." Invest. Ophthalmol. Vis. Sci. **50**(5): 4581-

6 Appendix

6.1 Acknowledgements

This work was funded by the Tistou und Charlotte Kerstan Stiftung and by the Neuroophthalmologische Gesellschaft, for which am very grateful. I would like to thank Prof. Eberhart Zrenner and Prof. Frank Rattay for their constant support and helpful advice. Many thanks are due to Dr. Daniel Rathbun for countless discussions and for proofreading this thesis. Furthermore, I would like to thank Dr. Robert Wilke, Prof. Thomas Euler and Dr. Cornelia Wenger for sharing their expertise with me. I would also like to thank the Retina Implant AG and the Max Planck Society for covering travel expenses. The graduation was completed in the International Max Planck Research School for Neural and Behavioural Sciences.

This thesis is dedicated to my father, who was not able to see me finish it.

6.2 SWC Files

The swc file format is non-proprietary and stores morphological information of neurons in a form that can be used by multi-compartment models. Except for the first two lines, which are required for the definition of a spherical soma, each line represents one compartment. One compartment is defined by its ID, type, endpoint in three-dimensional Cartesian coordinates, its radius and its parent compartment (starting point). Arbitrary types can be used. In this thesis the four types were soma (1), dendrites (2), axon (3) and synaptic axon terminal (4). The program parsing this swc file is then able to use different biophysical properties for each compartment type.

SWC FILE BP_Euler_95 type 9 ON

ID TYPE X Y Z R Par

t x y z r p

1	1		0		0		0	5.4825	-1
2	1	-0.4386	-10.9649	-0.2193	5.4825	1			
3	2	-2.3026	-24.2325	-0.8772	0.7675	2			
4	2	-4.2763	-28.5088	-0.4386	0.7675	3			
5	2	-3.1798	-30.4825	-0.9868	0.7675	4			
6	2	-3.5088	-33.0044	-2.8509	0.7675	5			
7	2	-1.0965	-35.1974	-5.0439	0.7675	6			
8	2	-0.2193	-40.1316	-3.6184	0.7675	7			
9	2	0.5482	-41.5570	-4.9342	0.7675	8			
10	2	-3.8377	-50	-7.2368	0.7675	9			
11	2	-2.9605	-64.3640	-10.5263	0.7675	10			
12	4	-5.9211	-65.0219	-13.8158	0.6579	11			
13	4	-6.6886	-66.4474	-12.1711	0.6579	12			
14	4	-8.1140	-66.8860	-13.0482	0.6579	13			
15	4	-10.3070	-65.6798	-11.6228	0.6579	14			
16	4	-12.8289	-65.1316	-8.7719	0.6579	15			
17	4	-14.9123	-66.0088	-9.4298	0.6579	16			
18	4	-16.5570	-66.6667	-7.6754	0.6579	17			
19	4	-17.3246	-69.1886	-0.7675	0.6579	18			
20	4	-18.5307	-69.5175	-1.5351	0.6579	19			
21	4	-19.6272	-70.0658	-0.4386	1.0965	20			
22	4	-8.4430	-69.2982	-13.8158	0.6579	14			
23	4	-8.4430	-69.2982	-11.1842	0.6579	22			
24	4	-10.6360	-70.6140	-12.1711	0.6579	23			
25	4	-12.2807	-71.7105	-13.1579	0.6579	24			
26	4	-12.5000	-74.0132	-11.6228	0.6579	25			
27	4	-15.4605	-74.2325	-11.6228	0.6579	26			
28	4	-16.2281	-75.1096	-13.2675	0.6579	27			
29	4	-16.7763	-75.7675	-18.4211	0.6579	28			
30	4	-7.0175	-70.7237	-14.5833	0.6579	23			
31	4	-7.0175	-70.7237	-15.8991	0.6579	30			
32	4	-7.0175	-74.2325	-14.0351	0.6579	31			
33	4	-4.9342	-75.1096	-12.3904	0.6579	32			
34	4	-3.6184	-75.3289	-11.0746	1.0965	33			
35	4	-0.2193	-65.6798	-8.1140	0.6579	11			
36	4	-0.2193	-65.6798	-8.5526	0.6579	35			
37	4	2.8509	-68.0921	-7.6754	0.6579	36			
38	4	2.7412	-69.5175	-7.7851	0.6579	37			
39	4	6.4693	-73.4649	-6.6886	0.6579	38			
40	4	9.7588	-74.7807	-7.1272	0.6579	39			
41	4	10.6360	-77.0833	-4.6053	0.6579	40			
42	4	11.8421	-76.9737	-8.3333	0.6579	41			
43	4	12.9386	-76.8640	-2.7412	1.0965	42			
44	4	8.3333	-72.8070	-7.3465	0.6579	39			
45	4	8.3333	-72.8070	-10.3070	1.0965	44			
46	4	1.5351	-70.2851	-10.6360	1.0965	38			
47	4	5.5921	-67.5439	-4.6053	0.6579	37			
48	4	5.5921	-67.5439	-6.9079	0.6579	47			
49	4	-0.2193	-67.1053	-7.5658	0.6579	36			
50	4	-0.2193	-67.1053	-9.5395	1.0965	49			
51	3	-3.6184	2.8509	2.3026	1.5351	1			
52	3	-3.6184	2.8509	0.9868	0.6579	51			
53	3	-4.3860	4.6053	-0.8772	0.5482	52			
54	3	-7.1272	5.4825	4.2763	0.5482	53			
55	3	-7.6754	4.2763	4.9342	0.5482	54			
56	3	-9.1009	3.7281	8.1140	0.5482	55			
57	3	-10.5263	3.3991	10.4167	0.5482	56			
58	3	-15.7895	3.3991	10.9649	0.5482	57			
59	3	-18.0921	4.4956	14.2544	0.5482	58			
60	3	-19.5175	4.6053	14.0351	0.5482	59			
61	3	-20.3947	5.1535	15.3509	0.5482	60			
62	3	-20.3947	6.2500	11.6228	1.0965	61			
63	3	-19.1886	6.6886	8.6623	0.5482	62			
64	3	-16.5570	6.0307	10.5263	0.5482	63			
65	3	-15.1316	7.0175	9.6491	0.5482	64			
66	3	-16.1184	2.1930	9.9781	0.5482	58			
67	3	-16.1184	2.1930	10.8553	0.5482	66			
68	3	-9.5395	4.7149	1.8640	0.5482	56			
69	3	-9.5395	4.7149	0.9868	0.5482	68			
70	3	-10.6360	4.7149	-1.6447	0.4386	69			
71	3	-10.9649	5.7018	-0.5482	0.5482	70			
72	3	-0.5482	3.2895	1.0965	0.5482	52			
73	3	-0.5482	3.2895	-2.5219	0.5482	72			
74	3	1.5351	5.7018	-2.7412	0.5482	73			
75	3	2.6316	5.1535	-3.2895	0.5482	74			
76	3	5.3728	4.2763	-2.0833	0.5482	75			
77	3	7.8947	5.5921	-3.6184	0.5482	76			
78	3	9.3202	5.1535	-6.7982	0.5482	77			
79	3	10.8553	6.4693	-7.0175	0.5482	78			
80	3	13.7061	7.1272	-5.8114	0.5482	79			
81	3	15.5702	7.1272	-4.9342	0.5482	80			
82	3	18.4211	7.5658	-3.3991	1.0965	81			
83	3	19.5175	7.8947	-5.5921	0.5482	82			
84	3	20.3947	7.2368	-7.6754	0.5482	83			
85	3	22.2588	8.4430	-9.3202	0.5482	84			
86	3	8.5526	7.4561	-2.1930	0.5482	77			
87	3	8.5526	7.4561	-1.5351	0.5482	86			
88	3	10.1974	8.5526	-0.6579	0.5482	87			
89	3	8.2237	8.2237	1.7544	0.5482	88			
90	3	3.9474	6.3596	-1.6447	0.5482	75			
91	3	3.9474	6.3596	-2.0833	0.5482	90			
92	3	4.6053	7.5658	-1.6447	1.0965	91			

SWC FILE BP_Euler_95 type 2 OFF

ID TYPE X Y Z R Par

t x y z r p

1	1		0		0		0	4.4742	-1
2	1	-0.4894	-8.9483	-0.9088	4.4742	1			
3	2	-1.5380	-10.8359	-3.8450	0.4894	2			
4	2	-1.6778	-23	-5.3131	0.4894	3			
5	4	-3.5653	-23.9088	-6.0122	0.4894	4			
6	4	-5.3131	-24.6079	-8.6687	0.4195	5			
7	4	-7.7599	-25.1672	-9.5076	1.1185	6			
8	4	-9.0182	-25.6565	-10.7660	0.4195	7			
9	4	-10.3465	-26.5653	-12.0243	0.4195	8			
10	4	-12.3040	-27.1945	-12.5137	0.8389	9			
11	4	-10.6261	-25.0274	-10.6261	0.4195	8			
12	4	-11.6261	-27.0274	-13.6261	0.4195	11			
13	4	-8.5289	-27.9635	-9.9271	0.4195	6			
14	4	-8.5289	-27.9635	-7.4103	0.4195	13			
15	4	-10.0669	-29.0821	-6.2918	0.8389	14			
16	4	-12.0243	-29.4316	-6.0821	0.4195	15			
17	4	-13.2827	-30.2705	-4.3343	0.4195	16			
18	4	-1.4681	-24.2584	-0.7690	0.4195	4			
19	4	-1.4681	-24.2584	-1.6079	0.4195	18			
20	4	-2.3070	-25.5866	-0.2796	0.4195	19			
21	4	-2.7264	-26.4954	-1.6079	0.4195	20			
22	4	-4.0547	-27.7538	-3.6353	0.8389	21			
23	4	-5.8024	-28.4529	-4.6839	0.4195	22			
24	4	-7.2006	-29.5714	-4.8237	0.8389	23			
25	4	-8.1793	-30.2006	-7.9696	0.4195	24			
26	4	-9.8571	-30.2705	-10.5562	0.4195	25			
27	4	-10.9757	-30.4103	-10.6261	0.8389	26			
28	4	0	-27.9635	-9.6474	0.4195	20			
29	4	0	-27.9635	-8.3891	0.4195	28			
30	4	0.0699	-29.2219	-7.6900	0.4195	29			
31	4	-1.6778	-31.1094	-7.9696	0.4195	30			
32	4	-3.3556	-31.8085	-7.1307	0.8389	31			
33	4	0.5593	-29.9909	-3.1459	0.4195	30			
34	4	0.5593	-29.9909	0	0.8389	33			
35	4	1.3283	-25.7964	-0.0699	0.4195	19			
36	4	1.3283	-25.7964	2.1672	0.8389	35			
37	4	3.1459	-21.9514	1.1884	0.4195	4			
38	4	3.1459	-21.9514	1.7477	0.4195	37			
39	4	4.5441	-22.8602	1.9574	0.4195	38			
40	4	4.6839	-25.1672	3.1459	0.4195	39			
41	4	2.5866	-27.1945	1.1884	0.4195	40			
42	4	3.4255	-28.6626	2.1672	0.8389	41			
43	4	3.9149	-29.6413	2.4468	0.4195	42			
44	4	6.0122	-29.7812	3.0061	0.4195	43			
45	4	7.0608	-30.5502	1.3283	0.8389	44			
46	4	6.2219	-25.4468	0.6991	0.4195	40			
47	4	6.2219	-25.4468	-1.7477	0.4195	46			
48	4	8.1793	-25.7264	-2.9362	0.8389	47			
49	4	10.4164	-26.8450	-4.4742	0.4195	48			
50	4	10.7660	-28.3131	-5.0334	0.4195	49			
51	4	12.6535	-29.0122	-4.7538	0.8389	50			
52	4	5.8723	-23.0699	-3.4255	0.4195	39			
53	4	5.8723	-23.0699	-5.1033	0.8389	52			
54	3	-3.6353	5.6626	-4.6140	0.4894	1			
55	3	-3.6353	5.6626	-2.8663	0.5593	54			
56	3	-2.3070	9.1581	-1.3283	0.3495	55			
57	3	-1.6079	12.4438	-3.8450	0.3495	56			
58	3	-5.2432	15.0304	-2.6565	0.2796	57			
59	3	-7.2006	14.6109	-2.9362	0.2796	58			
60	3	-8.1793	14.9605	-0.6991	0.2796	59			
61	3	-1.6778	13.9119	0.7690	0.3495	57			
62	3	-1.6778	13.9119	0.2097	0.3495	61			
63	3	-2.5866	14.8207	0.6292	0.3495	62			
64	3	-3.7751	14.2614	1.4681	0.3495	63			
65	3	1.1884	14.2614	-2.4468	0.3495	57			
66	3	1.1884	14.2614	-3.4255	0.3495	65			
67	3	3.1459	14.2614	-4.0547	0.3495	66			
68	3	3.5653	14.8207	-5.8723	0.3495	67			
69	3	0.0699	9.5775	-9.4377	0.3495	56			
70	3	0.0699	9.5775	-8.1094	0.3495	69			
71	3	1.2584	9.7872	-9.0881	0.3495	70			
72	3	2.5167	10.8359	-7.2006	0.3495	71			
73	3	4.7538	11.8845	-8.7386	0.6991	72			
74	3	6.7112	11.8146	-7.2006	0.3495	73			
75	3	8.4590	12.8632	-6.0821	0.6991	74			
76	3	11.8845	12.6535	-5.1733	0.3495	75			
77	3	12.7933	13.7720	-6.8511	0.6991	76			
78	3	4.5441	12.5836	-7.1307	0.3495	73			
79	3	4.5441	12.5836	-7.8997	0.2097	78			

6.3 Publication on the Tübingen Subretinal Implant

This section contains a recent publication on the current stage of development and clinical results in the Tübingen subretinal implant project. The author of this thesis contributed significantly to the publication by taking part in designing and performing psychophysical experiments, collecting, visualizing and processing the data and by assisting in the writing process.

Subretinal electronic chips allow blind patients to read letters and combine them to words

Eberhart Zrenner^{1,*}, Karl Ulrich Bartz-Schmidt¹, Heval Benav¹,
Dorothea Besch¹, Anna Bruckmann¹, Veit-Peter Gabel²,
Florian Gekeler¹, Udo Greppmaier³, Alex Harscher³, Steffen Kibbel³,
Johannes Koch¹, Akos Kusnyerik^{1,4}, Tobias Peters⁵, Katarina Stingl¹,
Helmut Sachs⁶, Alfred Stett⁷, Peter Szurman¹,
Barbara Wilhelm⁵ and Robert Wilke¹

¹Centre for Ophthalmology, University of Tübingen, Schleichstr. 12, 72076 Tübingen, Germany

²Eye Clinic, University of Regensburg, Franz-Josef-Strauss-Allee 11, 93053 Regensburg, Germany

³Retina Implant AG, Gerhard-Kindler-Str. 8, 72770 Reutlingen, Germany

⁴Department of Ophthalmology, Semmelweis University, Tomo u. 25-29, 1083 Budapest, Hungary

⁵Steinbeis Transfer Centre Eyetrial at the Centre for Ophthalmology, Schleichstr. 12-16,
72076 Tübingen, Germany

⁶Klinikum Friedrichstadt, Friedrichstr. 41, 01067 Dresden, Germany

⁷NMI Natural and Medical Sciences Institute at the University of Tübingen, Markwiesenstr. 55,
72770 Reutlingen, Germany

A light-sensitive, externally powered microchip was surgically implanted subretinally near the macular region of volunteers blind from hereditary retinal dystrophy. The implant contains an array of 1500 active microphotodiodes ('chip'), each with its own amplifier and local stimulation electrode. At the implant's tip, another array of 16 wire-connected electrodes allows light-independent direct stimulation and testing of the neuron-electrode interface. Visual scenes are projected naturally through the eye's lens onto the chip under the transparent retina. The chip generates a corresponding pattern of 38×40 pixels, each releasing light-intensity-dependent electric stimulation pulses. Subsequently, three previously blind persons could locate bright objects on a dark table, two of whom could discern grating patterns. One of these patients was able to correctly describe and name objects like a fork or knife on a table, geometric patterns, different kinds of fruit and discern shades of grey with only 15 per cent contrast. Without a training period, the regained visual functions enabled him to localize and approach persons in a room freely and to read large letters as complete words after several years of blindness. These results demonstrate for the first time that subretinal micro-electrode arrays with 1500 photodiodes can create detailed meaningful visual perception in previously blind individuals.

Keywords: subretinal neuro-prosthetics; retinal implant; retinitis pigmentosa; blindness; artificial vision; bionic vision

1. INTRODUCTION

Retinitis pigmentosa (RP) and age-related macular degeneration are diseases that predominantly affect photoreceptors of the retina and cause progressive vision loss—leading eventually to blindness in over 15 million people worldwide [1]. Although blindness owing to photoreceptor degeneration presently remains incurable, inner retinal nerve cells may continue to function for many years despite neuronal remodelling [2]. While gene therapy and application of neuro-protective factors may help maintain vision in the early stages of degeneration, survival of the inner retina encouraged us [3] and

others [4–11] to attempt a partial restoration of visual function using electric stimulation of the remaining retinal network.

Two fundamentally different approaches have been taken in this area: (i) implantation of electrode arrays which interface epiretinally with retinal ganglion cells that form the retinal output pathway [6–7,11–13], and (ii) implantation of microchips under the transparent retina to substitute the degenerated photoreceptors. The latter type of microchip senses light and generates stimulation signals simultaneously at many pixel locations, using microphotodiode arrays (MPDAs; [3,14]). While the first approach typically requires external image and data processing due to bypassing retinal image analysis, the second seeks to replace the function of degenerated photoreceptors directly by translating the light of the image falling onto the retina point by point into small

* Author for correspondence (ezrenner@uni-tuebingen.de).

Electronic supplementary material is available at <http://dx.doi.org/10.1098/rspb.2010.1747> or via <http://rspb.royalsocietypublishing.org>.

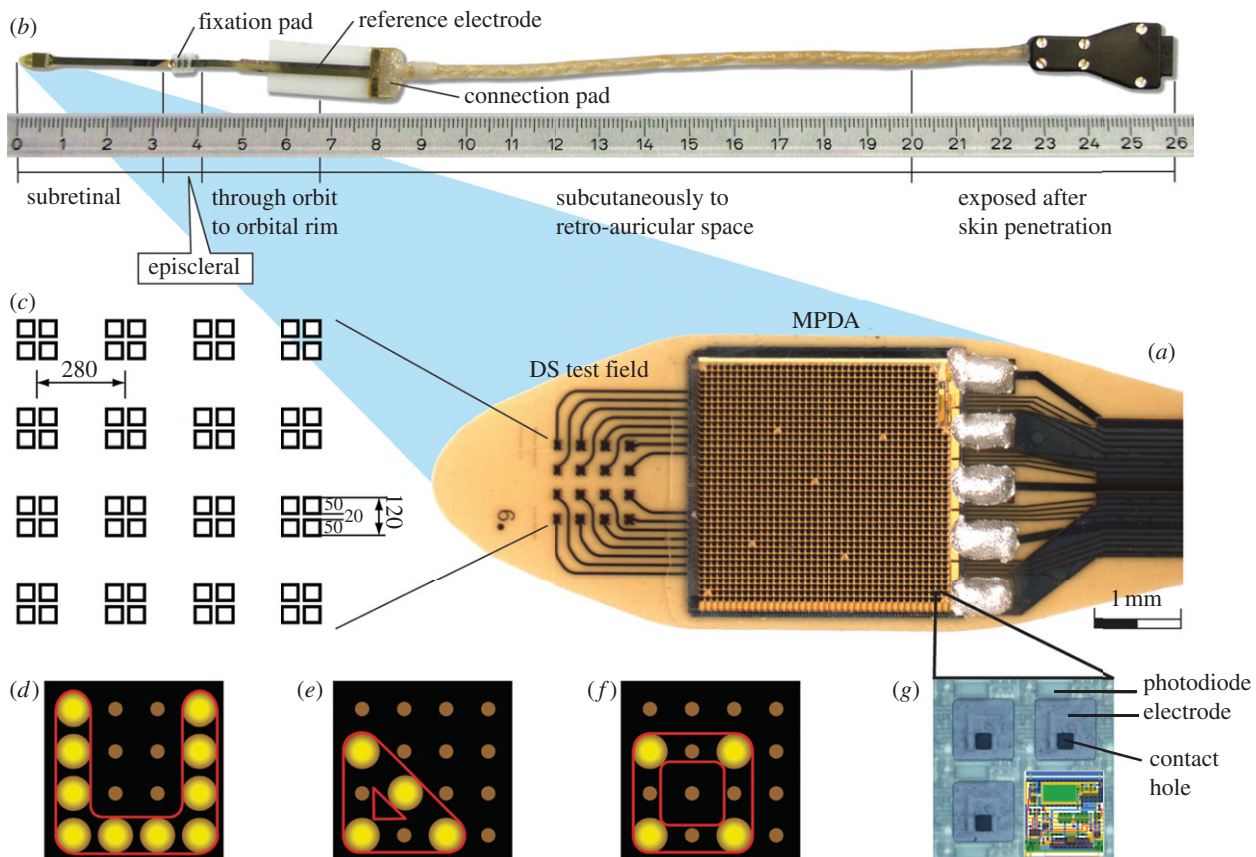


Figure 1. Subretinal implant. (a) The microphotodiode array (MPDA) is a light sensitive 3.0×3.1 mm CMOS-chip with 1500 pixel-generating elements on a $20 \mu\text{m}$ thick polyimide foil carrying an additional test field with 16 electrodes for direct electrical stimulation (DS test field). (b) The foil exits approximately 25 mm away from the tip at the equator of the eyeball and is attached to the sclera by means of a small fixation pad looping through the orbit to a subcutaneous silicone cable that connects via a plug behind the ear to a power control unit. (c) Magnification of the DS test field showing the 16 quadruple electrodes and their dimensions. (d) Pattern stimulation via DS array (e.g. ‘U’). (e,f) switching from a triangle to a square by shifting stimulation of a single electrode. (g) Magnification of four of the 1500 elements (‘pixels’), showing the rectangular photodiodes above each squared electrode and its contact hole that connects it to the amplifier circuit (overlaid sketch).

currents that are proportional to the light stimulus. Ours is the only approach where the photodiode–amplifier–electrode set is contained within a single pixel of the MPDA such that each electrode provides an electrical stimulus to the remaining neurons nearby thereby reflecting the visual signal that would normally be received via the corresponding, degenerated photoreceptor.

On the basis of *in vitro* measurements [15] and animal studies [16] our consortium developed a subretinal electronic implant that carefully accounts for biocompatibility [17], biostability, surgical feasibility by means of a transchoroidal surgical technique [18], safe threshold stimulation and dynamic range of stimulation and the limits of spatial resolution *in vitro* [19]. This report describes the results of a clinical pilot study, illustrating that subretinally implanted multi-electrode arrays restore sufficient visual function for object recognition and localization and for the performance of visual tasks essential in the daily lives of blind patients. The results of this pilot study provide strong evidence that the visual functions of patients blinded by a hereditary retinal dystrophy can, in principle, be restored to a degree sufficient for use in daily life.

2. THE SUBRETINAL IMPLANT

As shown in figure 1a, the tip of the implant consists of an MPDA with 1500 individual light-sensitive elements

and a test field for direct stimulation (DS) with 4×4 electrodes for electrical, light-independent stimulation. Both are positioned on a thin polyimide foil (figure 1b, far left). For details on the control unit that provides power and wireless control signals, see figure 2a,d electronic supplementary material, chapter 1c.

(a) The microphotodiode array

Each of the 1500 MPDA elements acts independently from its neighbours; four magnified elements ($72 \times 72 \mu\text{m}$ each) are shown in figure 1g. Each element includes a light-sensitive photodiode ($15 \times 30 \mu\text{m}$) that controls a differential amplifier (circuit shown as a sketch) whose output stage is coupled to a titanium nitride (TiN) electrode ($50 \times 50 \mu\text{m}$), connected to the amplifier via the contact hole (details see electronic supplementary material, chapter 1b). Essentially, an image is captured several times per second simultaneously by all photodiodes. Each element (‘pixel’) generates monophasic anodic voltage pulses at its electrode. Thus, pixelized repetitive stimulation is delivered simultaneously by all electrodes to adjacent groups of bipolar cells [15,19], the amount of current provided by each electrode being dependent on the brightness at each photodiode. Light levels ranging across approximately 2 log units are converted to charge pulses by each pixel with a sigmoidal relationship and the sensitivity can be shifted manually by several log units (see

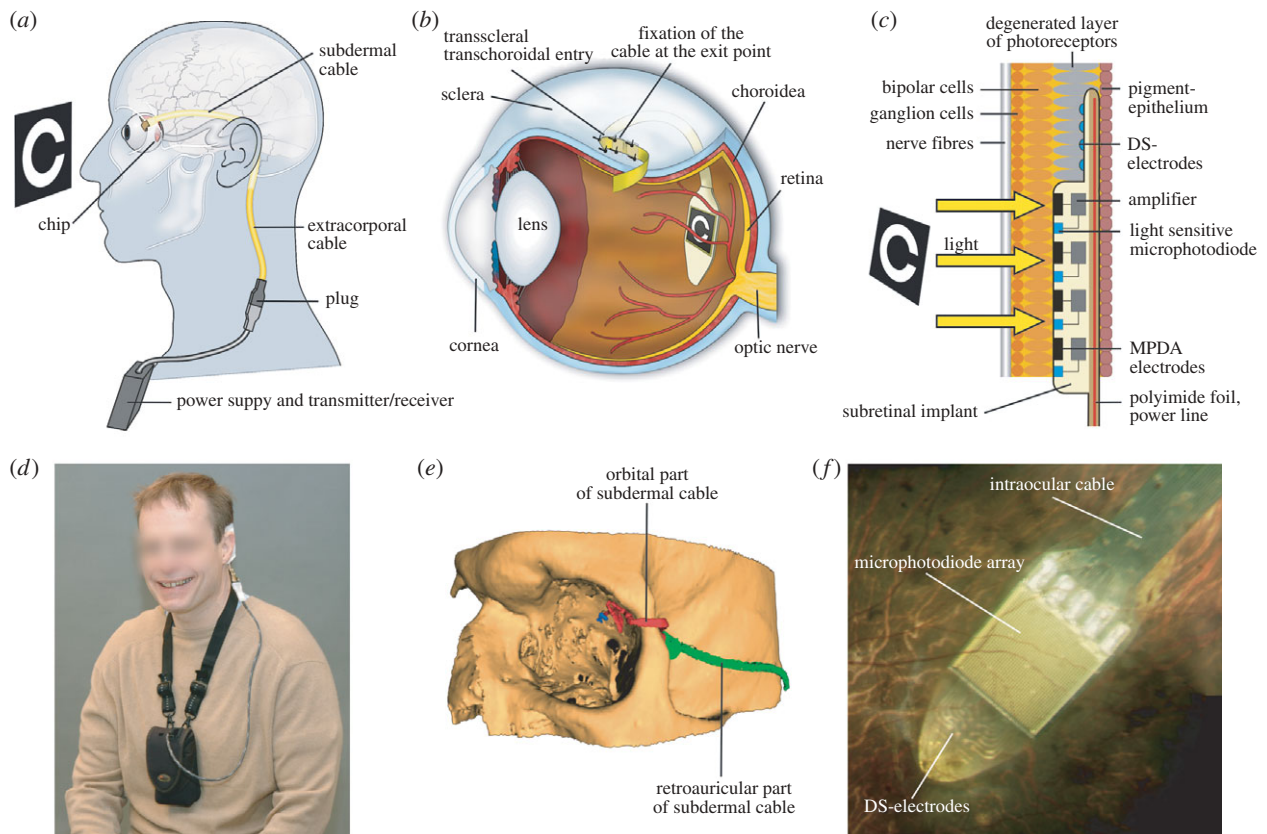


Figure 2. Implant position in the body. (a) The cable from the implanted chip in the eye leads under the temporal muscle to the exit behind the ear, and connects with a wirelessly operated power control unit. (b) Position of the implant under the transparent retina. (c) MPDA photodiodes, amplifiers and electrodes in relation to retinal neurons and pigment epithelium. (d) Patient with wireless control unit attached to a neckband. (e) Route of the polyimide foil (red) and cable (green) in the orbit in a three-dimensional reconstruction of CT scans. (f) Photograph of the subretinal implant's tip at the posterior eye pole through a patient's pupil.

electronic supplementary material, chapter 1, figure S1). The chip is estimated to cover a visual angle of approximately 11° by 11° (1° approx. $288 \mu\text{m}$ on the retina). The distance between two MPDA electrodes corresponds to a visual angle of 15 min of arc.

(b) The 4 by 4 test field for direct stimulation (DS test field)

The DS test field consists of 4×4 quadruple TiN electrodes ($100 \times 100 \mu\text{m}^2$, $280 \mu\text{m}$ apart laterally and $396 \mu\text{m}$ diagonally) for light-independent electrical stimulation (see figure 1c). The DS test field was added for assessment of the electrode-interface characteristics and to study current injections and efficacy of pulses with different shapes and polarities other than those provided by the MPDA. In a limited spatial testing range simple patterns can be created with the DS test field as well (figure 1d,e and f).

Threshold voltage to elicit a percept was assessed in an up-and-down staircase procedure. Typical charge transfer of a single electrode at threshold was between 20 and 60 nC per pulse (for details, see electronic supplementary material, chapter 1a). The maximum charge density at the electrodes in the DS field was $600 \mu\text{C cm}^{-2}$. These values were well within commonly accepted safety limits and have been proven safe even for continuous retinal stimulation *ex vivo* [20].

Impedance values of single electrodes were typically $300 \text{ k}\Omega$ (at 1 kHz sinusoidal AC). Although regular impedance measurements in the patients were not conclusive, analysis of all available data showed that charge

thresholds, but not voltage thresholds decreased significantly during the first days after implantation. Thereafter, both charge and voltage thresholds showed a slight tendency towards increasing values over the remaining implantation period.

3. PATIENTS

The patients (two males and one female, age 40, 44 and 38, respectively) were blind owing to hereditary retinal degeneration (patients 1 and 2: RP, patient 3: choroideraemia) but had good central vision previously. Disease onset was reported by patient 2 at age 16, by patients 1 and 3 at age 6. They had lost their reading ability at least 5 years before implantation. Bright light stimulation mediated some limited light perception without any recognition of shapes in all three patients. They reported neither general diseases nor regular medication (for details see electronic supplementary material, chapter 2c).

4. METHODS

(a) Surgical procedure

The implant, protected by a long steel tube, was advanced through a retroauricular incision to the lateral orbital rim and guided inside the orbit to the surface of the eyeball ([21]; figure 2a,b,e). The silicone cable (figure 2a) was implanted subperiostally beneath the temporal muscle. The polyimide foil was then protected by a silicone tube and guided from the lateral orbital rim, where it was fixed, to the equator of the eye. Subsequently pars plana vitrectomy

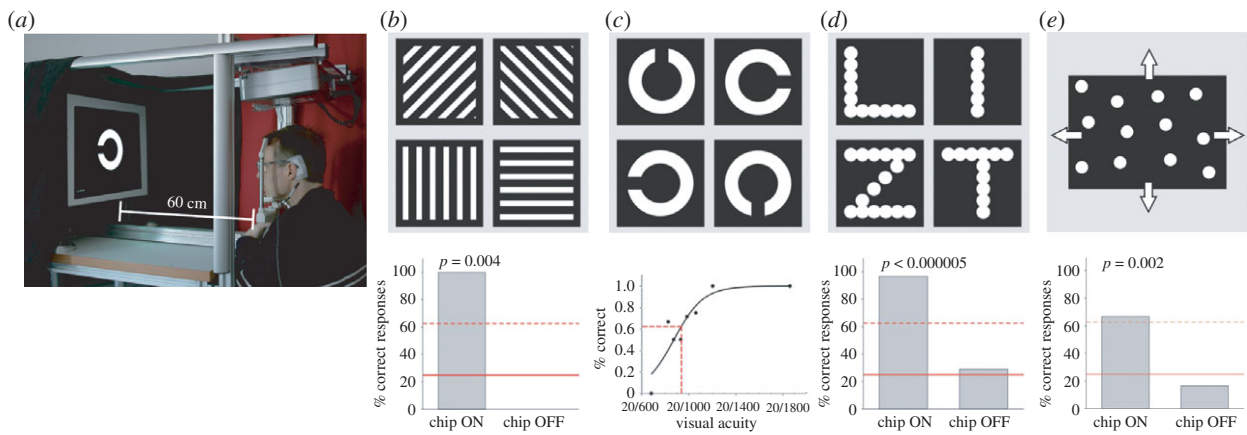


Figure 3. Recognition of projected targets (set up 1) (a) Set up for projecting targets on a screen. (b) Gratings of variable width, distance and luminance, presented individually in a ‘four-alternative forced choice’ mode (4AFC). (c) Landolt ‘C’ ring used in clinical tests of visual acuity. (d) Letters (8.5 cm high, 1.7 cm line width). (e) Random dot pattern moving in four different directions to assess spatio-temporal resolution. The inserts under each panel show the best results of patient 2 with the chip turned on and chip turned off. Solid line, chance rate; dashed line, psychometrically accepted recognition threshold; probability p as estimated from the binomial function.

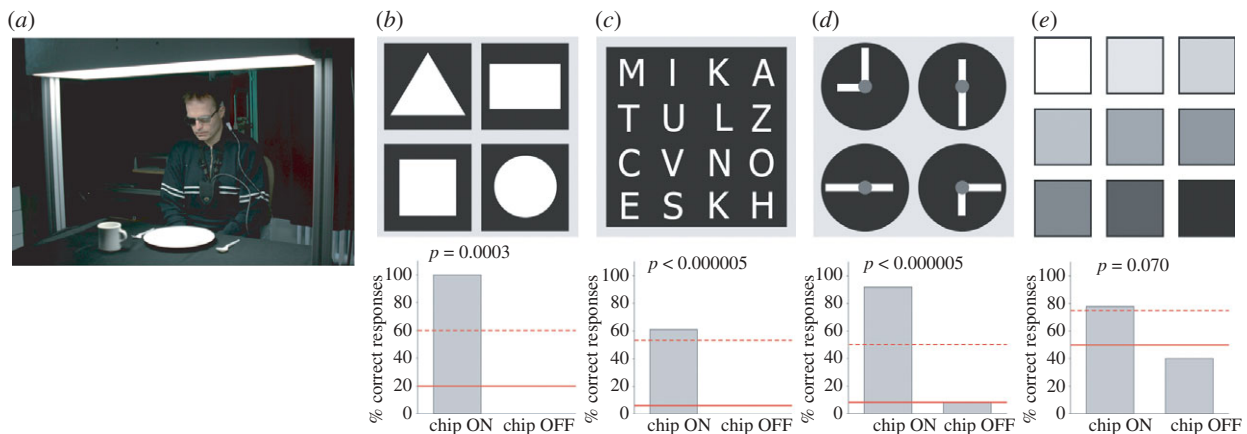


Figure 4. Recognition of objects (set up 2) (a) White items on a homogeneously illuminated black tablecloth. (b) Differentiation of four geometric objects with identical surface areas. (c) Differentiation of capital letters (height 5–8 cm). (d) Clock face for testing angle and size recognition. (e) Cards of different luminance presented in pairs to determine contrast vision. The respective inserts under each panel show the best results of patient 2 with the chip turned on and off. Solid line, chance rate; dashed line, psychometrically accepted recognition threshold; probability p as estimated from the binomial function (see electronic supplementary material, chapter 3b).

was performed. A localized retinal detachment was created by saline injection in the upper temporal quadrant above the planned scleral and choroidal incision area. After preparation of a scleral flap, the implant was advanced *ab externo* transchoroidally along a guiding foil into the subretinal space until it reached the preoperatively defined position ([22]; see electronic supplementary material, chapter 2c). Although putting a chip directly under the fovea has not turned out to be a surgical problem we had abstained in initial patients from placing the chip under the macula, but asked to place the chip closer and closer to the foveola as the surgical learning curve improved. Silicone oil was then injected into the vitreous cavity to support retinal reattachment. No serious adverse events were noted during the course of the study. For post-operative observations and consideration on surgical safety see electronic supplementary material, chapter 2f).

(b) Psychophysical tests

Beginning 7 to 9 days after surgery, tests with solely electrical stimuli were performed with the DS test field. Thereafter light evoked visual functions mediated by the MPDA-array were assessed using four psychophysical tests concerning light

detection, basic temporal resolution, object localization and movement detection using the ‘basic light and motion test’ (BaLM [23]) described in electronic supplementary material, chapter 2g.

If passed successfully, three further steps followed: tests for recognition of stripe patterns (BAGA [24]), localization and recognition of objects common to daily life and visual acuity assessment (Landolt-C rings presented in an up-and-down staircase procedure to estimate the visual acuity in terms of maximum likelihood by means of FrACT test [25]). If these tasks were completed successfully, more challenging tasks were set (figures 3a and 4a). Except for some optional tasks (indicated) well-established two- or four-alternative forced-choice methods (2AFC and 4AFC, respectively) were employed in order to test for statistical significance of a patient’s performance. All tests were performed separately in two conditions: with ‘Power ON’ and ‘Power OFF’ (‘baseline performance’).

Maximum screen luminance was approximately 3200 cd m^{-2} (for white light), neutral density filters (Schott NG filters 0.15–4 log U) served for attenuation (for details see electronic supplementary material, chapter 2).

5. RESULTS

(a) Electrical stimulation for pre-testing and learning via DS test field

Pulses of varying duration, polarity and shape were applied via the DS test field (16 electrodes, as shown in figure 1c–f) in a pre-testing routine. This procedure determined voltage thresholds for perception, accustomed the patients to electrically evoked visual impressions and tested retinal excitability and spatial resolution. An overview of the results including their statistical evaluation is given in a table presented in electronic supplementary material, chapter 3a.

All patients detected single-electrode single-pulse stimulation (0.5–6 ms pulses, typically 20–60 nC per electrode). Patients 1 and 2 consistently reported these stimuli as whitish round dot-like percepts, patient 3 reported percepts as elongated, short whitish/yellowish lines. Upon activation of four electrodes with a single pulse, all three patients correctly distinguished vertical lines from horizontal lines within seconds and spontaneously reported them as straight. Patients 1 and 2 distinguished multiple single dots upon simultaneous activation of several electrodes in a diagonal row and reported dark areas separating the dots. Patient 3 saw diagonal lines formed by four electrodes, but not the dark areas between the dots.

Simple patterns were also presented with the DS-array by pulsing electrodes sequentially (figure 1d); each electrode was switched on for 3–6 ms at intervals of 208 ms. Patients 1 and 2 correctly reproduced these patterns after the first single presentation; patient 3 failed to do so. Upon presentation of a four-alternative, forced-choice (4AFC) paradigm, patients 1 and 2 reliably differentiated four different positions of the opening of the letter ‘U’ (73% and 88% correct responses, respectively, see electronic supplementary material, chapter 5, movie 1). Furthermore, patient 1 correctly distinguished ‘U’ from ‘I’ and even squares from triangles when only a single activated electrode differed in position (16/16 correct, figure 1e,f). Patient 2 correctly distinguished four letters individually presented randomly in 4AFC-mode (e.g. C,I,L,O (36/36), I,L,V,T (10/12)) in repetitive tests on different days (see electronic supplementary material, chapter 5, movie 2). He also distinguished sequential stimulation in clockwise versus anticlockwise direction (15 of 16 tests correct).

(b) Light pattern perception with the microphotodiode array

The light-sensitive MPDA chip was operated at a sampling rate of 1 to 20 Hz with a pulse duration (PD) of 1–4 ms. The patient’s head was comfortably positioned on a chin-rest (set up 1, figure 3a), and refraction was corrected for the viewing distance of 60 cm. Chip settings were adjusted for a working range of 8–800 cd m^{-2} white light or 1.2–4.3 cd m^{-2} red light (for details see electronic supplementary material, chapter 2g). All standardized testing was performed using a functional baseline control, i.e. performance was also tested with the chip switched off at random intervals unknown to patient and observer, as summarized in electronic supplementary material, table ST1.

(i) Light perception and localization

All three patients were able to perceive light mediated by the chip. This was verified in task 1, using the BaLM-test in set up 1 (figure 3a):

- *BaLM flash test*: in task 1, the whole screen was illuminated briefly with one or two flashes (200 ms duration with 600 ms pause) after an auditory signal. All three patients passed this test for light detection (81.3%, 100% and 100% correct, respectively) and scored well-above chance rate; ($n = 16$; ON versus OFF: $p = 0.00005$, t -test).
- *BaLM localization test*: when testing the ability to localize large bright areas in the visual field (small triangle in relation to a central fixation point in BaLM test) only patient 2 (87.5%; $n = 16$) passed the test successfully.
- *BaLM movement test*: perception of movement was tested with a random dot pattern at an angular speed of $1.11^\circ \text{ s}^{-1}$ moving in one of four directions (dot diameter 1.4 cm, average distance 1.5 cm (s.d. 0.26)), passed only by patient 2 (8 of 12, 4AFC, figure 3e).

In task 2, spatial resolution was tested using grid patterns (figure 3b). Bright lines of 0.6 cm width separated by 1.8 cm wide dark lines as well as bright lines of 0.8 cm width separated by 2.4 cm wide dark lines were presented at 63 cm distance. The orientation of these patterns was correctly recognized by patient 2. In terms of spatial frequency this corresponds to $0.46 \text{ cycles deg}^{-1}$ (five of eight correct, 4AFC, $p = 0.02$) and $0.34 \text{ cycles deg}^{-1}$ (four of four correct, 4AFC, $p = 0.004$), respectively (see electronic supplementary material, chapter 3, table ST1 and chapter 5, movie 3). Patient 3 succeeded at $0.22 \text{ cycles deg}^{-1}$ (12 of 20, 4AFC, white light). Patient 1 had difficulty seeing the stripes, probably owing to her nystagmus, but distinguished horizontal from vertical lines projected onto her chip in a special set up using a fundus camera with comparable spatial arrangements and luminance.

As the spectral sensitivity of the chip is practically flat far into the infrared region, patients at several instances reported high sensitivity to infrared light.

(ii) Landolt C ring

In task 3, single letters and Landolt C rings were presented on the screen in various sizes (figure 3c). Patients 1 and 3 discerned neither the Landolt C rings nor the letters and were accordingly not presented with tests of higher difficulty in set up 1. Patient 2, the only one with the chip placed under the macula, was quite successful and his visual performance is therefore described in greater detail below.

Optimizing his implant settings resulted in an image recording time of 0.5 ms with a 7.5 Hz repetition frequency at a target luminance of 3.4 cd m^{-2} (red light), viewed with a correction of +7.0 dpt sph., –1.50 dpt cyl. at 121° . Landolt C rings (figure 3c) were presented in an up-and-down staircase procedure (FrACT [25]; for details see electronic supplementary material, chapter 2). A maximum of 60 s was allowed for the patient to find each C-ring on the screen in his small visual field; failure to respond in time counted as mistake. Maximum visual

acuity was up to 20/1000 (log MAR = 1.69)—corresponding to a Landolt ring with 4.5 cm outer diameter and a gap of 9 mm, viewed at about 60 cm distance. In three other trials on different days he achieved log MAR values of 1.75, 1.94 and 1.86, respectively (see electronic supplementary material, chapter 5, movie 4).

Patient 2 reliably differentiated also the letters L, I, T, Z on a screen (22 of 24, 4AFC, figure 3*d*; 8.5 cm high, 1.7 cm line width, corresponding to a height of approximately 9° of visual angle). He reported that having once found a letter, it appeared clearly in its natural form and was visible as a complete entity—even during its first presentation.

(iii) Recognition of objects on a table

In the fourth task, the ability to perceive more naturalistic scenes was tested by a standardized set up at a dining table, assessed by an independent, professional mobility trainer (figure 4*a*, for details see electronic supplementary material, chapter 2*g*). Patient 1 reliably localized a saucer, a square and a cup on the table; patient 3 correctly localized and differentiated a large plate from a saucer.

Patient 2 localized, and moreover recognized and correctly differentiated square-, triangle-, circle-, rectangular-, and diamond-shapes, which differed only in shape but not in area from each other (figure 4*b*, five of five correct, see electronic supplementary material, chapter 5, movie 5). Furthermore, he could localize and describe correctly a spoon, a knife, a cup (see electronic supplementary material, chapter 5, movie 6), as well as a banana and an apple (see electronic supplementary material, chapter 5, movie 7). Unlike the other dining table set ups this set up was entirely unknown to the patient and he was forced to make sense of an unfamiliar scene.

(iv) Optional tasks with letters, clock, grey papers of varying shades

The fifth group of tasks was performed only in patients who had successfully passed previous tasks. Patient 2 was able to distinguish between 16 different letters cut from white paper (5–8 cm high, font: Tahoma), placed on the black table (see figure 4*c*, 22/36 correct). The patient read letters (LOVE, MOUSE, SUOMI, etc.) correctly (five of five), also repeatedly on several days. He noted spelling mistakes in his name MIIKKA (mentioning that one ‘I’ and one ‘K’ were missing) when he first saw this word (see electronic supplementary material, chapter 5, movie 8), i.e. he perceived both individual letters and continuous, meaningful words—a prerequisite for reading.

As an additional task, a clock face was presented with two hands (6 × 1.5 cm for the hours, 12 × 1.5 cm for the minutes, figure 4*d*). Patient 2 was asked to indicate clock times set to full quarter hours. The patient correctly recognized 11 of 12 possible settings. Patient 2 also distinguished seven out of nine contrast differences of 15 per cent among nine neighbouring cards (10 × 10 cm, presented in 2AFC mode, $p = 0.07$) with linearly scaled shades of grey varying from 3 to 35 cd m⁻² (figure 4*e*).

All patients showed distinct learning effects which, while they could not be quantified in this first pilot study, are reported as ‘spontaneous observations’ in electronic supplementary material, chapter 3*d*.

(v) Pupillary reflexes

Pupillary constriction in response to light as an objective measure of MPDA efficacy was assessed by infrared pupillography (for methods and recordings, see electronic supplementary material, chapter 2*c*). The amplitude of pupillary constriction was clearly more pronounced when the chip was activated (see electronic supplementary material, chapter 2, figure S2). In all three patients the chip-on condition improved pupil reaction and was always accompanied by subjective light perception. An analysis of variance was calculated for the constriction amplitudes of all three patients (with chip-on or chip-off) and patient as factors (sum of squares 0.184, $F = 6.48$, $p = 0.022$).

6. DISCUSSION

(a) The general approaches to retinal prostheses

A number of research groups have taken up the challenge of developing a retinal prosthesis. Rizzo *et al.* [4] and Weiland *et al.* [26] have reported on first trial stimulations of the retina with single epiretinal electrodes. Chow *et al.* [27] were the first to subretinally implant well-tolerated multiphotodiode arrays, intending to use the energy created by incident light for neuronal stimulation directly without amplification. However, owing to insufficient energy from the small light sensors these failed to restore vision. Second Sight (Medical Products Inc., Sylmar, CA) has a multicentre study running with the epiretinal ARGUS II device with 60 electrodes; some patients were reported to recognize large single letters by scanning them with rapid head movements [28]. Clinical studies with epiretinal electrode arrays were also performed by Koch *et al.* [29] and Richard *et al.* [30]. Other groups developed approaches with electrodes placed between sclera and choroid [8,10]. These groups argue that this ‘suprachoroidal’ approach may have the benefit of being less invasive, therefore bearing fewer risks in terms of surgical procedures. At this time, as only limited peer-reviewed information is available from ongoing clinical trials using subretinal, epiretinal and suprachoroidal approaches, it is too early to compare the final long-term outcome of the various designs. All have inherent theoretical advantages and disadvantages; basic differences and their consequences are pointed out in the following.

Epiretinal implants seek to interact directly with the retinal output neurons; the image processing of the complex inner retinal network must be performed externally. The processing of camera-captured images can be more easily adjusted to account for individual electrode thresholds. However, the number of simultaneously addressed electrodes is limited by present technology. Several groups have developed externally powered, fully implantable epiretinal systems with arrays of up to 60 microelectrodes [7,28–32]. Although they have reported promising results, even for long term use, the low number of electrodes limit visual performance to object localization and shape perception [33]. Yanai *et al.* [6] reported no difference in patient performance when a single pixel or multiple pixels were activated using a prototype of the ARGUS I implant. In *epiretinal implants* that use head mounted cameras, eye movements are not correlated to the visually perceived scene. Such a mismatch of visual and proprioceptive information must render object localization difficult [34].

Subretinal approaches, in contrast, replace in principle only the lost function of diseased photoreceptors; thus, the remaining network of the inner retina can be used for more natural processing of the image as it is forwarded, point-by-point, several times per second to inner retinal neurons. Although the surgical procedure may be more demanding, the number of pixels can be much higher, presently limited only by the size of an implant and the spatial spread of electrical stimulation. Fixation of the chip in the subretinal space is easier and, once positioned, the chip remains in place, tightly connected to the inner retina without the need for scleral tacks as used in epiretinal approaches. Moreover, our subretinal implant (Retina Implant AG, Reutlingen, Germany) is the only one so far, where the image receiver array moves exactly with the eye. This has practical implications, outlined below, as natural eye movements can be used to find and fixate a target. On the other hand, the duration of our study was limited owing to time constraints of a transdermal cable; other studies have reported longer implantation times [33]. Moreover, the range of variations in online image processing is small in devices that work quasi-autonomously under the retina.

Suprachoroidal implants, although bearing lower surgical risks, are located further away from target cells. This may result in high stimulation thresholds, increased power consumption, and certainly loss of spatial resolution. While the surgery is easier and less invasive, the location between highly light absorbing sclera and choroid does not allow the implantation of a light sensitive array that moves with the eye.

In the following sections, the results obtained in our subretinal study are discussed in more detail.

(b) *The spatial domain*

Using simulated prosthetic vision Perez *et al.* [35] have shown that the precision in recognition tasks with normal sighted subjects increased with a density of pixels up to 1000 in a $10^\circ \times 7^\circ$ visual field on the retina. Thus, at least several hundred electrodes should be employed to provide significant vision—a daunting technical barrier [35]. The present study—the first to successfully employ electronic arrays with such a large number of electrodes—presents proof-of-concept that such devices can restore useful vision in blind human subjects, even though the ultimate goal of broad clinical application will take time to develop.

The size of the visual field ($11^\circ \times 11^\circ$) in our patients, although small, is sufficient for orientation and object localization, as is well established in patients with peripheral retinal dystrophies. Reading requires a field of 3 by 5 degrees according to Aulhorn [36].

Inter-individual variations in visual performance among the patients of this study can be assumed to result from their respective stages of degeneration [2], the duration of their blindness, and the retinal localization of the implant, although presently no convincing correlation can be established. Clearly spatial reorganization of the retina takes place; however, it is very slow, taking decades. As the inner retina is not dependent on choroidal perfusion, it also survives the complete loss of the choroid—as seen in our patient with choroïdæmia. This also explains why blockage of choroïdo-retinal

transport by our implant does not affect survival of the inner retina.

In our study, precise localization of the microelectrode array under the fovea appeared important for the restoration of useful percepts via spatially ordered electrical stimulation. High spatial resolution and the ability to read are restricted in normal observers to the central retina ($5^\circ \times 3^\circ$), which is significantly over-represented in the visual cortex relative to more peripheral areas of the retina.

(c) *The temporal domain and the problem of image fading*

Temporal resolution was investigated over a range from 1 to 20 Hz. When applying continuous electrical stimuli via the *DS-array* at a fixed retinal location with PD of 1–4 ms, patient percepts faded after approximately 15 s when presented at a 0.3 Hz repetition rate; after approx. 2 s at 2 Hz; and after approx. 0.5 s at 10 Hz. This is in close accordance with the observations of Perez *et al.* [37] with *epiretinal ARGUS II* devices that an image stabilized on the retina quickly disappears; to restore the image required a movement of the image across the retina, by means of rapid head shaking. Similarly, Jensen & Rizzo [38] observed in rabbit retina that the retinal response to a second or third electrical pulse rapidly decreases as compared to the first pulse with increasing repetition rates; apparently inner retina neurons suffer from a prolonged inhibition if stimulated electrically under conditions where the surrounding network under the electrode is being activated as a whole. By contrast, objects like grating patterns or letters can be perceived continuously with our light sensitive *subretinal MPDA*. Patients see the image constantly as a complete entity without head movements—even on the first day of stimulation. The source of this difference can be found in involuntary eye movements controlled by the superior colliculus. Even during fixation, our eyes continuously make slight movements (slow drifts and microsaccades up to 50 min of arc and 1 to 3 Hz) that refresh the image by constantly changing the activated photoreceptor population—even during strict fixation [39]. Objects viewed by our patients—with the chip moving in synchronization with natural eye movement—dynamically activate a range of adjacent pixels on the chip, as eye movements and microsaccades continuously shift the ‘electrical image’ on the retina for about 1–3 pixels, thus preventing mechanisms of local adaptation and image fading. Details on the role and magnitude of microsaccades in relation to pixel size are outlined in electronic supplementary material, chapter 3e (figure S3).

(d) *The cellular ‘interface’*

In vitro experiments have shown that subretinal stimulation, at least at threshold, preferentially stimulates bipolar cells [15,19]. This may be one reason for the correct retinotopic perceptions reported in this study, since local excitation of small groups of bipolar cells is recognized in the brain at the correct position in the visual field. By contrast, epiretinal stimulation of ganglion cell fibres may result in disparities between stimulation location and perceived visual field location because the axons of RGCs course across the retina on their way into the brain via the optic nerve. On the other hand, none of the different approaches has principal problems

with addressing simultaneously ON and OFF neurons (see electronic supplementary material, chapter 3c).

(e) *Learning and cognition*

With the subretinal approach and its retinotopically correct spatial transmission, no long-term learning procedure was necessary to enable the patients to recognize shapes correctly. Even at the first trial with the DS test field or with the MPDA, patients were able to correctly perceive the complete entity of an object in the presented physical geometric form, the bright parts appearing whitish or yellowish, the dark parts as grey or black; there were no reports on colour sensations although in very rare and brief instances coloured tinges were noticed by patients.

The observation that patient 2 could readily name an object upon its first presentation to his visual field is of particular importance, and is in line with our observation of retinotopically correct perception from DS experiments and from the other patients who recognized a line and its direction clearly. This does not mean that the patients had undisturbed percepts. Patients reported some wobbling of the image, probably owing to a relatively low image capture frequency (5–7 Hz) to which they adapted quickly.

As expected, patient performance improved over time. Practising with the MPDA between 4 to 6 h daily, they had to learn to control their eye position because each object was presented within a relatively small field of vision ($11^\circ \times 11^\circ$). Patient 2 reported that the two lines of the letter L were initially moving slightly independently of each other, but that they appeared connected at the corner after approximately one week. Apparently the binding of correlated motion cues can be regained quickly (see electronic supplementary material, chapter 3d and chapter 5, movie 9). If patients were asked to point to an object they had discovered there was clearly improvement of visuomotor abilities within a week.

(f) *Future concepts*

Methodological and technical aspects: our first approach was designed as a short duration study of up to several weeks in only a few patients in order to achieve a proof-of-concept for a cable bound version of a subretinal active implant. Our ongoing follow-up study is employing the next-generation system (Alpha IMS; [40], produced by Retina Implant AG, Reutlingen, Germany), where an encapsulated secondary coil for power and signal transmission is positioned subdermally behind the ear, with a primary coil clipped magnetically on top. We also anticipate that lateral processing in terms of mutual inhibition of pixels, as performed in centre-surround receptive field processing will improve contrast vision and spatial resolution. Penetrating three-dimensional electrodes as developed by various groups may improve the contact to the bipolar cell layer but may be more damaging to the retina.

7. CONCLUSION

This study demonstrated that subretinal micro-electrode arrays can restore visual percepts in patients blind from hereditary retinal degenerations to such an extent that localization and recognition of objects can provide

useful vision, up to reading letters. Despite all remaining biological and technical challenges, our results offer hope that restoration of vision in the blind with electronic retinal prostheses is a feasible way to help those who cannot profit from emerging gene therapy and/or the application of neuroprotective agents. The advantage of our approach is that all parts of the device can be implanted invisibly in the body, that inner retina processing can be used and that a continuous, stable image with unmatched spatial resolution is perceived. Still further development is necessary to provide long term stability, improved contrast, spatial resolution and increased field size through multiple chip implantation. Nevertheless, the present study provides proof-of-concept that electronic subretinal devices have the potential to improve visual function from a state of complete blindness to one of low vision that allows localization and recognition of objects up to reading capability.

We are very grateful to all who contributed to the 'SUBRET' project; for names of contributors, funding organizations and disclosure of interest we refer to electronic supplementary material.

REFERENCES

- Congdon, N., O'Colmain, B., Klaver, C. C., Klein, R., Munoz, B., Friedman, D. S., Kempen, J., Taylor, H. R. & Mitchell, P. 2004 Causes and prevalence of visual impairment among adults in the United States. *Arch. Ophthalmol.* **122**, 477–485.
- Jones, B. W. & Marc, R. E. 2005 Retinal remodeling during retinal degeneration. *Exp. Eye Res.* **81**, 123–137. (doi:10.1016/j.exer.2005.03.006)
- Zrenner, E. 2002 Will retinal implants restore vision? *Science* **295**, 1022–1025. (doi:10.1126/science.1067996)
- Rizzo 3rd, J. F., Wyatt, J., Loewenstein, J., Kelly, S. & Shire, D. 2003 Perceptual efficacy of electrical stimulation of human retina with a microelectrode array during short-term surgical trials. *Invest. Ophthalmol. Vis. Sci.* **44**, 5362–5369. (doi:10.1167/iops.02-0817)
- Dommel, N. B., Wong, Y. T., Lehmann, T., Lovell, N. H. & Suaning, G. J. 2009 A CMOS retinal neurostimulator capable of focussed, simultaneous stimulation. *J. Neural Eng.* **6**, 035006. (doi:10.1088/1741-2560/6/3/035006)
- Yanai, D., Weiland, J. D., Mahadevappa, M., Greenberg, R. J., Fine, Y. I. & Humayun, M. S. 2007 Visual performance using a retinal prosthesis in three subjects with retinitis pigmentosa. *Am. J. Ophthalmol.* **143**, 820–827. (doi:10.1016/j.ajo.2007.01.027)
- Hornig, R. *et al.* 2005 A method and technical equipment for an acute human trial to evaluate retinal implant technology. *J. Neural Eng.* **2**, S129–S134. (doi:10.1088/1741-2560/2/1/014)
- Fujikado, T. *et al.* 2007 Evaluation of phosphenes elicited by extraocular stimulation in normals and by suprachoroidal–transretinal stimulation in patients with retinitis pigmentosa. *Graefes Arch. Clin. Exp. Ophthalmol.* **245**, 1411–1419. (doi:10.1007/s00417-007-0563-z)
- Palanker, D., Vankov, A., Huie, P. & Baccus, S. 2005 Design of a high-resolution optoelectronic retinal prosthesis. *J. Neural Eng.* **2**, S105–S120. (doi:10.1088/1741-2560/2/1/012)
- Zhou, J. A., Woo, S. J., Park, S. I., Kim, E. T., Seo, J. M., Chung, H. & Kim, S. J. 2008 A suprachoroidal electrical retinal stimulator design for long-term animal experiments and *in vivo* assessment of its feasibility and biocompatibility in rabbits. *J. Biomed. Biotechnol.* **2008**, 547428. (doi:10.1155/2008/547428)

- 11 Gerding, H., Benner, F. P. & Taneri, S. 2007 Experimental implantation of epiretinal retina implants (EPI-RET) with an IOL-type receiver unit. *J. Neural Eng.* **4**, S38–S49. (doi:10.1088/1741-2560/4/1/S06)
- 12 Winter, J. O., Cogan, S. F. & Rizzo III, J. F. 2007 Retinal prostheses: current challenges and future outlook. *J. Biomater. Sci. Polym. Ed.* **18**, 1031–1055. (doi:10.1163/156856207781494403)
- 13 Walter, P., Kisvarday, Z. F., Gortz, M., Alteheld, N., Rossler, G., Stieglitz, T. & Eysel, U. T. 2005 Cortical activation via an implanted wireless retinal prosthesis. *Invest. Ophthalmol. Vis. Sci.* **46**, 1780–1785. (doi:10.1167/iovs.04-0924)
- 14 DeMarco Jr, P. J., Yarbrough, G. L., McLean, G. Y., Sagdullaev, B. T., Ball, S. L. & McCall, M. A. 2007 Stimulation via a subretinally placed prosthetic elicits central activity and induces a trophic effect on visual responses. *Invest. Ophthalmol. Vis. Sci.* **48**, 916–926. (doi:10.1167/iovs.06-0811)
- 15 Stett, A., Barth, W., Weiss, S., Haemmerle, H. & Zrenner, E. 2000 Electrical multisite stimulation of the isolated chicken retina. *Vision Res.* **40**, 1785–1795. (doi:10.1016/S0042-6989(00)00005-5)
- 16 Eckhorn, R. et al. 2006 Visual resolution with retinal implants estimated from recordings in cat visual cortex. *Vision Res.* **46**, 2675–2690. (doi:10.1016/j.visres.2006.01.034)
- 17 Guenther, E., Troger, B., Schlosshauer, B. & Zrenner, E. 1999 Long-term survival of retinal cell cultures on retinal implant materials. *Vision Res.* **39**, 3988–3994. (doi:10.1016/S0042-6989(99)00128-5)
- 18 Sachs, H. G., Schanze, T., Brunner, U., Sailer, H. & Weisenack, C. 2005 Transscleral implantation and neurophysiological testing of subretinal polyimide film electrodes in the domestic pig in visual prosthesis development. *J. Neural Eng.* **2**, S57–S64. (doi:10.1088/1741-2560/2/1/008)
- 19 Stett, A., Mai, A. & Herrmann, T. 2007 Retinal charge sensitivity and spatial discrimination obtainable by subretinal implants: key lessons learned from isolated chicken retina. *J. Neural Eng.* **4**, S7–S16. (doi:10.1088/1741-2560/4/1/S02)
- 20 Schmid, H., Herrmann, T., Kohler, K. & Stett, A. 2009 Neuroprotective effect of transretinal electrical stimulation on neurons in the inner nuclear layer of the degenerated retina. *Brain Res. Bull.* **79**, 15–25. (doi:10.1016/j.brainresbull.2008.12.013)
- 21 Besch, D., Sachs, H., Szurman, P., Gulicher, D., Wilke, R., Reinert, S., Zrenner, E., Bartz-Schmidt, K. U. & Gekeler, F. 2008 Extraocular surgery for implantation of an active subretinal visual prosthesis with external connections: feasibility and outcome in seven patients. *Br. J. Ophthalmol.* **92**, 1361–1368. (doi:10.1136/bjo.2007.131961)
- 22 Kusnyerik, A. et al. 2008 Preoperative 3D planning of implantation of a subretinal prosthesis using MRI Data. *Invest. Ophthalmol. Vis. Sci.* **49**, E-Abstract 3025.
- 23 Bach, M., Wilke, M., Wilhelm, M., Zrenner, E. & Wilke, R. 2010 Basic quantitative assessment of visual performance in patients with very low vision. *Invest. Ophthalmol. Vis. Sci.* **51**, 1255–1260. (doi:10.1167/iovs.09-3512)
- 24 Wilke, R., Bach, M., Wilhelm, B., Durst, W., Trauzettel-Klosinski, S. & Zrenner, E. 2007 Testing visual functions in patients with visual prostheses. In *Artificial sight: basic research, biomedical engineering, and clinical advances* (eds M. Humayun, J. D. Weiland, G. Chader & E. Greenbaum), pp. 91–110. New York, NY: Springer.
- 25 Schulze-Bonsel, K., Feltgen, N., Burau, H., Hansen, L. & Bach, M. 2006 Visual acuities ‘hand motion’ and ‘counting fingers’ can be quantified with the freiburg visual acuity test. *Invest. Ophthalmol. Vis. Sci.* **47**, 1236–1240. (doi:10.1167/iovs.05-0981)
- 26 Weiland, J. D., Humayun, M. S., Dagnelie, G., de Juan Jr, E., Greenberg, R. J. & Iliff, N. T. 1999 Understanding the origin of visual percepts elicited by electrical stimulation of the human retina. *Graefes Arch. Clin. Exp. Ophthalmol.* **37**, 1007–1013. (doi:10.1007/s004170050337)
- 27 Chow, A. Y., Chow, V. Y., Packo, K. H., Pollack, J. S., Peyman, G. A. & Schuchard, R. 2004 The artificial silicon retina microchip for the treatment of vision loss from retinitis pigmentosa. *Arch. Ophthalmol.* **122**, 460–469. (doi:10.1001/archophth.122.4.460)
- 28 daCruz, L. et al. 2010 Patients blinded by outer retinal dystrophies are able to identify letters using the Argus TM II retinal prosthesis system. *Invest. Ophthalmol. Vis. Sci.* **51**, E-Abstract 2023.
- 29 Koch, C., Mokwa, W., Goertz, M. & Walter, P. 2008 First results of a study on a completely implanted retinal prosthesis in blind humans. *Sensors, 2008 IEEE*, 1237–1240. (doi:10.1109/ICSENS.2008.4716667)
- 30 Richard, G. et al. 2008 Visual perception after long-term implantation of a retinal implant. *Invest. Ophthalmol. Vis. Sci.* **49**, E-Abstract 1786.
- 31 Humayun, M. 2009 Preliminary results from Argus II feasibility study: a 60 electrode epiretinal prosthesis. *invest. Ophthalmol. Vis. Sci.* **50**, E-Abstract 4744.
- 32 Walter, P., Mokwa, W. & Messner, A. 2008 The EPIRET3 wireless introcular retina implant system: design of the EPIRET3 prospective clinical trial and overview. *Invest. Ophthalmol. Vis. Sci.* **49**, E-Abstract 3023.
- 33 Horsager, A., Greenberg, R. J. & Fine, I. 2010 Spatio-temporal interactions in retinal prosthesis subjects. *Invest. Ophthalmol. Vis. Sci.* **51**, 1223–1233. (doi:10.1167/iovs.09-3746)
- 34 Klier, E. M. & Angelaki, D. E. 2008 Spatial updating and the maintenance of visual constancy. *Neuroscience* **156**, 801–818. (doi:10.1016/j.neuroscience.2008.07.079)
- 35 Perez Fornos, A., Sommerhalder, J., Pittard, A. & Safran, A. B. 2008 Simulation of artificial vision: IV. Visual information required to achieve simple pointing and manipulation tasks. *Vision Res.* **48**, 1705–1718. (doi:10.1016/j.visres.2008.04.027)
- 36 Aulhorn, E. 1953 Über Fixationsbreite und Fixationsfrequenz beim Lesen gerichteter Konturen. *Pflügers Arch. Eur. J. Physiol.* **257**, 318–328. (doi:10.1007/BF00363531)
- 37 Perez Fornos, A., Sommerhalder, J. & Pelizzone, M. 2010 Dynamics of visual perception upon electrical stimulation of the retina. *Invest. Ophthalmol. Vis. Sci.* **51**, E-Abstract 3057.
- 38 Jensen, R. J. & Rizzo III, J. F. 2007 Responses of ganglion cells to repetitive electrical stimulation of the retina. *J. Neural Eng.* **4**, S1–S6. (doi:10.1088/1741-2560/4/1/S01)
- 39 Pritchard, R. M. 1961 Stabilized images on the retina. *Sci. Am.* **204**, 72–78. (doi:10.1038/scientificamerican0661-72)
- 40 Rothermel, A., Aryan, L. L., Fischer, N. P., Wuenschmann, M., Kibbel, J. & Harscher, A. 2009 A CMOS chip with active pixel array and specific test features for subretinal implantation. *Solid-State Circuits IEEE J.* **44**, 290–300. (doi:10.1109/JSSC.2008.2007436)

6.4 Curriculum Vitae

EDUCATION	
International Max Planck Research School, IMPRS Eberhard Karls University Tübingen Ph. D. student at the Graduate School for Neural and Behavioural Sciences	11/2007 - today
Free University of Berlin Master of Science in Bioinformatics Thesis: „A Model for Spatio-Temporal Properties of Visual Sensations Evoked by a Subretinal Electrode Array for Restoration of Vision“	10/2004 - 10/2007
Bachelor of Science in Bioinformatics Thesis: „Contrast optimization in functional Nearinfrared-Spectroscopy (fNIRS) by variation of the stimulus-design“	10/2001 - 09/2004
Gymnasium Petrinum Recklinghausen Leaving certificate (Abitur)	08/1991 - 06/2000
WORK EXPERIENCE	
University Hospital Tübingen, Institute for Ophthalmic Research Retina Implant Project: analysis of functional tests with implant patients, integration of functional results into biophysical computer models	10/2006 - today
Harvard Medical School, Massachusetts General Hospital Modeling dynamic oxygen and pressure variables in cortical blood vessels using optical imaging methods	10/2005 - 04/2006
Charité Medical School, Berlin Neuroimaging Center Optical imaging methods: Development of a non-invasive imaging method for early detection of tumor tissue using near-infrared spectroscopy	12/2003 - 09/2005 & 05/2006 - 09/2006